Volume I

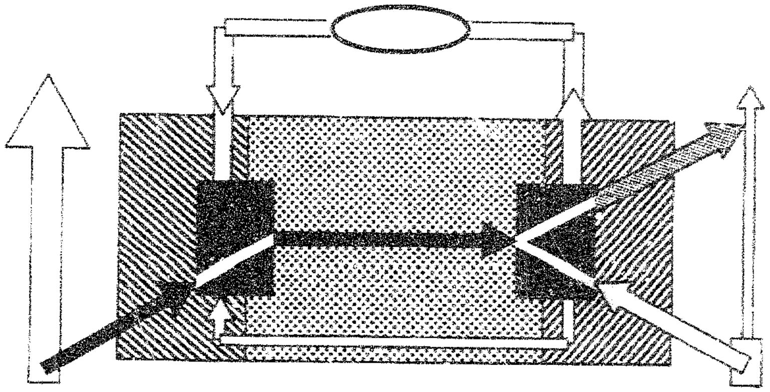

IEA Programme of R, D & D on Advanced Fuel Cells

Annex VII: Solid Oxide Fuel Cells
under Real Operating Conditions

Materials and Processes

10th SOFC WORKSHOP

A J McEvoy and K Nisancioglu

Date 28-31 January 1997 Les Diablerets, CH

IEA Classification Level 2: For unrestricted distribution by Contracting Parties to the Agreement within their countries

INTERNATIONAL
ENERGY AGENCY

IEA Annex VII "SOFC under Real Operating Conditions" 1996-98

The main objective will be to assist - through international cooperation - the development of natural gas-fuelled Solid Oxide Fuel Cell (SOFC) technologies through:

(a) the exchange of information to tackle complex problems in stack and systems design and operation;
(b) the consideration of end-user requirements on stack operation with the goal to optimise lifetime of cells and stacks;
(c) a better understanding of interfacial and bulk charge and mass transport mechanisms to optimise cell components under actual SOFC operating conditions; and
(d) the study of alternative materials in case traditional concepts are too expensive or are too short-lived.

Participating countries are Australia, Denmark, France, Germany, Japan, Netherlands, New Zealand, Norway, Switzerland, United Kingdom, United States. The work in the Task is divided into the following four Subtasks:

Subtask 1: "Balance-of-Plant Technology"
Activity 1.1 "Balance-of-Plant Optimisation by Modelling"
Tackle complex problems in stack and systems modelling by exchange of information. Main Workshop September 1996.
Activity 1.2 "SOFC Activities World-Wide"
Establish an information directory to encourage information exchange on critical aspects of SOFC development (1996, update 1998).
Activity 1.3 "Regulatory Requirements"
Collection of legal, utility and user regulations for installing and operating SOFC plant with the goal to provide SOFC system design code and statutory regulation compliance.

Subtask 2: "Stack and Cell Operating Conditions"
Activity 2.1 "Stack Operating Experience and Evaluation"
Enable comparison of stack performances on a common basis.
Activity 2.2 "Lifetime of Cells": Evaluate effects of operating conditions typical for end-user applications with the goal to improve and demonstrate SOFC lifetime. Main Workshop October 1997.

Subtask 3: "Materials under Operating Conditions"
Develop a better understanding of interfacial/ bulk charge and mass transport mechanisms to optimise cells under actual SOFC operating conditions. The emphasis will be on novel designs and performance of components based on relatively well known materials. Main Workshop January 1997.

Subtask 4: "Materials Innovation"
Develop and qualify new SOFC materials for long-term stability and reduced manufacturing costs. Investigate materials for low-temperature operation < 800°C (Catalogue January 1997, main Workshop May 1998).

Dr. Heinz Nabielek from the Research Centre Jülich, Germany, acts as Operating Agent.

Volume I

IEA Programme of R, D & D on Advanced Fuel Cells

Annex VII: Solid Oxide Fuel Cells
under Real Operating Conditions

Materials and Processes

10th SOFC WORKSHOP

A J McEvoy and K Nisancioglu

Date **28-31 January 1997** **Les Diablerets, CH**

Executive Summary

Jointly between Subtask 3 and Subtask 4, the 10th IEA SOFC Workshop was held on "Materials and Processes" in Les Diablerets, Switzerland, during 28-31 January 1997. It was attended by 45 people from ten participating countries.

Following the spirit of the 4th Lausanne Workshop and the 7th Wadahl Workshop, its highlights were on
- cathode processes
- cathode materials science
- anode processes and materials science
- electrolyte
- interconnect materials
- modelling
- fabrication
- new trends in cell fabrication and SOFC design

The 1992-95-97 Workshop series places on record the significant contribution of the IEA cooperation to the progress in the understanding of interfacial processes, the reduction of overpotentials, internal reforming and in the success of in-situ monitoring. A spectacular example of monitoring and diagnostics capability is the in-situ observation of a functioning SOFC with synchrotron radiation by the Risø group.

The optimum for thin electrolytes was clearly established and success can be demonstrated for long-term SOFC stability and cycling behaviour. Contact problems were addressed both theoretically and experimentally.

In contrast to some congresses and symposia, controversial subjects were discussed openly, e.g. the problems related to the measurement of electrode (half-cell) overpotentials in thin electrolyte cells. To clarify the issue, ECN suggested a dedicated IEA topical meeting on the investigation and standardisation of electrochemical measurements.

A further highlight of the present meeting was the reports from Imperial College London and University of Delft, Netherlands on enhancement of spray pyrolysis technology by the synergy of an applied electric field, which enhances spray dispersion and enables SOFC-related materials to be fabricated to high quality with low costs.

It is evident that the innovative and constructive spirit of previous Workshops has been effectively maintained.

Looking to the future, the Meeting ended with a reminder by the Operating Agent of upcoming events: an Annex Meeting in association with the 5th International Symposium at Aachen in June; a September Workshop at ECN specifically on issues of lifetime and degradation; and in May 1998, at a location still to be determined, a materials innovation joint Workshop. There was also the possibility to organise a topical meeting on the issue which had stimulated so much discussion - the reference electrodes and theoretical definitions - should there be sufficient interest and motivation for that within the IEA SOFC group.

Heinz Nabielek Forschungszentrum Jülich Germany	Augustin J McEvoy EPFL Lausanne Switzerland

INDEX

IEA Workshop: "Materials and Processes"
Annex VII: SOFC under Real Operating Conditions
January 28 - 31 , 1997
Les Diablerets, Switzerland

Volume I

IEA Workshop: "Materials and Processes"

Annex VII: SOFC under Real Operating Conditions

January 28 - 31 , 1997
Les Diablerets, Switzerland

INTRODUCTION

The first word of our Workshop is a word of welcome to Les Diablerets. To welcome you on behalf of the International Energy Agency will be the pleasant duty of our Operating Agent, Heinz Nabielek. I have been asked by Leo Dubal to act on his behalf and extend the welcome of the Swiss Federal Office of Energy, as well as my own greetings to you all, colleagues in the SOFC community. This country has been solidly committed to this international collaboration in SOFC research and development since the first Workshop in Charmey in July 1989. We have all tried to contribute, and we are all certainly at a benefit, not least by the construction of that world-wide SOFC community which has already assembled here in Switzerland several times.

On the technical side there was originally a naivety - the accepted idea that the appropriate materials, adjusted for obvious parameters like thermal expansion, and placed in contact will result in a functional fuel cell. In practice it has not been so easy, but the obvious technical progress and increased understanding since then owes a lot to the IEA cooperation. It is not so much that spectacular breakthroughs have been announced at our Workshops, but rather that on these occasions we have a stimulating venue, marked by friendship and respect rather than rivalry, in which good ideas have been exchanged and nurtured by an open exchange of views. I could mention several, if only as examples. Michel Kleitz refining the simple "three phase boundary" model by his presentation on "reaction pathways"; the realisation that control of structure on the micron scale must be complemented by a sensitivity to effects on the nanometric scale, particularly at interfaces; the importance of defect chemistry and nonstoichiometry of cell components in which as a consequence reaction and transport properties differ from those of the standard materials; the hysteresis effects induced by current, thermal cycling or other operational parameters, to which the fuel cell reacts as a dynamic system by change of characteristics, not just a passive assembly with behaviour determined only by materials specification. Several items are promised for this Workshop to carry on that innovative tradition, for example the in-situ monitoring of the reaction of cell materials to operating conditions using synchrotron radiation, an elegant procedure to be described by Finn-Willy Poulsen.

Before ending these words of welcome and introduction, some events must be mentioned. Firstly the death of Svein Sunde's father, so Svein has had to withdraw from our meeting, Svein has the sympathy of us all. Then there is the award of the doctoral degree to our colleague Fred van Heuveln. He has been a member of the IEA SOFC community for so long and has contributed so significantly that we had all awarded him an honorary doctorate in our minds years ago. He is to be congratulated on the academic endorsement. Finally Joep Schoonman is unable to be present due to illness, but is represented by an associate.

The Workshop schedule has been arranged to enable you to benefit also from the spectacular environment of the Vaud Alps surrounding Les Diablerets. So please make of this week's meeting an event to remember!

Augustin McEvoy,
EPFL, Lausanne.

Operating Agent's Report - IEA Workshop, Les Diablerets, Jan. 1997

Dr. Heinz Nabielek
IEA SOFC Operating Agent (Annex VII)
KFA-IEV
Forschungszentrum Juelich GmbH
D-52425 Jülich, Germany

The agreed topics and engagements in the Subtasks of the IEA SOFC action which converged in the present Workshop are recalled.

Subtask 3: Materials under Operating Conditions (Nisancioglu): 165 staff-months. Optimise cell components by the development of a better understanding of interfacial and bulk charge/ mass transport under actual SOFC operating conditions. Focus on micro- and nanoscale processes and three-phase boundary regions with emphasis on novel designs and performance of components based on relatively well known materials.

Subtask 4: Materials Innovation (Naoumidis): 155 staff-months. Develop and qualify new SOFC materials for long-term stability and reduced manufacturing costs. Investigate materials for low temperature operation (600-800 C).

Jointly between Subtask 3 and Subtask 4, the 10th IEA SOFC Workshop was held on "Materials and Processes" in Les Diablerets, Switzerland, 28-31 January 1996 (with many thanks to Augustin McEvoy who - in addition to the Subtask Leaders - contributed strongly to the scientific and organisational success). It was attended by 45 people from 10 participating countries.

Following the spirit of the 4th Lausanne Workshop and the 7th Wadahl Workshop, its highlights were on

- cathode processes
- cathode materials science
- anode processes and materials science
- electrolyte
- interconnect materials
- modelling
- fabrication
- new trends in cell fabrication and SOFC design

Significant progress is discernible in the 1992-95-97 workshop series in the understanding of interfacial processes, the reduction of overpotentials, internal reforming and in the success of in-situ monitoring (Risoe investigation of the interface with synchrotron radiation). The optimum for thin electrolytes was clearly established and success can be demonstrated for long-term SOFC stability and cycling behaviour.

Different from large congresses and symposia, controversial subjects were discussed openly, e.g. the problems related to the measurement of overpotentials in thin-electrolyte cells (getting worse as overpotentials

becoming smaller). To resolve the controversy, ECN suggested a dedicated IEA activity on the investigation and standardisation of electrochemical measurements. Largely missing were discussion and presentations on sealing and contact problems, an area which shall be addressed in the 12th IEA SOFC Workshop May 1998.
After the workshop, Subtask 4 leader (Naoumidis) contacted IEA partners in 10 countries on the content of the cooperation on "Materials Innovation", the preparation of a jointly developed catalogue and on the plans for the 12th Workshop.

IEA SOFC Meeting Sequence

Time	Occasion	Location	Country
May 96	Annex Meeting #1(completed)	ECN Petten	NL
Sep. 96	Workshop SOFC BOP (Subtask 1, completed)	EdF Paris	F
Jan. 97	Workshop Materials & Processes (Subtasks 3+4, completed)	Les Diablerets	CH
June 97	Annex Meeting #2 after SOFC V in Aachen	Aachen	D
Sep. 97	Workshop Lifetime (Subtask 2)	ECN Petten	NL
June 98	Workshop Materials & Processes (Subtasks 3+4)	KFA	D
Oct. 98	Annex Meeting #3 (SOFC Systems, End-of-Annex, Final Reports)	To be determined.	

IEA SOFC
Results from Annex II in the years 1993-95
Targets of Annex VII during the period 1996-98

international energy agency implementing agreements

ENERGY TECHNOLOGY INFORMATION CENTRES

- Centre for the Analysis and Dissemination of Demonstrated, Energy Technologies (CADDET)
- IEA Coal Research
- Energy Technology Data Exchange (ETDE)
- Energy Technology Systems Analysis Programme (ETSAP)
- Greenhouse Gas Technology Information Exchange (GREENTIE)
- International Centre for Natural Gas Technology Information
- East-West Electricity Technology Centre*

FOSSIL FUELS TECHNOLOGIES

- Coal Combustion Sciences
- Coal-Liquid Mixtures
- Enhanced Oil Recovery
- Fluidised Bed Combustion
- Fossil Fuel Multiphase-Flow Sciences
- Greenhouse Gases from Fossil Fuel Use
- Testing of High-Temperature, High-Pressure Filters

RENEWABLE ENERGY TECHNOLOGIES

- Bioenergy
- Hydrogen
- Hydropower Technologies*
- Photovoltaic Power Systems
- Solar Heating and Cooling
- Solar Power and Chemical Energy Systems (SolarPACES)
- Wind Turbine Systems

EFFICIENT ENERGY END-USE TECHNOLOGIES

- Advanced Fuel Cells
- Alternative Motor Fuels
- Buildings and Community Systems
- Demand-Side Management
- District Heating and Cooling
- Electric Vehicles
- Energy Conservation in Combustion
- Energy Storage
- Heat Pumping Technologies
- Heat Transfer and Heat Exchangers
- High Temperature Materials
- High-Temperature Superconductivity
- Process Integration Technology for Industrial Systems*
- Pulp and Paper

NUCLEAR FUSION TECHNOLOGY

- Environmental, Safety and Economic Aspects of Fusion Power
- Fusion Materials
- Nuclear Technology of Fusion Reactors*
- Plasma Wall Interaction in TEXTOR
- Reversed Field Pinches
- Stellarator Concept
- Superconducting Magnets for Fusion Power
- Three Large Tokamak Facilities
- Toroidal Physics in, and Plasma Technologies of, Tokamaks with Poloidal Field Divertors

**Implementing Agreements in Preparation*

Results from Annex II in the years 1993-95

All Activity Reports Available

A1 Micromodelling	B1 Lifetime
A2 Stack Modelling	B2 Thermomech. Evaluation
	B3 Sample & Data Bank
	B4 Stack Evaluation
	B5 Instrumentation&Diagnostics

WORKSHOPS

	Location	Date	Title/ Objective
1st Workshop	Charmey CH	July 1989	Mathematical Modelling
2nd Workshop	Hertenstein CH	June 1990	SOFC Evaluation and Characterisation
3rd Workshop	Holmenkollen N	Aug. 1991	Recommended Practices / Models
4th Workshop	Lausanne CH	Aug. 1992	Fundamental Barriers to SOFC Performance
5th Workshop	Jülich D	Mar 1993	Materials, Process Eng. & Electrochemistry
6th Workshop	Rome I	Feb. 1994	General Workshop on all 8 Activities
7th Workshop	Wadahl N	Jan. 1995	Theory and Measurement of Microscale Processes
8th Workshop	Ovronnaz CH	Nov. 1995	Diagnostics Activitiy & End-of-Annex II Workshop
9th Workshop (Subtask 1)	Paris F	Sep. 1996	Balance-of-Plant SOFC Cost Optimization for Base Load Operation
10th Workshop (Subtask 3+4)	**Diableret CH**	**Jan. 1997**	**Materials and Processes**
11th Workshop (Subtask 2)	TBD	Fall 1997	SOFC Lifetime and Degradation
12th Workshop (Subtask 4)	TBD	1998	New SOFC Materials

SOFC Activity Matrix (Person-Months for the three year period 1993-95)

SUBTASK	Country Participating Organisations Activity	DK Risø ELSAM DTH Lyngby Univ. Odense	I ENEA CISE Eniricerche Univ. Genova CNR-TAE CNR-CSTE	J NEDO Fuji Sanyo Mitsui CRIEPI EPDC Murata	NL ECN Univ. Delft Univ. Twente	N NTH Statoil IFE Uni Oslo	CH EPFL ETHZ EMPA Sulzer	UK Imp. College British Gas Univ. Keele ETSU Harwell Tioxide Cookson	D KFA Jülich DLR Stuttgart Siemens Dornier Univ. Dresden	Sum Activity
SUBTASK A: Numerical Modelling, Experimental Data Base and Validation	***A1 Micro Modelling***	10	8	0	2	30 ▨	12	8	12	82
	A2 Stack Modelling	6	14	0	2	12	0	12	25 ▨	71
SUBTASK B: Recommended Practices and SOFC Products Evaluation	***B1 Long-term stability under operating cond.***	0	3	0	28 ▨	0	12	8	6	57
	B2 Thermomechanical Evaluation	0	35 ▨	6	1	0	4	0	4	50
	B3 Sample and Data Bank	24 ▨	0	0	11	3	6	8	6	58
	B4 Stack evaluation from Systems viewpoint	6	0	41 ▨	2	0	1	5	16	71
	B5 Instrumentation & Diagnostics	1	5	0	1	3	12	3	1	26
	B6 Patent search	1	0	1	1	0	1	4	1	9
	Total	48	65	48	48	48	48	48	71	424 424

▨ *……………Activity Leader*

Heinz Nabielek
Operating Agent SOFC

FORSCHUNGSZENTRUM JÜLICH GmbH **KFA**

FUEL CELL PROGRAMME

Future Research Areas in Micromodelling

- **Measurement of thermochemical data; thermodynamic modelling**
- **Solid state reactions under operational conditions**
- **Effect of large current densities on the properties of interfaces and the bulks of materials**
- **Basic research on electrocatalytic (and autocatalytic) properties of materials**
- **Surface diffusion**
- **Effect of impurity elements on interfacial and bulk properties**
- **Mathematical modelling of micro/nano-scale processes for electrode optimisation and interfacial engineerir**

Heinz Noble

IEA Operating Agent

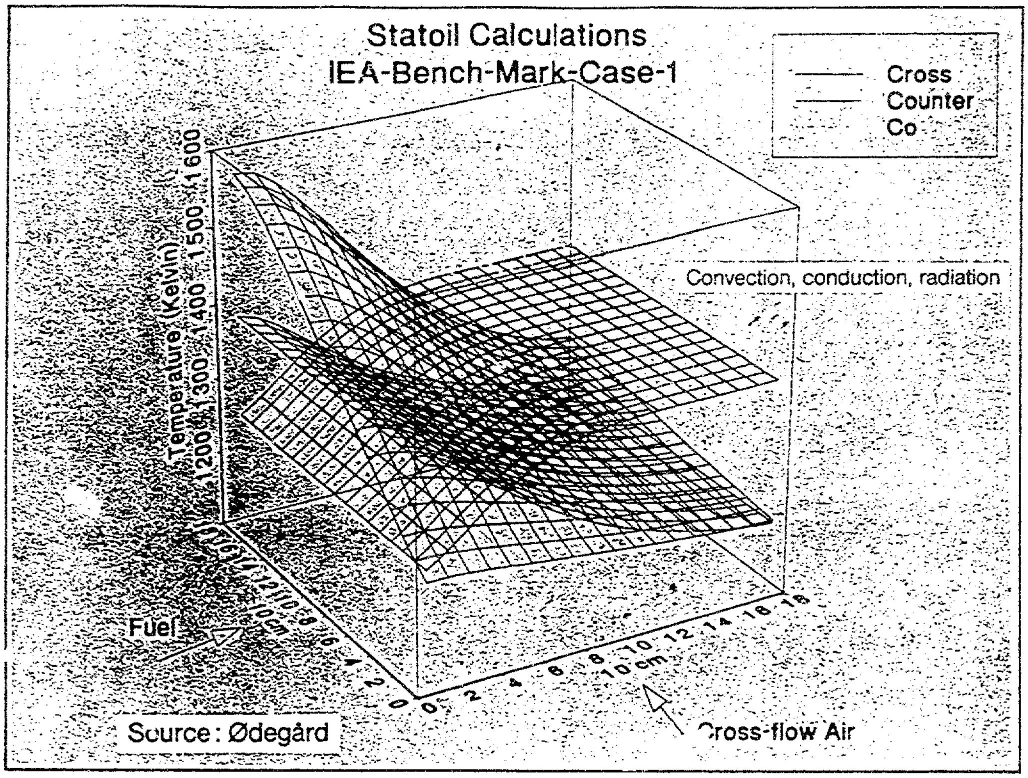

Source: Ødegård

Single-cell stack

A2: Stack Modelling Benchmark Test #1

Comparison of cell voltages (V)

Participant	**Crossflow**	**Counterflow**	**Coflow**
Dornier	0.707	0.713	0.707
ECN	——	——	0.704
Eniricerche	0.723	0.730	0.722
Inst. f. Energiteknikk	0.700	0.710	0.710
Uni Genova	0.717	——	——
KFA	0.708	0.712	0.706
Siemens	0.715	0.716	0.712
Statoil	0.704	0.709	0.702
Risø	0.707	0.710	0.703

—— Available model did not allow the computation

Result

- **Benchmark test #1 has demonstrated that 2-D SOFC simulation codes are available, within the IEA community, able to predict performance reliably.**
- **Good agreement between participants**

ROUND ROBIN ECN CELLS

FREE TESTING PROTOCOL

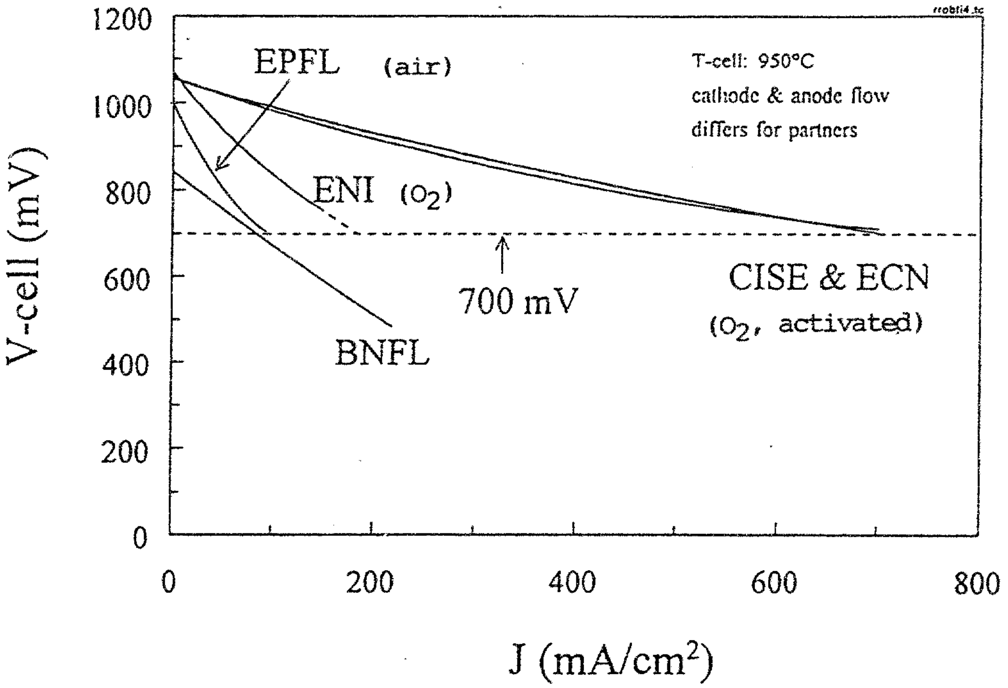

FORSCHUNGSZENTRUM JÜLICH GmbH **KFA**

FUEL CELL PROGRAMME

Thermomechanical Evaluation

GEOMETRICAL PARAMETERS	
thickness	**completed phase 1**
roughness	**completed phase 2**
waviness	**completed phase 2**
warpage	**completed phase 2**
porosity	**completed phase 1**

THERMAL PARAMETERS	
specific heat	
thermal diffusivity/ conductivity	**in progress**
thermal cycling resistance	
thermal expansion	**in progress**
thermal shock resistance	

PHYSICAL/ MECHANICAL PARAMETERS	
apparent density	completed phase 1
gas tightness	
Young's modulus	completed phase 2
biaxial flexure strength	
--piston on 3 ball test method	completed phase 1
--double ring test method	completed phase 2
fracture toughness	completed phase 2
adhesion	
crack propagation	

B4 Activities		Contribution			
		A Inform.	B Report	C Contrib.	D Review
(L 1)	List Existing Information	ELSAM ECN BG	NEDO CRIEPI		
(S 1)	Reforming Method and Conditions	KFA	EPDC		ELSAM KFA Dornier
(S 2)	Air / Fuel Preheating	ECN Sanyo KFA	NEDO		ELSAM BG Dornier
(S 3)	Air / Fuel Utilization	ECN KFA	Sanyo		ELSAM Dornier
(S 4)	Anode Gas Recycling	ECN BG NEDO KFA	NEDO		ELSAM Dornier
(S 5)	Working Pressure	ECN NEDO	Fuji	CRIEPI	ELSAM
(S 6)	Working Temperature	ELSAM ECN BG Fuji	CRIEPI	ELSAM	
(S 7)	Startup and Shutdown Sequence Stand-by Mode	BG EPDC NEDO	Fuji		ELSAM Dornier
(S 8)	Use of Recovered Heat	ELSAM ECN Mitsui	ELSAM		BG
(S 9)	SOFC Combined Cycle	ELSAM ECN	ELSAM		BG
(S 10)	BOP Components (1000°C)	ELSAM BG NEDO	NEDO	ELSAM	ECN Dornier
(M 1)	Customers Requirements	ELSAM NEDO	NEDO		ELSAM ECN BG
(M 2)	Competing Technology	ELSAM EPDC	ECN	Mitsui	ELSAM ECN BG
(E 1)	Stack Design Requirements Operating Conditions	ELSAM ECN	NEDO		ELSAM ECN

Contribution A: Provide information and / or data for the writers and NEDO
B: Responsible for writing draft and final report
C: Write a part of report
D: Review draft report and give comments to the writers and NEDO

Annex VII SOFC 1996-98

SOLID OXIDE FUEL CELLS
UNDER REAL OPERATING CONDITIONS

Participating countries:

Australia
Denmark
France
Germany
Japan
Netherlands
New Zealand
Norway
Switzerland
United Kingdom
United States

Heinz Nabielek
September 199

IEA Operating Agent

Annex VII SOFC 1996-98

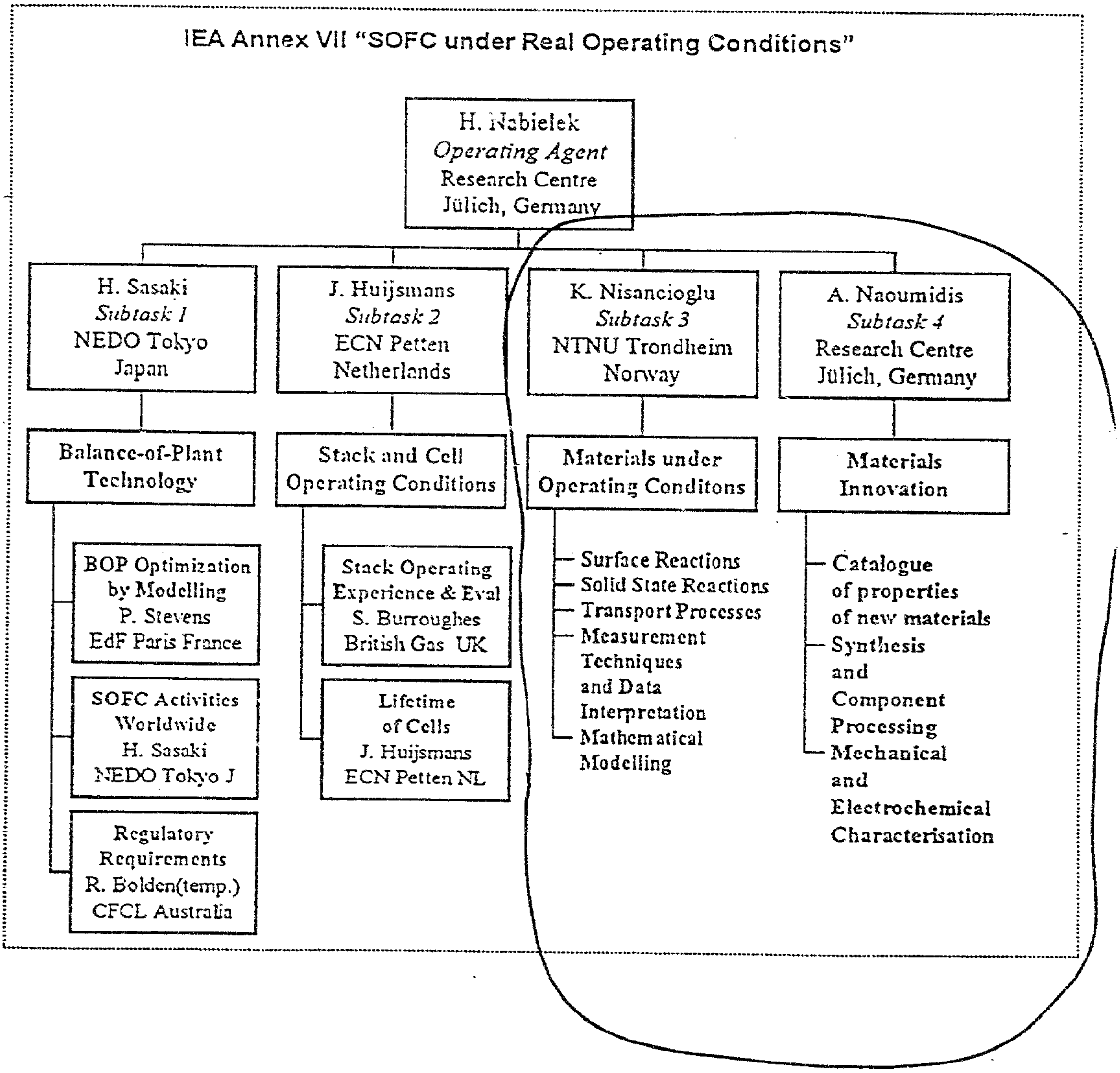

IEA Annex VII "SOFC under Real Operating Conditions"

H. Nabielek
Operating Agent
Research Centre
Jülich, Germany

- H. Sasaki, *Subtask 1*, NEDO Tokyo Japan
  - Balance-of-Plant Technology
    - BOP Optimization by Modelling, P. Stevens, EdF Paris France
    - SOFC Activities Worldwide, H. Sasaki, NEDO Tokyo J
    - Regulatory Requirements, R. Bolden(temp.), CFCL Australia
- J. Huijsmans, *Subtask 2*, ECN Petten Netherlands
  - Stack and Cell Operating Conditions
    - Stack Operating Experience & Eval, S. Burroughes, British Gas UK
    - Lifetime of Cells, J. Huijsmans, ECN Petten NL
- K. Nisancioglu, *Subtask 3*, NTNU Trondheim Norway
  - Materials under Operating Conditons
    - Surface Reactions
    - Solid State Reactions
    - Transport Processes
    - Measurement Techniques and Data Interpretation
    - Mathematical Modelling
- A. Naoumidis, *Subtask 4*, Research Centre Jülich, Germany
  - Materials Innovation
    - Catalogue of properties of new materials
    - Synthesis and Component Processing
    - Mechanical and Electrochemical Characterisation

Objectives of SOFC Work 1996-98

The main objective of this Task will be to assist - through international cooperation - the development of natural gas-fuelled Solid Oxide Fuel Cells (SOFC) technologies through:

–the exchange of information to tackle complex problems in stack/systems design and operation;

–the consideration of end-user requirements on stack operation with the goal to optimise lifetime

–a better understanding of interfacial and bulk charge and mass transport mechanisms to optimise cell components under actual SOFC operating conditions; and

–the study of alternative materials in case traditional concepts are too expensive or are too short-lived

ANNEX VII: SOFC under Real Operating Conditions

Activity Matrix:

	Subtask 1	Subtask 2	Subtask 3	Subtask 4
Australia	6	9	6	27
Denmark	0	16	16	16
France	12	0	18	18
Germany	15	13	10	20
Japan	29	7	6	6
Netherlands	10	30	7	7
New Zealand	12	2	18	18
Norway	1	0	28	19
Switzerland	0	16	32	0
UK	13	28	4	5
United States	3	9	20	19

Subtask 3: Materials under Operating Conditions (Nisancioglu) *165 staff-months*

Goals:

- **Optimise cell components by the development of a better understanding of interfacial and bulk charge/mass transport**
- **Focus on processes and three-phase boundary regions with emphasis on novel designs and performance of components based on relatively well known materials.**

Workplan:
– Design of electrodes and electrode-electrolyte interfaces, such as (i) multilayered/ multicomponent powder composite electrodes (ii) doped electrolytes (iii) doped dense electrodes; for the purpose of lowering the cell overpotential, lowering the operating temperature, stability, increased lifetime etc.
– The following processes have to be investigated under conditions relevant to SOFC operation: **Surface Reactions** (electrochemical reactions, surface exchange reactions, adsorption/ adsorbed species, catalytic properties-high current densities-high overpotentials). **Solid State Reactions** (bulk phases, interfacial phases-their formation and properties-effects on component performance). **Transport Processes** (bulk diffusion, fast diffusivity paths-grain boundary-pores, exchange at grain surfaces, surface diffusion, effect of electric field, limitations in the gas phase).
– Measurement techniques and data interpretation for investigation of the above processes of interest.
– Mathematical modelling as a tool for correlating complex data, understanding of coupled phenomena and development of theoretical tools for design purposes.

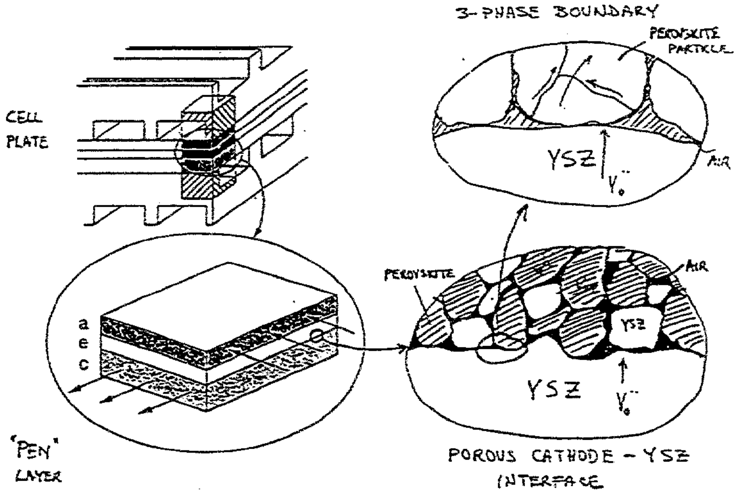

Figure 2. The scope, scale and processes of subtask on micromodeling.

Source: Nisancioglu

Subtask 4: Materials Innovation (Naoumidis) *155 staff-months*

Goals:

- Develop and qualify new SOFC materials for long-term stability and reduced manufacturing costs.
- Investigate materials for low temperature operation (600-800°C).

Workplan:
Literature/ laboratory research
Materials manufacture and characterisations, component fabrication.
Mechanical and electrochemical testing.

Schedule:

Catalogue of properties of new materials	
Identify and contact partners	December 1996
Initiate cooperation during Subtask 3+4 Workshop	January 1997
Main Workshop on New Materials	early in 1998
Complete Final Report	by October1998

ANNEX VII: SOFC under Real Operating Conditions

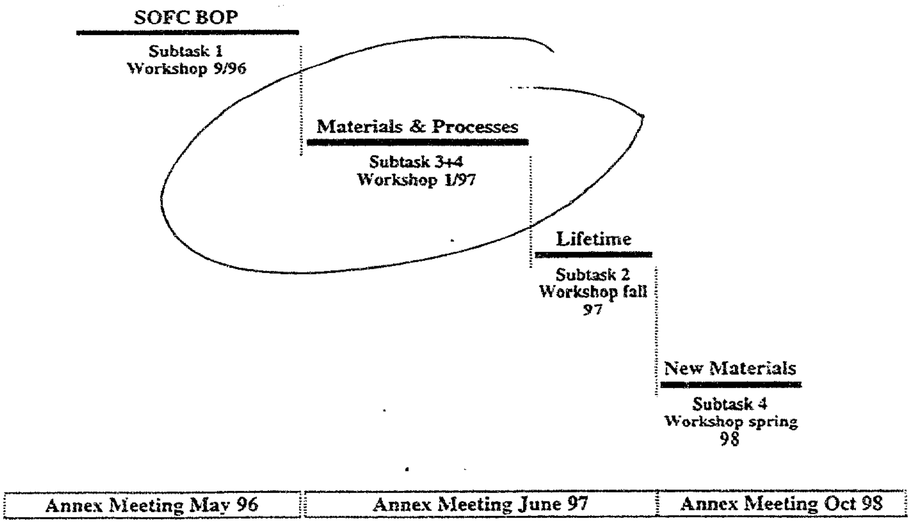

SOFC BOP
Subtask 1
Workshop 9/96

Materials & Processes
Subtask 3+4
Workshop 1/97

Lifetime
Subtask 2
Workshop fall 97

New Materials
Subtask 4
Workshop spring 98

Annex Meeting May 96 | Annex Meeting June 97 | Annex Meeting Oct 98

This Workshop

- I would like to express my warm welcome to participants from all parts of the world
- I am impressed with the good preparation of this Workshop as shown, i.a., by the titles of papers.
  With many thanks to Kemal Nisancioglu and Gus McEvoy.
- Subtask leaders and Operating Agent will prepare Proceedings summary suitable for
  FINAL REPORT 1998
- I wish you an enjoyable time and that you will be able to return home with solutions to your long-standing problems.

TUE	WED	THU	FRI
	CATHODE PROCESSES	ANODE MATERIALS	METHODOLOGY
			FABRICATION
	CATHODE MATERIALS	ELECTROLYTE	WORKSHOP "new trends"
		INTERCONNECT	
	ANODE PROCESSES		
		MODELLING	
WELCOME & INTRODUCTION	WORKSHOP "cathode"	WORKSHOP "electrolyte & interconnect"	

Definition and Measurement of Oxygen Transport Properties in Ceramic Oxides

Svein Sunde
Centre for Materials Science, University of Oslo, Gaustadalleen 21, N-0371 Oslo, Norway

Introduction

In many ceramic oxides of the fluorite or the perovskite type, lattice oxygen is highly mobile. This property alludes to the possibility of using these materials in dense membranes for oxygen separation [1]. High rates of oxygen transport are also expected to play a role in the electrocatalytic properties of porous or dense cathodes for solid-oxide fuel-cells (SOFCs) [2,3]. Oxygen-conducting yttria-stabilized zirconia (YSZ) is currently regarded as the state-of-the-art electrolyte in SOFCs [3]. On the other hand, in ceramic interconnect materials rates of oxygen transport as low as possible are desired [3,4]. The measurement and prediction of transport coefficients for these oxides are therefore of considerable practical importance, in addition to any contribution to our fundamental understanding of transport phenomena in solids that might emerge from such a study. Needless to say, attempts at characterizing transport rates of oxygen and relating these to the various transport coefficients for oxides are numerous, and many experimental methods exist that may or has been developed or adapted to this end [4-15]. Nevertheless, interpretation of results is often hampered by complications introduced by sample quality, or by practical problems and limitations associated with the methods used. In addition, the definition of a transport property and its relation to a given measurement method appear to cause complications [16], exacerbating comparison of transport properties of different materials. In some cases, materials of a very similar or identical composition are claimed to have widely different transport coefficients [7].

The purpose here is to briefly review the basic definitions of some frequently used transport coefficients, to point out the assumptions underlying these definitions and some current problems concerning relations between definitions and experimental methods. Below we will first present thermodynamic and statistical descriptions of transport of charged species in solids in general, before discussing briefly some selected experimental methods. Since many of the concepts and methods introduced are covered extensively in the literature already, the focus of the latter section will be on some issues of special concern when dealing with oxygen transport in oxides.

Thermodynamic definitions of transport parameters

In general terms, transport coefficients enable one to calculate a flux given the magnitude of one or more driving force(s) on which the flux depend(s). Converserly, transport coefficients are determined by relating measurements of fluxes to measured driving forces. Therefore, careful definitions of the two latter quantities are required for the unambigous definition of a transport coefficient. Fluxes are uniquely defined once their units and a frame of reference is given. For example, mass flux may in general be defined in molar, mass or particle number units, and may be given relative to a fixed frame of reference or relative to some average velocity [17]. If a concentration gradient causes a flow of neutral species from one location to another, the driving force may be defined in terms of the concentration gradient itself, the activity gradient associated with the concentration gradient, or the associated gradient in chemical potential [10]. In addition, the functional dependency of the flux on the driving force is not given *a priori*. I view of these comments we will make the following assumptions:

1) The fluxes depend linearly on the driving forces. This empirical relation, of which the most famous example is probably Ohm's law, is observed to hold in a large number of systems, and is also often argued for by linearizing Boltzmann factors in atomistic models of transport properties [18]. It is expected to hold as long as the gradients are small compared to interpotential distances, therefore with the notable exception of interphases in many electrochemical systems [19].

2) We consider the flux of one or more species in a solid. However, the mobility of at least one component in the solid is sufficently low that its sublattice may serve as a reference in rest with respect to the laboratory frame [16].

The most general equation we can write for the flux vector $\vec{N}_i$ of species i is now

$$\vec{N}_i = \Sigma_j L_{ij} \vec{X}_j \ ; \quad L_{ij} = L_{ji} \tag{1}$$

where $\vec{X}_j$ is a vector quantity representing a driving force, and L_{ij} are transport coefficients of flux i with respect to driving force j. (We will for most of the remainder use $[\vec{N}_j]$= particles $cm^{-2}\ s^{-1}$.) For isothermal systems, $\vec{X}_j$ is usually taken to be the negative of the gradient of the electrochemical potential of species j for charged species, and the chemical potential for neutral species. The relation to the right in Eq. 1 is known as the Onsager reciprocity relation, valid in systems not involving magnetic fields [18]. In addition to the assumptions above, the following assumptions are also commonly made when defining and measuring transport propertes:

3) L_{ij}=0 if i≠j. This is, among other things, tantamount to assuming that all species transported have a single, stable valency [13,20].

4) If exchange of species with the surrounding atmosphere, or with a contacting solid phase, is involved this exchange is reversible.

5) Effects due to volume changes or macroscpic transport are negligible [12].

6) Quasi-neutrality in the solid prevails [12].

7) The system under study is isotropic, and the transport coefficients are consequently scalar quantities.

8) There is local equilibrium between the various species in the system [12].

9) There are no external or internal short circuits for transport of the species for which the flux is measured.

10) One-dimensional theory is applicable.

11) The following definition of electrochemical potential η_j (in V A s) of species j is applicable:

$$\eta_j = \mu_j + z_j q \phi \tag{2}$$

where z_j the charge number, q the elementary charge, and ϕ the electric potential. μ_j is the chemical potential of species j

$$\mu_j = \mu_j^0 + kT\ln a_j \tag{3}$$

in which μ_j^0 is a reference chemical potential, k the Boltzmann constant, T the temperature, and a_j the activity of species j.

The right hand side of Eq. 2 thus assumes that one may identify the free energy of species j as the sum of a free energy due to the chemical interaction of species j with all other species in its environment and a contribution due to an electric potential (spatially averaged [21]). Note that this separation of chemical interaction from electric interaction, although intuitively acceptable, is associated with problems in terms of experimental determination, as discussed in Ref [19]. There are several solutions to this problem [18,19], but here we will simply work with the ill-defined quantities in Eq. 2 as long as necessary, and see to it that they are combined into physically well-defined quantities in the final expressions.

Instead of working with the general transport coefficients L_{ij}, transport coefficients are often defined by classifying the transport process according to the nature of the prevailing driving force. We will do so also here. We therefore consider below the two special cases of a) an externally applied gradient in electric potential as the only driving force (migration, drift) and b) transport in a compositional gradient in the absence of an externally applied electric field (chemical diffusion).

Transport in an external electric field in the absence of compositional gradients; Ohm's law. If $\nabla\mu_i=0$, the driving force for the flux of species i is equal to a gradient in the electric potential alone. The total current i is defined as the charge crossing a crossection normal to current flow per area per time, and the total conductivity σ relates i to the gradient in electric potential through Ohm's law. Likewise, a partial conductivity σ_i for species i is defined by the charge flux of species i_i and the gradient in electric potential from

$$i_i = -\sigma_i \frac{\partial\phi}{\partial x} \tag{4}$$

where we have assumed one-dimensional transport. With assumption 3), we see that σ is equal to Σ_i-$L_{ii}z^2_i q^2$ since $i=\Sigma_i i_i$ ($\sigma_i=-L_{ii}z^2_i q^2$). The transference number t_i of species i is then defined as the fraction of the current carried by species i:

$$\sigma_i = t_i\sigma \ ; \quad t_i = \frac{\sigma_i}{\Sigma_j \sigma_j} \tag{5}$$

It is common to define a general (mechanical) mobility b_i ($[b_i] = cm^2s^{-2}V^{-1}A^{-1}$) as the ratio between the mean velocity of particles of type i, v_i, and the driving force [10],

$$b_i = \frac{|\vec{v}_i|}{|\vec{X}_i|} \tag{6}$$

where vector notation has been used. Since the flux is equal to the product of the particle concentration of species i, c_i (here in units of particles cm^{-3}), and the mean particle velocity ($cm\ s^{-1}$), the partial conductivity and the general mobility are related as $\sigma_i = b_i z_i^2 q^2 c_i$. Similarly, if an electric mobility u_i ($cm^2\ V^{-1}\ s^{-1}$) is defined as the ratio between v_i and the electric field, then $\sigma_i = u_i|z_i|qc_i$ [12]. Mobilities are usually taken to reflect microscopic kinetic properties, i.e. the facility with which species move. If these properties are concentration-independent, σ_i is thus proportional to c_i.

Transport in a compositional gradient when externally applied fields are zero; Chemical diffusion. Using the definition of general mobility introduced above, we may write for a particle in a one-dimensional gradient of the electrochemical potential

$$N_i = -c_i b_i \frac{\partial \eta_i}{\partial x} \tag{7}$$

or

$$N_i = -b_i kT \left[\frac{\partial \ln a_i}{\partial \ln c_i} \frac{\partial c_i}{\partial x} + \frac{z_i q c_i}{kT} \frac{\partial \phi}{\partial x} \right] \tag{8}$$

by the use of Eq. 2. The factor $b_i kT$ has the dimension length squared per time, and is defined as the component diffusion coefficient D_{Ki} of species i, i. e.

$$D_{Ki} = b_i kT \tag{9}$$

which is known as the Nernst-Einstein relation. Since we assume that we can arrange our experiment so that externally aplied electric fields are zero, we must have

$$\Sigma_i z_i N_i = 0 \tag{10}$$

to maintain the charge-balance flux. Inserting Eq. 8 into Eq. 10, solving for $\partial\phi/\partial x$, and backsubstituting the resulting expression into Eq. 8 gives [12]

$$N_i = -D_{Ki} \left[\frac{\partial \ln a_i}{\partial \ln c_i} - \Sigma_j t_j \frac{z_i}{z_j} \frac{\partial \ln a_j}{\partial \ln c_i} \right] \frac{\partial c_i}{\partial x} \tag{11}$$

or

$$N_i = -D_{Ki} \left[(1 - t_i) \frac{\partial \ln a_i}{\partial \ln c_i} - \Sigma_{j \neq i} t_j \frac{z_i}{z_j} \frac{\partial \ln a_j}{\partial \ln c_i} \right] \frac{\partial c_i}{\partial x} \tag{12}$$

As a special case of assumption 8), we now assume ionization equilibrium between ions and electrons in the solid. Thus, we define the activity of neutral species i (ion i plus z_i electrons), a_i^*, through the relation

$$d\ln a_i + z_i d\ln a_e = d\ln a_i - z_i d\ln a_h = d\ln a_i^* \tag{13}$$

where subscript 'e' refers to electrons and 'h' to holes. Transforming Eq. 12 via Eq. 13 gives [12]

$$N_i = -D_{Ki}\left[(1-t_i)\frac{\partial \ln a_i^*}{\partial \ln c_i^*} - \Sigma_{j\neq i,e,h} t_j \frac{z_i}{z_j}\frac{\partial \ln a_j^*}{\partial \ln c_i^*}\right]\frac{\partial c_i}{\partial x} \tag{14}$$

where c_i^* is equal to c_i. In Eq. 14, the flux N_i has now been expressed in terms of transference numbers t_j and activity gradients, i. e. (in principle) measurable quantities. The quantity in the bracket is a so-called enhancement factor, which we shall give the symbol W,

$$W = \left[(1-t_i)\frac{\partial \ln a_i^*}{\partial \ln c_i^*} - \Sigma_{j\neq i,e,h} t_j \frac{z_i}{z_j}\frac{\partial \ln a_j^*}{\partial \ln c_i^*}\right] \tag{15}$$

Eq. 14 may be identified as a Fick's first law,

$$N_i = -D_{Ki} W \frac{\partial c_i}{\partial x} = -\tilde{D}_i \frac{\partial c_i}{\partial x} \tag{16}$$

where we have defined the chemical diffusion coefficient $\tilde{D}$

$$\tilde{D}_i = D_{Ki} W \tag{17}$$

W is tabulated in Ref. [12] for a large number of special cases. Of special interest in connection with oxygen transport in oxides is the case with only one mobile ionic and one mobile electronic species, for which

$$W = t_e \frac{\partial \ln a_i^*}{\partial \ln c_i^*} \tag{18}$$

and

$$\tilde{D}_i = D_{Ki} t_e \frac{\partial \ln a_i^*}{\partial \ln c_i^*} \tag{19}$$

If the material is a predominantly electronic conductor, then $t_e \rightarrow 1$, and the expressions simplify even further.

The enhancement factor W is thus for binary systems proportional to the derivatives of the logarithm of the activity of neutral species with respect to the logarithm of their concentration. For an electronically conducting oxide ($t_e \rightarrow 1$) in which oxygen ions are the predominantly mobile ionic species, W is therefore proportional to $\partial \ln a_o / \partial \ln c_o$, where a_o and c_o are the activity and concentration of atomic oxygen, respectively, Eq. 13. For oxides of the perovskite type, for example, this derivative sometimes take very large values, up to 10^5 [22,23]. Such large enhancement factors are sometimes explained in terms of a model in which the more mobile species tend to move ahead of the others. This creates an internal field, which in turn serves to accelerate the slower species in order to preserve electroneutrality. It is thus interesting to note that the expressions above lead for a binary ideal system to a chemical diffusion coefficient similar to that calculated for ambipolar diffusion, c. f. expressions in [12] and [19].

It is important to notice that one may in general expect the chemical diffusion coefficient and the component diffusion coefficient to display different dependencies on temperature and composition, since W will depend on temperature and composition. In some systems, e. g. metal hydrides [24], D_{Ki} and D_i may even change in opposite directions as composition changes. Also, while the Nernst-Einstein relation, Eq. 9 is generally valid, a similar relation with the chemical diffusion coefficient is only valid in the case of ideal solutions.

Note that the definition of chemical diffusion coefficient hinges crucially on the electroneutrality condition, assumption 6). Where deviations from this condition may be expected, for example in interface regions, the definition of a chemical diffusion coefficient may not be meaningful [25].

For a transport mechanism involving jumps of lattice ions to nearby vacant sites, one may expect the diffusion coefficient to be proportional to the vacancy concentration (see below). For such systems, it is therefore common to define a vacancy diffusion coefficient D_V as the proportionality constant between the the component diffusion coefficient and relative vacancy concentration. Thus, for oxygen diffusion,

$$D_{Ko} = D_V \frac{[V_O^{\cdot\cdot}]}{[O_O^x]} \tag{20}$$

where $[V_O^{\cdot\cdot}]$ is the concentration of oxygen vacancies of effective charge +2, and $[O_O^x]$ the concentration of lattice oxygen of zero effective charge. D_{Ko} is the component diffusion coefficient for lattice oxygen.

Statistical treatment. Correlations.

We now want to link the macroscopic transport coefficients introduced above to microscopic properties. To do this, we consider the process of ions (or atoms) moving in a crystal lattice from the viewpoint of sucessive jumps from one lattice position to another [10], Fig. 1.

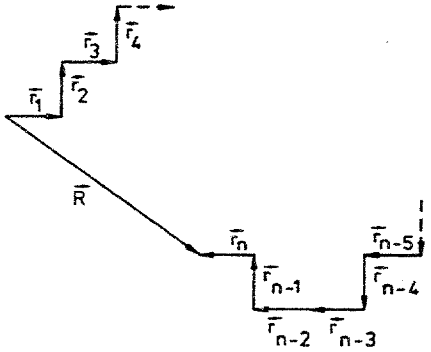

Fig. 1. Path traced by a particle in a (correlated or uncorrelated) random walk in a crystal lattice.

The mean distance between two such positions we shall denote by r, and the number of jumps n made by one particle per time t, $\nu=n/t$, is called the jump frequency. In the three-dimensional case, we must also take into account the direction of jumps for a complete description, and the i-th jump a particle makes from time t=0 is the vector $\vec{r}_i$ After time t, the particle has moved from the origin at which it started at t=0 to some other position $\vec{R}$,

$$\vec{R}(t) = \sum_{i=1}^{n} \vec{r}_i \tag{21}$$

and the square of the displacement is

$$\vec{R}^2(t) = \left(\sum_{i=1}^{n} \vec{r}_i \right)^2 \tag{22}$$

If we assume all jumps to be equal in magnitude, and use the definition of a vector product, we obtain

$$\vec{R}^2(t) = nr^2 + 2 \sum_{i=j+1}^{n} \sum_{j=1}^{n-1} r^2 \cos\alpha_{ij} \tag{23}$$

where α_{ij} is the angle between jump i and jump j. The mean square of the displacement over all possible paths $<R^2(t)>$ follows from Eq. 23 as

$$<\vec{R}^2(t)> = <R^2(t)> = nr^2 + 2 \sum_{i=j+1}^{n} \sum_{j=1}^{n-1} r^2 <\cos\alpha_{ij}> \tag{24}$$

If jumps are uncorrelated, then $<\cos\alpha_{ij}>=0$, and

$$R^2(t) = nr^2 \qquad (uncorrelated) \tag{25}$$

If jumps are correlated, i. e. the direction of a jump depends on the direction of previous ones, $\langle\cos\alpha_{ij}\rangle \neq 0$, and

$$R^2(t) = fnr^2 \qquad (correlated) \tag{26}$$

where we have introduced the correlation factor

$$f = 1 + \left(\frac{2}{n}\right) \sum_{i=j+1}^{n} \sum_{j=1}^{n-1} \langle\cos\alpha_{ij}\rangle \tag{27}$$

The central point is now that $R^2(t)$ can also be calculated from a macroscopic diffusion equation similar to the three-dimensional version of Eq. 16 above, in conjunction with a material balance for the tracers. The resulting equation, Fick's second law, yields with appropriate boundary conditions $R^2(t)=6D_{Tr}t$ in three dimensions, where D_{tr} is the so-called tracer diffusion-coefficient or self-diffusion coefficient [10]. (In other words, $\tilde{D}$ in Fick's first law is replaced by D_{Tr}.) This diffusion coefficient is defined by an experiment in which a number of labelled particels, e. g. radioactive tracers or isotopes that can be distinguished by mass spectrometry, is allowed to diffuse into the solid from an initially known position, with a simultaneous counter diffusion of non-labelled particles [10]. For oxygen transport, ^{18}O is commonly used to distinguish the in-diffusing atoms from those initially present in the solid (predominantly ^{16}O) [5]. Thus we have

$$D_{Tr} = \frac{1}{6} f\nu r^2 \tag{28}$$

which relates the diffusion coefficient defined by a tracer experiment to the microscopic quantities f, ν and r. While r can be deduced from the structure of the lattice, which in turn can be obtained by methods such as X-ray diffraction, the calculation of ν given chemical composition and structure is considered more complicated. The correlation factor depends in general both on the relative jump frequencies of the labelled and non-labelled atoms, on the geometry of the lattice, and on diffusion mechanism [25]. For a vacancy mechanism, if the two jump frequencies are approximately equal, f becomes a function of lattice structure alone [25]. For example, for diffusion in a simple cubic lattice by the vacancy mechanism, f is equal to 0.65 [10,25].

It now remains to establish the link between D_{Tr} and the transport parameters in the previous section, and thus between the latter and f, ν and r. We will outline the argument in terms of a vacancy mechanism. We first notice that the Nernst-Einstein relation implies that D_{Ki} describes a net movement of charge. If the jump frequency of each charge carrier is ν_q and the jump distance is r_q and the correlation factor for charge jumps is f_q, then by an argument similar to that above,

$$D_{Ki} = \frac{1}{6} \nu_q r_q^2 f_q \tag{29}$$

Combining Eqs. 9, 28 and 29, and using $\sigma_i=b_iz_i^2q^2c_i$, we find,

$$D_{Tr} = b_ikT\frac{\nu}{\nu_q}\left(\frac{r}{r_q}\right)^2\frac{f}{f_q} \tag{30}$$

If we adopt the picture that charge movement is equivalent to transport of (effectively) charged vacancies, it follows that $r_q=r$, and that $\nu_q=\nu$ (neglecting any difference in jump frequencies of the labelled and non-labelled species). Moreover, we do not expect vacancy movements to be correlated [25], and $f_q=1$. Therefore,

$$D_{Tr} = fb_ikT = fD_{Ki} \tag{31}$$

In the more general case, where e. g. a number of mehanisms may contribute to charge transport, the factor f in Eq. 31 may be generalized to the so-called Haven-ratio $H_R=D_{Tr}/D_{Ki}$. H_R is, depending on mechanism, a function of correlation factors, jump frequencies etc. An experimental determination of H_R, for example by separate measurments of D_{Tr} and D_{Ki}, might therefore be of considerable diagnostic value in terms of transport mechanism. Alas, the precision with which D_{Tr} and D_{Ki} can be determined in ceramic oxides is usually not sufficient for calculating a reliable f (or H_R); Our purpose here has merely been to explain parameters commonly occuring in the literature.

Measurement methods

Having established some basic relations between transport coefficients, we now turn to the use of these definitions in experimental measurements. These may be divided into the following groups, where the transport parameters usually calculated are indicated:

I. Electrochemical methods [11].

- Conductivity measurement with selective sinks and sources (σ_i)
- Transference measurements (t_i)
- Emf measurements (t_i)
- Polarization measurements (σ_i, σ_e)
- Transient electrochemical techniques/coulometric titration ($\tilde{D}_i$,W)

II. Permeability measurements (t_i, σ_i) [25]

III. Gravimetric methods and similar techniques ($\tilde{D}_i$,W) [15]

IV. Isotopic exchange (D_{Tr}) [5]

There is not room for an extensive description of each technique here, and we can discuss only briefly each group separately in terms of the assumptions made in the section "Thermodynamic definitions..." above. For further details, the reader is referred to the references given.

Electrochemical methods. *Measurements of partial conductivity in predominantly ionic conductors* may be carried out by interposing the sample between a sink and a source for the species for which the partial conductivity is to be determined [11]. Sinks and sources should be blocking to all other ionic species and be electronically conducting. Separate potential probes may be used to avoid problems of reversibility at the sink and source, and the ionic conductivity is calculated from the ratio of the current to the potential gradient (c. f. Eq. 4). (Instead of separate potential probes, an ac method may be used to exclude polarization effects.)

Alternatively, the transference numbers for ions may be determined from the increase in mass changes at the sinks and sources in so-called *transference measurements* [11,13]. The fraction of current carried by the ionic species, i. e. t_i, is related to the mass change via Faraday's law, and the partial conductivity is readily calculated using Eq. 5, provided that the total conductivity is known. Another way to determine t_i's, is by means of the *emf technique*. In this method, the sample is sandwiched between electrodes at different chemical potentials for the electroactive species (e. g. oxygen). This approach makes use of the effect of a partial, internal short circuit of electrons or holes, which results in a decrease of the externally measurable voltage of the galvanic cell. The transference number for the electroactive species can then be shown to be equal to the ratio of this potential and the theoretical value (Nernst equation) [11]. (Actually, used this way, the method yields an average t_i across the sample. Alternatively, the interpretation may be improved by the use of a detailed defect model, or it can be used in a differential mode.) Finally, there is the *Hebb-Wagner*, or the *asymmetric polarization technique*, in which the sample is placed between an ionically blocking electrode and a reversible reference electrode [11]. In this case the partial conductivities of electrons and holes can be determined by fitting steady-state current-potential data to theoretical relationships containing these conductivities as parameters. The method can also be used in a transient mode.

Measurements of partial conductivity in mixed conductors employ techniques which are similar to those described above. In measurements of partial ionic conductivity, however, the potential is sampled across ionically conducting probes reversible to the ions moving in the sample [10,11,13], rather than potential probes in the form of electronic leads as for ionic conductors.

As far as oxygen transport in mixed conductors is concerned, the most serious complication with measurements of partial conductivity by the methods above is probably due to external short-circuits (assumption 9). Such short-circuits may occur if the sample exchanges oxygen rapidly with the ambient (oxygen-containing) atmosphere. Sealing of the sample is then required, but not necessarily straightforward. A more general problem pertains to assumption 3). If cross-coefficients are not close to zero, the results of the different techniques will not agree. For systems with two moving species, the degree of disparity is discussed in Ref. [13], which also suggests methods for assessement of L_{ij}. Problems specific to the Hebb-Wagner technique are reviewed in Ref. [28], which also contains a number of suggestions for improvement.

Transient electrochemical techniques are devised to measure first of all the chemical diffusion coefficient of for example oxygen in mixed conductors, but a number of transport parameters can be calculated from the data. An example of an experimental setup recently used is shown in Fig. 2 [7].

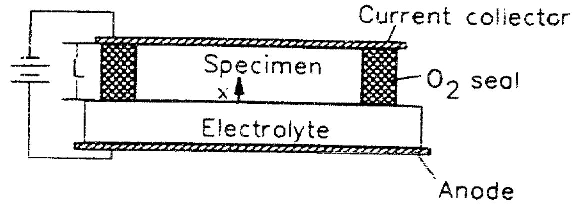

Fig. 2. Experimental setup for potential step measurements of chemical diffusion coefficient for oxygen in a predominantly electronically conducting sample.

In the setup shown in Fig. 2, the sample is interposed between an ion-blocking electronic conductor and an oxygen-conducting electrolyte. The sample is assumed to be predominantly electronically conducting with a conductivity much higher than that of the electrolyte, and no reference electrode is necessary [7,11]. The edges are sealed. A potential step is applied across the cell, which is under these conditions equivalent to a step in the oxygen activity at the sample-electrolyte interface, and oxygen diffuses out of or into the sample depending on the direction of the step. This corresponds to a chemical-diffusion process, since there is a stoichiometry gradient across the sample. The current I is monitored as a function of time, and can under the assumptions listed above be compared with theoretical expressions derived from the solution to Fick's second law (written in terms of the chemical diffusion-coefficient) with appropriate boundary conditions. Thus at short times ($t \ll L^2/\tilde{D}$),

$$I(t) = \frac{Q}{L}\left(\frac{\tilde{D}}{\pi t}\right)^{1/2} \qquad \textbf{(32)}$$

where Q is the total charge flowing during the transient, and L is sample thickness. At long times ($t \gg L^2/\tilde{D}$) one has,

$$I(t) = \frac{2Q\tilde{D}}{L^2}\exp\left(-\frac{\pi^2\tilde{D}t}{4L^2}\right) \qquad \textbf{(33)}$$

Therefore, the diffusion coeffcient can in principle be found from the slope of plots of I vs. $t^{-1/2}$ (Eq. 32) or plots of ln I vs t (Eq. 33). The charge Q can be found coulometrically, by integration of the current, or using the intercept and slope of plots of ln I vs t in combination. Also this method is complicated by problems associated with external short-circuits due to leaks in the seal. This can be corrected for under the assumption of a constant leak current [7]. More serious, however, is that the presence of high-diffusivity paths, i. e. internal short circuits, in the sample may render interpretation in terms of Eqs. 32 and 33 completely useless. Such high-diffusivity paths may be grain-boundaries or simply porosity, as discussed in Ref. [7]. In the absence of such complications, the electrochemical step-technique should be a useful one, due to the possibility of calculating also transport parameters other than $\tilde{D}$ [7,11,14]. The setup in Fig. 2 can in principle be used with other signals than potential steps as in Ref. [14], but this may cause problems in terms of asessing the effect of leaks. On the other hand, these may have advantages in dealing with finite kinetics at the electrolyte-sample interface [14].

Another problem with potential-step and similar techniques, is that they do not work very well with specimens whose stoichiometry do not change sufficiently in the activity domain of interest. In such cases, the current may be completely dominated by leaks. Since these are usually of a diffusive nature, they may easily be taken for transients associated with the sample itself. Measurements should therefore ascertain that extensive quantities calculated from the results (like charge) really are related to sample mass.

Permeability measurements. In a permeability measurement, a disc (or a similar shape) of the sample is exposed to a gradient in chemical potential in (here) oxygen, and the oxygen flux at steady state is measured and related to appropriate theory [27]. Permeability measurements thus resemble and complement emf measurments, because they may be considered more appropriate for predominantly electronic conductors. (The emf technique would result in detection problems for very low t_i ($i \neq e,h$).) Usually, the oxygen flux is written in terms if partial conductivities of oxygen ions and electrons. As for emf measurements, permeability measurements may therefore be used to define an average partial conductivity (or transference number), they may be used in a differential mode, or the may be related to a detailed defect model. Problems asociated with the method are first of all leaks and internal short-circuits. (A recent attempt to correct for grain-boundary diffusion did not give consistency with SIMS measurements (see below) [27].)

Gravimetric methods. Gravimetric methods are based on monitoring the weight change due to a step in the partial pressure of (here) oxygen. The method thus resembles the potential-step technique, and some of the problems associated with it are described above, notably those associated with high-diffusivity paths. Other techniques that may be considered similar to these two, employ measurements of a specimen property (like e. g. conductivity) that changes as the sample changes stoichiometry.

Isotopic exchange. There are two major types of techniques for measuring the self diffusion-coefficient for oxygen (which both correspond to the definition of the process given above). Both methods require that the specimen is annealed in a gas in which the ^{18}O content is different from that initially present in the sample. In gas phase measurements, the isotopic composition of the gas phase is followed during the anneal. In depth-profiling techniques, the concentration profiles of the isotopes are probed after the specimen has been annealed for a specified time. With the Secondary Ion Mass Spectrometry (SIMS) method, depth profiling is achieved by bombarding the specimen with highly energetic ions (e. g. Xe^+), which is followed by mass analysis of the flux of ions sputtered away. The features and problems associated with these methods have been discussed elsewhere [5], and we will not treat them in detail here. However, we would like to point out that depth profiling technique appears at present to be the method that best deals with high-diffusivity paths. The presence of such paths frequently results in easily detectable tails in the diffusion profiles [28], and theoretical expressions have been developed and analyzed that enables calculation of the influence of grain-boundary diffusion on the total diffusion process as well as the grain-boundary diffusion coefficient from certain types of plots [28-33].

Note that in order to convert isotopic-exchange data to e. g. chemical diffusion-coefficients, additional experiments are needed. Also, while the gravimetric and electrochemical transient techniques offer the possibility to perform measurements on powder samples [7,15], this appears not feasible with the SIMS technique, which therefore in a sense puts more severe restrictions on sample quality and type. Finally, compared with the electrochemical methods, SIMS is quite equipment intensive, and not many laboratories operate such instruments for the purpose of characterization of oxygen transport in oxides.

Summary

A number of transport coefficients exist that can be used to characterize transport of oxygen in ceramic oxides. Those considered here are total and partial conductivities, transference numbers, mobility, and the tracer (self), vacancy, component and chemical diffusion-coefficients. These quantities are related to each other, and may be obtained by a number of experimental techniques, each with their advantages and disadvantages. However, as for example the component and chemical diffusion coefficients differ by an enhancement factor that may reach very high values, it is important that the different quantities are not confused when comparing different materials. Also, since the enhancement factor will display a dependence on temperature and composition, the temperature and compositional dependence of component and chemical diffusion-coefficients are not necessarily the same. Finally, when analyzing experimental data, it is important to ascertain that the assumptions behind the theoretical concepts used and the experimental technique itself are fulfilled.

REFERENCES

1. B. C. H. Steele, Mat. Sci. Eng., **B13**, 79 (1992)
2. A. M. Svensson, S. Sunde and K. Nisancioglu, Submitted (1996)
3. A. Hammou, in *Advances in Electrochemical Science and Engineering*, Vol. 2 (Edited by H. Gerischer and C.W. Tobias), p. 87 - 139, VCH, Weinheim (1992)
4. B. A. van Hassel, T. Kawada, N. Sakai, H. Yokokawa, and M. Dokiya, Solid State Ionics, **66**, 41 (1993)
5. J. Kilner and R. A. de Souza, in *High Temperature Electrochemistry: Ceramics and Metals* (Edited by F. W Poulsen, N. Bonanos, S. Linderoth, M. Mogensen, and B. Zachau-Christiansen), p. 41, Proc. 17th Risø Int. Symp., Risø (1996)
6. I. Yasuda, K. Ogasawara, and M. Hishinuma, in *Ionic and Mixed Conducting Ceramics* (Edited by T. A. Ramanarayanan, W. L. Worrell, and H. L. Tuller), PV 94-12, p. 164, The electrochemical Society Proceedings Series. Pennington, NJ (1994)
7. S. Sunde, K. Nisancioglu, and T. M. Gür, *J. Electrochem. Soc.*, **143**, 3497 (1996)
8. I. Riess, in *Ionic and Mixed Conducting Ceramics* (Edited by T. A. Ramanarayanan, W. L. Worrell, and H. L. Tuller), PV 94-12, p. 286, The electrochemical Society Proceedings Series, Pennington, NJ (1994)
9. J. Kilner, *ibid.*, p. 174
10. H. Rickert, *Electrochemistry of Solids*, Springer, Heidelberg (1982)
11. W. Weppner and R. A. Huggins, *Ann. Rev. Mater. Sci.*, **8**, 269 (1978)
12. W. Weppner and R. A. Huggins, *J. Electrochem. Soc.*, **124**, 1569 (1977)
13. C. Wagner, *Progr. Solid State Chem.*, **10**, 3 (1975)
14. C. J. Wen, C. Ho, B. A. Boukamp, I. D. Raistrick, W. Weppner, and R. A. Huggins, *Int. Met. Rev.*, **5**, 253 (1981)
15. J. Kjær, I. G. Krogh Andersen, N. Mogensen, E. Skou, and H. Boye, in *High Temperature Electrochemical Behaviour of Fast Ion and Mixed Conductors* (Edited by F. W. Poulsen, J. J. Bentzen, T. Jacobsen, E. Skou, and M. J. L. Østergård), p. 281, Proc. 14th Risø Int. Symp., Risø (1993)
16. D. S. Tannhauser, *J. Solid State Chem.*, **55**, 40 (1984)
17. R. B. Bird, W. E Stewart, and E. N. Lightfoot, *Transport Phenomena*, John Wiley and Sons, New York (1960)

18. K. S. Førland, T. Førland, and S. K. Ratkje, *Irreversible Thermodynamics, Theory and Applications*, Wiley, Chichester (1988)
19. J. S. Newman, *Electrochemical Systems*, 2nd ed., Prentice Hall, Englewood Cliffs, NJ (1991)
20. J. Maier, in *Ionic and Mixed Conducting Ceramics* (Edited by T. A. Ramanarayanan and H. L. Tuller), PV 91-12, p. 133, The Electrochemical Society Proceedings Series, Pennington, NJ (1991)
21. N. W. Ashcroft and N. D. Mermin, *Solid State Physics*, Holt-Saunders, Philadelphia (1986), pp. 534-539
22. A. Belzner, T. M. Gür, and R. A. Huggins, *Solid State Ionics*, **57**, 32 (1992)
23. T. M. Gür, A. Belzner, and R. A. Huggins, *J. Membrane Sci.*, **75**, 151 (1992)
24. H. Züchner and N. Boes, *Ber. Bunsenges. Phys. Chem.*, **76**, 783 (1972)
25. J. Maier, in *High Temperature Electrochemistry: Ceramics and Metals* (Edited by F. W Poulsen, N. Bonanos, S. Linderoth, M. Mogensen, and B. Zachau-Christiansen), p. 67, Proc. 17th Risø Int. Symp., Risø (1996)
26. Le Claire, *Correlation Effects in Diffusion in Solids*, in Physical Chemistry, Vol. X. (Edited by H. Eyring, D. Henderson, and W. Jost), pp. 261 - 330, Academic Press, New York (1970)
27. T. Kawada, T. Horita, N. Sakai, H. Yokokawa, and M. Dokiya, *Solid State Ionics*, **79**, 201 (1995)
28. N. L. Peterson, *Int. Met. Rev.*, **28**, 65 (1983)
29. R. T. P. Whipple, *Philos. Mag.*, **45**, 1225 (1954)
30. A. D. Le Claire, *J. Appl. Phys.*, **14**, 351 (1963)
31. G. H. Gilmer and H. H. Farrell, *J. Appl. Phys.*, **47**, 3792 (1976)
32. G. H. Gilmer and H. H. Farrell, *J. Appl. Phys.*, **47**, 4373 (1976)
33. W. Preis and W. Sitte, *J. Appl. Phys.*, **79**, 2986 (1996)

Oxygen Reduction on Lanthanum Strontium Manganites Investigated by the Use of Cone Shaped Electrodes

M. Odgaard and E. Skou

Department of Chemistry, University of Odense,
Campusvej 55, DK-5230 Odense M, Denmark

Abstract

The oxygen reduction kinetics has been investigated by impedance spectroscopy on two different cone shaped electrodes of $La_{0.85}Sr_{0.15}MnO_3$ in contact with either YSZ or CGO electrolyte pellets. The contact area has been varied by varying the mechanical load on the electrode on both polarized and unpolarized electrodes. The experiments showed the activation of the electrode observed after a cathodic polarization to be caused by the creation of an active zone on the electrolyte close to the triple phase boundary. As a result of this, the oxygen reduction on polarized electrodes probably takes place by several parallel routes making an kinetic investigation complicated. Impedance analysis of unpolarized electrodes at different oxygen partial pressures showed a charge transfer process at high frequencies involving oxygen defects and a mass transport limited reaction at lower frequencies.

1. Introduction

The performance of the cathode material in a solid oxide fuel cell is of great importance, since the oxygen electrode overpotential is a major cause of energy losses. Therefore, in order to improve SOFC cathodes a deeper understanding of the reaction mechanism is desired. In particular, the mechanism behind the activation of the electrode (current increase with time) observed after a cathodic polarization when lanthanum strontium manganites (LSM) is used as electrode material is still not fully understood.

The technique of using cone shaped electrodes was developed by Fabry and Kleitz [1-3] for metal electrodes and later used by M. Kleitz and coworker in numerous studies on LSM electrodes (e.g. [4-7]). By using dense cone shaped electrodes the effect of porosity and morphology was hoped to be eliminated.

Due to the very low oxygen ion conductivity in LSM materials the reaction zone is limited to an area close to the triple phase boundary. The extension of this reaction zone depends both on oxygen partial pressure, overpotential and size of contact area [5-7]. This means that even with cone shaped electrodes with tip diameters in the order of tenth of mm. the whole contact area may not participate in the electrode reaction [6,7]. This makes a comparison of results obtained with different electrodes difficult and a separation of the morphology effects from the inherent electrocatalytic activity dubious.

In the present work, cone electrodes with a tip diameter of c. 0.5 mm but composed of many small contact points of sub μm size is used in order to ensure the total contact area to participate in the electrode process.

2. Experimental

The powder for the electrodes was of the composition $La_{0.85}Sr_{0.15}MnO_{3+\delta}$ and was produced and characterized by the method described in [8]. Dense cylinders with a diameter of 13 mm were prepared from the material by the method described in [9]. After sintering, cones with a tip diameter of 0.35 mm (cone 1) and 1.0 mm (cone 2) were made using a diamond tool. The contact area of the tip was not machined and thus left untouched after sintering. A disc was cut from the other end of the cylinder for SEM investigations.

The measurements were carried out using the three electrode cell shown in fig 1. The cell was closed and could be purged with different gases. The mechanical load on the electrode could be varied by changing the air pressure in a closed stainless steel bellows used to support the electrode. A detailed description of the cell and the electrochemical equipment used is given in [10].

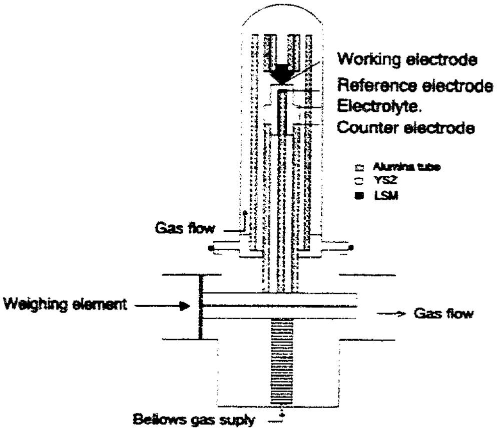

Fig. 1: Experimental setup

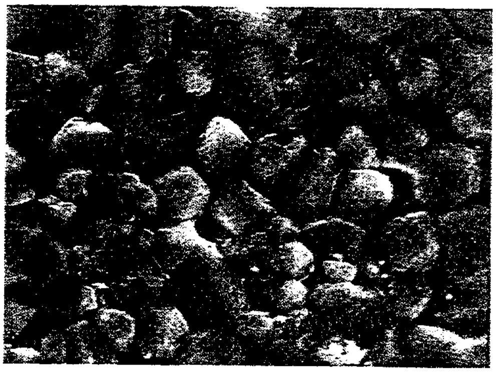

Fig 2: 7.5*10 mm section of the sintered electrode surface

3. Results and discussion.

3.1. Normalization of results obtained on unpolarized electrodes.

A SEM picture of a sintered LSM surface taken from a disc of the sintered sample is shown in fig 2. The surface is seen to consist of a dense packing of single crystals with a diameter of 0.5 to 1.5 μm with well defined edges and corners.

A typical impedance plot is shown in fig 3. The diagram consists of two overlapping semicircles originating from the electrode process and an offset at high frequencies caused by the ohmic drop in the electrolyte. Due to the current constriction close to the small cone tip the area in electronic contact with the electrolyte can be determined by the use of Newmans formula [11] (radius = $1/(4*\sigma*R)$, where σ is the specific conductivity of the electrolyte material and R is the resistance determined from the high frequency offset). For a multipoint contact with well separated contact points, as is believed to be the case in the present case [10], the formula is seen to give a determination of the sum of diameters of the contact zones.

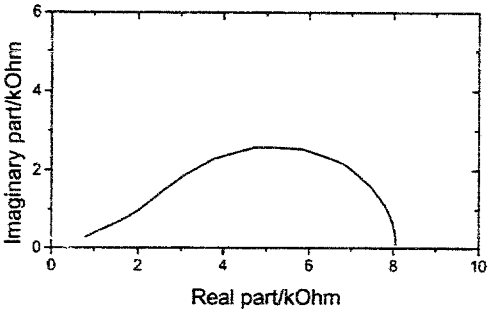

Fig. 3: Impedance plot of LSM electrode/ YSZ interphase in air at 1000 °C

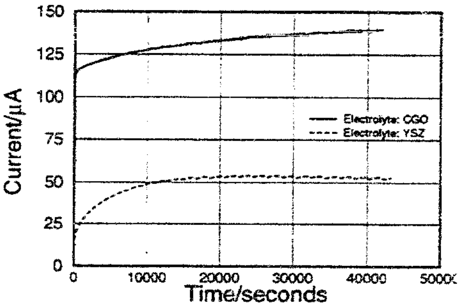

Fig. 5: Current increase after a cathodic polarization of 83 mV in air on two different electrolytes, but using the same cone electrode

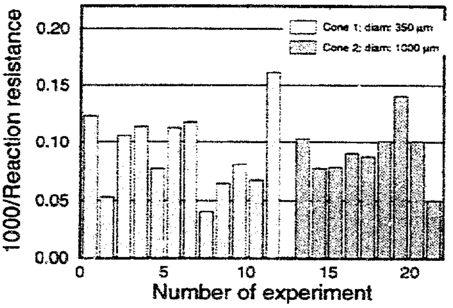

Fig. 4a: Reaction resistances determined from impedance plots in a number of experiments using two different cone electrodes.

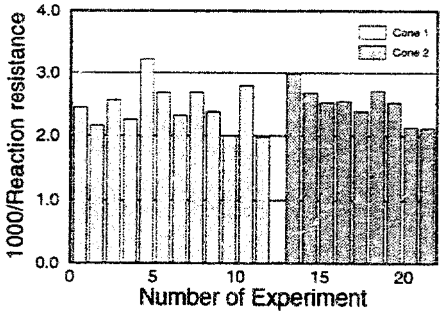

Fig. 4b: The reaction resistances from fig 4a normalized with respect to the diameter of the contact zone.

In fig. 4 is shown the results of polarization resistances determined on the unpolarized electrodes during the measurements with different mechanical loads. The unnormalized resistances are seen to vary by a factor of 8. When the resistances are normalized with respect to the diameter determined from Newmans formula the values are seen to vary less than 30% and there is no difference between the two electrodes. The results from cone 1 has been reported earlier [10], but normalized with respect to the area (squared diameter). The normalization with respect to area gives similar results as the normalization with respect to diameter. The diameter, however, is the experimental determined quantity and it is not clear exactly how this parameter relates to the area of a multipoint contact. Therefore, the normalization with respect to diameter is preferred.

The consistent results obtained after normalization is believed to be due to the multipoint character of the contact zone. For an electrode process which is limited by the diffusion of oxygen vacancies Siebert et al. [6] has defined a characteristic

diffusion length, l, for oxygen diffusion in the material. They have shown that an approximate value of the ratio between this length and the diffusion coefficient of the material can be estimated from the frequency at the top of the semicircle in the impedance diagrams ($f_D \approx 0.4*(D/l^2)$).
For the LSM material used in this work the diffusion coefficient has been determined by thermogravimetry to approx. 10^{-12} cm^2/s [12]. Using the top frequency from the impedance diagrams the estimation gives a characteristic diffusion length of approx. 0.5 µm. This lengtn is significantly larger than the diameter of the individual contact points in the multipoint electrodes used in the present work, but much smaller than the contact diameters used in most of the investigations reported in the literature.

3.2 The effect of mechanical load on polarized and unpolarized electrodes.

The time development of the current after the application of a cathodic polarization of 83 mV in air is shown in fig 5 for the same electrode on two different electrolytes, yttria stabilized zirconia, YSZ (TOSOH TZ-8Y) and gallium doped ceria, CGO (40% gadolinium substituted, from Risø National Laboratory). For both electrolytes, the current is seen to increase with time and with time constants in the order of thousands of seconds. This type of behavior has also been reported by Hammouche et al. [4, 5], who explains the activation to be caused by a reduction of the electrode material thereby increasing its oxide vacancy concentration. The result of this is the formation of an area of mixed conductivity at the interphase between the electrode and the electrolyte thereby extending the reaction zone from the triple phase boundary. For the multipion electrodes used in the present work this mechanism may be expected to be of less importance as the oxygen diffusion length already covers the whole contact area between the electrode and the electrolyte as pointed out above. To investigate whether the reaction zone may also protrude out on the surface of the electrolyte an experiment with varying load on polarized and unpolarized electrodes were performed.

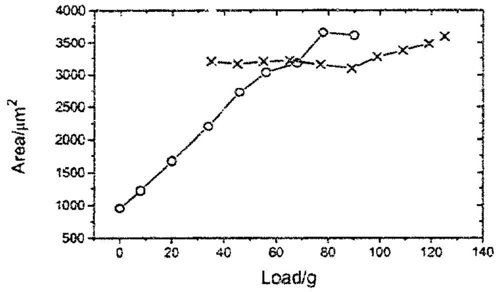

Fig. 6: Contact area determined from the electrolyte resistance as function of the mechanical load. o: Unpolarized electrode. x: Polarized -83 mV and allowed to reach steady state.

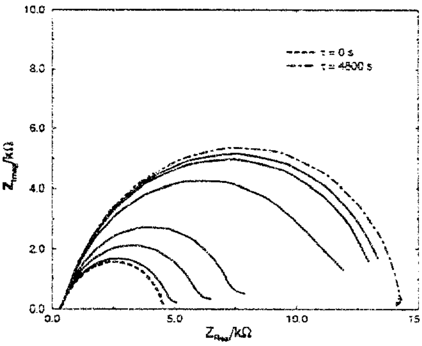

Fig. 7: Impedance plots as function of time after a change of the atmosphere from air to 1% oxygen in nitrogen

The result of such an experiment is shown in fig 6. When the electrode is kept in air at open circuit potential and the mechanical load is increased, the diameter of the contact area determined by Newmans formula is found to increase showing the area of physical contact to increase. At the same time the electrode resistance is found to decrease showing an increased activity of the electrode. The behavior was found to be reversible i.e. the curve could be repeated by releasing the mechanical load and increasing it again. When the same experiment was performed after the electrode had been polarized by a cathodic polarization and allowed to reach a steady state the behavior was completely different. By changing the mechanical load the diameter determined by Newmans formula did not change until a relatively high load was used. Also this behavior was reversible. If then the electrode polarization was removed and the electrode allowed to relax the behavior of the original unpolarized electrode was found again. This difference in response to changes in mechanical pressure between the unpolarized and polarized electrodes has been explained by a reaction zone predating out on the electrolyte surface [10] formed as a result of the activation process.

It should be pointed out, that the electrolyte resistance determined from the high frequency offset in the impedance diagrams only reflects the areas in direct electronic contact with the electrode. At these high frequencies charge transfer through the interphase through the double layer capacity is possible, no electrode reaction is necessary. However, the semicircles corresponding to the electrode reaction is also found to decrease during the activation of the electrodes, showing also the electrode reaction to spread out.

The role of the electrolyte for the activation process is also shown in fig 5, where two different electrolytes were used in contact with the same electrode. If the activation process was solely caused by an increased ionic conductivity in the electrode material the activation process should be expected to be insensitive to the choice of electrolyte. As can be seen, both the specific activity of the electrolyte/electrode interphase is sensitive to the choice of electrolyte, but also the time constants for the activation process and the degree of activation. Kleitz et al. [13] discuss the importance of the electronic conduction of the electrolyte for the activity of the electrode/electrode couple. The higher electronic conductivity of the CGO compared to YSZ may explain the increased overall activity of the LSM/CGO couple but it cannot account for the increase in activity with time.

3.3. The response to changes in the oxygen partial pressure.

A spreading of the electrode reaction zone due to electronic conductivity on the surface of the electrolyte has been discussed by Kleitz et al. [13]. The activation process may be coupled to the change in oxygen activity at the electrolyte/electrode interphase caused by the change in electrode potential. If this is the mechanism of the activation process an activation will be expected also to take place if the partial pressure of the oxygen is changed to a value corresponding to the partial pressure defined by the cathodic potential in the potential step experiment. Impedance spectra were recorded during the activation period following a cathodic polarization of 83 mV and after a change of the cell atmosphere from air to 1% oxygen in nitrogen. As reported above both the electrolyte and the electrode resistances were found to decrease during the activation period following a change in the electrode potential.

The result of the experiment where the oxygen partial pressure is changed is shown in fig 7. The behavior of the electrodes in this experiment is found to completely different from the behavior in the polarization experiment. Now the electrolyte resistance is found to be constant and the electrode resistance is found to increase with time. This shows the activation process to be connected to the charge passing the interphase during the activation period [14]. The very large time constants also indicate that transport of ions may be involved in the process.

3.4. Impedance analysis of unpolarized electrodes.

If the above analysis of the activation process is correct, the electrode reaction on polarized electrodes may be expected to take place on at least two different contact zones: an "unactivated" part and an "activated" part. This will probably cause the electrode response to be composed of contributions from different reaction paths, complicating an elucidation of the reaction mechanism. As an attempt to separate these contributions, impedance analysis has been performed on the unpolarized electrodes, both in the mechanical load experiments and in the atmosphere change experiments.

The impedance spectra, of which one is shown in fig. 3, consisted typically of a small semicircle at high frequencies followed by a larger semicircle at lower frequencies. The shape and frequency windows covered by the semicircles indicate that the high frequency semicircle is caused by a charge transfer reaction while the low frequency semicircle is caused by a mass transport reaction, probably involving an oxygen specie. A. similar interpretation has also been proposed by Østergård and Mogensen [15] and by Kleitz et al. [6, 13].

Table 1: Development of impedances after a change in atmosphere from air to 1% oxygen

time/s.	R_{ellyt}/ohm	R_1/ohm	R_2/ohm	R_{1+2}/ohm
0	300	277	4014	4281
60	303	148	4492	4640
180	300	160	5736	5935
300	300	208	7149	7357
420	300	152	9492	9644
480	300	164	11580	11744
600	300	184	12590	12774
1140	300	181	13680	13861
4200	300	181	14095	14276

The results of the separation of the semicircles from the experiment with different oxygen partial pressures are shown in table 1. The electrolyte resistance is seen to stay constant as pointed out earlier. The diameter of the small semicircle at higher frequencies (R_1) is seen to drop momentarily and then remain approximately constant. This is in accordance with the non activated behavior indicated by the time independent electrolyte resistance. The electrode reaction adopts immediately to the change in partial pressure, but remains then constant because the contact area stays constant. It should be noticed, however, that the drop in resistance when the partial pressure of oxygen is reduced corresponds to a negative reaction order with respect to oxygen.

The increase of the diameter of the second semicircle (R_2) is also in accordance with the interpretation presented above. Transport of an oxygen containing specie may be expected to be more difficult when the concentration of oxygen is reduced. The long time constant are, however, surprising and indicate that the process may be influenced by the stoichiometry change of the material. At the change in partial pressure used in this work the oxygen stoichiometry of the LSM material will change from 3.04 to 3.02 [9,16] and this process will have a long time constant due to the compact nature of the electrode.

The results presented above points to three steps in the reduction of oxygen on nonactivated LSM electrodes to be able to limit the reaction rate. (1): Diffusion of oxygen on the surface of the electrode to the sites of charge transfer. The adsorption of oxygen cannot in itself be rate limiting. If the surface diffusion is fast compared to the adsorption rate the electrode reaction would just use oxygen adsorbed on an increasingly larger portion of the electrode not in contact with the electrolyte [17]. (2): A charge transfer reaction involving oxygen vacancies in the LSM material, probably incorporation of adsorbed oxygen atoms into the crystal lattice of the electrode material and (3): The ionic conductivity of the material has also to be limiting. If that is not the case, the whole electrode area would be active and no dependency on the contact area would be see.

The following reaction scheme may therefore be proposed:

1. Oxygen gas is adsorbed on the electrode surface

$$O_2(\mathrm{gas}) + 2\square \Leftrightarrow 2O_{ads} \tag{1}$$

where $\square$ represents an adsorption site. This process is probably relatively fast.

2. Adsorbed oxygen diffuses to the reaction zone:

$$O_{ads} \rightarrow O_{ads}(\text{reaction zone}) \tag{2}$$

This process may be rate limiting

3. The adsorbed oxygen goes into the LSM lattice on an oxygen vacancy and receive two electrons:

$$O_{ads} + V_O^{\cdot\cdot} + 2e' \rightarrow O_O^x(\mathrm{LSM}) \tag{3}$$

4. The oxygen ion is transferred from LSM to YSZ:

$$O_O^x(LSM) + V_O^{\cdot\cdot}(YSZ) \rightarrow O_O^x(YSZ) + V_O^{\cdot\cdot}(LSM) \quad (4)$$

The rate of this process depend on the oxide ion conductivity of the electrode material and determine the extension of the reaction zone on the electrode material.

The rate of the charge transfer reaction (3) will be proportional to the concentration of oxygen vacancies and to the surface concentration of oxygen atoms:

$$v_3 = k \cdot [O] \cdot [V_O^{\cdot\cdot}] \quad (5)$$

The equilibrium vacancy concentration will be determined by the vacancy equilibrium:

$$O_2(gas) + 2V_O^{\cdot\cdot} \Leftrightarrow 4h^{\cdot} + 2O_O^x$$

In a LSM material the hole concentration will be determined by the amount of Mn(IV). With a strontium substitution of 15 mole% neither this amount or the oxygen content will be changed significantly by a small change in the oxygen stoichiometry. Under these conditions the equilibrium constant for the vacancy equilibrium will be given by:

$$K = p_{O_2} \cdot [V_O^{\cdot\cdot}]^2$$

If dissociative adsorption of oxygen is assumed the equation can be rewritten as:

$$K_{vac} = [O] \cdot [V_O^{\cdot\cdot}]$$

This shows the product $[O] \cdot [V_O^{\cdot\cdot}]$ in the rate equation (5) to be independent of the oxygen partial pressure. The rate constant, however, may be expected to depend on the electrode potential.

The potential dependency of an electrochemical rate constant is given by:

$$k = k^o \exp\left(-\frac{(1-\alpha)nF(E-E^o)}{RT}\right) \quad (6)$$

as we are dealing with a cathodic reaction. k^o is a potential independent rate constant, n the number of electrons exchanged in the reaction and α a symmetry factor, usually with a value of 0.5.

For small deviations from equilibrium, which is the case for impedance measurements at high frequencies, the potential difference, E - E°, can be derived from the Nernst equation, which for an oxygen electrode has the form:

$$E = E^o + \frac{RT}{4F}\ln\left(\frac{p_{O_2}}{[O^{--}]^4}\right) \Rightarrow E - E^o = \frac{RT}{4F}\ln(p_{O_2})$$

when the oxygen ion concentration is taken to be independent of the oxygen partial pressure.

If this expression is substituted into (6), the rate constant shows the following dependency on the oxygen partial pressure:

$$k = k^{o} p_{O_2}^{-0.5}$$

showing a negative overall reaction order with respect to the oxygen partial pressure.

The impedance diagrams may then be interpreted as follows:

At equilibrium, the oxygen activity at the surface will be identical all over the system, also in the interphase between the electrode and the electrolyte. Only at this contact zone oxygen ions can be exchanged directly with the electrolyte. The participation of any other part of the electrode has to rely on transport of oxygen or oxide ions in bulk or at the surface. At high frequencies the charge exchanged during an ac cycle will be small and concentration gradients will not be created. Under this condition, only the contact area between the electrode material and the electrolyte will be active. At lower frequencies the charge exchanged during an ac cycle will create concentration gradients. This means that the central part of the contact area will be exhausted and the reaction zone will only penetrate some distance from the triple phase boundary limited by the ionic conductivity of the electrode material and by the surface diffusion of oxygen to the region near the triple phase boundary. This means, that the high and low frequency semicircles probably are caused by processes taking place on different parts of the electrode surface. Such a separation has also been proposed by others [6], but in the interpretation presented here, the reaction area is going away from the interior of the reaction zone towards the triple phase boundary and the external surface when the frequency is reduced.

The proposed interpretation of the impedance diagrams also have implications on the normalization of electrode activities. The part of the electrode taking place in the electrode reaction at low frequencies will be different from the area determined by Newmans formula because this only takes areas with direct electronic contact into account. The difference between the two areas will depend on the characteristic diffusion length defined by Siebert et al. [6] and on the detailed morphology of the contact zone. In contrast, the high frequency semicircle will reflect the contact area determined by Newmans formula and should therefore be used in comparisons between different electrodes.

4. Conclusion.

The nature of the electrolyte in the electrolyte/electrode couple is important for the overall activity of activated electrodes probably due to an extension of the reaction zone to the surface of the electrolyte at the vicinity of the triple phase boundary. The shape of impedance diagrams on unpolarized electrodes is caused by different areas of the electrode participating in the electrode reaction in different frequency domains. At high frequencies only the area in physical contact with the electrolyte is active. Depending on the ionic conductivity of the electrode material the central part of the electrode/electrolyte interphase may be inactive at lower frequencies while areas on the bare electrode surface may then contribute.

Acknowledgements.

Dr. T. Jacobsen and Dr. B. Zachau-Christiansen, Department of Chemistry, The Technical University of Denmark is gratefully acknowledged for many stimulating discussions. Part of the work has been supported by the danish SOFC - program (DK-SOFC 1993-96)

References

[1].P. Fabry, M. Kleitz and C. Desportes: *J. Solid State Chem.* **5** (1972) 1.

[2].P. Fabry and M. Kleitz: *J. Electroanal Chem.* **57** (1974) 165.

[3].M. Kleitz, L. Dessemond, T. Kloidt and M.C. Steil: *Proc. 4th. Int. Symp. on SOFC*, (Eds.: M. Dokiya, O. Yamamoto, H. Tagawa and S.C. Singhal), p 527. The Electrochemical Society, Pennington, NJ (1995).

[4].A. Hammouche, E. Siebert, M. Kleitz and A. Hammou: *Proc. 1th. Int. Symp. on SOFC*, (Ed.: S.C. Singhal), p 265. The Electrochemical Society, Pennington, NJ (1989).

[5].A. Hammouche, E. Siebert, A. Hammou and M. Kleitz: *J. Electrochem. Soc.* **146** (1991) 1313

[6].E. Siebert, A. Hammouche and M. Kleitz: *Electrochimica Acta* **40** (1995) 1741

[7].H. Lauret and A. Hammou: *J. Europ. Ceram. Soc.* **16** (1996) 447

[8].I.G. Krogh Andersen, E. Krogh Andersen, P. Norby and E. Skou: *J. Solid State Chem.* **114** (1994) 320

[9].J. Kjær and E. Skou: *Proc. 4th. Int. Symp. on SOFC*, (Eds.: M. Dokiya, O. Yamamoto, H. Tagawa and S.C. Singhal), p 404. The Electrochemical Society, Pennington, NJ (1995).

[10].M. Odgaard and E. Skou: *Solid State Ionics* **86-88** (1996) 1317.

[11].J. Newman: *J. Electrochem. Soc.* **114** (1966) 501.

[12].J. Kjær, I.G. Krogh Andersen, N. Mogensen, E. Skou and H. Boye: *High Temperature Electrochemical Behaviour of Fast Ion and Mixed Conductors*, (Eds.: F.W. Poulsen et al.), p. 281. Risø National Laboratory 1993.

[13].M. Kleitz, T. Kloidt and L. Dessemond: *High Temperature Electrochemical Behaviour of Fast Ion and Mixed Conductors*, (Eds.: F.W. Poulsen et al.), p. 89. Risø National Laboratory 1993.

[14].M. Odgaard and E. Skou: *High Temperature Electrochemistry: Ceramics and Metals*, (Eds.: F.W. Poulsen et al.), p. 387. Risø National Laboratory 1996.

[15].M.J.L. Østergård and M. Mogensen: *Electrochimica Acta* **38** (1993) 2015.

[16].J. Kjær and E. Skou.: unpublished results.

[17].T. Jacobsen: Personal communication.

Electrical Behavior of Dense LSM/YSZ Composites

Cl. Roux, E. Djurado and M. Kleitz
Laboratoire d'Electrochimie et de Physicochimie des Materiaux et des Interfaces
(INPG and CNRS)
B.P. 75 - 38402 Saint Martin d'Hères (France)
Tel (33) 4 76 82 65 66, Fax (33) 4 76 82 66 70

Abstract

Composites with low concentrations in LSM have been investigated by impedance spectroscopy. The variations of the "bulk" semicircle reveal a strong alteration of the electrolyte conductivity by the dissolution of the electrode components. It depends on the annealing temperature. At medium LSM concentrations the behavior predicted by the Effective Medium Theories becomes observable.

Introduction

Various composites made up of $La_ySr_xMnO_{3-\delta}$ (or LSM) and Yttria-Stabilized Zirconia (or YSZ) have been investigated (1-3) to assess the risk of detrimental chemical reaction at the SOFC cathode interface. The main compounds which can form at the interface are $La_2Zr_2O_7$ and $SrZrO_3$. Both materials are insulators and partly block the electrode reaction (4). Porous composites based on the same materials are also recommended by Mogensen and his collaborators (5,6) as cathode materials. So far, the reported studies have been focused on composites containing approximately 50 vol% of each compound. The composition range investigated here spans from 0 to 20 vol% of LSM. Besides the interest in the electrical properties of these materials, we have been encouraged to launch this investigation because of recent and systematic studies (7) of alumina / YSZ composites and other similar systems which have shown that the electrical behavior of composites with fairly low concentrations in one component can be simple enough to be exploitable. This supposes that the grain size distributions of both components are sufficiently narrow, their grain dispersions sufficiently homogeneous and the densification of the composite fairly good.

Experimental

SAMPLE PREPARATION

The composites investigated were mixtures of strontium-doped lanthanum manganite and YSZ co-sintered conventionally. The initial sintering temperature was selected as low as possible to minimize the chemical reaction at the interface before further annealings. A technical solution frequently recommended to reduce the reaction at the interface, is the use of an A-site deficient manganite (that we will call LSdM). Most of the work reported here is relevant to this type of electrode material. The selected compositions were $(La_{0.85}Sr_{0.15})_{0.95}MnO_{3-\delta}$ for the LSdM and $La_{0.50}Sr_{0.50}MnO_3$ for the LSM that we will use for a few comparisons.

The LSdM and LSM powders were synthetized by ultrasonic spray pyrolysis (8). Essentially, the technique was a pyrolysis at 1173 K, in a tubular furnace, of an aerosol produced by a quartz vibrating at 850 kHz. The precursor was an aqueous solution of $La(NO_3)_3.6H_2O$, $Sr(NO_3)_2$ and $Mn(NO_3)_2.4H_2O$. The total nitrate concentration was $5.\ 10^{-2}$ M. A preliminary investigation in a NETZSCH STA 409 thermal analyser showed that the total decomposition of these nitrates occured at 848 K.The powders obtained were examined by transmission electron microscopy (JEOL 200CX - 200 kV). The micrographs show spherical aggregates with average diameters ranging from 0.5 to 3 µm and crystallite sizes from 75 to 100 Å. The X-ray diffraction patterns confirm that the phases are pure. The broad picks also indicate that the crystallites are small.

The YSZ powder was purchased from TOSOH Europe (TZ8Y).

Various LSdM / YSZ composites were prepared. Their compositions are listed in Table 1. They are called Ldx, x indicating the content in vol% of LSdM in the material, (for instance Ld5 contains 5 vol% of LSdM). For each composition, appropriate amounts of the components were mixed in ethanol. After solvant evaporation, the mixture was co-grinded. Note that this process introduced additional impurities. Then, it was uniaxially pressed at 40 MPa and isostatically at 250 MPa. The pellets were sintered at 1573 K for 2 hours in air. In a previous study (9), this sintering temperature was found sufficient for a densification of about 98% of the TZ8Y powder. For reasons which will become clear below (the partial dissolution of the electrode material in the electrolyte), it was difficult to determine the exact density of our composites by conventional techniques. The scanning electron micrographs revealed a non-negligible porosity.

One composition containing 15 vol% of the LSM, referred to as L15, was also prepared in the same way.

Samples of the Ld15 composite were further annealed at 1673 and 1773 K for 2 h in air.

SAMPLE CHARACTERIZATION

Composite surfaces were examined by scanning electron microscopy (JEOL JSM-35). (On the micrographs the YSZ matrix appears as a grey background, the LSdM grains are clearer and the pores are black (Fig. 1a and b)). The YSZ grain sizes are in the 0.2-2.5 µm range, the larger the LSdM content, the bigger the YSZ grains. The LSdM grains were smaller than the YSZ, for instance in the Ld20 composite the average LSdM grain size is 0.4 µm and that of the YSZ is 2.5 µm.

Electron micro-probe analysis (EPMA CAMECA SX50) was carried out to quantify the dissolution of LSdM in the YSZ grains. Six composites (Ld1 to 20) were investigated by EPMA. Five elements were analyzed: La, Sr, Mn, Zr, and Y (the standards used for this will be detailed in another paper). For each composite, the measurements were taken in 10 points from inside the YSZ grains (measurement duration: 30 s).

Powder X-ray diffraction patterns were obtained with a Siemens θ/2θ D500 diffractometer using the $CuK_{\alpha 1}$ radiation (λ= 1.5406Å).

ELECTRICAL MEASUREMENTS

The electrical behavior of the composites was investigated by impedance spectroscopy analysis using a HEWLETT-PACKARD 4192A LF impedancemeter in the 5 to 10^7 Hz frequency range with a signal amplitude V= 50mV. The samples were small cylinders of 8.4 mm in diameter and 2.6 mm thick. Silver paint (Demetron # 204) was used as the electrode material. The measurements were carried out in the 605 - 783 K temperature interval, most of them at 717 K. At this temperature the electrical response of interest is fully covered (Fig. 2a and b)

Results and discussion

GENERAL FEATURES

* Figure 2a and b compare the impedance diagrams of a pure YSZ sample and of the LSdM composites. At this stage, the main observations to be noted are:

- The general aspect of the nominally pure YSZ diagram, with its bulk and grain boundary semicircles, is not markedly altered by the addition of the electrode material.
- Up to LSdM concentrations slightly higher than 5 vol%, both semicircles swell. The relative magnitude of the semicircles is maintained (with a slight relative decrease in the blocking-effect semicircle). The degree of their separation is not significantly modified, either.
- With higher LSdM concentrations, the evolution radically changes with a shrinkage of the specific semicircle, a relative increase of the blocking-effect semicircle and a deeper valley between the two responses, indicating an increase in the ratio of their relaxation frequencies.

* On the SEM micrographs no LSdM grains are visible when the LSdM content is low (Fig, 1a). They are clearly visible when it is high (Fig, 1b). Here again the limit between the two regimes is an LSdM content slightly higher than 5 vol%.

ELECTRODE MATERIAL DISSOLUTION IN THE ELECTROLYTE

The chemical analysis of the inside of the YSZ grains, which is summarized in Fig. 3, shows that the low LSdM contents are fully dissolved into the YSZ matrix, as suggested by the SEM observations. It can be added that the dissolution of the Mn, La and Sr oxides in the matrix is also detected by a tiny shift of the X-ray peaks (for instance 0.31° for the 511 peak, expressed in 2θ,, between the compositions Ld1 and Ld10), as previously observed by Wiik et al (3). With high contents, the dissolution of the oxide components seems to reach saturation. Note that the saturation levels shown in Fig. 3 should not be regarded as the thermodynamic solubilities because the annealing times were short and equilibrium was probably not reached.

We can therefore conclude that the electrical behavior of the low-LSdM-content composites simply describes the effect of the dissolution of the manganese, lanthanum and strontium oxides on the electrical properties of yttria- stabilized zirconia.

The first notable consequence of this dissolution is a marked decrease in the YSZ conductivity indicated above by the swelling of the specific semicircle (Fig. 2a). This is more clearly shown by the first part of the "bulk" conductivity curve in Fig. 4. A similar observation was made by Kawada et al (10) for the dissolution of the manganese oxide.

The impedance diagrams (Fig. 5) of the Ld15 composite samples which were annealed at 1673 and 1773 K clearly show that the amounts of oxides dissolved in YSZ and their effects on its conductivity significantly depend on the annealing temperature, the higher the temperature, the larger the decrease in conductivity.

On the positive side it is to be noted that the chemical interaction of a small quantity of strontium-doped lanthanum manganite has a favorable incidence on the blocking factor of the electrolyte (see the first part of the curve in Fig. 6). Relatively speaking, the blocking effect decreases with the dissolution of small quantities of LSdM.

In terms of technical consequences, the decrease in conductivity induced by the reactivity with the electrode material, results in:

- an increase in ohmic drop; this might not be important in a fuel cell if the manganese, lanthanum and strontium ions do not diffuse deep into the electrolyte during the high temperature curing,
- an increase in the cathode overpotential; this has not yet been established but is very likely to occur. Changes in the electrolyte resistivity are frequently acccompanied by similar changes of the cathode overpotential resistance,
- a decrease of the electrolyte conductivity in the vicinity of micro-electrodes. This should be remembered when the Newman formula is applied:

$$r = \frac{1}{4\sigma_{el} R_{el}}$$

This formula is frequently used to determine the average radius r of the micro-electrode investigated from the measurement of the electrolyte resistance R_{el} and the knowledge of the electrolyte conductivity σ_{el}. If this last parameter is altered in the experiment, the application of the formula may lead to an erroneous value for the radius r.

COMPOSITE BEHAVIOR

A recent analysis (11) of the theoretical predictions of the Effective Medium Theories has demonstrated that composites made of materials with conductivities as different as the manganites investigated here and the YSZ give a single specific semicircle on their impedance diagrams. These theories have established that the corresponding "bulk" conductivity σ varies as:

$$\sigma = \sigma_m \frac{2\sigma_m + \sigma_{in} - 2v_{in}(\sigma_m - \sigma_{in})}{2\sigma_m + \sigma_{in} + v_{in}(\sigma_m - \sigma_{in})}$$

where σ_m and σ_{in} are the conductivities of the matrix (YSZ) and the inclusion (LSdM) and v_{in} the inclusion volume content which is supposed to be "sufficiently" low.

In the case of our composites, the inclusion conductivity σ_{in} (that of the LSdM) is much higher than that of the matrix σ_m (that of the YSZ). Under these conditions, the above equation can be simplified into:

$$\sigma = \sigma_m \frac{1 + 2v_{in}}{1 - v_{in}}$$

This expression indicates that the bulk semicircle should decrease with the additions of LSdM. The experimental observations summarized in Fig. 2b confirm this prediction. When an excess of LSdM remains present in the material as a separate phase (as shown by the SEM observations and the analysis reported in (Fig. 3)) the bulk semicircle shrinks with the increase in the LSdM content. If one assume that about 7 vol% of LSdM is dissolved at saturation, in the Ld20, for instance, the concentration in the LSdM phase should be around 13 vol%. The application of the above formula predicts for this material a decrease in conductivity of about 40%. The diagrams of Fig. 2b give 30%.

BLOCKING EFFECT and CHEMICAL REACTION PRODUCTS

It is clear from the observations reported above that, as soon as the LSdM material is present as a separate phase, the blocking effect increases markedly. This is most likely to be ascribed to the presence of reaction products which develop at the contacts between the two conductors forming the composite.

The comparison of the diagrams obtained with the Ld15 and L15 samples (Fig. 7) shows that with the electrode material richer in strontium and with no manganese excess, the effect of the dissolution on the electrolyte conductivity is less important (probably because less manganese is dissolved). On the other hand, the relative magnitude of the blocking effect is greater (Fig. 6). An X-ray analysis of these compounds (Fig.7) shows that the concentrations in the blocking species $SrZrO_3$ which results from the chemical reaction between the composite components is, in fact, higher in the L15 material. In this material, the presence of the species is visible on the X-ray patterns; for the Ld15 its concentration is too small to make it detectable.

Bibliography

1- H. Yokokawa, N. Sakai, T. Kawada and M. Dokiya, Solid State Ionics **40/41** 398 (1990).

2- G. Stoichniol, E. Syskakis and A. Naoumidis, J. Am. Ceram. Soc. **78** 929 (1995).

3- K. Wiik, C. R. Schmidt S. Shamsili, M.-A; Elnarsrud and T. Grande, in High Temperature Electrochemistry: Ceramics and Metals, Ed. F. W. Poulsen, N. Bonanos, S. Linderoth, M. Mogensen and B. Zacau-Christiansen, Riso Nat. Lab., Roskilde (Denmark) pp 491 (1996).

4- M. Mitterdorfer and L.J. Gaukler, in High Temperature Electrochemistry: Ceramics and Metals, Ed. F. W. Poulsen, N. Bonanos, S. Linderoth, M. Mogensen and B. Zacau-Christiansen, Riso Nat. Lab., Roskilde (Denmark) pp 357 (1996).

5- M. J. L. Ostergard, C. Clausen, C. Bagger and M. Mogensen, Electrochem. Acta **40** 1971 (1995).

6- M. Juhl, S. Primdahl, C Manon and M. Mogensen, J. Power Sources **61** 173 (1996).

7- M. Kleitz, L. Dessemond and M. C. Steil, Solid State Ionics **75** 107 (1995).

8- J. C. Viguie and J. Spitz, J. Electrochem. Soc. **122** 585 (1975).

9- M. C. Steil, F. Thevenot and M. Kleitz, to appear in J. Electrochem. Soc. (1997).

10- T. Kawada, N. Sakai, H. Yokokawa and M. Dokiya, Solid state Ionics **50** 189 (1992).

11- M. Kleitz and M. C. Steil, to appear in J. Europ. Ceram. Soc. (1997).

Composite	x LSdM (vol%)	(1-x) YSZ (vol%)
Ld1	1	99
Ld2	2	98
Ld5	5	95
Ld10	10	90
Ld15	15	85
Ld20	20	80

Table I : Compositions of LSdM/YSZ composites

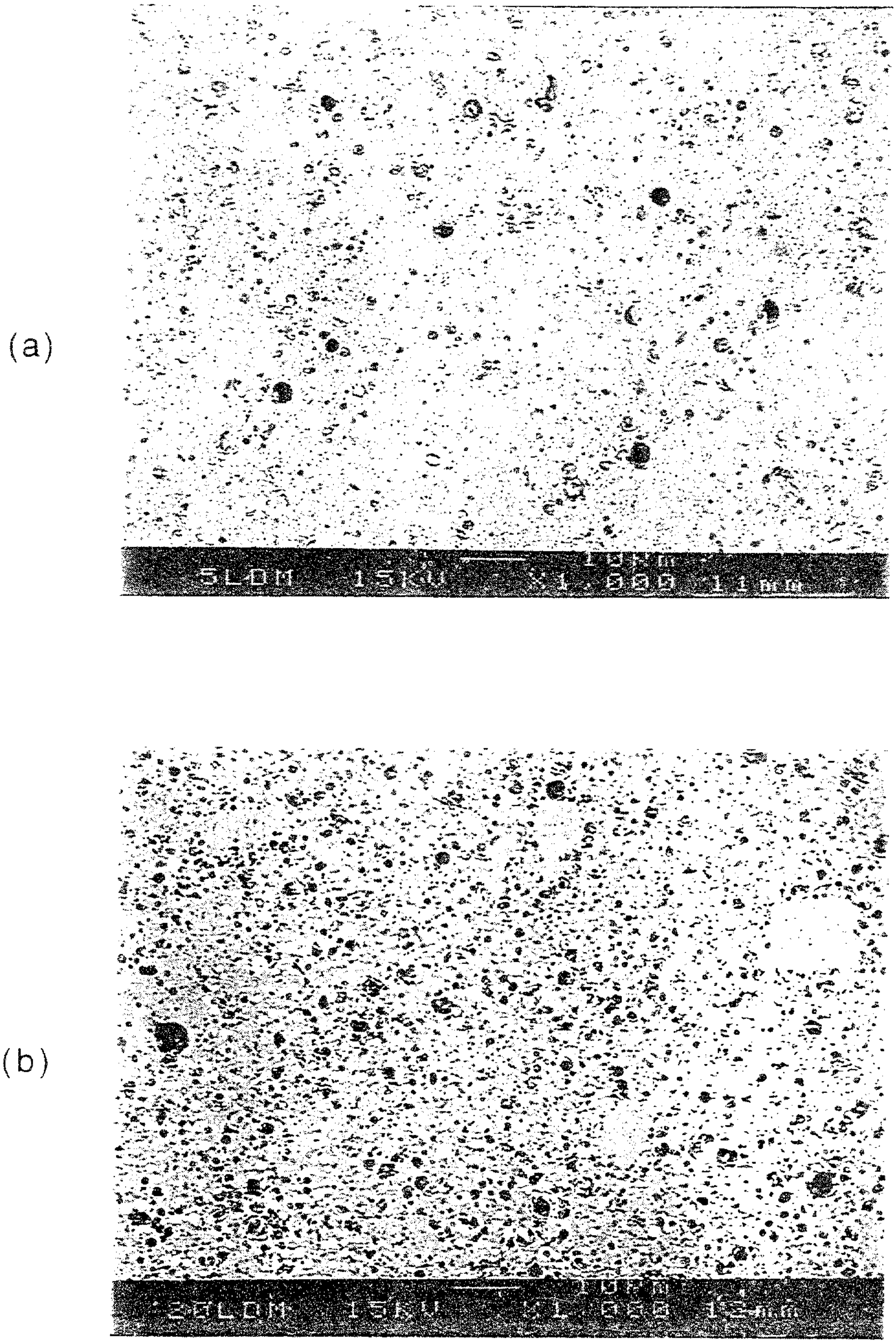

Fig.1- Scanning electron micrographs of composites containing:
a) 5 vol% of $(La_{0.85}Sr_{0.15})_{0.95}MnO_{3-\delta}$
b) 20 vol% of $(La_{0.85}Sr_{0.15})_{0.95}MnO_{3-\delta}$
grey background: YSZ matrix; black spots: pores;
white grains: $(La_{0.85}Sr_{0.15})_{0.95}MnO_{3-\delta}$.

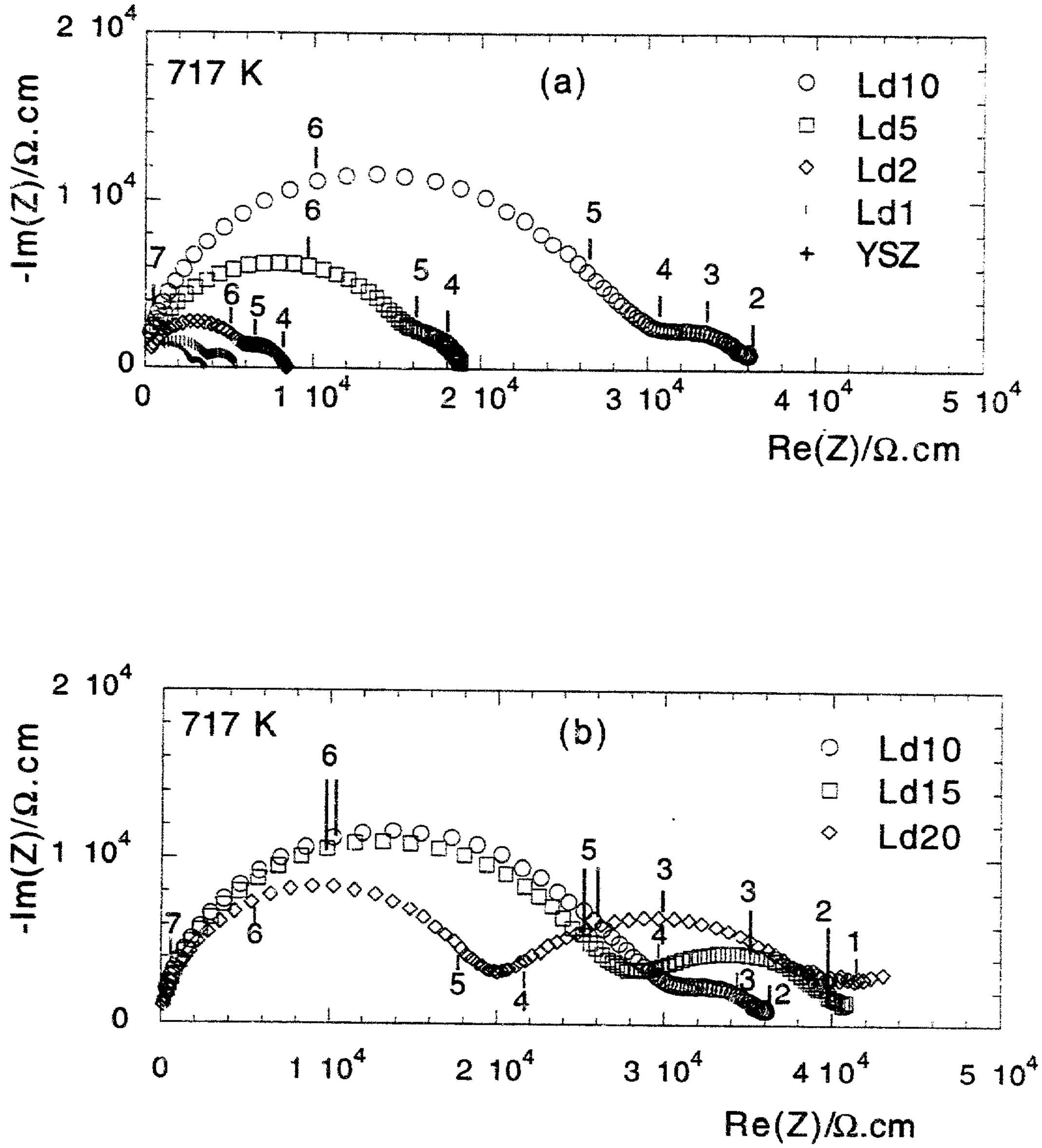

Fig.2 - Typical impedance diagrams as a function of the LSdM content (composites sintered at 1573 K). The number on the diagrams indicate the log(measurement frequency).

(a) low LSdM contents (0 - 10%)

(b) medium LSdM contents (10 - 20 vol %)

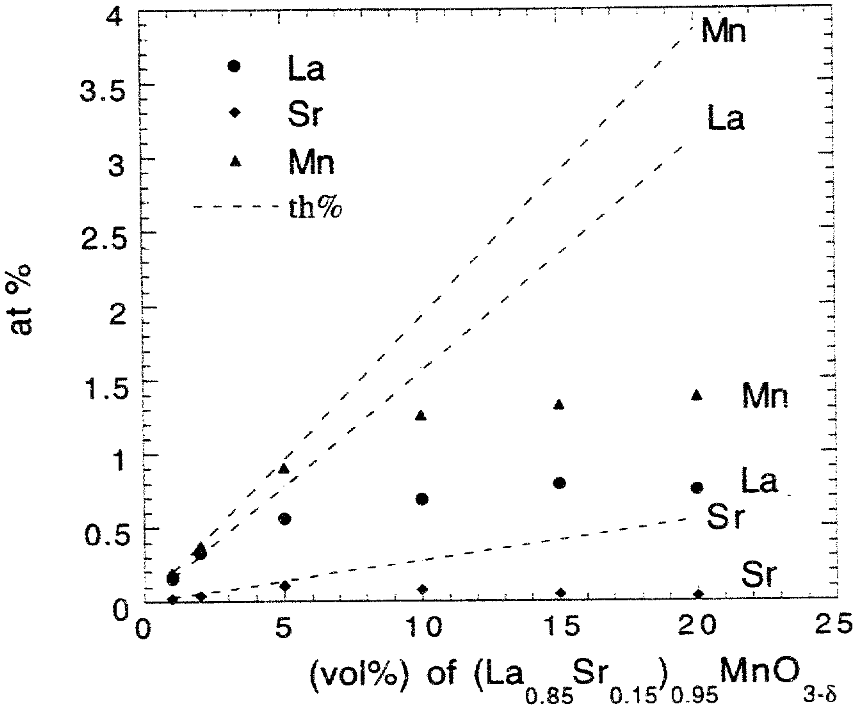

Fig.3 - La, Sr and Mn atomic fraction dissolved in YSZ - composites sintered at 1573 K

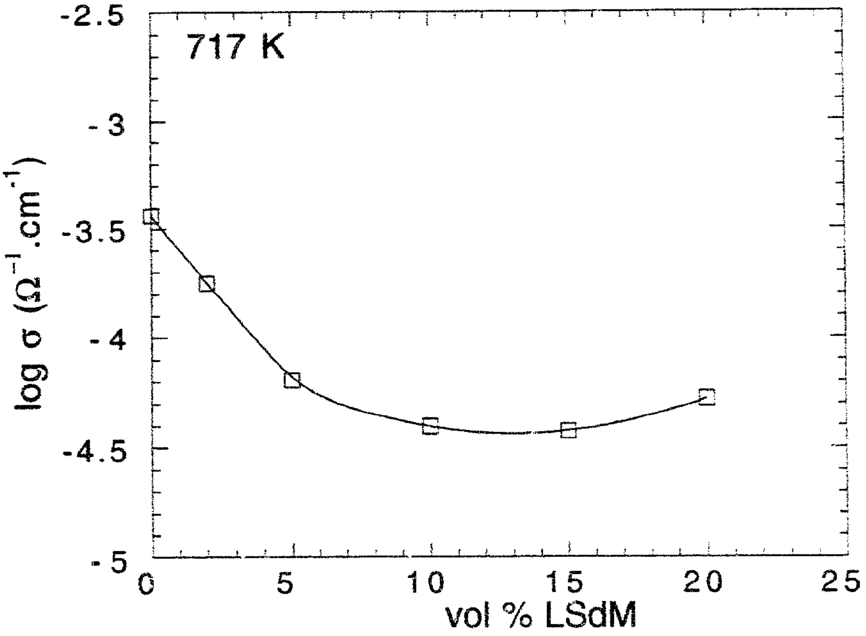

Fig.4 - Dependence of "bulk" electrical conductivity on the LSdM content -

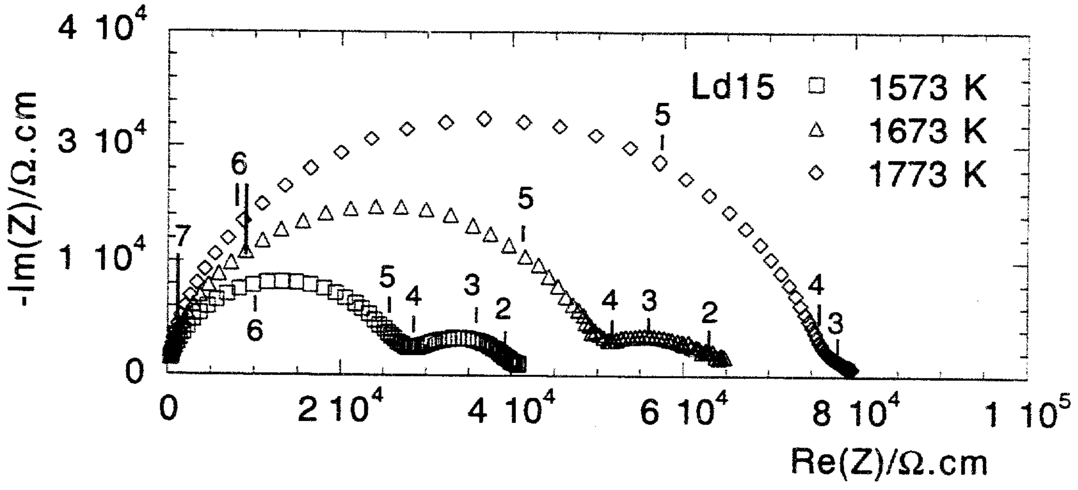

Fig.5 - Influence of the annealing temperature on the impedance diagrams of the composite - (measurement temperature : 717 K)

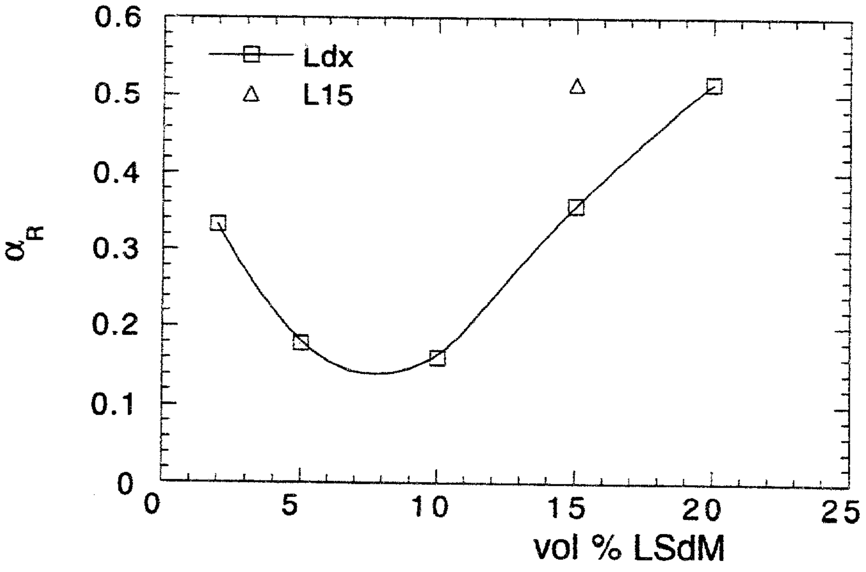

Fig.6 - Variations of the blocking factor ($\alpha_R = R_{bulk} / R_{dc}$) with the LSdM content -

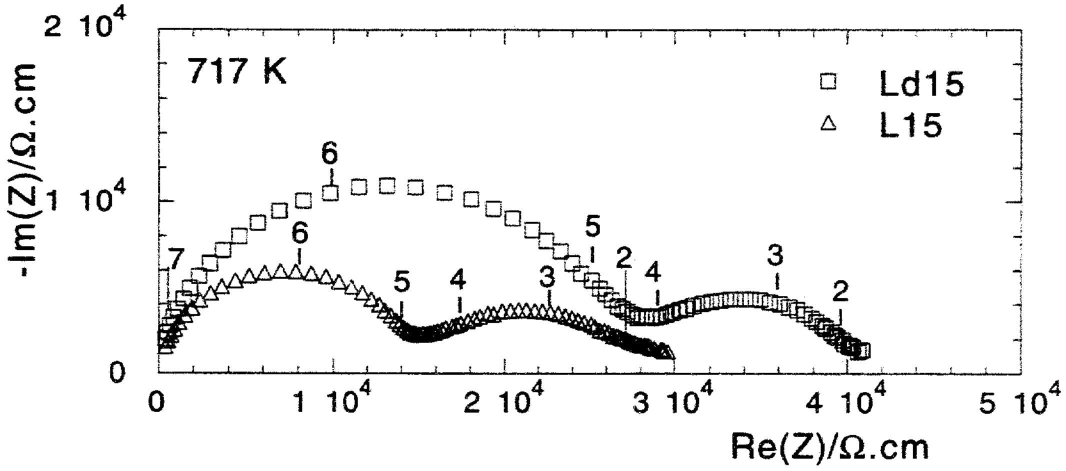

Fig.7 - Influence of the nature of the electrode material on the impedance diagrams of the composite. (composites sintered at 1573 K)

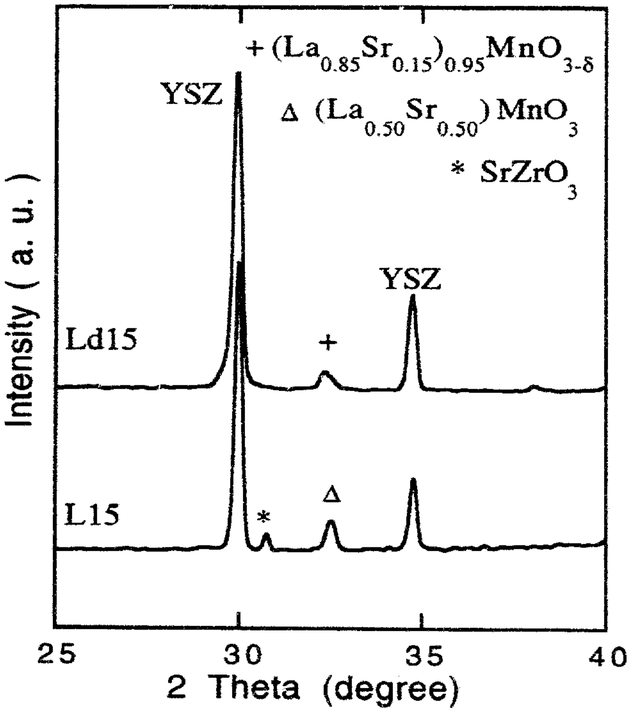

Fig.8 - XRD patterns of L15 and Ld15 - (composites sintered at 1573 K).

Impedance Spectroscopy Characterization of the Parasitic Chemical Reactions at Cathode Interfaces

L. Dessemond and M. Kleitz
Laboratoire d'Electrochimie et de Physicochimie des Materiaux et des Interfaces
(INPG and CNRS)
B.P. 75 - 38402 Saint Martin d'Hères (France)
Tel (33) 4 76 82 65 66, Fax (33) 4 76 82 66 70

Abstract

With "point" micro-electrodes requiring no pre-sintering or annealing, the chemical reactions which occur at the cathode interfaces, can be monitored from their very start. Preliminary results obtained with stronium-rich $La_{1-x}Sr_xMnO_3$ on YSZ are reported. They indicate that the electrolyte response may exhibit additional semicircles which characterize voids present along the electrode interface or reaction products. Even at 1373 K the electrode characteristic proper shows a marked degradation which increases with time. Surprisingly enough, at this relatively low curing temperature, the degradation appears reversible after a cooling down of the electrode.

Introduction

The operating temperature of the conventional SOFC's is around 1273 K and their components must be sintered at higher temperatures. These operating and processsing conditions induce detrimental chemical reactions between the electrode materials and the electrolyte. The paper deals with the reactivity of the $La_{1-x}Sr_xMnO_3$/YSZ couple. The chemical reaction products which form between these materials have already been thoroughly investigated by various groups (1-15). With a low strontium content (x smaller than approximately 30 mol%), the main component obtained is $La_2Zr_2O_7$, with a high content, it is $SrZrO_3$. The formation of $Sr_2Zr_2O_7$ has also been observed. The experimental procedures reported are based on the use of composites or bi-layers of the two materials. Typically the samples are cured under selected temperature and time conditions, cooled down to room temperature and then examined by appropriate microscopies and X-ray spectroscopies.

The technique presented here allows us to monitor the interface chemical reaction as it develops from its very start and to determine its effects on the electrode reaction rate. Furthermore, any change in the electrical properties of the electrolyte, in the vicinity of the interface, can also be characterized.

Strontium-rich manganites have been selected in this study as electrode materials to favor the formation of $SrZrO_3$.

Experimental

SAMPLE PREPARATION

The electrolyte pellet was prepared from a YSZ commercial powder containing 8 mol% of Y_2O_3 (TZ8Y from Tosoh Corp.). The compacted powder was isostatically pressed under 400 MPa and sintered at 1773 K for 2 hours in air. The final density of the sample was around 98 % of the theoretical value.

The electrode material compositions under study were $La_{0.45}Sr_{0.55}MnO_3$ and $La_{0.40}Sr_{0.60}MnO_3$. They will be called respectively, LSM55 and LSM60. The samples were synthesized by calcination of appropriate mixtures of $SrCO_3$, $MnCO_3$ and La_2O_3, at 1673 K for 4 hours. The products were then ground, compacted at 0.2 MPa and isostatically pressed at 300 MPa. They were sintered at 1673 K for 4 hours in air. This procedure was repeated twice in order to obtain single phased samples of relative density higher than 95 %. The final grain size was less than 5 µm. The working electrodes were shaped as shown in figure 1 with diamond tools.

The counter and reference electrodes were made of platinum paint (Degussa 308 A).

The measurements were carried out in synthetic air.

IMPEDANCE MEASUREMENTS

The impedance spectroscopy measurements were carried out in a 4-electrode cell (Figure 1) which has already been described elsewhere (16). Two working electrodes can be investigated simultaneously. The counter electrode is annular and broad enough to cover the area opposite the working electrodes. The reference electrode is central and small.

The impedance diagrams were recorded under zero dc conditions. The electrode characteristics were obtained with an Autolab potentiostat/impedance frequency analyser (Eco-Chemie) in the frequency range 10^{-3}-10^4 Hz. The amplitude of the measuring signal was 30 mV. The electrolyte responses corresponding to the 2-electrode cells formed by the working and the counter electrodes were plotted by using a Hewlett-Packard impedancemeter (HP 4192 A LF) in the frequency range 5-1.3 10^7 Hz. The amplitude of the measuring signal was around 100 mV to obtain well defined diagrams. It was checked that both pieces of apparatus give the same impedances for the same cells in the common frequency interval.

EXPERIMENTAL PROCEDURE

Two reference temperatures were selected:

- 823 K for the electrolyte. At this temperature, the interesting part of the electrolyte response is fairly well described in the frequency range of our equipment (Figure 2.a).
- 1173 K for the electrode. This is the lowest temperature where we can get a reasonably complete description of the electrode characteristic (Figure 2.b) in the frequency range extending to 10^{-3}Hz. Furthermore, at this temperature the electrode was found to be stable after heating from room temperature.

The procedure we applied was the following:

- Preliminary measurements were carried out from 773 K up to 1123 K (impedance diagrams were recorded every 12 hours during 2 days).
- Then, impedance measurements were performed systematically during heating and cooling cycles between 673 K and the chosen curing temperatures: 1223, 1373 and 1473 K.
- The annealings at 1373 and 1473 K were investigated in more detail. During each annealing, the diagrams were plotted, over the all frequency range of our equipment (10^{-3}-1.3 10^{7} Hz), every 24 hours. After each annealing, diagrams were also plotted at the reference temperatures: 1173 and 823 K.

The annealing times were of the order of 10 days (Table I). The heating and cooling rates were of the order of 200 K/h.

Results and Discussion

DIAGRAM COMPONENT ASSIGMENT

Typical diagrams recorded at 823 K and 1173 K are shown in figure 2. The low frequency part visible in figure 2.b is a typical electrode characteristic and this assignment was not regarded as questionable. On the other hand, the diagram shown in figure 2.a is rather unusual. It is in fact composed of three components: two are easily detectable on this figure, the third one is at the high frequency end of the diagram. It can be viewed by magnifying this part and more easily on diagrams recorded at lower temperature (Figure 3). To assign these three components we referred to the relaxation frequency criteria (17-19). According to these criteria, the bulk and grain-boundary relaxation frequencies are independent of the geometrical factor of the sample. Therefore, at a given temperature, the semicircle which characterizes the bulk of the electrolyte should relaxe at a frequency of the order of that of the bulk semicircles obtained with symetrical cells (20). These criteria indicate unambiguously that the bulk component is the high frequency additional semicircle (that more easily visible in figure 3). Furthermore, the application of the Newmann equation (21):

$$r = \frac{1}{4\sigma_{el} R_{el}} \qquad [1]$$

which relates the electrolyte conductivity σ_{el} and the measured electrolyte resistance R_{el} to the electrode interface radius r, gives, with this assumption, electrode interface radii of the order of 400 µm which are in concordance with the optical observations (the Newmann equation can be applied either with the bulk or the dc parameters).

The criteria also indicate that the low frequency semicircle visible in figure 2.a relaxes at the same frequencies as the grain boundaries of the electrolyte investigated and that the medium frequency semicircle could be the characteristic of thicker blockers such as small pores. However, in terms of magnitude, the low frequency semicircle is far too large compared to the bulk one to be the conventional electrolyte grain-boundary response. For further informations, the diagrams examined here can also be compared to other reported results:

- Figure 4 shows a diagram obtained with a bi-crystal of YSZ (18). It characterizes the responses of the bulk and that of two families of blockers (very thin voids and pores) present along the interface between contacted single crystals. After "normalisation" to the temperatures of our measurements, the coincidence with the relaxation frequencies of our point electrodes is significant.
- Steil (22) also reports a diagram similarly shaped obtained with electrodes made of silver foils imperfectly pressed in contact with the electrolyte sample. The analysis given in this document demonstrates that the voids present along the electrode interface generate an additional semicircle which squeezes in between the bulk and the grain boundary semicircles of the electrolyte.
- The theoretical analysis by Fleig and Maier (23) also demonstrates that imperfect contacts at electrodes can generate additional semicircles of the blocking effect type.

Accordingly, we will interpret the semicircles shown in figure 2.a as the responses of voids present along the electrode interface i.e. as a characteristic response of the microstructural imperfections of the electrode contact.

An important point to be stressed is that the resistance which can be measured at the "valley" between the electrode reaction characteristic (Figure 2.b) and these "interface blocking effects" should not be confused with the dc resistance of the electrolyte. Applying the Newmann equation with this resistance gives electrode interface radii which are far too small. This remark is especially important for the high temperature data processing. At such temperatures, the detail of the "electrolyte response" (shown in figure 2.a) are not accessible and one may be tempted to extrapolate the electrode reaction characteristic to get the electrolyte dc resistance. According to the results reported here, this is likely to give erroneous data.

MICROSTRUCTURAL DEFECTS AT THE ELECTRODE INTERFACE

The results shown in figure 5 clearly indicate that a curing at high temperature reduces the importance of the blocking effects by the interface microstructural defects. The evolution is already significant after the annealing at 1223 K. It is greater after that at 1373 K.

On the other hand, during the annealing at 1473 K, a new blocking effect develops. This is likely to be associated with the formation of a chemical reaction product such as $SrZrO_3$ at the electrode interface. Figure 6 shows the evolution of the corresponding semicircle, for the LSM60 electrode. It was obtained by mathematical difference between the diagram recorded at time t and the initial one chosen as the reference. With the LSM55 electrode which contains less strontium, the results are qualitatively similar but smaller (by a factor of about 10). By assuming that the relaxation frequencies of all semicircles vary with an activation energy of 1 eV as a function of temperature, one can deduce that this additional "$SrZrO_3$" semicircle is located on the low frequency side of interface microstructural defect response that we have examined before. The results obtained at 823 K show that they strongly interfere with each other.

All these last results indicate that, as for the grain boundaries, voids and second phases may generate blocking effects at the electrode interface.

Concerning the blocking effects due to the interface microstructural defects, an important observation should be noted regarding the cathode reaction rate: there is apparently no simple correlation between the evolution of these blocking effects and the characteristic of the cathode, and especially the corresponding overpotential resistance. Figure 7 shows the LSM55 electrode characteristic recorded initially at 1173 K and that determined at the same temperature, after the first annealing at 1373 K. Despite the strong decrease in the blocking effects at the interface shown by figure 5, there is no significant evolution of the electrode characteristic (a decrease of only 15 % is observed).

AGING OF THE CATHODE CHARACTERISTIC

Intermediate measurements at 1273 and 1323 K over periods of 5 days showed that, up to 1323 K, the electrode characteristics are stable (within about 20 %). On the other hand, at 1373 K, they exhibit a marked aging as shown in figure 8. At this stage, the features we have noted are the following:

- The curves are not homothetic with each other. Therefore, the evolution is not related to a simple reduction of the active electrode reaction zone. It is an alteration in the electrode reaction mechanism itself.
- There is a significant shift in the frequency distribution indicating that the observed "swelling" of the loops is due to an increase of a low frequency component. Figure 9 shows the evolution of the "maximum" frequency measured at the top of the loop as a function of the curing time.
- According to this observation, we have examined quantitatively the variation of the electrode overpotentials ΔR_η that we determined by mathematical difference between the loop characteristics measured at time t and the initial ones. Figure 10 shows their variations with curing time. It seems that for both electrodes, a square root law is obeyed, suggesting a diffusion controlled of the phenomenon described. The variation is significantly greater for the electrode with the high strontium content (LSM60).

A peculiar feature that we could verify several times is the reversibility of this aging after a cooling at medium temperatures. For instance, after the first annealing at 1373 K the system was cooled down to 823 K (where we recorded the interface characteristic) and then re-heated to 1373 K. The interface diagrams which were recorded on reaching this temperature for the second time were very similar to the initial ones, and afterwords approximately the same agings were observed (The second time they were slightly more rapid).

At 1473 K, where chemical reaction products start to be detectable in the high frequency part of the electrolyte diagram:

- similar agings were observed with similar square root laws (Figure 10)
- the aging rate is markedly greater for the LSM60 electrode
- the reversibility is no longer complete. A permanent aging remains after the cooling down of the electrode.

References

(1) E. Ivers-Tiffee, M. Schieβl, H.J. Oel, W. Wersing, in Proceedings of the Third International Symposium on Solid Oxide Fuel Cells. Eds. S.C. Singhal and H. Iwahara. The Electrochemical Society, Pennigton, NJ, 1993, pp. 613-622.

(2) G. Stochniol, E. Syskakis, A. Naoumidis, in Proceedings of the 5th IEA Workshop, *Materials, Process Engineering and Electrochemistry*. Eds. P. Biedermann and B. Krahl-Urban. Forschungszentrum Jülich GmbH, Jülich, Germany, 1993, pp. 25-31.

(3) Y. Takeda, Y. Sakaki, T. Ichikawa, N. Imanishi, O. Yamamoto, M. Mori, N. Mori, T. Abe. Solid State Ionics, 72 (1994), 257-264.

(4) C. Claussen, C. Bagger, J.B. Bilde-Sorensen, A. Horsewell, in Proceedings of the 14th International Symposium on Materials Science, *High Temperature Electrochemical Behaviour of Fast Ion and Mixed Conductors*. Eds. F.W. Poulsen, J.J. Bentzen, T. Jacobsen, E. Skou, M.J.L. Ostergard. Riso National Laboratory, Roskilde, Denmark, 1993, pp. 237-242.

(5) A. Mitterdorfer, L.J. Gauckler, in Proceedings of the 17th International Symposium on Materials Science, *High Temperature Electrochemistry : Ceramics and Metals*. Eds. F.W. Poulsen, N. Bonanos, S. Linderoth, M. Mogensen, B. Zachau-Christiansen. Riso National Laboratory, Roskilde, Denmark, 1996, pp. 357-362.

(6) C. Claussen, C. Bagger, J.B. Bilde-Sorensen, A. Horsewell
Solid State Ionics, 70/71 (1994), 59-64.

(7) O. Yamamoto, Y. Takeda, R. Kanno, T. Kojima, in Proceedings of the First International Symposium on Solid Oxide Fuel Cells. Eds. S.C. Singhal. The Electrochemical Society, Pennigton, NJ, 1989, pp. 242-253.

(8) C.C. Chen, M.M. Nasrallah, H.U. Anderson, in Proceedings of the Third International Symposium on Solid Oxide Fuel Cells. Eds. S.C. Singhal and H. Iwahara. The Electrochemical Society, Pennigton, NJ, 1993, pp. 598-612.

(9) J.W. Stevenson, T.R. Armstrong, W.J. Weber, in Proceedings of the Fourth International Symposium on Solid Oxide Fuel Cells (SOFC-IV). Eds. M. Dokiya, O. Yamamoto, H. Tagawa, S.C. Singhal. The Electrochemical Society, Pennigton, NJ, 1995, pp. 454-462.

(10) C. Brugnoni, U. Ducati, M. Scagliotti
Solid State Ionics, 76 (1995), 177-182.

(11) C. Brugnoni, U. Ducati, C. Chemelli, M. Scagliotti, G. Chiodelli
Solid State Ionics, 76 (1995), 183-188.

(12) G. Stochniol, E. Syskakis, A. Naoumidis
J. Am. Ceram. Soc., 78 [4] (1995), 929-932.

(13) J.A.M. van Roosmalen, E.H.P. Cordfunke
Solid State Ionics, 52 (1992), 303-312.

(14) K. Wiik, C.R. Schmidt, S. Shamsili, M.-A. Einarsrud, T. Grande, in Proceedings of the 17th International Symposium on Materials Science, *High Temperature Electrochemistry : Ceramics and*

Metals. Eds. F.W. Poulsen, N. Bonanos, S. Linderoth, M. Mogensen, B. Zachau-Christiansen. Riso National Laboratory, Roskilde, Denmark, 1996, pp. 491-496.

(15) G. Stochniol, H. Grübmeier, A. Naoumidis, H. Nickel, in Proceedings of the Fourth International Symposium on Solid Oxide Fuel Cells (SOFC-IV). Eds. M. Dokiya, O. Yamamoto, H. Tagawa, S.C. Singhal. The Electrochemical Society, Pennigton, NJ, 1995, pp. 995-1005.

(16) H. Lauret, A. Hammou
J. Eur. Ceram. Soc., 16 (1996), 447-451.

(17) M. Kleitz, H. Bernard, E. Fernandez, E. Schouler, in Advances in Ceramics, *vol. 3, Science and Technology of Zirconia*. Eds. N. Claussen, L.W. Hobbs. The American Ceramic Society, Columbus, OH, 1981, pp. 310-336.

(18) M. Kleitz, C. Pescher, L. Dessemond, in Science and Technology of Zirconia V. Eds. S.P.S. Badwal, M.J. Bannister, R.H.J. Hannink. Technomic Publishing Company, Inc., Lancaster, P, 1993, pp. 593-608.

(19) L. Dessemond, J. Guindet, A. Hammou, M. Kleitz, in Proceedings of the Second International Symposium on Solid Oxide Fuel Cells. Eds. F. Grosz, P. Zegers, S.C. Singhal, O. Yamamoto. Office for Official Publications of the European Communities, Brussels, 1991, pp. 409-416.

(20) M.C. Steil, F. Thevenot, M. Kleitz, to be published in J. Electrochem. Soc.

(21) J. Newmann
J. Electrochem. Soc., 113 (1966), 501-502.

(22) M.C. Steil, PhD Thesis, Ecole Centrale de Lyon et Ecole Nationale Supérieure des Mines de Saint Etienne, France, 1996.

(23) J. Fleig, J. Maier
Solid State Ionics, 85 [1-4] (1996), 17-24.

annealing	temperature /K	time /min	
		LSM55	LSM60
HT1	1223	3990	3990
HT2	1373	15680	15585
HT3	1373	18385	18245
HT4	1473	14320	14320

Table 1. High temperature curing conditions of LSM55 and LSM60 electrodes.

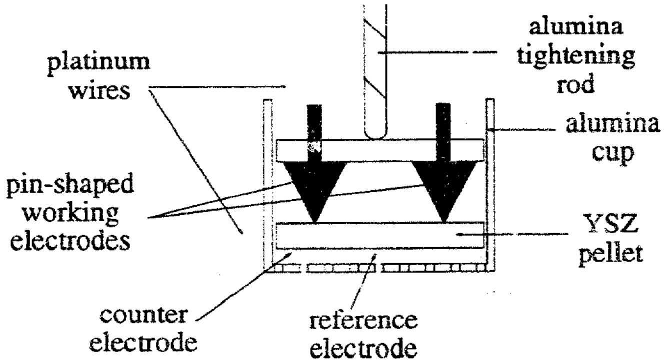

Figure 1. 4-electrode cell using pin-shaped working electrodes.

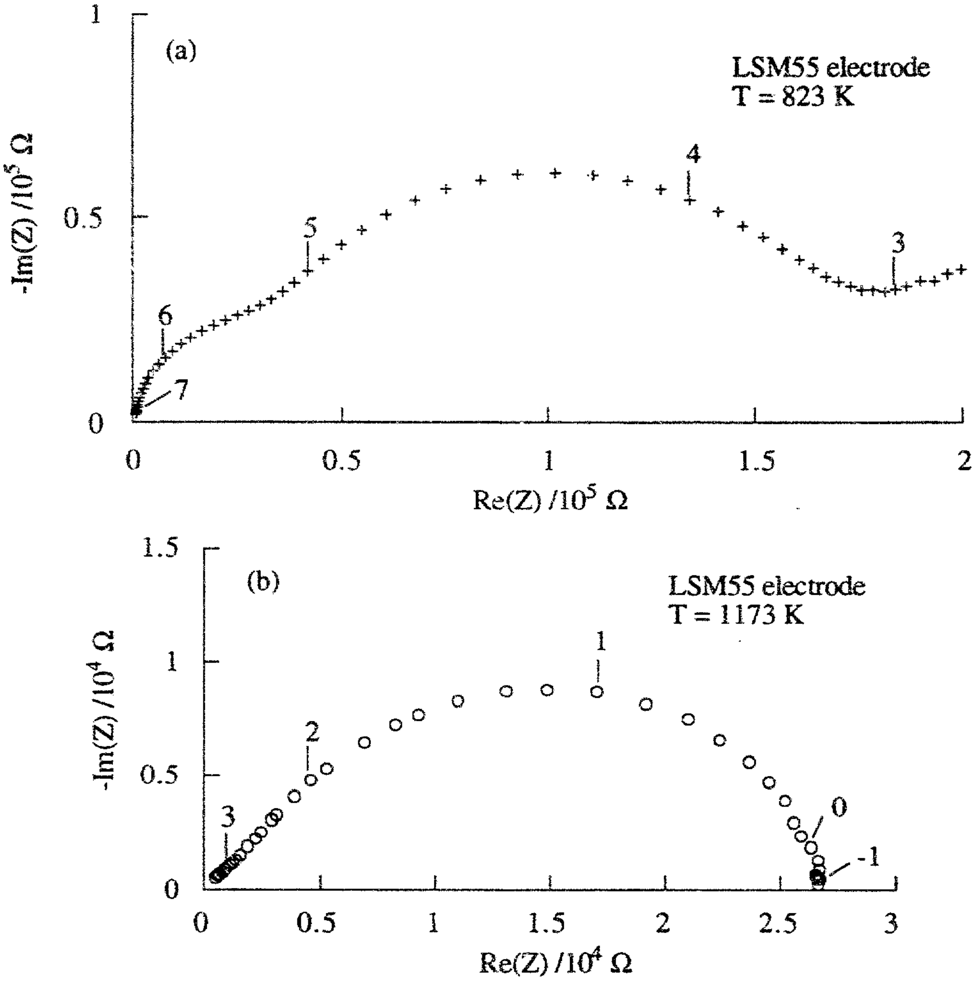

Figure 2. Impedance diagrams of (a) LSM55 electrode interface, at 823 K in air, and (b) LSM55 electrode, at 1173 K in air (the overall resistance of the interface has been substracted). (Diagrams recorded after preliminary measurements and before any annealing. The numbers indicate the logarithm of the measuring frequency).

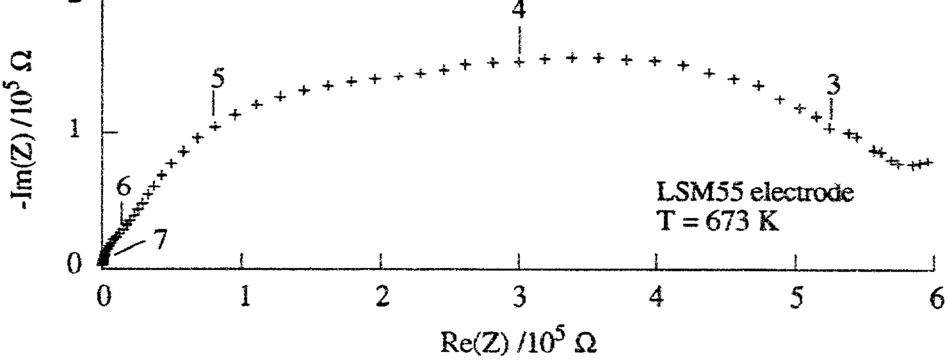

Figure 3. Impedance diagram of the LSM55 electrode interface recorded at 673 K in air.

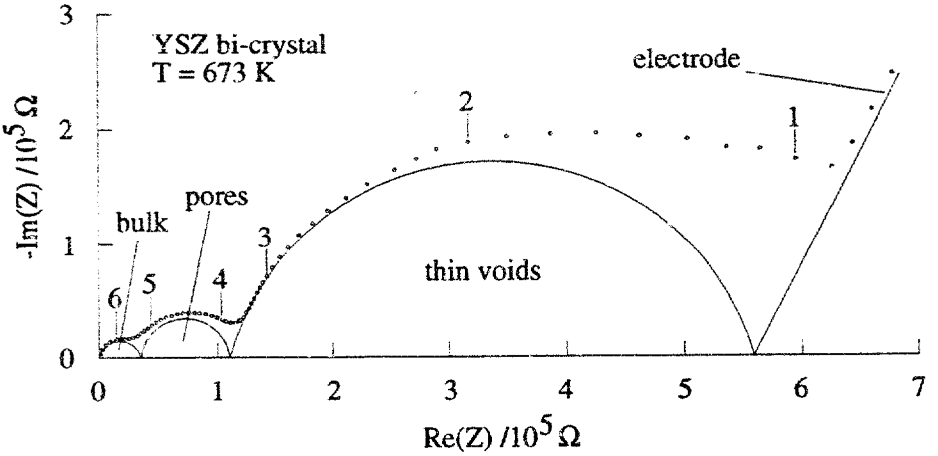

Figure 4. Impedance diagram of two contacted single crystals of YSZ (10 mol% Y_2O_3) at 673 K in air.

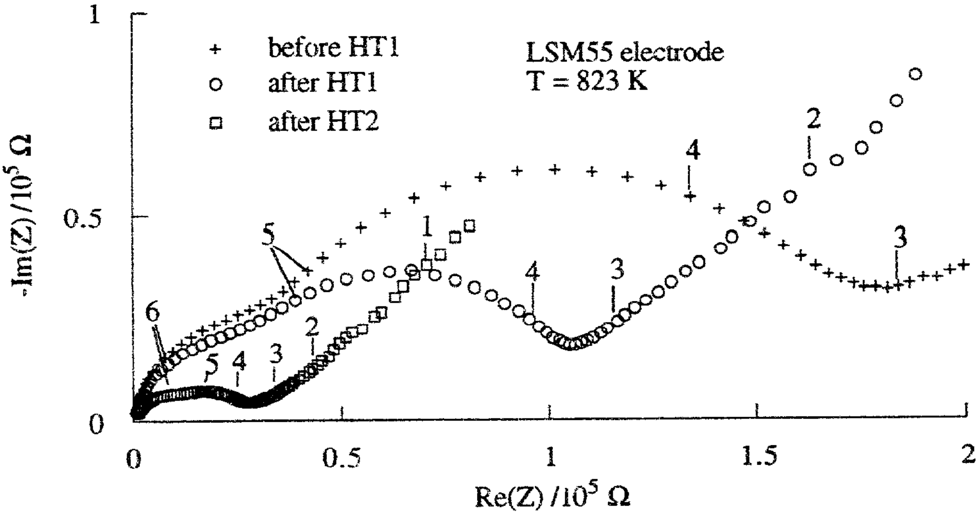

Figure 5. Characteristic of the LSM55 electrode interface before and after annealings at 1223 and 1373 K. Impedance diagrams recorded at 823 K in air.

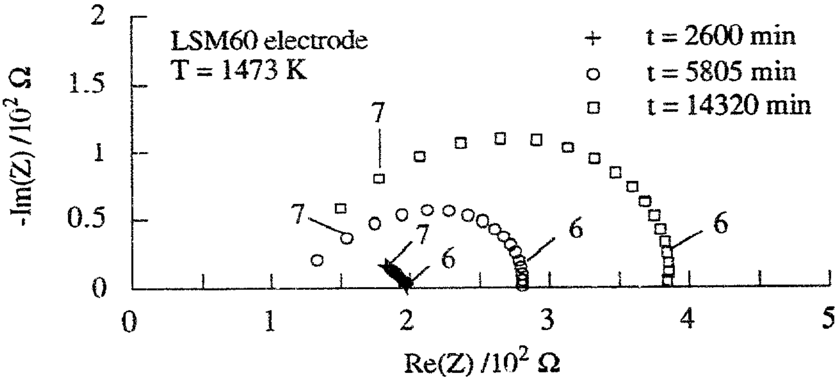

Figure 6. Response of $SrZrO_3$ formed at the LSM60 electrode interface during annealing at 1473 K in air.

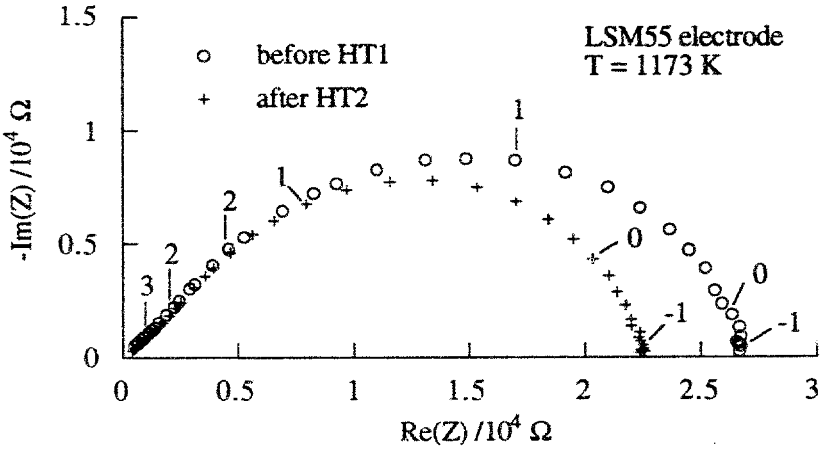

Figure 7. Characteristic of the LSM55 electrode recorded at medium temperature before and after annealing at 1373 K and cooling to 773 K.
(The overall resistance of the interface has been substracted).

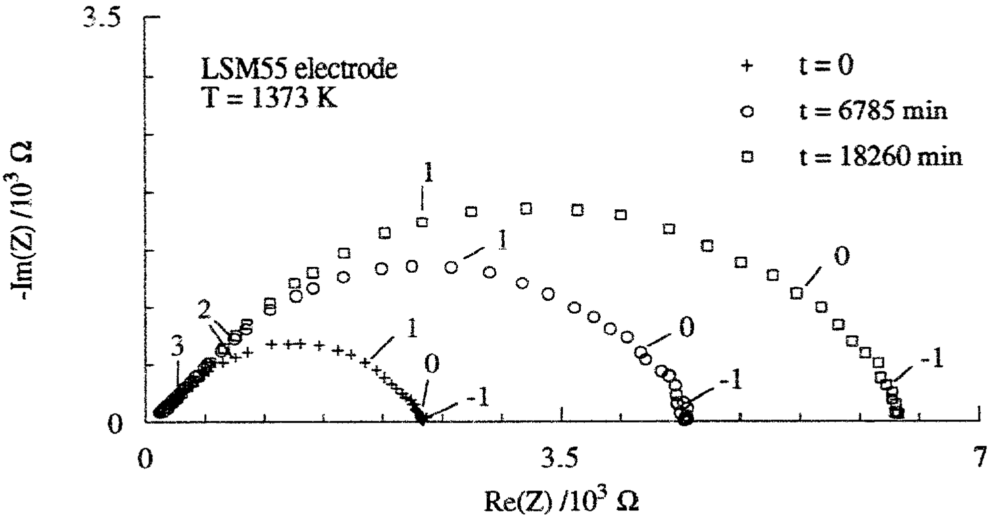

Figure 8. Characteristic of the LSM55 electrode as a function of curing time at 1373 K in air. (The overall resistance of the interface has been substracted).

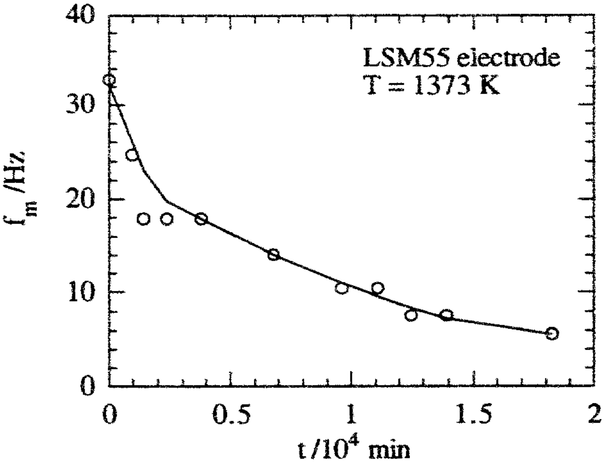

Figure 9. Frequency determined at the top of the LSM55 electrode characteristic as a function of curing time (experimental conditions of figure 8).

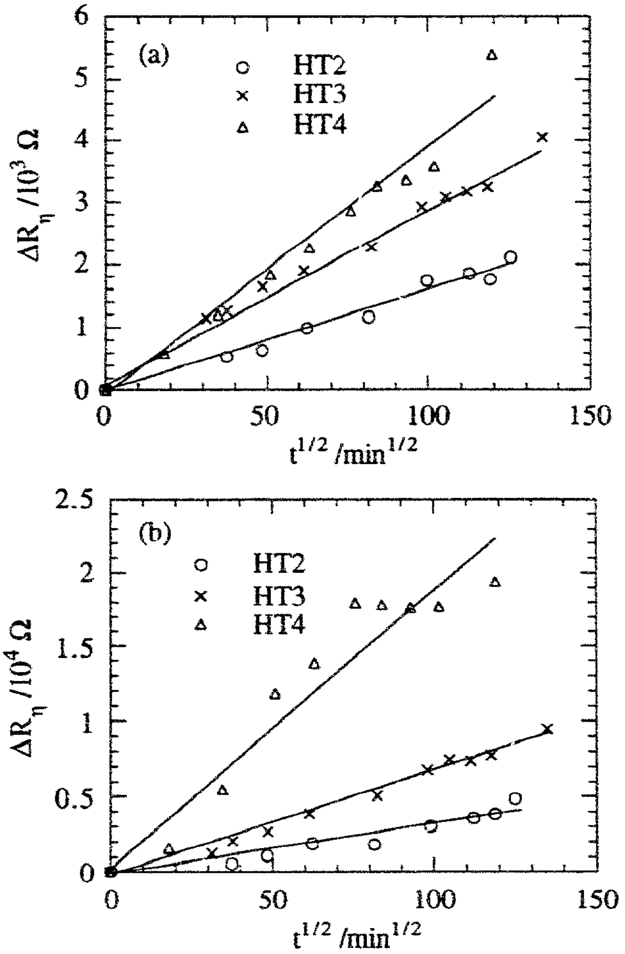

Figure 10. Variation of the electrode overpotential resistance of (a) LSM55 electrode and (b) LSM60 electrode, as a function of the square root of curing time.

Materials Behavior under an Oxygen Potential Gradient at High Current Densities

Harumi Yokokawa, Katsuhiko Yamaji, Teruhisa Horita, Natsuko Sakai,
Masahiko Ishikawa, and Masayuki Dokiya
National Institute of Materials and Chemical Research
and
Tatsuya Kawada
Research Institute of Scientific Measurements, Tohoku University

abstract

The materials behavior under a real cell operation has been examined from viewpoints of overpotentials, temperature distribution and oxygen potential gradient which provide driving forces for chemical reactions and diffusion. Particularly, an emphasis is placed on the roles of oxygen as (1) oxygen potential dependent phase relations, (2) reactants or products which need oxygen path for transportation, and (3) oxygen potential gradient causing an inverse gradient of elemental chemical potential which allows cations to diffuse to the oxidative side.

1. Introduction

Materials problems associated with solid oxide fuel cells can be categorized as follows;

1) stability of cell components during fabrication processes
2) stability on heat cycles
3) stability under cell operation

In the early stage of development of SOFC materials, the firs two aspects of materials problems have been of the primary concern. During a fabrication process, chemical reactions at interfaces between cell components are to be avoided. On heat cycles, significant mismatch in the thermal expansion may give rise to the mechanical instability. Even so, recent successful construction and operation of SOFC stacks makes it necessary to investigate the materials behavior of the cell components for a long operational period of time.

To predict the material behavior for a long period of time, the thermodynamic considerations based on chemical reactions and diffusion will be of the technological importance. The equilibrium properties tell us the ultimate chemical forms when the equilibrium can be fully established. On the other hand, the irreversible thermodynamics provides a basis of investigating driving forces for mass transfer and resulting concentration distribution. In the present paper, recent results of investigations are reviewed with an emphasis on stability under an operational condition.

2. Thermodynamic features of Electrochemical Cell

2.1 Mass flows across cell components and associated potential distribution

Figure 1 shows schematic mass flows and related electrochemical reactions in a high temperature electrochemical cell. Since the fuel cell can be characterized as an energy converter from chemical energy to electricity and heat, flows of chemicals, electricity and heat arise together with corresponding respective gradients of chemical potentials, electrical potential, and temperature. When an oxide ion conductor is used as electrolyte, the oxygen potential becomes of importance. In Fig. 1, the oxygen potential distribution across the cell components is given.

As shown in Fig.1, one of the most important materials problems is the interface stability[1]. A solid oxide fuel cell consists of the major four cell components, namely, electrolyte, cathode, anode and interconnect; for a planar SOFC, sealing materials and gas manifold materials can be the fifth and the sixth components, respectively. Any interfaces between two components should be stable in chemical, mechanical and morphological senses.

Another important materials problem is the behavior under an oxygen potential gradient. Inevitably, electrolyte and interconnect should be placed in a large oxygen potential difference. In addition, a electrical current with a high density passes through such materials. Overpotential caused by this high current density lead to changes in oxygen potential distribution around the electrode/electrolyte interface. Since electrode reactions emit or absorb heats, temperature distribution may also arise in the electrode vicinity. These gradients give rise to driving forces for cation diffusion. Usually, cation diffusion is not significant at 1273 K for a short period of time but may become significant after a long term operation.

2.2 Requirements of SOFC materials

The SOFC materials should meet many requirements to realize a compatible energy converter. Particularly, the high current density and the high power density are required. For this purpose, for example, the electrolyte should be a good oxide ionic conductor to minimize the Joule loss.

In addition to such requirements as respective cell components, the SOFC materials should meet the following requirements as well.

1) Chemical stability; Gibbs energies of compounds involved are required to construct those chemical potential diagrams which provide information of the interface stability or of the phase stability in various chemical environments.
2) mechanical stability; in addition to the mechanical properties, volume data as functions of temperature and oxygen potential are required to evaluate stresses caused by thermal cycles or oxygen potential gradient.
3) morphological stability, information on diffusion and chemical reactions is required.

These stabilities are required not only for the normal chemical environments but also for cases under a steep oxygen potential gradient and at high current density.

2.3 Important roles of oxygen

Since the high temperature SOFC is based mainly on the oxide-ion conductor such as yttria stabilized zirconia, oxygen plays key roles in materials chemistry associated with the SOFC materials. These can be summarized as follows;

1) Oxygen potential dependent physical properties/phase relations

   The SOFC components have to be optimized by changing composition to meet many requirements. Very often, their physical properties show strong dependence on the oxygen potential because the valence can be changed over a wide oxygen potential range of the SOFC operation and as a result, the concentrations of main defects may change correspondingly. One particular example is the volume expansion of doped lanthanum chromites or doped ceria at the reductive environment[2,3]. This is due to the change in the valence and resulting increase of the number of the oxide ion vacancies. In addition to such effects in the defect chemistry, the oxygen potential is one of the fundamental thermodynamic variables which affect phase relations for compounds with changeable valence. For such relations, the valence stability of the binary oxides and the stabilization energy of double oxides are useful[4].

2) Oxygen flow as reactants or reaction products

When reduction or oxidation takes place in the oxide systems, the valence should change and as a result, oxygen gas should evolve or is absorbed. This means that oxygen gas itself is quite import reactants or reaction products. Therefore, the availability of the oxygen path is one of the major factors of determining the materials behavior. As important oxygen path, the gaseous channel in electrode and the grain boundaries in solid materials can be considered. For the chemical reaction between YSZ and LSM, the difference in porosity in LSM affects the reactivity[5].

3) Oxygen potential gradient as driving force for cation diffusion

Inside electrolytes and interconnects, there arise steep gradients of the oxygen potential. On the other hand, around cathode and anode, some oxygen potential distribution can be developed depending on the oxygen flows in the electrode/electrolyte interfaces. Inside the SOFC materials($A_lB_mO_n$), the local equilibrium condition can be established within a reasonable approximation.

$$l\,\mu(\mathrm{A}) + m\,\mu(\mathrm{B}) + n\,\mu(\mathrm{O}) = \Delta_f G^\circ(\mathrm{A}_l\mathrm{B}_m\mathrm{O}_n) \qquad [1]$$

This suggests that a steep gradient of the oxygen potential developed in electrolyte and interconnect should be accompanied with inverse gradients of the chemical potentials of their constituent elements.

$$l\,\mathrm{d}\mu(\mathrm{A}) + m\,\mathrm{d}\mu(\mathrm{B}) + n\,\mathrm{d}\mu(\mathrm{O}) = 0 \qquad [2]$$

This may provide a driving force of cation migration in such materials[1]; this is the same driving force as in the kinetic decomposition or kinetic demixing investigated first by Schmalzried and coworkers[6].

3. Stability and Mass Transfer Associated with Electrode Reactions

Here, we consider the mass transfer which is caused indirectly by the electrode reactions. In an elemental electrode reaction, charge transfer occurs, some chemical species is incorporated and heats are emitted or absorbed. This produces the oxygen potential drop and temperature distribution in addition to the electrical potential drop (that is, overpotential) as illustrated in Fig. 2, which can in turn provide driving forces for mass transfer of other species.

3.1 Cathode Overpotential and Related Mass Transfer

The following features on the lanthanum manganite based cathode have been clarified recently;

1) the oxide ion conductivity is not large in the lanthanum strontium manganite in the "oxygen-rich" region because of a small number of oxide ion vacancies[7,8];
2) the oxygen gas therefore is incorporated into the electrolyte along the electrode/electrolyte/gas three phase boundaries[9];
3) the cathode overpotential corresponds to the oxygen potential drop in the cathode layer which should be a driving force for oxygen (gas or adsorbed atom) to migrate to the three phase boundaries.

These features, particularly the oxygen potential drop, affect the mass transfer in the cathode/electrolyte interfaces. In recent years, the chromium migration from alloy interconnect and the $La_2Zr_2O_7$ migration at the LSM/YSZ interfaces have been clarified.

3.2 Chromium migration

When an alloy interconnect is used, cathodes will degrade soon because of the chromium evaporation from the alloy interconnect and migration to the cathode[10]. This phenomena can be discussed in terms of the following steps;

a) vaporization from interconnect and diffusion barriers
b) chromium getter
c) gaseous diffusion through gas channel in cathode
d) deposition on the cathode

Hilpert et al.[11] reported that the presence of water enhances the vaporization of the chromium component from alloys. Although the vapor pressure is one of the most important properties in this phenomena, the magnitude of the vapor pressure alone cannot explain the phenomena fully. The diffusion or migration process is quite important. For example, Akiyama et al.[12] in Sanyo found an interesting tendency of the cathode degradation due to the chromium vapor. They changed temperature and cathode materials; they found that the most useful variable to interpret the degradation was the oxygen activity derived from the cathode overpotential, η^c, and temperature; that is,

$$\log a(O_2) = (4F/2.303RT)\ \eta^c \qquad [3]$$

This strongly suggests that the major factor is not the magnitude of the vapor pressure but the oxygen potential drop inside the cathode layer. Instead of the normal cathode reaction, the following reaction can occur at the three phase boundaries;

$$2\ CrO_3(g) + 6\ e^-(\text{in Cathode}) = Cr_2O_3(s) + 3\ O^{2-}(\text{in Electrolyte}) \qquad [4]$$

As a result, chromia has to be deposited at the three phase boundaries which are the most important position for the electrode reaction. After the deposition of Cr_2O_3, the cathode activity should be degraded and the overpotential should increase resulting in the enhanced driving force for the above reaction. In this sense, the chromium migration can take place catastrophically.

On the other hand, the chromium migration has not attracted attentions for the oxide interconnect. This is due to the difficulty in diffusion of the chromium component in the lanthanum chromites. As Sasamoto et al.[13] clarified, the vaporization of the chromium component from the lanthanum chromite based materials leaves the chromium-poor layer on the top of the surface so that this layer prohibits further vaporization. This is the main reason why the chromium migration cannot be observed in the oxide interconnect. A similar phenomenon was observed by Akimoto et al.[10] who tested alloys after the chromium oxide scale was removed. Since the formation of chromium oxide created a chromium-poor layer, they observed the less degradation of cathode by using this alloys.

3.3 Manganite/YSZ interface

Not only the three phase boundaries but also the inside cathode/electrolyte interface becomes more reductive during a cell operation. This tendency becomes more significant with increasing the current density because the overpotential is usually more significant at higher current density. This affects the stability of the lanthanum manganite/YSZ stability. There should occur two chemical processes at the interfaces; that is, the oxidative $La_2Zr_2O_7$ formation and the reductive manganese dissolution from the manganite into YSZ[5,14]. Since the dependence on the oxygen potential is different between the two processes, we can see the interesting features of the interface chemistry depending on the chemical conditions.

1) Roosmalen et al.[15] observed that no manganese dissolution was detected when rather dense LSM was used with YSZ. On the other hand, Kaneko et al.[16] observed a significant manganese dissolution into YSZ after an operation of an electrochemical cell consisting of YSZ and porous LCM (lanthanum calcium manganite).
2) The above two observation by SEM has been distinguished in a more significant and impressive manner by TEM. Tricker and Stobbs[17] observed by TEM the difference in the geometrical features of the $La_2Zr_2O_7$ phase formed at the LSM/YSZ interface between a sample just after a heat treatment in air at a high temperature and another sample after a 24 h cell operation at 1273 K.
3) These observation by TEM can be well interpreted in terms of the thermodynamic properties described above in combination with considerations on the plausible oxygen potential distribution in the interface vicinity.
4) The prediction based on the thermodynamic considerations that the formed $La_2Zr_2O_7$ will disappear from the interface to the inside of LSM or to the three phase boundaries has been confirmed by the TEM observation made by Siemense[18] that the $La_2Zr_2O_7$ phase formed at the fabrication process disappeared from the interface after a long term operation at 1273 K.
5) These features are consistent with the observed long term stability of the cell performance. It is also interesting to compare with behavior of LSM in electrolyzer. Koshiro et al.[19] in MHI reported that LSM is degraded in electrolyzer because of the formation of $La_2Zr_2O_7$. Even for the A-site deficient LSM, $La_2Zr_2O_7$ can be formed according to the oxidative nature of this reaction. In view of this, it is quite interesting to point out that Dornier has adopted a $La_{0.5}Ca_{0.5}MnO_3$ cathode probably because they started using this materials as air electrode for water electrolyzer.

3.4 Endothermic Anode Reaction and Silica Transfer

Hishinuma et al.[20] observed that silica migrated significantly on anode specially when methane is used as fuel. When hydrogen gas is used as fuel, the temperature distribution across the cell is not significantly large. On the other hand, the endothermic reactions should take place at anode for methane so that the anode electrode can be significantly cooled. If silica is present, the temperature drop can be a driving force for silica migration. In a reducing atmosphere, silica can be decomposed as follows;

$$SiO_2(s) = SiO(g) + 0.5\ O_2(g) \qquad [5]$$

The evolving SiO(g) migrates to the anode and may react as follows;

$$SiO(g) + O^{2-}(\text{electrolyte}) = SiO_2(s) + 2e^-(\text{in Anode}) \qquad [6]$$

Although the equilibrium partial pressures of two gaseous species on SiO_2 are less than 10^{-10} atm[21], the silica migration can be taken place inside the anode atmosphere at 1273 K. Again, this strongly suggests that the migration via the gas phase can be taken place under a steep gradient of temperature or other thermodynamic valuables even when the vapor pressures themselves are quite small.

Takagi et al.[22] in Murata successfully used zircon $ZrSiO_4$ as additive to Ni/YSZ cermet anodes in order to adjust the thermal expansion coefficient without anode degradation. In this case, any silica migration was reported. This seems partly because the vapor pressure is lowered by forming double oxides and partly because the silica poor region can be formed after a small part of silica evaporated in a similar manner to the chromium vaporization in lanthanum chromite described in 3.2.

3.5 Platinum migration in cathode/electrolyte vicinity

In experimental investigations on the SOFC materials, platinum is often used as electrode and or as lead wire. From our experience, the followings should be noted;

1) After a test on stability of lanthanum calcium chromite between air and fuel at a high current density, platinum particles were observed along grain boundaries outside an effective platinum electrode area. This can be interpreted as one of possibilities as follows;

   $$Pt(\text{wire}) + O_2(g) = PtO_2(g) \qquad [7]$$
   $$PtO_2(g) = Pt(\text{on LCC}) + O_2(g) \qquad [8]$$

   Platinum in lead wires is self-heated at a high current density and reacts with oxygen to form $PtO_2(g)$. Vapors are deposited on cooler surfaces of LCC.

2) A similar platinum migration has been recently observed when platinum electrodes and platinum lead wires were used for measuring the electrochemical cell performance of $(La_{0.9}Sr_{0.1})(Ga_{0.8}Mg_{0.2})O_{2.85}$ electrolyte. A significant amount of platinum was observed along grain boundaries. Compared with Pt on LCC, platinum on LSGM is not in particles. In addition, platinum was spread over surfaces; some of them were detected in the oxide state. These observations suggest that there appears chemical interactions between Pt and LSGM. It is hope to investigate such platinum migration from the points of view of surface diffusion of Pt and solubility of Pt in perovskite phases.

4. Stability and Mass Transfer through Electrolyte and Interconnect

4.1 Oxygen potential profiles under OCV condition and at a high current density

Under the zero current condition, the oxide ion flux in electrolyte and interconnect is determined by the following equations;

$$J(O^{2-}) - 2\,J(e^-) = 0; \qquad [9]$$

$$J(O^{2-}) = \frac{RT}{4F}\,\frac{\sigma(O^{2-})\sigma(e)}{\sigma(O^{2-}) + \sigma(e)}\,\frac{d \ln p(O_2)}{d x} \qquad [10]$$

where $\sigma(O^{2-}),\sigma(e)$ are the conductivity of oxide ions and electrons, respectively. In a steady state, the oxide ion flux can be constant throughout the material so that the oxygen potential can be calculated from the above equation as a function of location.

Under a cell operation, the current is no longer zero but at the finite value. In such a case, the external current flux can be related with those for oxide ions and electrons;

$$J(O^{2-}) - 2\,J(e^-) = J_{ext} \qquad [11]$$

Since the flux changes, the oxygen potential should correspondingly change with the external current density.

In Figures 3 and 4, profiles of oxygen potential and electrochemical potentials of oxide ions, electrons and holes are shown for YSZ and calcium doped lanthanum chromite. In YSZ, the oxide ions move fast so that the electrochemical potential of oxide ions is rather flat. On contrary, the electrochemical potential of electrons has a steep gradient at the oxygen potential region where both electrons and holes have low conductivity. In the calcium lanthanum chromite, the electrochemical potential of electrons is rather flat, whereas the electrochemical potential of oxide ions shows steep gradients particularly in the oxidative side.

4.2 Diffusion of impurities

1) Manganese dissolution into YSZ

In an atmosphere with a fixed oxygen potential, the manganese dissolution into YSZ from LSM can be treated as a normal diffusion process so that the concentration profile can be obtained by assuming that the manganese activity n LSM does not change;

$$C(\mathrm{Mn}) = C_0(\mathrm{Mn})\left[1 - \mathrm{erf}\left(\frac{x}{2\sqrt{Dt}}\right)\right] \qquad [12]$$

Within an infinitely dilute solution approximation, this concentration profile can be translated into that of the chemical potential of manganese chemical potential as follows;

$$\mu(\mathrm{Mn}) = \mu^{o}(\mathrm{Mn}) + RT \ln c(\mathrm{Mn}) \qquad [13]$$

This is plotted in Fig. 5. The manganese chemical potential decreases linearly in the diffuison front, whereas this becomes rather flat in the interface with LSM. Inside an electrolyte, the electrochemical potential of electrons is no longer flat so that the relation between $\mu(\mathrm{Mn})$, $\eta(\mathrm{Mn}^{n+})$ and $\eta(e^-)$ should be satisfied as follows;

$$\eta(\mathrm{Mn}^{n+}) + n\ \eta(e^-) = \mu(\mathrm{Mn}) \qquad [14]$$

As described above, the distribution of $\eta(e^-)$ inside an electrolyte depends on the SOFC operational condition. At the zero current density, the steep gradient in $\eta(e^-)$ appears in the oxidative side, whereas a nearly linear change in $\eta(e^-)$ is developed at a high current density. Such gradients appearing in $\eta(e^-)$ makes the gradient of $\eta(\mathrm{Mn}^{n+})$ steeper than that of $\mu(\mathrm{Mn})$. This can give an explanation for why Kaneko et al.[16] observed a significant dissolution and diffusion of manganese in YSZ after a cell test at 1273 K. Note also that the manganese solubility limit in YSZ is expected to increase with lowering oxygen potential[23]. This is also one of the reasons for significant manganese distribution[5].

2) Manganese migration in strontium lanthanum chromite

Recently, Suzuki et al.[24] in Osaka gas have reported that a significant manganese diffusion occurred deeply into a thin layer of strontium lanthanum chromite from strontium lanthanum manganite at 1273 K for 2000 h.

3) Effect of impurity diffusion on oxygen permeation

Although the amount of impurities which diffuse along the oxygen potential gradient is expected to be small, they can affect seriously the characteristics required as the SOFC materials. Particularly, oxygen permeation is important for both electrolyte and interconnect. For the case of the manganese dissolution in YSZ, this does not give rise to serious effects on the electrochemical characteristics[25]. As shown in Fig. 4, the oxygen potential difference in LCC is maintained by a quite thin layer of the oxidative side. If the conductivity of the oxide ions in this part would increase by impurities diffusion, oxygen permeation should be affected seriously by such phenomena, Unfortunately, experimental information is limited for the manganese dissolution in LCC or LSC.

4.3 Diffusion of the main components

Schmalzried et al.[6] found that the non-oxide ion conductive double oxides undergo kinetic decomposition or kinetic demixing under an oxygen potential gradient. This is due to the difference in diffusion coefficient between two cations. At present it is recognized that this phenomena generally occur under a gradient of any thermodynamic variables. Actually, Monceau et al.[26] observed the concentration demixing in yttria stabilized zirconia at a high current density at a high temperature. This suggests that similar phenomena might occur even under an SOFC operational condition. Even when cation diffusion cannot be detected because of their small diffusion coefficient, the chemical potential of elements should develop the gradient across the plate from the air side to the fuel side. In the electrolyte or interconnect, the oxygen potential gradient is developed so that the chemical potentials of the main metallic elements should have the inverse gradient so as to give a rather constant values of the chemical potential of metal oxides.

In an electron conductor such as LCC, the electrochemical potential of electron,

$\eta(e^-)$, is nearly constant.

$$d\eta(e^-) = d\{\mu(e^-) - F\phi\} \approx 0 \qquad [15]$$
$$Fd\phi \approx d\mu(e^-) \qquad [16]$$

The change in electrochemical potential of cation, M^{n+}, is therefore written as

$$\begin{aligned} d\eta(M^{n+}) &= d\{\mu(M^{n+}) + nF\phi\} \approx d\{\mu(M^{n+}) + n\mu(e^-)\} \\ &= d\mu(M) \qquad [17] \end{aligned}$$

This equation shows that under a steep oxygen potential gradient in electron conductors, cations have also a large gradient in electrochemical potentials as driving force for diffusion.

On the other hand, in an oxide ion conductors, the electrochemical potential of oxide ion becomes nearly constant;

$$d\eta(O^{2-}) = d\{\mu(O^{2-}) - 2F\phi\} \approx 0 \qquad [18]$$
$$Fd\phi \approx 0.5\ d\mu(O^{2-}) \qquad [19]$$

In such a case, the change in $\eta(M^{n+})$ is given as

$$\begin{aligned} d\eta(M^{n+}) &= d\{\mu(M^{n+}) + nF\phi\} \approx d\{\mu(M^{n+}) + 0.5n\mu(O^{2-})\} \\ &= d\mu(MO_{0.5n}) \qquad [19] \end{aligned}$$

This means that the magnitude of the oxygen potential gradient is not a good measure for cation diffusion. Fig. 3 shows that at a high current density, $d\eta(O^{2-})$ has some gradient in electrolyte. This suggests that even when $\mu(MO_{0.5n})$ is nearly constant, the driving force arises for cation diffusion to the cathode. In Table 1, the behavior of the electrochemical potential of cations are compared between the cases in interconnects and in electrolytes.

Table 1. The gradient of the electrochemical potential of cations as driving for ce for cations diffusion in interconnects and electrolytes.

	in Interconnect	in Electrolyte
$d\eta(M^{n+})$	$d\mu(M)$	$d\mu(MO_{0.5n})$
dependence on $d\mu(O_2)$	in the same order of $d\mu(O_2)$	does not depend directly on $d\mu(O_2)$ but on $d\eta(O^{2-})$
Effect of valence	no	large
Effect of current density	essentially no	linearly dependent

1) Calcium migration in calcium lanthanum chromite

Calcium doped lanthanum chromite can be air sinterable when the composition of the calcia excess is adopted[27]. This implies that in the calcium doped lanthanum chromite, the activity of CaO is close to unity throughout the materials placed between air and fuel.

As described above, the electrochemical potential of the oxide ions in calcium doped chromite exhibits a significant steep gradient in the air side and a rather flat one in the fuel side as shown in Fig. 4(a). When the activity of CaO is almost unity, the chemical potential of CaO can be regarded as constant. This leads to the following relations;

$$\eta(\mathrm{Ca}^{2+}) + \eta(\mathrm{O}^{2-}) = \mu(\mathrm{CaO}) \sim \text{constant} \qquad [20]$$

From this equation, the extremely steep gradient of $\eta(\mathrm{Ca}^{2+})$ should appear in the air side, which is shown in Fig. 4(b). Since the diffusion coefficient of calcium ions along the grain boundaries is high, the calcium migration to the surface in the air side has been often observed under an SOFC operational condition[28].

2) Chemical reactivity of LSM/LCC interface caused by calcium migration

As a result of the calcium migration, calcium arrives at the interface with the lanthanum manganites. Since the features of the reactivity at the interface between LCC and LSM depend on the porosity of LSM and the A-site nonstoichiometry of LSM[29], the role of the migrated calcium can be categorized as follows;

i) Catalytic activity for the precipitation of manganese oxides at the interface of a dense and A-site deficient LSM with LCC. Since the dense A-site deficient LSM has a oxygen potential drop in it, the interface with LCC shifts to the reductive side. This implies that migrated calcium may be in the chemical form of calcium oxide.

ii) Catalytic activity for the reaction between LCC and porous LSM. The porous LSM has an interface with LCC at the oxygen potential in air. This suggests that the migrated calcium forms the calcium chromate which is very close to the melting point. This substance can be considered as catalyst for the chemical reaction at the interface which occurred only when the porous LSM is used.

3) Kinetic decomposition of Sr doped Ceria

Milliken et al.[30] in SOFCo recently reported that the strontium doped ceria was degraded seriously under the cell operation condition (1073 K for 1000h), whereas no changes have been observed when they exposed these materials in air or fuel and placed between air and fuel. This suggests that the electrical current or related properties may affect this phenomena from the kinetic or the equilibrium reasons. Possible reasons can be given as follows;

i) Change of the solubility limit of SrO in $\mathrm{CeO_2}$ as a function of oxygen potential:

ii) Difference in diffusion coefficients between strontium and ceria.

iii) possible kinetic effect of passing electrical current.

Since no such a catastrophic degradation has been reported for ceria doped with other than strontium, the above possibilities should be carefully examined from various points of view.

5. Some remarks on alloy interconnect

Across alloy interconnects for planar SOFC, the oxygen potential distribution is also developed in a similar manner to that in the oxide interconnects. However, there are several differences in the oxygen potential distribution and the mass transfer in alloys and oxide scales as follows;

1) Inside alloy interconnects, the oxygen potential should be extremely low so that steep oxygen potential gradients should appear in both air and fuel side as shown in Fig. 6.
2) Such a steep oxygen potential drop should be maintained by the formation of an oxide layer or by coating an oxide layer. In the air side, the dense film of a conductive oxide such as lanthanum chromite is to be coated, whereas no good coating material has been proposed for the fuel side so far.

Control of the mass transfer through these oxide layers is crucial in developing alloy interconnects which can be used for a long term operation. Since the electrical path should pass across alloy interconnects of a planar SOFC, these oxides should be electron conductors. When the oxide ion conductivity cannot be neglected, this makes a significant contribution directly to the oxygen permeation. In this case, permeated oxygen cannot penetrate the alloy region and can be blocked. This leads to the accumulation of the oxygen at the interface between alloy and oxide. In other ward, the growth of another oxide may happen at the interface; typically this may be Cr_2O_3. When this oxide is not electron conductive, the resistivity of the interconnect should increase with increasing the amount of the permeated oxygen. To avoid it, the oxide with lower oxide ion conductivity should be used as coating materials. For this purpose, lanthanum chromite-base perovskite is most plausible. This implies that the mass transfer phenomena through lanthanum chromite is crucial even for alloy interconnects.

6. Conclusive Remarks

Since there arise inevitably steep gradients of chemical potential, electrical potential and temperature in any SOFC stacks, it is quite important to control the mass transfer in stacks caused by slow diffusion of cations.

References

1. H. Yokokawa, T. Horita, N. Sakai, and M. Dokiya, "Thermodynamic Considerations on Interfaces in Electrochemical Devices," proceedings of International Workshop on Ceramic Interfaces: Properties and Applications III," July 10-13, 1966 Kuranda Rainforest Resort, Cairns, Queensland, Australia.
2. I. Yasuda and M. Hishimuna, "Mathematical Analysis of Stress Distribution in Acceptor-doped Lanthanum Chromites Under an Oxygen Potential Gradient," Proc. Solid Oxide Fuel Cells IV, The Electrochem. Soc. PV95-1, pp.924-933.
3. I. Yasuda and M. Hishinuma, "Lattice Expansion on Reduction and Internal Stresses of CeO_2-Gd_2O_3 Electrolytes," Extended abstracts of the 5th symposium on Solid Oxide Fuel Cells in Japan, 1996, pp. 107-110.
4. H. Yokokawa, N. Sakai, T. Kawada and M. Dokiya, *Solid State Ionics.* **52**,43-56 (1992).
5. H. Yokokawa, T. Horita, N. Sakai, T. Kawada and M. Dokiya, "Thermodynamic Considerations on Plausible Effect of Oxygen Flow on Morphology of Reaction Products at the YSZ/Lanthanum Manganite Interface in Solid Oxide Fuel Cells," in Proc. First European Solid Oxide Fuel Cell Forum, ed. U. Bossel, 3-7 October 1994, Lucerne, Switzerland, pp. 425-434.
6. H. Schmalzried, *J. Chem. Soc. Faraday Ttran.* **86**, 1273 (1990).
7. S. Carter, A. Selcul, R. J. Chater, Kajda, J. A. Kilner, B. C. H Steele *Solid State*

Ionics **53-56**, 597 (1992).

8. A. Belzner, T. M. Gür, and R. A. Huggins, Solid State Ionics **57**, 327 (1992).
9. J. Mizusaki and T. Tagawa pp. 75-87 proc. Smp. High Temperature Electrode materials and Characterization, ed. D.D. MacDonald and A. C. Khandkar, The Electrochem. Soc. (1991).
10. Y. Akiyama, T. Yasuo, S. Tanuguchi, M. Kadowaki, and T. Saito Extended Abstract pp.5-8, the 2nd symposium of Solid Oxide Fuel Cells in Japan 1993.
11. D. H. Peck, M. Miller, H. Nickel, D. Das and K. Hilpert, "The SrO-Cr_2O_3-La_2O_3 phase diagram and Volatility of $La_{1-x}Sr_xCrO_3$ (x = 0 - 0.3) in comparison to Cr Base Interconnect Alloys," Proc. Solid Oxide Fuel Cells IV, The Electrochem. Soc. PV95-1, pp. 858-868.
12. Y. Akiyama, T. Yasuo, S. Tanuguchi, M. Kadowaki, Y. Miyake and T. Saito Extended Abstract pp.5-8, the 3rd symposium of *Solid Oxide Fuel Cells in Japan* 1994.
13. T. Sasamoto and T. Sata *Yogyou-Kyoukai-shi* **79**, 408 (1971).
14. H. Yokokawa, N. Sakai, T. Kawada, M. Dokiya, *J. Electrochem. Soc.* **138**, 2719 (1991).
15. J. A. M. Roosmalen, and E. H. P. Cordfunke, *J. Solid State Chem.* **52**, 303-312(1992).
16. H. Kaneko, H. Taimatsu, K. Wada, and E. Iwamoto *Proc. 1st International symposium on Solid Oxide Fuel Cells* EC, pp. 673- 680(1991).
17. D. M. Tricker, and W. M. Stobbs *High Temperature Electrochemical Behaviour of Fast Ion and Mixed Conductors* ed by Poulsen, F.W. et al. RISØ National Laboratory, Roskilde, pp. 453- 460 (1993).
18. W. Wersing private communication(1994).
19. I. Koshiro, K. Mori, H. Miyamoto, F. Nanjyo, Extended Abstract pp. 33-36, the 4th symposium of Solid Oxide Fuel Cells in Japan 1995.
20. M. Hishimuna presented in the meeting of the SOFC Society of Japan.
21. H. Yokokawa, T. Horita, N. Sakai, B. A. van Hassel, T. Kawada, M. Dokiya, "Oxygen Permeation and Related Phenomena of Lanthanum Calcium Chromites As SOFC Interconnects," Proceedings of the third international symposium on Solid Oxide Fuel Cells, ed. by S. C. Singhal and H. Iwahara, pp. 364-373, The Electrochemical Society. 1993.
22. H. Takagi presented in the meeting of the SOFC Society in Japan.
23. H. Yokokawa, N. Sakai, T. Kawada, M. Dokiya, "Phase Diagram Calculations For ZrO_2 Based Ceramics: Thermodynamic Regularities in Zirconate Formation and Solubilities of Transition Metal Oxides," pp. 59-68, in Science and Technology of Zirconia V, ed. by S. F. S. Badwal, M. J. Bannister, R. H. J. Hannink, the Australasian Ceramic Society, 1993.
24. M. Suzuki, O. Yamazaki, A. Kajimura and S. Yamaguchi, Extended Abstract pp. 59-62, the 5th symposium of Solid Oxide Fuel Cells in Japan 1996.
25. T. Kawada, N. Sakai, H. Yokokawa and M. Dokiya, *Solid State Ionics* **53-56**, 418-425 (1992).
26. D. Monceau, M. Filal, M. Tebtoub, C. Petot, G. Petot-Ervas, *Solid State Ionics* **73**, 221 (1994).
27. N. Sakai, T. Kawada, H. Yokokawa, M. Dokiya, I. Kojima, *J. Am. Ceram. Soc.*

76[3], 609- 616(1993).

28. N. Sakai, T. Kawada, H. Yokokawa, M. Dokiya, "Chemical Stability of $(La,Ca)CrO_3$ Interconnects of Solid Oxide Fuel Cell," pp. 764-775, in Science and Technology of Zirconia V, ed. by S. P. S. Badwal, M. J. Bannister, R. H. J. Hannink, the Australasian Ceramic Society, 1993.
29. H. Nishiyama, M. Aizawa, H. Yokokawa, T. Horita, N. Sakai, M. Dokiya, and T. Kawada, *J. Electrochem. Soc.* **142**, 2332 (1996).
30. C. Milliken, S. Elangovan and A. Khandkar, "Instability in Strontia-Ceria SOFC Electrolyte," presented in the 2nd International meetings of Pacific Rim Ceramic Societies, 15-17 July 1996, Cairns, Australia.

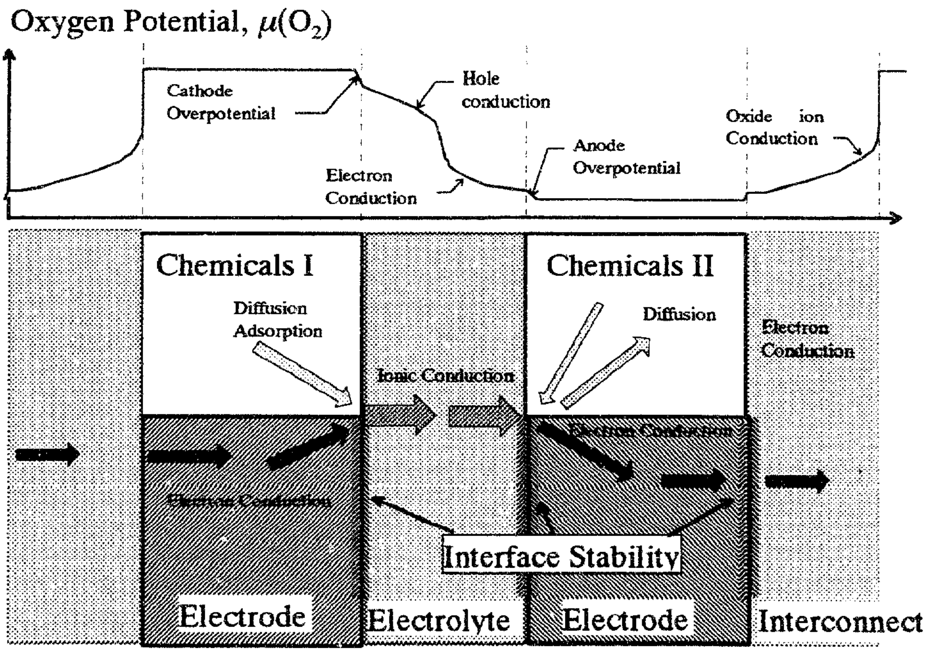

Fig. 1 Schematic diagram of mass flows in electrochemical cells and associated potential distribution across cells.

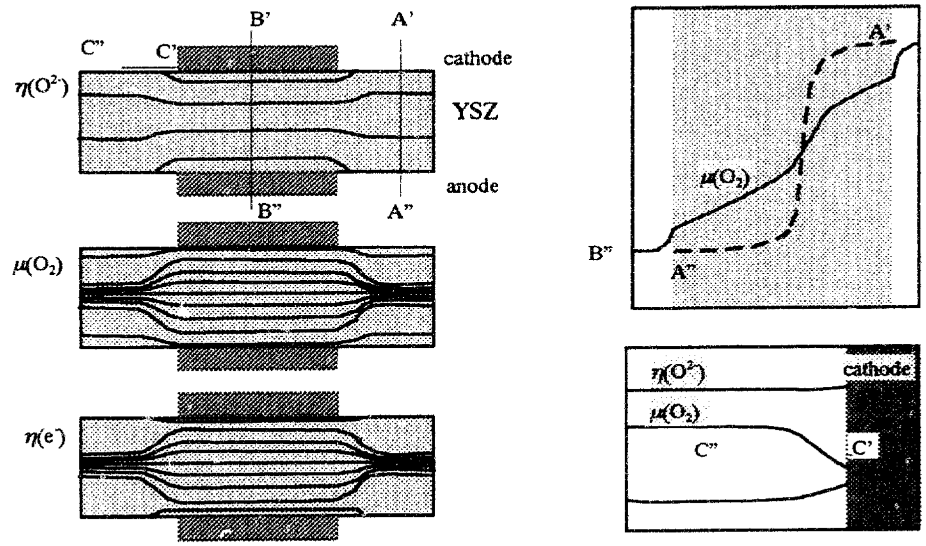

Fig. 2 Schematic distribution of oxygen potential, and electrochemical potentials of oxide ions and electrons inside an electrolyte including edge parts of effective electrode area.

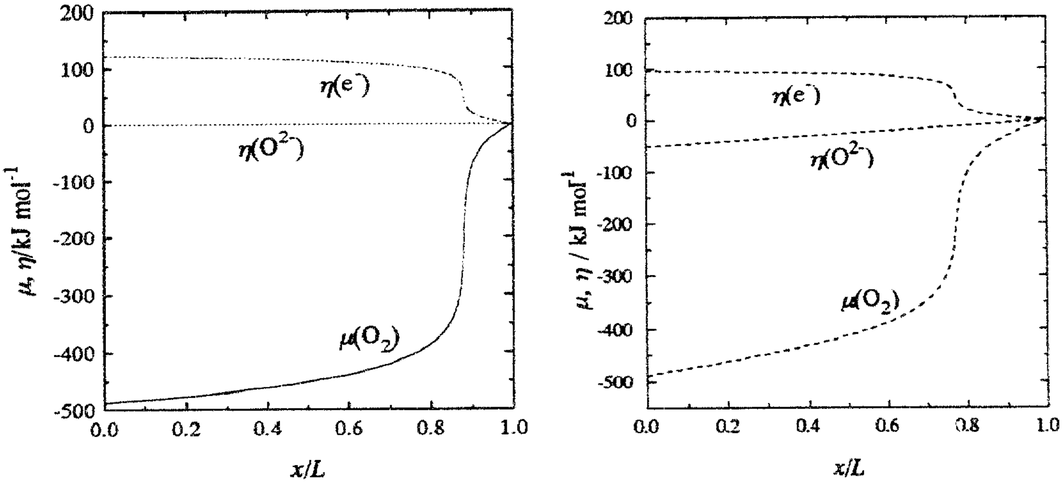

Fig. 3 $\mu(O_2)$, $\eta(O^{2-})$, $\eta(e^-)$ in yttria stabilized zirconia(0.3 mm thick) at 1273 K between air and fuel. (a) for a case of zero current; (b) for $i = 0.88$ A/cm^2. Overpotentials at electrodes are neglected here.

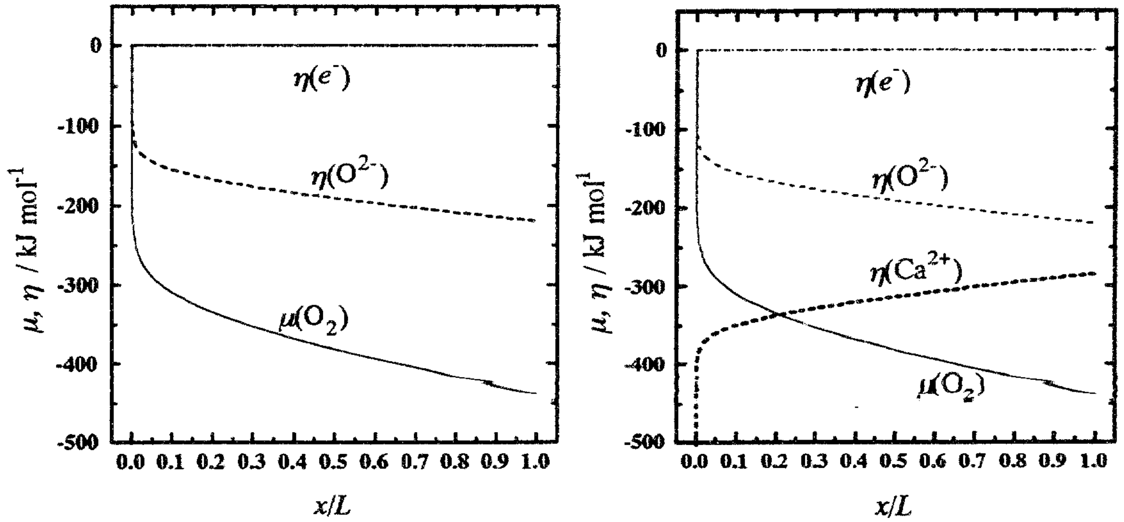

Fig. 4 (a) $\mu(O_2)$, $\eta(O^{2-})$, $\eta(e^-)$ in lanthanum calcium chromite at 1273 K between air and fuel. These profiles do not change even with increasing current density. (b) Change in the electrochemical potential of calcium ions along the oxygen potential gradient.

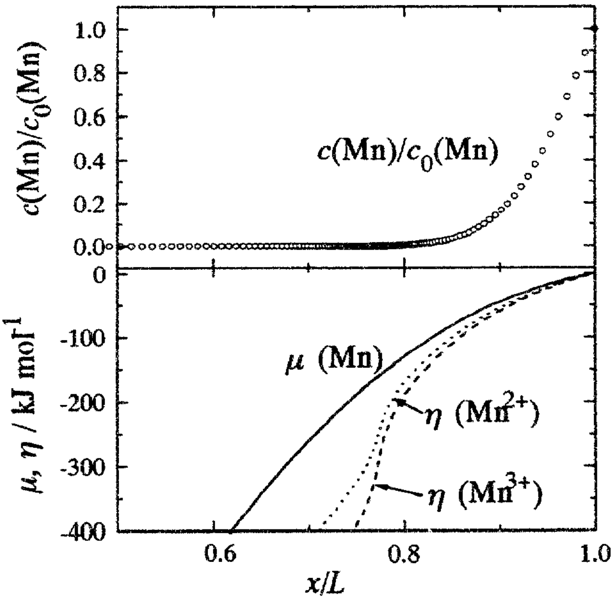

Fig. 5 Schematic distribution of manganese after diffusion from LSM at x=1 and changes in the electrochemical potential of Mn^{2+} and Mn^{3+} at j = 0.88 mA/cm^2 for which case, the electron electrochemical potential is given in Fig. 3.

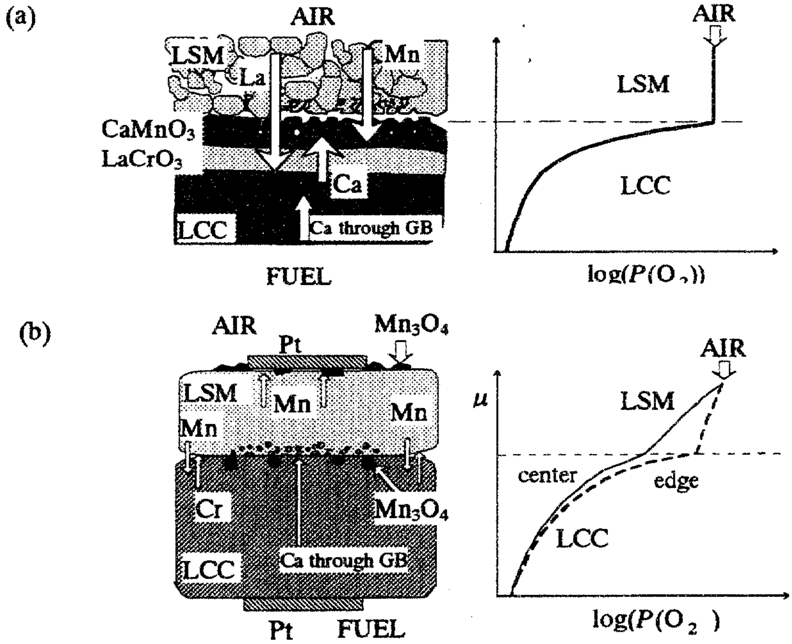

Fig. 6 Schematic illustration of the (La,Sr)MnO_3[LSM]/(La,Ca)CrO_3[LCC] interfaces after being placed between air and fuel at 1273 K for 200 h. (a) a porous manganite showed a significant interdiffusion to be considered as chemical reaction. (b) a dense manganite showed precipitation of manganese oxide at the interface. Both processes can be interpreted as a result of migration of calcium oxide in LCC under an oxygen potential gradient.

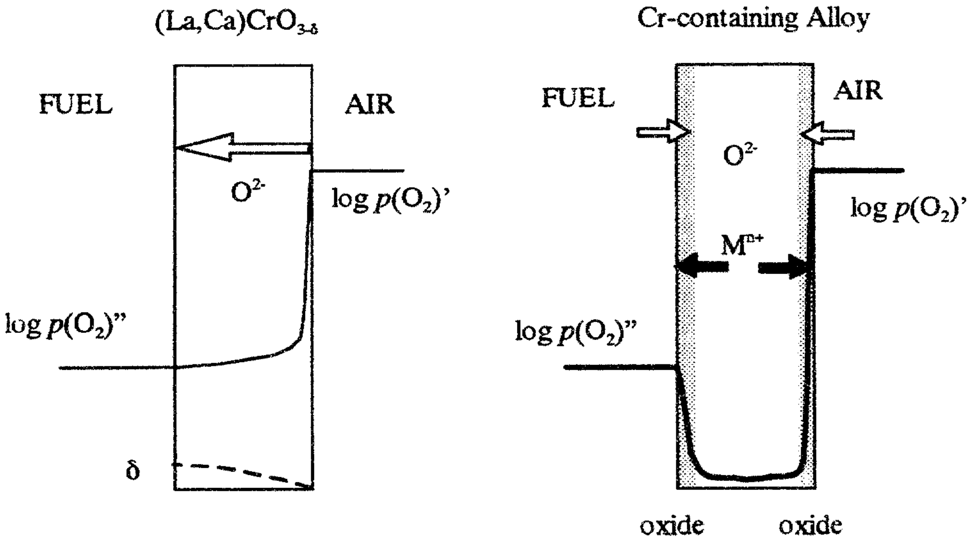

Fig. 7 Comparison in oxygen potential profile and associated mass transfer between oxide and alloy interconnects.

Proceedings of IEA-Workshop: Materials and Processes.
Annex VII: SOFC under Real Operating Conditions
January 28-31, 1997
Les Diablerets, CH

In-situ studies of air electrodes in Solid Oxide Fuel Cells at 850°C using synchrotron diffraction.

F.W. Poulsen, L. Sörby*, H.F. Poulsen and S. Garbe
Materials Department, Risø Nat. Laboratory,
DK-4000 Roskilde Denmark
Kemiska Institutionen*, Uppsala University,
S-75121 Uppsala Sweden

Abstract

The design of a synchrotron diffraction experiment on a working LSM-electrode is outlined. A massive body of data were successfully collected from LSM/YSZ/Ag cells under polarisation at 850°C. The strategy for data analysis is given. Only preliminary results and interpretations are given in this paper. Reproducible changes in lattice parameters, integrated intensities and FWHM's of the LSM phase were observed, when the LSM air electrode was polarised electrochemically in reducing or oxidizing direction. The peak positions from YSZ are unchanged. This is the first experimental proof that the oxygen stoichiometry of LSM can be strongly influenced by the electrochemistry taking place. The lattice expands under reducing conditions, presumably due to a decrease in the oxygen content in LSM.

Background.

The kinetics of oxygen reduction at high temperature in solid oxide fuel cells is currently under discussion. The air electrode is typically a Sr-doped lanthanum manganite perovskite (LSM) deposited on yttria stabilised zirconia ceramics (YSZ). Oxygen from the gas phase, as well as oxygen from the air electrode material itself, may be involved in the reduction. The latter possibility seems relevant to consider for situations such as i) high cathodic polarisation, ii) depletion of gaseous oxygen in closed pockets/crevices at the LSM/YSZ interface, iii) polarisation at lower temperatures, where O_2 reduction may be inhibited, and the lattice oxygen in LSM remains the only exploitable source.

In a preliminary synchrotron experiment in 1995 we used Pt-paint as current collector, allowing us to do in-situ electrochemistry/diffraction up to 1000°C. Pt as current collector, however, had the disadvantage that some of the diffraction peaks of metallic Pt coincides (at high temperature!) with those of LSM. In the present experiment (August 1996) we used silver as current collector and anode and no peak overlap occurred, however now we were limited with respect to high temperatures by the high vapour pressure and low melting point of Ag (960°C).

Experimental details.

Diffraction studies were performed at the BW5 diffractometer at Doris, Hamburg (DESY). This is still one of the very few hard x-ray diffractometers available throughout the world. A versatile, vertical furnace with quarts windows (max. operating temperature 1000°C), housing a plug-in sample holder system has been developed and successfully tested. The transmission through windows and the electrochemical cell at BW5, using 0.124Å radiation (approximately 100 keV), is ~50%. In a conventional two-axis set-up we used a CCD 2D detector (Photonic Science) at a distance of 3.6 m from the sample, allowing inspection of the 2Θ-range from 2-4°. Images were acquired at 1 to 10 min intervals, with corresponding exposure times. The beam size, at the sample position was confined by means of slits to 3 mm height and .3 mm width. A total of approx. 2000 images were recorded from 6 different electrochemical cells. The stored data, obtained during 5 days (and nights), corresponds approximately to 1.5 Gbite.

The cells had silver foil/net current collectors on both sides - a silver painted counter electrode and a 5-50 μm LSM layer on a 150 μm thin YSZ ceramic plate. Active electrode areas were 1 cm^2. Cells were mounted in a pseudo 4-wire circuit. Reduction/oxidation was driven by an external constant current source. Here we report on experiments with the two sides of the cells being exposed to the same atmosphere (.21 atm O_2). Cell current, total cell voltage, temperature of furnace, temperature of cell and a signal proportional to the synchrotron current ($\propto$ beam intensity) were simultaneously datalogged.

Some cells were characterised by impedance spectroscopy prior to the diffraction experiment and some only post mortem to check for short circuit and/or bad contacts between current collector and cell, and between silver counter electrode and the YSZ. It was decided to be too ambitious to due simultaneous polarisation, diffraction and impedance spectroscopy at the same time, although this in general should be recommended.

Data analysis.

Integration of sections of the Debye-Scherrer pictures allows conventional powder diffractograms to be obtained, cf. fig 1. As seen on the left hand side of Fig. 1 the Debye-Scherrer rings are very uneven in intensity in certain directions. This is especially the case for the diffraction peaks from metallic silver, indicating a very coarse and non-random texture of this metallic component. The diffraction rings from YSZ and LSM show much less (if no) texture. Careful analysis will be done in the future.

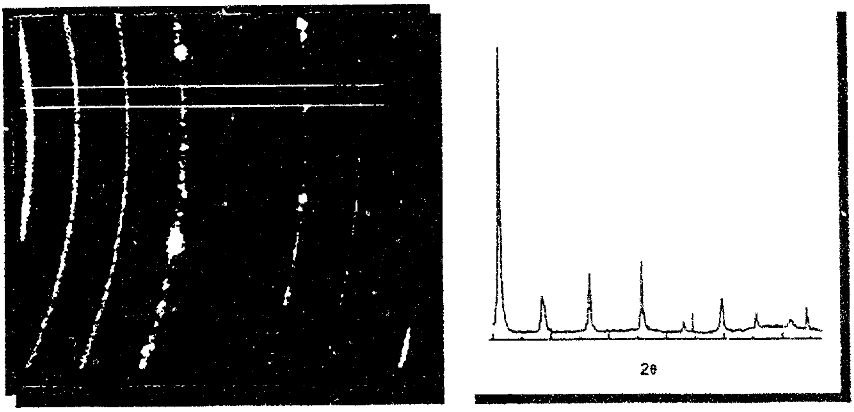

Figure 1. Debye-Scherrer CCD-picture and corresponding "conventional" diffractogram from a LSM/YSZ/Ag cell in synchrotron beam. Integration of intensities is performed between the two horizontal lines.

The "raw" diffractograms then have to be converted: intensities must be normalised with respect to the beam intensity (Doris current); the x-axis, sofar being a pixel-scale, will have to be transformed into a true 2Θ scale. Especially the latter transformation is quite involved, since we have to "reconstruct" the zero point/centre for the Debye-Scherrer rings (actually ellipses) by a complicated matrix-calculus.

Results.

Figure 2. shows a series of diffractograms obtained during the initial heating of a cell. Peak positions shift to lower °2Θ-values upon heating, due to thermal expansion. The shift is much higher for metallic silver as for the ceramic components.

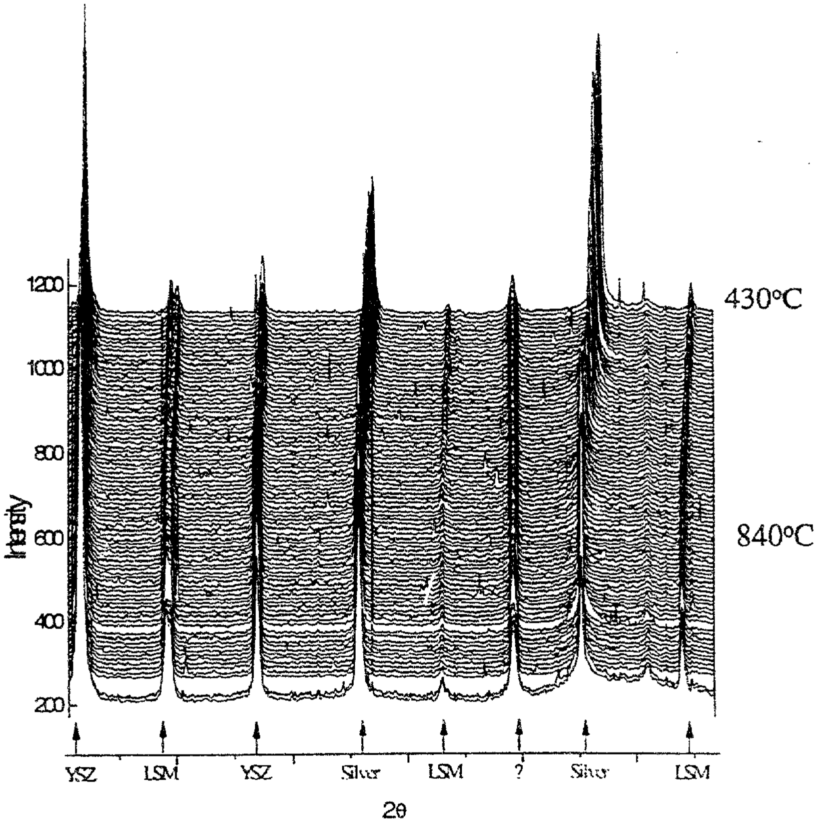

Figure 2. Diffractograms of a LSM/YSZ/Ag cell during heating.

At the max. temperature the cells were then polarised in cathodic and sometimes also in anodic direction. Figure 3 displays such an experiment.

Systematic changes in lattice parameters, integrated intensities and FWHM's of the LSM phase are observed, when the LSM air electrode is polarised electrochemically in reducing or oxidizing direction, cf. Figure 3. The peak positions from YSZ are unchanged, eliminating the explanation that peak shifts were due to Ohmic and/or Peltier heating. This is the first experimental proof that the oxygen stoichiometry of LSM is strongly influenced by the electrochemistry taking place. The lattice expands under reducing conditions due to a decrease in the oxygen content in LSM. The change in lattice parameter of LSM is however below .5%, proving the sensibility of our diffraction technique. Rietveld refinements on the data are in progress; we assume a rhombohedral indexing for LSM at the high temperature to be valid.

Results

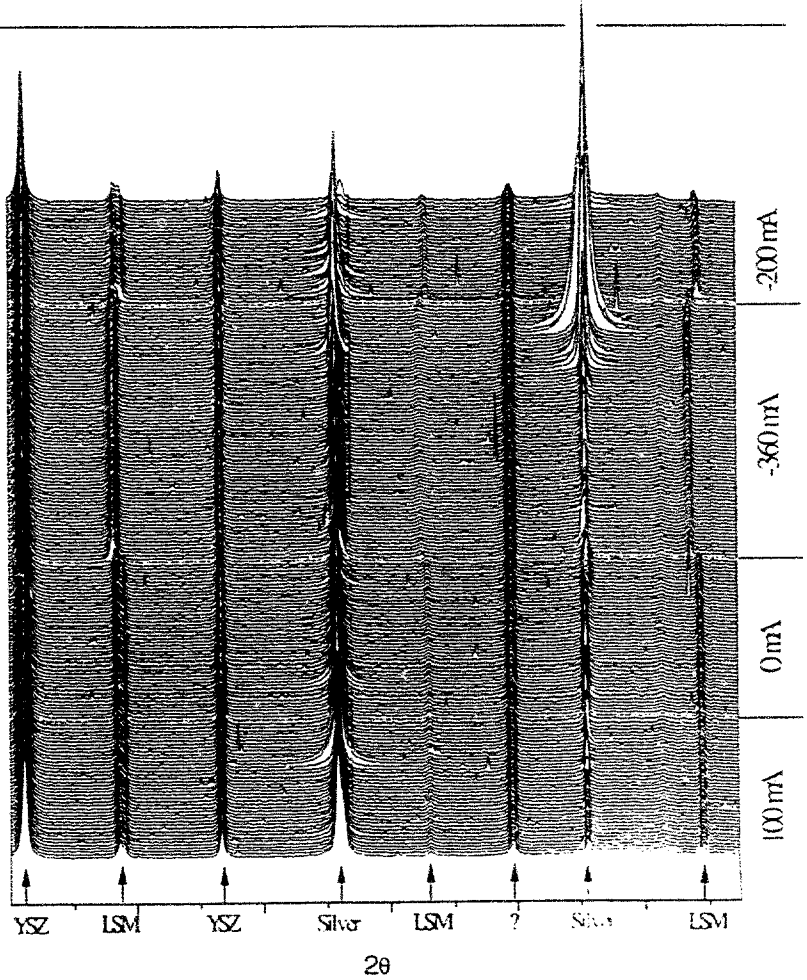

Figure 3. Diffractograms from a LSM/YSZ/Ag electrochemical cell under cathodic (-360mA/cm^2) and no polarisation. Cell at 850°C in air. Transmission experiment at BW5 with 0.124Å radiation. Snapshots were obtained at 1-2 minute intervals.

Acknowledgements

The authors want to thank the Danish Research Council for financial support to the synchrotron experiment. FWP is indebted to the DK-SOFC 97 project, financed by Energistyrelsen, for his participation in the IEA-SOFC Annexes. The present study is a result of a joint project between Risø National Laboratory and the Nordic Energy Research Program for fuel cells (NEFP). L. Sörby acknowledges a dr-scholarship from NEFP. Finally prof. Josh Thomas, Uppsala University, is thanked for valuable guidance.

BEHAVIOUR OF OXIDE CATHODES
OXYGEN SURFACE EXCHANGE KINETICS AS A SELECTION CRITERIA

B.C.H.Steele, Imperial College, London SW7, UK
e-mail < b.steele@ic.ac.uk>

It will be argued that the following reaction almost always controls the rate of the cathodic reduction of oxygen on oxide cathodes, and oxygen surface exchange data can therefore be used to select and optimise oxide cathode materials:

$$\tfrac{1}{2}O_2 + V_o^{\cdot\cdot} + 2e^- \Rightarrow O_o^x \ (\mathbf{O^-}, \mathbf{O^{2-}}, O_2^-)$$

surface, bulk

It is important to realise that the above reaction is **NOT** a charge transfer reaction as it involves the neutral combination of charged species. At equilibrium it is possible to measure this neutral flux density via the surface exchange coefficient, k $cm.s^{-1}$. Steele et al (1) first used values of k to interpret the cathode kinetics on Bi_2O_3-Er_2O_3 electrolytes more than 10 years ago. In the intervening period further papers (2,3,4) have provided semi-quantitative interpretations of a variety of oxide cathode/electrolyte structures, and more recently a detailed quantitative analysis of this approach has been published (5).

The pathways available for the cathodic reduction of oxygen are depicted in the following diagram

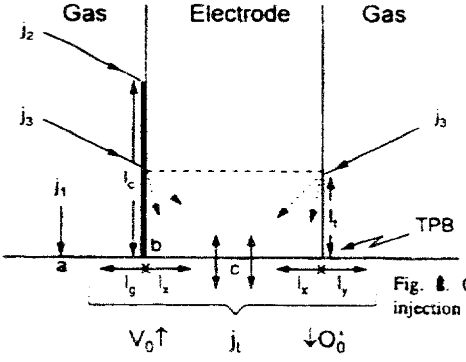

Fig. 1. Cathodic reaction pathways for oxygen reduction and injection into ceramic electrolytes.

Reaction pathway (j_1) is not important except at very high temperatures, when significant electronic charge carriers become available at the electrolyte surface. This pathway is not considered further in the present discussion.

Reaction pathway (j_2) involves the dissociative-adsorption of oxygen molecules and surface diffusion of the oxygen ion surface species towards the triple-phase-boundary (tpb) designated b in Fig 1.

Reaction pathway (j3) involves the the surface exchange reaction followed by dissolution and diffusion of oxygen ions within the oxide towards the cathode/electrolyte interface It should be noted that the changeover from surface to bulk control is given by, $L_c = D/k$ (3). As the value of L_c is typically between 1-100 microns for mixed conducting oxides, and the grain size in porous oxide cathodes is ~ 1 micron, then the surface exchange reaction is invariably rate-controlling.

DISTRIBUTION OF OVERPOTENTIAL

The contribution of the electronic charge-transfer reaction at the current collector/oxide cathode interface to the overpotential will usually be quite small. Whilst the ionic charge transfer at the electrode/electrolyte interface will often provide a significant fraction of the overpotential, it is the chemical changes associated with the nonstoichiometric oxide cathode that often make the major contribution to the total cathodic overpotential. These chemical changes are associated with the difference between the electrochemical potential of the electrons (δμe) and oxygen ion vacancies (δμv) as indicated on the acompanying diagram.

CHARGE TRANSFER LOSSES

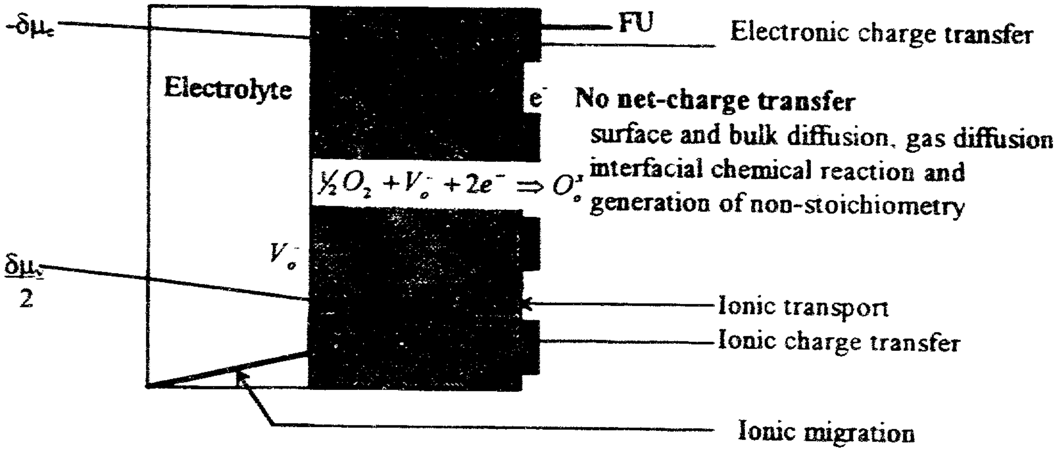

CHEMICAL LOSSES

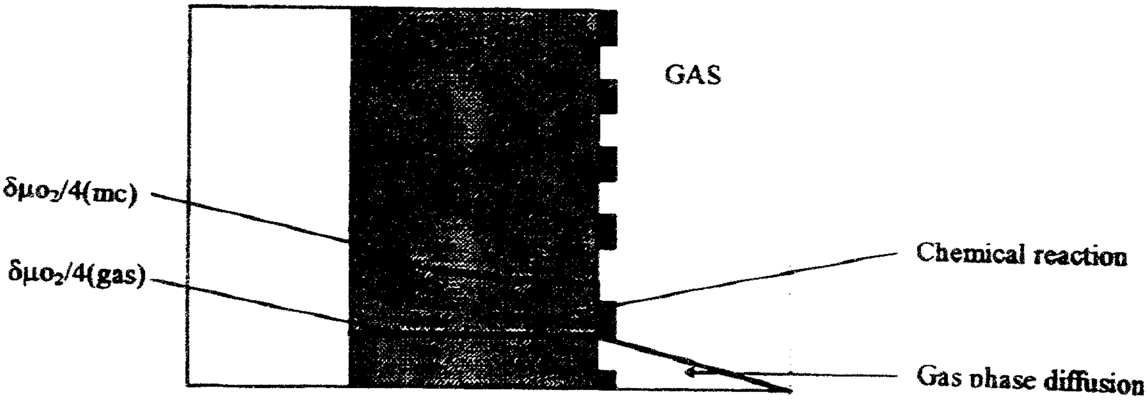

$\frac{1}{2}O_2 + V_o^{\cdot\cdot} + 2e^- \Rightarrow O_o^x$
ie: $\Delta\mu_s = 1/2\mu_{O_2} + \mu_v + 2\mu_e$
$\therefore \delta\mu_{O_2}/4 = -\delta\mu_e - \delta\mu_v/2$

$\Delta G = RT\ln P_{O_2} = -4\eta F$
ie: $\eta = RT/4F.\ln(P_{O_2})^{-1}$
Also $j \ \alpha \ [V_o^{\cdot\cdot}] \ \alpha \ (P_{O_2})^{-1/2}$
$\therefore \eta \ \alpha \ RT/2F.\ln j$

It follows that an apparent Tafel Law behaviour is not necessarily associated with a charge transfer process

INFLUENCE OF OXYGEN SURFACE EXCHANGE KINETICS (k $cm.s^{-1}$)

Low field approximation of Butler-Volmer equation

$j = j_o zF\eta/RT$ ......[A] $\qquad$ $R_e = \eta/j = RT/zF.j_o$ ....[B]

Surface exchange coefficient (k$cm.s^{-1}$) ⇒ neutral flux density for following reaction at equilibrium:

$$\tfrac{1}{2}O_2 + V_o^{\cdot\cdot} + 2e^- \Rightarrow O_o^x$$
$$J = k/V_m \ mol.cm^{-2}.s^{-1}$$

This can be represented as a surface exchange current density: $j_s = zFk/V_m$ Acm^{-2}

By analogy[+] with [B], $R_s = RT/zFj_s$, ie: $R_s = RTV_m/(zF)^2k$
eg: $k = 10^{-7} cm.s^{-1}$, $T = 1273K$, $R_s = 9.38\Omega cm^2$

NOTE

At a disordered surface, k expected to be a weak function of $[V_o^{\cdot\cdot}]$ and Po_2
(In contrast, D* is obviously a strong function of $[V_o^{\cdot\cdot}]$ and Po_2)

Therefore probably appropriate to consider k as a constant over small changes in Po_2, eg: $\Delta Po_2 = 10^2 \sim 100mV$ (1000K)
Approach thus relevant for SOFC operation around 0.7V, where cathodic over-potentials should not exceed 100-150mV

[+] Care should be exercised in taking analogy wth expression [B] too far, see: Adler et al., J. Electrochem. Soc. 143, 3554,1996

MICROSTRUCTURAL PARAMETERS

cubic grains of size w.

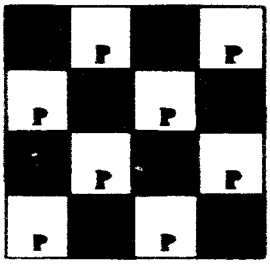

(cubic grain = hatched areas, P = pore), number of grains per cm^2 is $1/2 \cdot 1/w^2$, length of TPB per grain $= 4w$. Total TPB length in 1 $cm^2 = (1/2 \cdot 1/w^2) \cdot 4w = 2/w$ $cm \cdot cm^{-2}$. Assume an area of 1 cm^2 and current density (j_c) of 0.7 $A \cdot cm^{-2}$.

w μm	TPB $cm \cdot cm^{-2}$	TPB current $mA \cdot cm^{-1}$
1	2×10^4	0.035
5	4×10^3	0.175
10	2×10^3	0.35

Clearly in the previous example, when $k = 10^{-7}$ $cm.s^{-1}$, the derived surface resistance is relatively high, $9.38 \Omega cm^2$. It is necessary therefore to have an extended area over which the rate controlling surface exchange reaction can take place so that higher oxygen fluxes can be provided at the electrode/electrolyte interface. Assuming that surface diffusion is not rate-controlling, then on a single grain surface this area will be bounded by the length of the tpb and a collection height, lc.

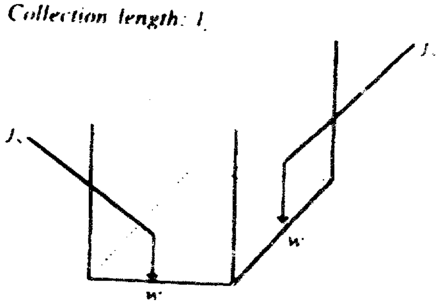

$$\mathbf{R_c = R_s \text{ x } w/2 \text{ x } 1/l_c}$$

Changeover from surface to bulk diffusion control

$L_c = D/k$ cm (10^{-4}- 10^{-2}cm, ie: 1-100 micron)

$$\mathbf{R_d = L_d V_m RT/D^*(zF)^2}$$

Extension of TBP zone (δ_c)

$\delta_c = \sqrt{(1-\phi)L_c / \tau.s}$, where ϕ is the fractional porosity, τ is the tortuosity, and s cm^{-1} represents the internal surface area/unit volume

OCCAM,S razor

'Concepts should not be more complicated than necessary'

William Ockham (1300-1349)

B.C.H.Steele ,Solid State Ionics, <u>86/88</u>, 1223, 1996

LSM/YSZ

$$R_e = R_s \text{ x } w/2 \text{ x} 1/l_c$$

$$= RTV_m/(zF)^2k \text{ x } w/2 \text{ x } 1/l_c$$

At 1000C(1273K)

$k = 10^{-7}$cm.s^{-1}, $R_s = 9.38\Omega cm^2$

Microstructural examination, w(grain size) ~ 1 micron
Also know that optimal thickness of cathode is ~ 25-30 micron
Allowing for tortuosity factor of 3-4, then l_c ~ 100 micron
ie: $R_e = 9.38 \text{ x } 1/2 \text{ x } 1/100 = 0.47\Omega cm^2$

Temperature dependence

$$k = 5.5x10^{-2} \exp(-1.44eV/kT)cm.s^{-1}$$

1. G.E.Youngblood, C.F.Windisch, and J.L.Bates
   p.479 in Proc. 14th RISO Intl. Symp. on Materials Science
   (RISO National Lab., Roskilde, Denmark,1993)
2. C.C.Chen, M.M.Nasrallah, H.U.Anderson
   p.598 in Proc. 3rd Intl. Symp. on SOFC, Proc. Vol. 93-4
   (Electrochem. Soc., New Jersey, USA, 1993)

Data published in the above papers does indicate activation energies around 1.4eV, and it may be significant that the fabrication routes used in these publications involve relatively low temperatures thus minimising the chance of any reaction between the electrolyte and cathode. However many other papers report higher activation energies (1.6-2.0eV).

HIGHER ΔE VALUES (1.6-2.0eV) REPORTED IN LITERATURE

- **PRESENCE OF SiO_2 AT TPB**
- **REACTION AT TPB (HREM examination necesary)**
- **k VALUES FOR PELLETS NOT SAME AS FOR PARTICLES?**

ELECTRODE KINETICS AT INTERMEDIATE TEMPERATURES

LSM/YSZ, $La_{0.8}Sr_{0.2}MnO_{3+x}$

$$k = 5.5 \times 10^{-2}\exp(-1.44/kT)\ cm.s^{-1}$$

$$R_s = RTV_m/(zF)^2k \quad \Omega cm^2$$

$$R_e = R_s \times w/2 \times 1/l_c \quad \Omega cm^2$$

T(C)	T(K)	k $cm.s^{-1}$	R_s Ωcm^2	w micron	l_c micron	R_e Ωcm^2
1000	1273	1.1 E-7	85.28	1	100	0.43
900	1173	3.6 E-8	240.5	1	100	1.20
800	1073	9.5 E-9	829.6	1	100	4.15
700	973	2.6 E-9	3737	1	100	18.63

Strategies to reduce R_e at intermediate temperatures

- noble metal catalysts to enhance k
- composite (electrolyte/electrode mixtures) electrodes to increase effective interfacial area
  Area increases limited to around 3x ?
- dense mixed conducting thick film interfacial layers as diffusion barriers with porous layer of alternative superior electrocatalyst

The last strategy could be appropriate for 700C as otherwise it is difficult to understand how LSM can provide sufficient oxygen flux to sustain the high power densities ($0.5Wcm^{-2}$) reported by Minh (Allied Signal) at this temperature.

MIXED CONDUCTING OXIDES AS DIFFUSION BARRIERS

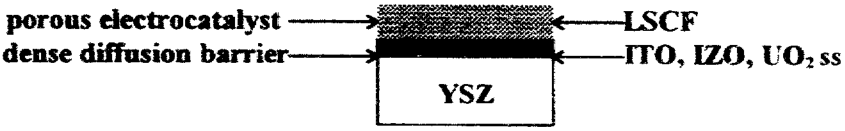

$$R_d = L_d V_m RT/D^*(zF)^2$$

T(K)	D^*cm^{-2}	L_d micron	$R_d\ \Omega cm^{-2}$
1073	10^{-8}	1	0.07
973	10^{-9}	1	0.72

Provided $D^* > 10^{-8}cm^{-2}$ then R_d has a low value and may be neglected

ITO, IZO, and UO$_2$ ss satisfy this requirement at 800C and are compatible with YSZ, but the resistance values are marginal at 700C

A similar approach has been suggested by:

P. van Den Berghe and H. Tannenberger
US Patent No. 4,130,693 (19.12.78)

Role of SiO2

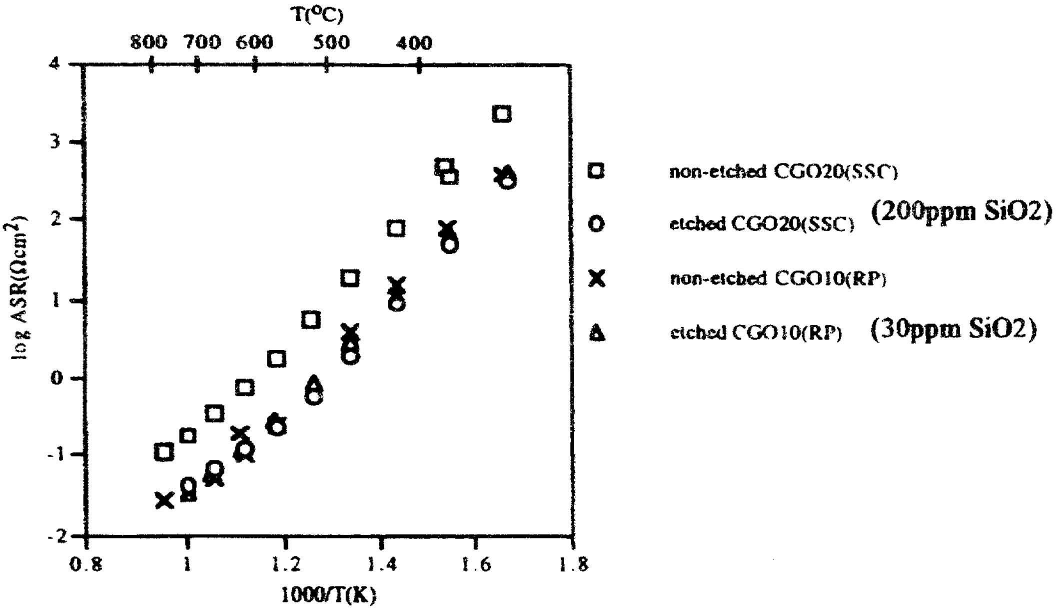

Figure 6. Electrode resistivity of LSCF double layer on etched and non-etched CGO electrolyte.

$La_{0.6}Sr_{0.4}Co_{0.2}Fe_{0.8}O_{3-x}$ (LSCF)

$k = 9.3 \exp(-1.1eV/kT)\ cm.s^{-1}$
$D = 3.8 \exp(-1.8eV/kT)\ cm^{-2}s^{-1}$

SEE REFERENCE 6

700C

$k = 1.9x10^{-5}\ cm.s^{-1}$
$R_e = R_s \times w/2 \times 1/l_c$
$= 0.38 \times 1/2 \times 1/1$
$= 0.19\Omega cm^2$

w = 1 micron
l_c = 1 micron

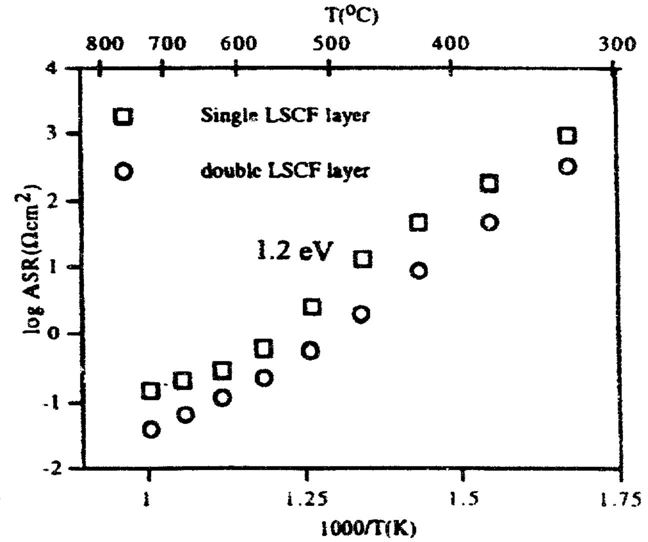

973K (1/T = 1.03 E-3)
log R = -0.8
R = 0.16 ohm.cm2

Figure 7. Electrode resistivity of single(thick) and double layer LSCF on etched CGO20(SSC).

CONCLUSIONS

The kinetics of oxygen surface exchange (k $cm.s^{-1}$) can provide an appropriate interpretation for the cathodic reduction of oxygen on oxide electrocatalysts, at least, for small overpotentials. It is necessary to consider this alternative approach (paradigm) as a replacement for classical electrochemical concepts in order to make progress in the optimisation of fuel cell cathodes.

ACKNOWLEDGEMENTS

Colleagues in Group for Ceramic Ion Conducting Membranes, Imperial College, particularly the SIMS section directed by Prof. J.Kilner.

References

1. B.C.H. Steele et al. Solid State Ionics, 18/19, 1038, 1986
2. B.C.H.Steele, Mater.Sci. and Engin. B13,79,1992
3. B.C.H.Steele, Solid State Ionics, 75,157,1995
4. B.C.H.Steele, Solid State Ionics, 86/88,1223,1996
5. S.Adler et al., J.Electrochem.Soc.,143, 3554,1996
6. J-M. Bae and B.C.H.Steele, submitted to Solid State Ionics

$La_{0.75}Sr_{0.2}Mn_{0.9}Co_{0.1}O_3$ AS A POTENTIAL CATHODE MATERIAL FOR SOFC

G. Stochniol, A. Gupta, A. Naoumidis and D. Stöver
Institut für Werkstoffe der Energietechnik (IWE)
Forschungszentrum Jülich GmbH,
D-52425 Jülich, Germany

INTRODUCTION

The high SOFC operating temperature of about 1223K can cause degradation during a long term service life because of chemical interactions between cell components. $LaMnO_3$-based cathodes are known to be chemically compatible with the electrolyte 8 mol% Y_2O_3 stabilised ZrO_2 (YSZ) when La is partially replaced by Sr or Ca (1-8), especially when substoichiometric perovskites are used. $La_{0.65}Sr_{0.3}MnO_3$ (LSM) is presently used for the cathode of the SOFC substrate supported system of Forschungszentrum Jülich because of does not form low conducting zirconates at the interface between cathode and the electrolyte YSZ (6) and exhibits excellent electrochemical performance (9,10).

The main interest in the SOFC investigation is the reduction of the operating temperature to 1073K or even below. At this temperature chemical interactions are less problematic but the electrochemical performance of the cathode decreases. Co-containing perovskites $La_{1-x}Sr_xMn_{1-u}Co_uO_3$ (LSMC) exhibit a high oxygen reduction ability but these compositions are also known to form zirconates at high Co contents. The present investigation introduces $La_{0.75}Sr_{0.2}Mn_{0.9}Co_{0.1}O_3$ as a potential candidate for reduced temperature SOFC application having good chemical compatibility with the electrolyte material YSZ.

EXPERIMENTAL

Nitrate salts (Merck, p.a) in appropriate mixtures were dissolved in water and the perovskite powder was then produced using the spray-drying technique. The partially decomposed and dried powder was calcined at 900°C in flowing air. X-ray analysis (Siemens D500) was used for phase analysis of the produced perovskite powder. Chemical compatibility was studied by XRD on powder mixtures of perovskite and YSZ in a molar ratio of 1:1. Interfacial reactions were studied with SEM (CamScan) equipped with EDX (Noran) on cross-sections of perovskite-YSZ double-layered pellets. The electrical conductivity was measured in 4-point d.c. technique on bar-shaped bodies fired at 1573K for 5 h. Ag wires and Ag paste was used for contacting. Electrochemical performance was tested in the potentiostatic mode using a Bank LB81M device on screen printed perovskite layers on YSZ tape cast substrates. The correction of the current-potential curves due to ohmic losses in the electrolyte was performed by subtracting the ohmic resistance obtained from impedance spectra determined with a Schlumberger Solartron 1255. Contacting was carried out with Pt paste and Pt wires.

RESULTS AND DISCUSSION

The X-ray analysis of the long term annealing experiment at 1223K for 2300 h confirmed the chemical stability according to the formation of zirconates. In addition to the reflections of reactants, additional reflections of monoclinc ZrO_2 (m-ZrO_2) were observed in the diffraction pattern, indicating an instability of YSZ in contact with $La_{0.75}Sr_{0.2}Mn_{0.9}Co_{0.1}O_3$.

After a reaction time of 200 h at 1473K no reaction product could be detected by XRD in the powder mixture experiments. The result in Fig. 1 is correlated with previous experiments (11) and the thermodynamic calculation of Yokokawa et al. (12) for substoichiometric Sr-free perovskites $La_{y-x}MnO_3$.

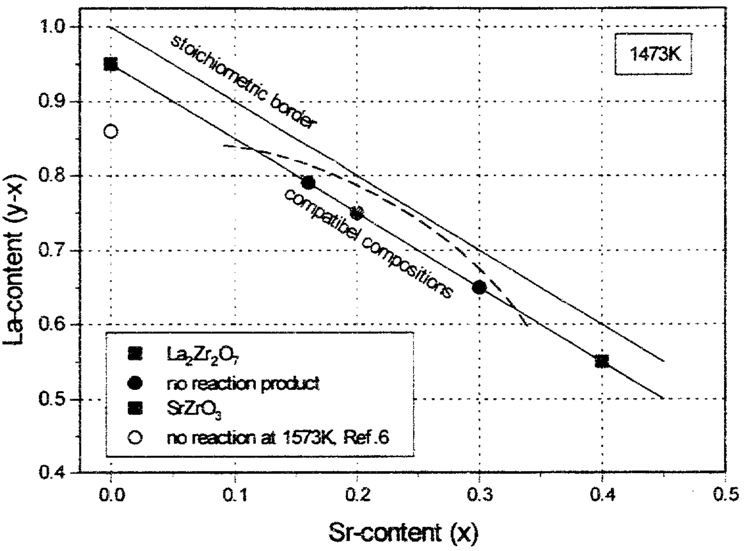

Fig. 1: Results of chemical compatibility tests between various substoichiometric LSMC perovskites. o: $La_{0.86}MnO_3$ which will not form $La_2Zr_2O_7$ with YSZ at 1573K after Yokokawa et al. (12)

The perovskite $La_{0.75}Sr_{0.2}Mn_{0.9}Co_{0.1}O_3$ can be seen in the middle of a regime of compatible compositions that do not form any zirconates. Therefore it can be regarded as a highly inert perovskits although containing 10% Co on Mn lattice sites. In comparison to earlier results for YSZ/perovskite powder mixture experiments with Co-free substoichiometric perovskites $La_{y-x}Sr_xMnO_3$ (7) the centre of the inert regime was shifted from a Sr content of 30% on Mn-lattice sites to a lower Sr content of about 20% in connection with Co. The increased tendency to form $SrZrO_3$ with increasing the Sr content for Co-containing LSMC can be thermodynamically explained by the instability of unusual and high oxidation states of d-group elements. In LSMC perovskites Co^{4+} will be formed for electroneutrality reasons. In combination with high Sr contents the $SrZrO_3$ formation can be described according to:

$$SrMO_3 + ZrO_2 \leftrightarrow SrZrO_3 + MO_2 \quad (1)$$

$$2MO_2 \leftrightarrow M_2O_3 + 1/2O_2 \quad (2)$$

$$M_2O_3 \leftrightarrow 2MO + 1/2O_2 \quad (3)$$

with M = Mn or Co. The remaining oxides will dissolve in ZrO_2.

No reaction products for the powder mixture YSZ/$La_{0.75}Sr_{0.2}Mn_{0.9}Co_{0.1}O_3$ were detected after an exposure at 1673K for 20 h. Small amounts of $La_2Zr_2O_7$ were detected by XRD after 95 h annealing time, whereas $La_{0.65}Sr_{0.3}MnO_3$ is known not to form zirconates (6). The higher reactivity of Co-containing LSMC perovskites with YSZ for the formation of $La_2Zr_2O_7$ can be explained in the same way as discussed by Yokokawa et al. (13) for the different $La_2Zr_2O_7$ formation behaviour of $LaMnO_3$ and $LaCoO_3$.

The interface of a YSZ/$La_{0.75}Sr_{0.2}Mn_{0.9}Co_{0.1}O_3$ double layered pellet was investigated by SEM/EDX on a cross-section. Frame scans of 5×20 μm^2 were used to analyse the chemical composition of YSZ and the perovskite at an average distance 5 µm parallel to the interface area in comparison to the bulk material 20 µm away from the reaction zone. Y could not be detected in the perovskite material because of the overlapping EDX signals for Sr and Y. On the other hand, small amounts Zr were found in the perovskite close to the interface. Additional point measurements were carried out on YSZ about 2 µm from the interface in YSZ, which confirmed the diffusion of the perovskite elements La and Mn.

The single point analysis resulted in a changed ratio of Zr/Y in YSZ, confirming a diffusion of Zr into the perovskite, as was detected. The relative enrichment of Y in YSZ at the interface even stabilises the cubic modification of YSZ. The results of SEM/EDX analyses on the YSZ/LSMC cross-section indicate a change in the phase stability of cubic YSZ which occurs when further elements are added to the system Y_2O_3-ZrO_2.

The linear thermal expansion coefficient α was determined to be 11.5×10^{-6} K^{-1} at 1273 K, a value that matches the value of 10.7×10^{-6} K^{-1} for the electrolyte material.

The result of the electrical conductivity measurement of $La_{0.75}Sr_{0.2}Mn_{0.9}Co_{0.1}O_3$ in comparison with $La_{0.65}Sr_{0.3}MnO_3$ can be seen in Fig. 5. 100 S×cm^{-1} was reached in a p-type characteristic by the Co-containing material at 1213K in air, about half the value of the standard perovskite composition used in Forschungszentrum Jülich but sufficient for the in plane conductance of the porous perovskite/YSZ composite cathode layer.

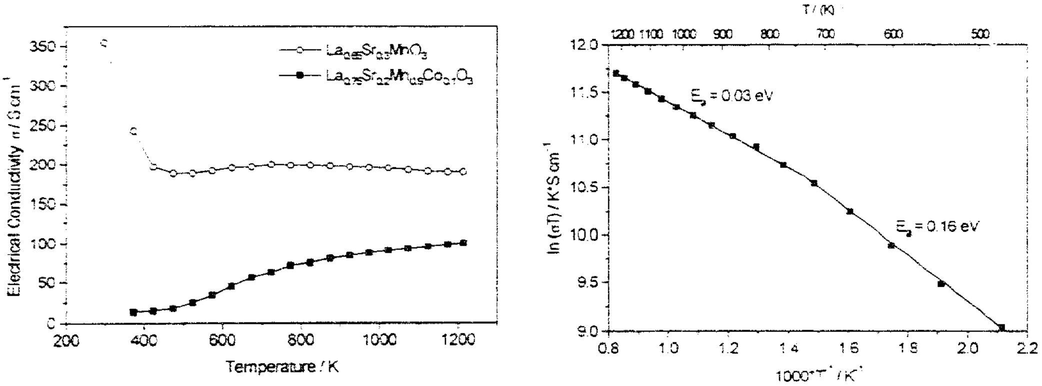

Fig. 5: Electrical Conductivity of $La_{0.75}Sr_{0.2}Mn_{0.9}Co_{0.1}O_3$ in comparison to $La_{0.65}Sr_{0.3}MnO_3$ (left) and Arrhenius plot (right) for LSMC

The Arrhenius plot showed a change in slope at about 700K that might be attributed to thermally induced spin transitions from low-spin to high-spin states for Co or Mn, known for such perovskite materials materials (14).

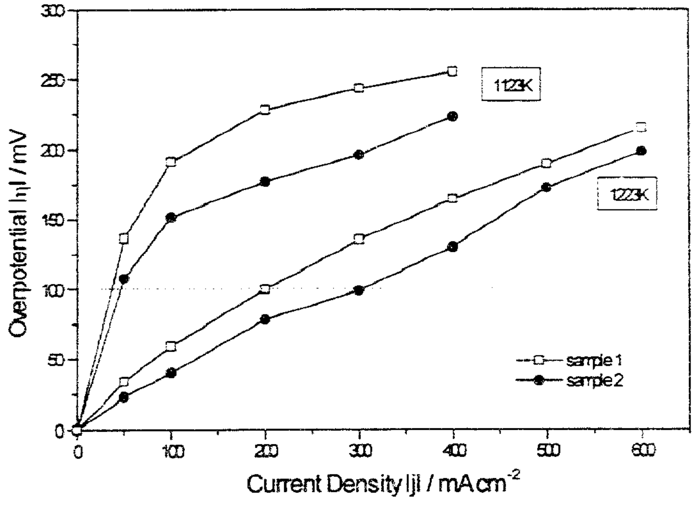

Fig. 6: Current-voltage measurement for $La_{0.75}Sr_{0.2}Mn_{0.9}Co_{0.1}O_3$ sintered on YSZ at 1273K

The result of electrochemical measurements for two perovskite layers annealed at 1273K can be seen in Fig. 6. The characterisation was investigated at 1123 and 1223K. The dotted line presents the limitation of 100 mV for acceptable cathode overpotentials. The variation in the I-U characteristic indicate that the microstructures of the cathode layers were not optimised. Thus Co-containing perovskite measured was not optimised for its microstructure and porosity the current density data are within the regime of pure standard perovskite $La_{0.65}Sr_{0.3}MnO_3$ used in Forschungszentrum Jülich.

CONCLUSION

$La_{0.75}Sr_{0.2}Mn_{0.9}Co_{0.1}O_3$ has shown a high chemical compatibility with the electrolyte material YSZ. An acceptable sufficient electrical conductivity, a thermal expansion coefficient matching the other electrolyte material and a good cathodic behaviour may bring an advantageous performance of a perovskite/YSZ cathode composite in reduced temperature SOFCapplication.

ACKNOWLEDGEMENT

The authors thank W. Jungen for the preparation of perovskite powders, P. Lersch for X-ray measurements and T. Kloidt for electrochemical measurements.

REFERENCES

(1) S.K. Lau, S.C. Singhal, in Fuel Cell Seminar Abstracts p. 107, Courtesey Associates, Washington D.C. 1985.

(2) H. Kaneko, H. Taimatsu, K. Wada, E.Iwamoto, The Electrochem. Soc., Proc. of the 2nd Int. Symp. on SOFC; Athens (1991) 673.

(3) E. Ivers-Tiffeé, B. Jobst, I. Kraus, R. Schachtner, M. Schiessl, The Electrochem. Soc., Proc. of the 2nd Int. Symp. on SOFC; Athens (1991) Addendum, 97.

(4) J.A.M. van Roosmalen, E.H.P. Cordfunke, Solid State Ionics, **52** (1992) 303.

(5) Y. Takeda, Y. Sakai, T. Ichikawa, N. Imanishi, O. Yamamoto, M. Mori, N. Mori, T. Abe, Solid State Ionics, **72** (1994) 257.

(6) G. Stochniol, E. Syskakis, A. Naoumidis, J. Am. Ceram. Soc., **78** [4] (1995) 929.

(7) D. Kuscer, J. Holc, M. Hrovat, S. Bernik, Z. Samarzija, D. Kolar, Solid State Ionics, **78** (1995) 79.

(8) G. Stochniol, H. Grübmeier, A. Naoumids, H. Nickel, The Electrochem. Soc., Proc. of the 4th Int. Symp. on SOFC (1995) p. 995.

(9) L.G.L de Haart, Th. Hauber, K. Mayer, U. Stimming, Proc. of the 2nd European SOFC Forum, p. 229, Oslo 1996.

(10) R. Wilkenhöhner, W. Malléner, H.P. Buchkremer, Th. Hauber, U. Stimming, Proc. of the 2nd European SOFC Forum, p. 279, Oslo 1996.

(11) G. Stochniol, E. Syskakis, K. Wippermann, W. Schaffrath, A. Naoumidis, H. Nickel, Proc. 6th IEA Workshop, Edts.: M. Brocco, G. Cosoli, H. Nabiele, M. Ronchetti, E. Scafè, Rome 1994, 211.

(12) H. Yokokawa , N. Sakai, T. Kawada, M. Dokiya, J. Electrochem. Soc., **138** [9] (1991) 2719.

(13) H. Yokokawa, N. Sakai, T. Kawada, M. Dokiya, Denki Kagaku, **57** [8] (1989) 821.

(14) M.A. Señarís-Rodríguez, J.B. Goodenough, J. Solid State Chem., **116** (1995) 224.

Transport Processes and Methane Reforming Reactions in the SOFC-Cermet Anodes

J. DIVISEK, D. FRONING, W. LEHNERT, J. MEUSINGER, U. STIMMING
Institute of Energy Process Engineering
Research Centre Jülich, D-52425 Jülich, Germany

Abstract

The values of the volume reaction constants of the steam reforming reaction, which takes place inside the SOFC cermet anode prior to the electrochemical anodic oxidation of the natural gas, were estimated for the first time. The experiments were performed by evaluating the gas concentration changes after variation of the anode thickness at constant temperature. The computer simulation of the reforming reaction was performed using the Finite Integration Technique. With a steam/methane ratio of 3:1, the depth of the reaction zone is 300 - 400 µm at 800° C for the standard composition of the SOFC anode cermet structure.

List of Symbols

A	surface of the control volume $[cm^2]$
D	diffusion coefficient $[cm^2\, s^{-1}]$
$\vec{E}$	velocity gradient $[cm\, s^{-1}]$
F	molar flow rate in x direction $[mol\, s^{-1}]$
$\boldsymbol{F}$	Faraday constant $[C\ g\text{-}eq^{-1}]$
G	Gibbs reaction enthalpy $[J\, mol^{-1}]$
i	current density $[A\, cm^{-2}]$
I	surface current density $[A\, cm^{-2}]$
k	reaction constant $[mol\, cm^{-3}\, bar^{-2}\, s^{-1}]$
K	equilibrium constant of the shift reaction
L_1	right x boundary
L_2	lower y boundary
n	type of component
$\vec{N}$	vector of molar flux density $[mol\, cm^{-2}\, s^{-1}]$
p	pressure $[bar]$
R	source or sink $[mol\, cm^{-3} s^{-1}]$
$\boldsymbol{R}$	gas constant $[J\, deg^{-1}\, mol^{-1}]$
S	stream potential function $[cm^2\, s^{-1}]$
t	time $[s]$
T	temperature $[K]$
V	volume $[cm^3]$
$\hat{x}$	molar fraction of the single component
x	length coordinate of the anode $[cm]$
y	thickness coordinate of the anode $[cm]$
z	width coordinate of the anode $[cm]$
X, Y, Z	scalar lattice points in the space directions x, y, z
X', Y', Z'	flux density lattice points in the space directions x, y, z

Greek symbols

κ	conductivity constant [mol cm^{-3}]

Subscripts

D	diffusion flux index
i	index number in the x direction
j	index number in the y direction
k	index number in the z direction
m	multicomponent diffusion index
n	type of component
p	index of the pressure equilibrium constant
r	reforming reaction
$r,+$	reforming reaction, forward direction
$r,-$	reforming reaction, backward direction
s	shift reaction
$s,+$	shift reaction, forward direction
$s,-$	shift reaction, backward direction
x	length coordinate of the anode
y	thickness coordinate of the anode

Superscripts

CO	CO reaction index
H	hydrogen reaction index
s	index of the pressure equilibrium constant of the shift reaction

1. Introduction

Solid oxide fuel cells (SOFC) operate at temperatures between 800 and 1000° C using hydrogen as the fuel and atmospheric oxygen as the oxidant. Since pure hydrogen is expensive for this purpose, hydrocarbons must be used instead. The most interesting hydrocarbon is natural gas consisting mainly of methane. It was shown, however, that the direct electrochemical oxidation of methane

$$CH_4 + 4O^{2-} = CO_2 + 2\,H_2O + 8\,e^- \qquad (1)$$

causes practical difficulties even at the high temperature level involved [1]. For this reason, a methane steam reforming reaction according to the overall reaction scheme

$$CH_4 + 2\,H_2O = 4\,H_2 + CO_2 \qquad (2)$$

is used as the source of hydrogen, which can be oxidized electrochemically according to the reaction

$$H_2 + O^{2-} = H_2O + 2e^- \qquad (3)$$

In order to achieve a high energetic efficiency of the fuel cell, internal reforming of the methane is necessary, which takes place directly within the anode. Due to the great difference between the reaction rates of the endothermic methane reforming reaction (2) and exothermic electrochemical hydrogen oxidation (3), cooling effects arise with resulting intolerable temperature gradients inside the anodic structure in this case. At the usual working temperature of SOFC, e.g. for 1000°C, the relative mutual reaction rate of both reactions (2) and (3) is about a factor of 80 [2]. Based on the constant c.d. of the fuel cell as a measure of the electrochemical reaction rate, it was shown that the mutual velocity ratio of reactions (2) and (3) is a function of temperature, being still 7.5 at 700°C [2]. It can therefore be supposed that both reactions will become comparable below a certain temperature level. There is only a small amount of kinetic reforming data available obtained from Ni cermet material [2,3,4]. Up to now, only surface phenomena have been investigated [2,3,5]. In order to control the course of reforming, detailed knowledge of the space reaction rates is necessary, which are still unknown at present. This study deals with this problem.

2. Experimental details

The purpose of the experiments was to determine the values, temperature dependences and activation energies of the velocity constants of the chemical reaction (2) as a volume reaction. The experiments were therefore performed isothermally at various temperatures, with the heat exchange being treated so intensively that the endothermic properties of the reforming reaction (2) were practically eliminated. It was possible to keep the reaction temperature constant up to 1000 °C. Reaction constants in the range of practical interest between 800 - 900 °C were to be calculated so that the measurements were performed in this temperature range.

Both the experimental details and a full description of the experiments are given in [5]. The setup of the apparatus for steam reforming experiments was analogous to that described in Ref. [2]. It consists of a gas supply section, an electric furnace and a gas analysis system. The anode material consists of Ni/YSZ cermet formed originally from a sintered heterogeneous mixture of NiO and $ZrO_2(8\%Y_2O_3)$ powder particles. Methane steam reforming takes place on the nickel particles, which act as a catalyst. For this reason, the NiO-containing cermet anodes were prepared as described in Ref. [6] and the NiO was gradually reduced in situ to metallic Ni in a gas stream consisting of 5 % H_2 and 95 % N_2 at 600° C. The resulting anode samples with a thickness of between 0.36 and 1.90 mm were placed in a tube of stainless steel (Incoloy 800) with an inside diameter of 12 mm and a length of approximately 1 m. The investigated anodes with a uniform length of 10 mm were fixed vertically in the slit of a metallic strip at a distance of 30 cm from the tube inlet. Hydrogen and nitrogen feed gases from bottles were used for heating up and reducing the primarily formed NiO to metallic Ni in the cermet structure. Pure CH_4 was used for the reforming reaction. The necessary steam was produced by an electric heater. All the gases were mixed together immediately before entering the test tube. It was assumed that after an entrance length of about 30 cm a complete gas mixture can be achieved which contacts the anode surface. The anode was exposed to the reaction mixture from both sides. The temperature decrease along the cermet anode caused by the endothermic reforming reaction was detected by means of three thermocouples located inside the sample carrier or in the gas stream beside the anode, whereby the temperature in the centre of the anode was taken for temperature evaluation. This value was considered to be the reforming temperature. The product gases were cooled down to room temperature to remove the water by condensation and for separation of the steam. The resulting dry gas mixture was continuously analysed for CH_4, CO, CO_2 and H_2.

In order to obtain the data necessary for evaluating the space reaction rate of the reforming reaction, the methane conversion rates were estimated as a function of the anode thickness by measuring the concentrations of the species in the outlet gas stream and compared with the theoretical ones. To perform the calculations, the original comparative composition of the outlet gases prior to the water condensation was estimated as will be shown in the discussion section.

Details concerning the conditions of the experiment and the anode geometry are given in Tab. 1.

It can be seen from the values given in Tab. 1 that a change in the methane conversion rate takes place up to the double sided anode thickness of 0.66 mm. In the thickness range from 0.66 to 1.9 mm no significant difference in methane conversion was observed.

3. Theoretical analysis of the reforming reaction

The methane steam reforming reaction (2) is actually a two-stage process taking place according to the scheme

$$\begin{aligned} CH_4 + H_2O &\underset{k_{r-}}{\overset{k_{r+}}{\Leftrightarrow}} 3H_2 + CO \\ CO + H_2O &\underset{k_{s-}}{\overset{k_{s+}}{\Leftrightarrow}} CO_2 + H_2 \end{aligned} \tag{4}$$

The first reaction is the reforming reaction characterized by the reforming constants k_{r+} and k_{r-}, and the subsequent reaction is the shift reaction characterized by the constants k_{s+} and k_{s-}. Both reactions produce the actual electrochemically active gases, H_2 and CO, which cause the oxidation products H_2O and CO_2 to be formed in the anodic reactions

$$\begin{aligned} H_2 + O^{2-} &\rightarrow H_2O + 2e^- \\ CO + O^{2-} &\rightarrow CO_2 + 2e^- \end{aligned} \tag{5}$$

The first reaction (5) is identical with reaction (3). Both reactions (4) and (5) can only take place inside the anode structure of the fuel cell. This anode consists of a Ni/ZrO_2 cermet, which has catalytic properties for both the chemical reactions (4) and the subsequent electrochemical reactions (5). The total reaction scheme is shown in Fig. 1.

The flow scheme of the reforming reaction in the SOFC anode can be described as follows: the reforming gas flows through the gas channel from left to right in the direction of the x-coordinate (Fig.2). The coordinate $x = 0$ is assigned to the gas inlet point. The gas outlet is at the coordinate $x = L_1$ with a gas composition which can be determined by gas analysis [5]. The bottom boundary of the gas channel is given the coordinate $y = 0$. In order to describe the volume processes in an uncomplicated manner, it is assumed here for the sake of simplicity that the z-direction has homogeneous properties. This assumption does not restrict the basic considerations of the method. The reactions involved (4) and (5) proceed in the anode cermet which is then defined in the x-y region between $[0 \leq x \leq L_1; 0 \leq y \leq L_2]$. In the gas channel, a laminar flow takes place along the coordinate $y = 0$ in the x-direction. Due to diffusion and convection, the introduced gases CH_4 and H_2O migrate in the y-direction where they are consumed by reactions (4) and (5). Assuming that $F_{n,x}$ is the molar flow rate of the component n in [mol s^{-1}] in the x-direction, $\vec{N}_{n,y}$ the convective molar flux density of the component n in [mol cm^{-2} s^{-1}] in the y-direction and p_n is the corresponding partial pressure, the relation

$$\frac{1}{z}\frac{\partial F_{n,x}}{\partial x} = \frac{D_{n,m}}{RT}\frac{\partial p_n(x,0)}{\partial y} + \vec{N}_{n,y} \tag{6}$$

is valid for the change in $F_{n,x}$, which implies that the change of the flow along the channel bottom equals the sum of the diffusive and convective flows in the y-direction. $D_{n,m}$ is the effective multicomponent diffusion coefficient, which is defined in Ref. [7] and can be calculated using the software according to Ref. [8].

For first value assignment, the integral values are important which are determined by the relation

$$\frac{1}{z}\int_0^{L1}\frac{\partial F_{n,x}}{\partial x}\,dx = \iint_A R_n\,dA \tag{7}$$

where R_n represents all the chemical and electrochemical sources and sinks in the cermet region. Assuming that $\hat{x}_n$ is the molar fraction of the component n of the gas mixture, defined as $\hat{x}_n = p_n / \sum_k p_k$, the Stefan-Maxwell equation applies to the vector of the molar flow $\vec{N}_n$ in the form of

$$\begin{aligned} \vec{N}_n &= -\frac{p_{tot}}{RT} D_{n,m}\,\nabla\hat{x}_n + \hat{x}_n \sum_k \vec{N}_k \\ div\ \vec{N}_n &= \sum R_{Ch,Ec} \end{aligned} \tag{8}$$

Here the multicomponent diffusion coefficient $D_{n,m}$ is used instead of the binary diffusion coefficients [7]. The total pressure of the system is p_{tot}, $R_{Ch,Ec}$ are the corresponding chemical and electrochemical sinks. When using the Stefan Maxwell equations in the form (8), it must be noted that the vector of the molar flow $\vec{N}_n$ is composed of a diffusion and a convection term, which gives too complicated a system of equations. For this reason, the fact is used that the gas mixture in the cermet moves without eddy formation, so that a vector field with the velocity gradient $\vec{E}$ is formed there, for which the equations

$$curl\ \vec{E} = 0; \qquad \vec{E} = -grad\ S \tag{9}$$

are valid. A scalar function S (stream potential) then exists in this region, which has the properties of a potential function [9]. According to the definition $\vec{N} \equiv \kappa\ \vec{E}$, where κ is a fictitious relative conductivity constant that drops out of the calculations, the potential function S can then be used for calculating the total molar flow $\vec{N}$ independently of eq. (8). Then the vector $\vec{N} = \sum_k \vec{N}_k$ no longer has diffusive terms, so that the calculations are simpler. For its determination according to (7) all the chemical and electrochemical sinks and sources present in the system must be defined. The chemical sinks R_r and R_s [mol cm^{-3} s^{-1}] are postulated as the reactions

$$\begin{aligned} R_r &= -\frac{1}{RT}\frac{d\,p_{CH4}}{d\,t} = k_{r,+}\,p_{CH4}\,p_{H2O} - k_{r,-}\,p_{CO}\,p_{H2}^3 \\ R_s &= -\frac{1}{RT}\frac{d\,p_{CO}}{d\,t} = k_{s,+}\,p_{CO}\,p_{H2O} - k_{s,-}\,p_{CO2}\,p_{H2} \end{aligned} \tag{10}$$

Since only the chemical sinks (4) are associated with a volume change and not the electrochemical ones (5), the following is generally true for each volume element

$$div\,\vec{N} = div\,(-\kappa\ grad\ S) = 2\,R_r \tag{11}$$

with the boundary conditions

$$\begin{aligned} &y \le 0: \quad S = 0\ ; && x = 0: \quad \frac{\partial S}{\partial x} = 0 \\ &x = L_1: \quad \frac{\partial S}{\partial x} = 0\ ; && y = L_2: \quad \frac{\partial S}{\partial y} = 0 \end{aligned} \tag{12}$$

Whereas only the chemical sinks are relevant for the calculation of the total molar flow $\vec{N}$, this can be different for the partial flows $\vec{N}_n$. In this case, the electrochemical reactions (5), which can take place in the entire volume of the anode, must also be taken into consideration. Assuming that i_1 is the electronic current through the metal phase of the cermet and i_2 the corresponding ionic current flowing through the ion-conducting ZrO_2 phase, the divergence condition generally applies between the two currents

$$\nabla \bullet i_1 + \nabla \bullet i_2 = 0 \tag{13}$$

The electronically and ionically conducting phases in the respective potentials Φ_e and Φ_i are governed in each elementary volume ΔV by the Butler-Volmer equation which, however, is not dealt with in this study. Moreover, for the H_2 and CO oxidation currents, the following is valid:

$$\nabla \bullet i_2 = \nabla \bullet i_2^H + \nabla \bullet i_2^{CO} \tag{14}$$

The currents i_2^H and i_2^{CO} can be separately determined. With the expression $div\left[-\frac{D_{n,m}}{R\,T}\nabla p_n - \hat{x}_n \kappa \; \nabla S \right] \equiv div\,\vec{N}_n$ the balance equations for the individual gases read as follows:

$$\begin{aligned}
CH_4: &\quad div\,\vec{N}_{CH4} = -R_r \\
CO: &\quad div\,\vec{N}_{CO} = R_r - R_s - \frac{\nabla \bullet i_2^{CO}}{2F} \\
H_2: &\quad div\,\vec{N}_{H2} = 3R_r + R_s - \frac{\nabla \bullet i_2^{H}}{2F} \\
H_2O: &\quad div\,\vec{N}_{H2O} = -R_r - R_s + \frac{\nabla \bullet i_2^{H}}{2F} \\
CO_2: &\quad div\,\vec{N}_{CO2} = R_s + \frac{\nabla \bullet i_2^{CO}}{2F}
\end{aligned} \tag{15}$$

The set of equations (15) still has to be completed by defining the boundary conditions. The following boundary conditions apply to the individual partial pressures p_i:

$$\begin{aligned}
CH_4: &\quad y=0:\; p_n = p_{n,Channel}(x); &&\quad y = L_2:\; \frac{\partial p_n}{\partial y} = 0; \\
&\quad x=0:\; \frac{\partial p_n}{\partial x} = 0; &&\quad x = L_1:\; \frac{\partial p_n}{\partial x} = 0 \\
CO: &\quad y=0:\; p_n = p_{n,Channel}(x); &&\quad y = L_2:\; -D_{n,m}\frac{\partial p_n}{\partial y} = \frac{I_{CO}}{2F}; \\
&\quad x=0:\; \frac{\partial p_n}{\partial x} = 0; &&\quad x = L_1:\; \frac{\partial p_n}{\partial x} = 0 \\
H_2: &\quad y=0:\; p_n = p_{n,Channel}(x); &&\quad y = L_2:\; -D_{n,m}\frac{\partial p_n}{\partial y} = \frac{I_{H2}}{2F}; \\
&\quad x=0:\; \frac{\partial p_n}{\partial x} = 0; &&\quad x = L_1:\; \frac{\partial p_n}{\partial x} = 0 \\
H_2O: &\quad y=0:\; p_n = p_{n,Channel}(x); &&\quad y = L_2:\; -D_{n,m}\frac{\partial p_n}{\partial y} = -\frac{I_{H2}}{2F}; \\
&\quad x=0:\; \frac{\partial p_n}{\partial x} = 0; &&\quad x = L_1:\; \frac{\partial p_n}{\partial x} = 0 \\
CO_2: &\quad y=0:\; p_n = p_{n,Channel}(x); &&\quad y = L_2:\; -D_{n,m}\frac{\partial p_n}{\partial y} = -\frac{I_{CO}}{2F}; \\
&\quad x=0:\; \frac{\partial p_n}{\partial x} = 0; &&\quad x = L_1:\; \frac{\partial p_n}{\partial x} = 0
\end{aligned} \tag{16}$$

The charge balance is performed together with material balancing. It is based on the application of the divergence equation (13). This will also be performed in the next study, so that the electrochemical sources and sinks as well as the corresponding boundary conditions were set equal to zero here for determining the chemical constants.

4. Numerical approach

The model assumptions essentially proceed from two equations:
the Butler-Volmer equation for the electrochemical sinks and sources, and the Stefan-Maxwell equation for the mass flux. In connection with the laws of conservation of charge and mass, these equations are set up in the following way: the cermet anode is subdivided into individual control volumes ΔV, for each of which the balance equation

$$\iint_{\partial V} flux \; dA \; = \; \iiint_{\Delta V} sources \; dV \qquad (17)$$

should be valid according to the Gauss theorem. In this equation, ΔV represents the control volume with dA as the element of the volume surface A. Equation (17) is valid both for mass and also for charge fluxes. The discretization of the equations is shown by Fig. 3. For this purpose, a dual grid is defined after Steffen [10], in which the scalar values $S_{i,j}$ are defined in the lattice points $\left[X'_i\,; Y'_j\,; Z'_k\right]$ and the fluxes $\vec{N}_i\,, \vec{N}_j$ in the lattice points $[X_i\,; Y_j\,; Z_k]$. Points $Z_k\,, Z'_k$ were kept constant. As a first step, equation (11) has to be calculated for the stream potential S, which in the Stefan-Maxwell equation (8) represents the mass flux caused by the increase in mass. It can be seen from the form of eq. (11) that the overall reactions (4), (5) are associated with an increase in volume, whose source is only to be found in the first chemical reactions (4). At the same time, it follows from Fig. 2 that the direction of volume increase proceeds in a positive direction from bottom left to top right (shown in Fig. 3 by the direction of the arrow). The following defining equations result for positive flux directions

$$\vec{N}_{x+1} = \vec{N}_{i+1,j} = -\overline{\kappa}_{i+1}\,\frac{S_{i+1,j} - S_{i,j}}{X'_{i+1} - X'_i}\;;\quad \vec{N}_{y+1} = \vec{N}_{i,j+1} = \overline{\kappa}_{j+1}\,\frac{S_{i,j+1} - S_{i,j}}{Y'_{j+1} - Y'_j} \qquad (18)$$

The following relations are valid for the average harmonic conductivity coefficients $\overline{\kappa}$ in the lattice points $[X_i\,; Y_j\,; Z_k]$

$$\overline{\kappa}_{i+1} = \frac{\kappa'_{i+1,j}\cdot\kappa'_{i,j}\,(X'_{i+1}-X'_i)}{\kappa'_{i+1,j}\,(X_{i+1}-X'_i)+\kappa'_{i,j}\,(X'_{i+1}-X_{i+1})}$$

$$\overline{\kappa}_{j+1} = \frac{\kappa'_{i,j+1}\cdot\kappa'_{i,j}\,(Y'_{j+1}-Y'_j)}{\kappa'_{i,j+1}\,(Y_{j+1}-Y'_j)+\kappa'_{i,j}\,(Y'_{j+1}-X_{j+1})} \qquad (19)$$

where the scalar measurable conductivity values κ' are defined in the lattice points $\left[X'_i;Y'_j;Z'_k\right]$. In the terms of equation (11), equation (17) then takes on the following discretized form:

$$\left(\vec{N}_{x+1} - \vec{N}_x\right)(Y_{j+1}-Y_j) + \left(\vec{N}_y - \vec{N}_{y+1}\right)(X_{i+1}-X_i) = 2\,R_r\,(i,j)\times(Y_{j+1}-Y_j)(X_{i+1}-X_i) \qquad (20)$$

In the second step, the diffusive terms of the Stefan-Maxwell equation are calculated with the aid of eq. (15). The corresponding mass fluxes for the x and y coordinate directions are as follows

$$\vec{N}_{D(x+1)} = -\overline{D}_{i+1}\,\frac{1}{RT}\,\frac{p_{i+1,j} - p_{i,j}}{X'_{i+1} - X'_i}; \quad \vec{N}_{D(y+1)} = \overline{D}_{j+1}\,\frac{1}{RT}\,\frac{p_{i,j+1} - p_{i,j}}{Y'_{j+1} - Y'_j} \qquad (21)$$

$\overline{D}_{i+1,j}$ is the average harmonic diffusion coefficient at the phase boundary *i/i+1*. This is correspondingly true of $\overline{D}_{i,j+1}$. Its calculation corresponds to that of the average conductivity coefficient $\overline{\kappa}$ according to formula (19).

The operator expression *div* $\vec{N}_n$ in the conditional equations (15) then takes on the following form

$$div\,\vec{N}_n = \left(\vec{N}_{D(x+1)} - \vec{N}_{D(x,y)} + \hat{x}_{x+1}\,\vec{N}_{x+1} - \hat{x}_x\,\vec{N}_{x,y}\right)(Y_{j+1}-Y_j) + \left(\vec{N}_{D(x,y)} - \vec{N}_{D(y+1)} + \hat{x}_y\,\vec{N}_{x,y} - \hat{x}_{y+1}\,\vec{N}_{y+1}\right)(X_{i+1}-X_i) \qquad (22)$$

The mass flux equations can thus be calculated according to eq. (15). In principle, the same procedure can be used in calculating the electrochemical equations. The application of equations (18) to (22) in the cermet anode space as an overall scheme follows from Fig. 4.

5. Discussion and results

The SOFC anode material consists of a sintered Ni/ZrO_2 cermet (ceramic-metal) formed from a sintered heterogeneous mixture of Ni and $ZrO_2(8\%Y_2O_3)$ powders. The steam methane reforming reaction only proceeds on the Ni particles distributed in space and is thus a function of the current state of aggregation of Ni in the anode cermet. The results must also be evaluated in this sense.

The original gas composition of the gases leaving the reaction tube must first be calculated to determine the reaction constants of the reactions (4). This can be determined from the expected behaviour of the two parts of the overall reforming reaction (4). The overall course of reaction (2) can be represented as the sum of the two parts of (4), where the shift reaction is assumed to be much faster than the reforming stage so that it was formulated as an equilibrium reaction [11]. The original gas composition is calculated by balancing the two reaction stages of (4), where the entrance composition of the gases should correspond to the molar fractions $H_2O : CH_4 = 3 : 1$ (equal to **A** in total), so that the molar fractions result as:

CH_4: $\mathbf{A} - x$, H_2O: $3\mathbf{A} - x - y$, H_2: $3x + y$, CO: $x - y$, CO_2: y.

Balancing of reaction (4) leads to a volume change in the ratio $4\,\mathbf{A} : (4\,\mathbf{A} + 2x)$, i.e. volume is produced. On the basis of the analytical values from Tab. 1, the original composition of the escaping gases can be determined by this balance equation with a simple rule of three and used as a control criterion for the distribution of the gas concentrations.

Equation systems (10) - (12) and (15) - (16) were calculated by the Finite Integration Technique (control-volume approach) (FIT) [12] to describe the process flow in the SOFC cermet structure. The electrochemical terms were set equal to zero for merely determining the velocity constants k_{r+} , k_{r-} , k_{s+} and k_{s-} in equations (15), (16). The values for the individual reaction rate constants k_{r+}, k_{r-}, k_{s+} and k_{s-} were obtained by comparing the calculated and analytically determined concentration values in the gas inlet and outlet channels by means of the usual vector-gradient method with the least squares approximation as the criterion. The allowed relative differences between the experimental and calculated concentrations were as high as 10 % for the CO and CO_2 and less than 1 % for the H_2, CH_4 and H_2O. In this way, it was possible for the first time to determine the velocity constants of the methane reforming reaction and the shift reaction as volume reactions thus enabling the computational fitting of the SOFC anode properties to the internal reforming process.

The calculated concentration profiles of the individual CH_4, H_2, CO and CO_2 gases in the SOFC anode cermet and in the gas channel are shown in Fig. 5 for the temperature of 802 °C and the anode thickness of 1900 µm. Due to the high rate of the shift reaction [11], the following formulation was chosen for the constants k_{s+} , k_{s-}

$$K_p^s = \frac{k_{s+}}{k_{s-}} = \frac{p_{CO_2}\, p_{H_2}}{p_{CO}\, p_{H_2O}} = e^{-\frac{\Delta G}{RT}} \tag{23}$$

with $\Delta G = -39.258 + 40.55\ T - 0.00438\ T^2$ [13] so that only one of the two constants had to be calculated even outside of equilibrium.

By comparing the calculated and analytically determined concentration values in the gas inlet and outlet, the following values for the individual velocity constants shown in Tab. 2 can be obtained on the basis of the mass balances.

The activation energies shown in Tab. 3 for these velocity constants are obtained from the data in Table 2. The composition of the escaping gas does not permit a reliable numerical calculation of k_{r-} so that their activation energy was not calculated.

Due to the experimental difficulties, the accuracy of the experiments is not yet completely satisfactory and must be improved. For this reason, the above values of the reaction constants must be considered as first approximations which are to be checked in the near future. It should also be mentioned that the three-point temperature dependency can only give a rough estimation and a first approximation of the activation energies. The activation energy of methane reforming shown in Tab. 3 is about three times as great as previously assumed [2,3]. However, in these studies the reactions (4) were regarded and evaluated as surface reactions, which is not completely correct. The activation energy is about twice as great as that of electrochemical hydrogen oxidation [14]. This may explain the relative approximation of the two reaction rates when the temperature is lowered.

Acknowledgements

We thank Dr. B. Steffen for fruitful discussions concerning the mathematical problems.

References

[1] M. Mogensen and J.J.Bentzen, *in* Proceedings of the First Int.Symp. on Solid Oxide Fuel Cells, S.C. Singhal, ed., The Electrochemical Society, Proc. Vol. 89-1, Pennington, NJ, 1989, p. 99

[2] E. Achenbach and E. Riensche, *J. Power Sources* **52** (1994) 283.

[3] A.L. Lee, R.F. Zabransky and W.J. Huber, *Ind. Eng. Chem. Res.* **29** (1990) 766

[4] I.V. Yentekakis, S.G. Neophytides, A.C. Kaloyinannis and C.G. Vayenas, Proc.3rd Int. Symp. on Solid Oxide Fuel Cells, Proc. Vol. 93-4, The Electrochemical Soc., Pennington, 1993, p. 904

[5] W. Lehnert, J. Meusinger, U. Stimming, E. Riensche, Proc. 2nd Europ. Solid Oxide Fuel Cell Forum, Oslo, Norway, (1996), B. Thorstensen, ed., Europ. SOFC Forum, ISBN 3-922 148-19-O , p. 143

[6] H.P. Buchkremer, U. Diekmann, D. Stöver, Proc. 2nd Europ. Solid Oxide Fuel Cell Forum, Oslo, Norway, (1996), B. Thorstensen, ed., Europ. SOFC Forum, ISBN 3-922 148-19-O , p. 221

[7] R.B. Bird, W.E.Stewart, E.N.Lightfoot, *Transport Phenomena*, J. Wiley & Sons, N.Y., 1960, p. 571

[8] N. Kostka, K. Hammeke, Ermittlung von Stoffdaten der Gase und der Mischungen aus diesen Gasen, *Jül-Bericht 2112*, Jan. 1987, ISSN 0366-0885

[9] K. Habetha, *Höhere Mathematik für Ingenieure und Physiker, Band 3,* Klett Studienbücher, Stuttgart, 1979, p. 14

[10] J. Divisek, B. Steffen, *in* Proc. Symp. Chlor-Alkali Prod. and New Mathematical Computing Methods in Electrochem. Eng., T.C. Jeffrey, J. Fenton, eds., The Electrochemical Soc., Pennington, Proc. Vol. 93-14, 1993, p. 297

[11] J.R. Rostrup-Nielsen, *Catalytic Steam Reforming*, Springer-Verlag, 1984, p. 57

[12] T. Weiland, *Particle Accelerators* 15 (1984) 245

[13] Ch. Rechenauer, "Dreidimensionale mathematische Modellierung des stationären und instationären Verhaltens oxidkeramischer Hochtemperartur-Brennstoffzellen", PhD Dissertation, Technical University of Aachen, 1992

[14] P. Holtappels, "Elektrochemische Umsetzung verschiedener Brenngase an Nickel-Cermet-Elektroden in der Hochtemperaturbrennstoffzelle", PhD Dissertation, University of Bonn, 1997

Tab. 1 Experimental conditions and rest gas analysis of the reforming reaction

Experimental Conditions					**Rest gas analysis (vol.%)**			
temp. (°C)	pressure (bar)	CH_4 velocity ($Ncm^3.s^{-1}$)	CH_4 area load ($Ncm^3.cm^{-2}.s^{-1}$)	H_2O/CH_4 mol. ratio	H_2	CO	CH_4	CO_2
Anode thickness 0.36 mm								
888.5	1.5	9.166	2.78	3	19.0	1.98	75.4	3.63
853.9	1.5	9.166	2.78	3	11.8	1.38	84.8	2.03
Anode thickness 0.66 mm								
884.7	1.5	9.588	2.78	3	33.1	3.7	57.5	5.2
851.5	1.5	9.588	2.78	3	26.2	2.5	66.7	4.4
802.3	1.5	9.588	2.78	3	17.8	1.5	78.9	3.3
Anode thickness 1.35 mm								
892.1	1.5	10.800	2.78	3	32.1	3.86	58.4	5.34
848.8	1.5	10.800	2.78	3	25.8	2.67	67.0	4.50
798.5	1.5	10.800	2.78	3	16.2	1.47	80.2	2.98
Anode thickness 1.90 mm								
893.5	1.5	8.366	2.78	3	34.8	3.32	53.9	5.94
847.6	1.5	8.366	2.78	3	26.9	2.82	65.0	4.47
802.3	1.5	8.366	2.78	3	18.6	1.88	75.9	3.06

Tab. 2 Reaction rate constans of the reforming and shift reactions in bulk

Temp. °C	k_{r+} [$mol.cm^{-3}.bar^{-2}.s^{-1}$]	k_{r-} [$mol.cm^{-3}.bar^{-4}.s^{-1}$]	k_{s+} [$mol.cm^{-3}.bar^{-2}.s^{-1}$]	k_{s-} [$mol.cm^{-3}.bar^{-2}.s^{-1}$]
890	$1{,}6 \times 10^{-3}$	$(1{,}5 \times 10^{-6})$	$3{,}6 \times 10^{-3}$	$4{,}3 \times 10^{-3}$
850	$8{,}0 \times 10^{-4}$	$(1{,}5 \times 10^{-6})$	$3{,}2 \times 10^{-3}$	$3{,}5 \times 10^{-3}$
800	$2{,}3 \times 10^{-4}$	$(1{,}4 \times 10^{-6})$	1.5×10^{-3}	1.4×10^{-3}

Tab. 3 Activation energies of the reforming and shift reactions

	k_{r+} [kJ/mol]	k_{r-} [kJ/mol]	k_{s+} [kJ/mol]	k_{s-} [kJ/mol]
E_A	230	----	90	125

Fig. 1: Scheme of the reforming and electrochemical reactions in the anode space

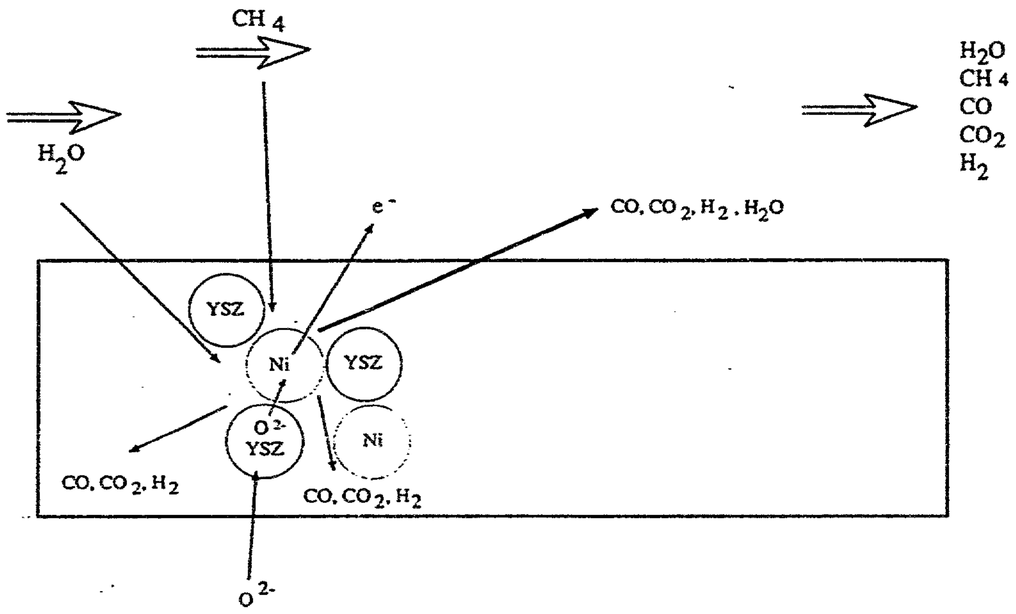

Fig. 2: Schematic of the reforming reaction in the anode space

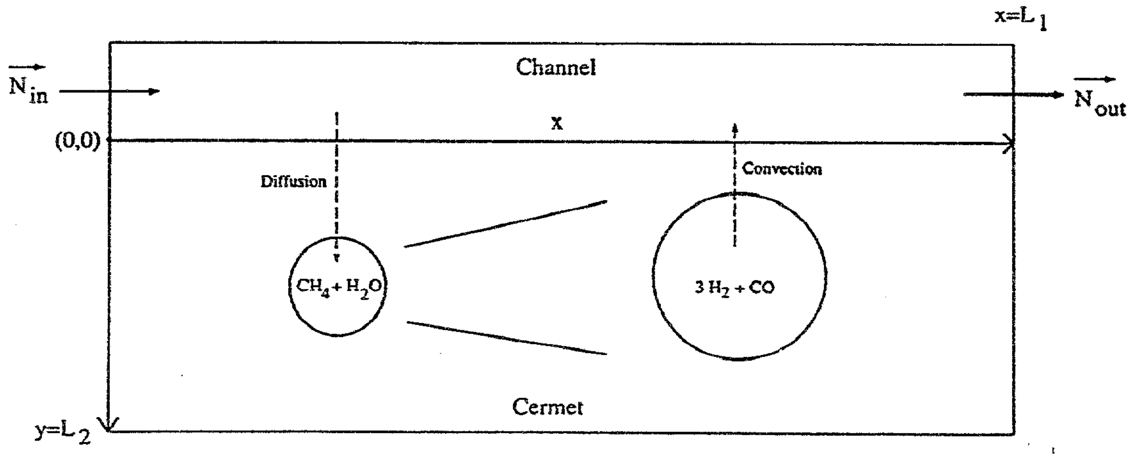

Fig. 3: Discretization scheme of the anode space as a dual grid

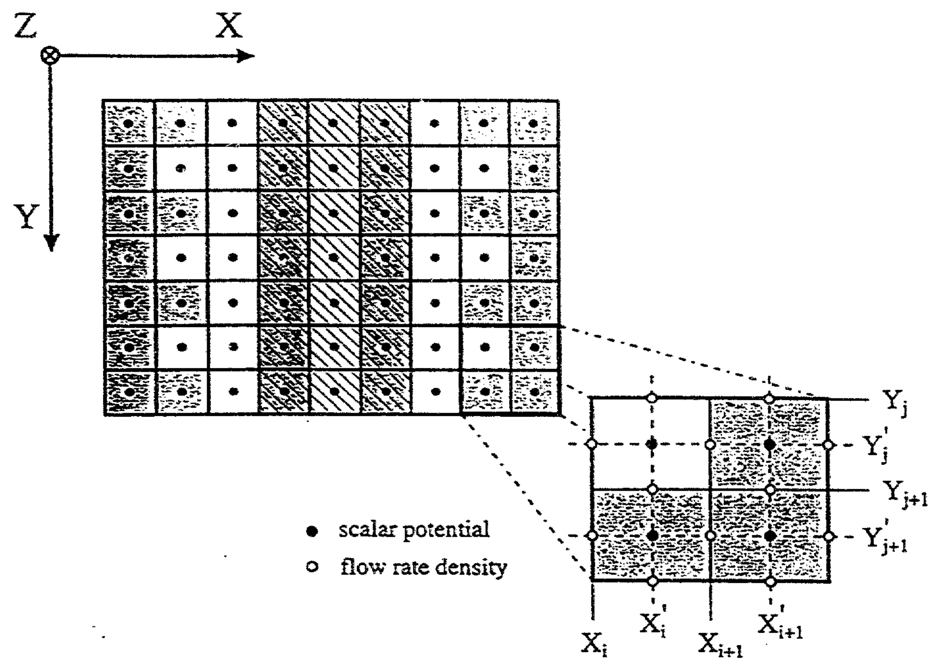

Fig. 4: Discretized scheme of the reforming reaction in the bulk of the SOFC anode

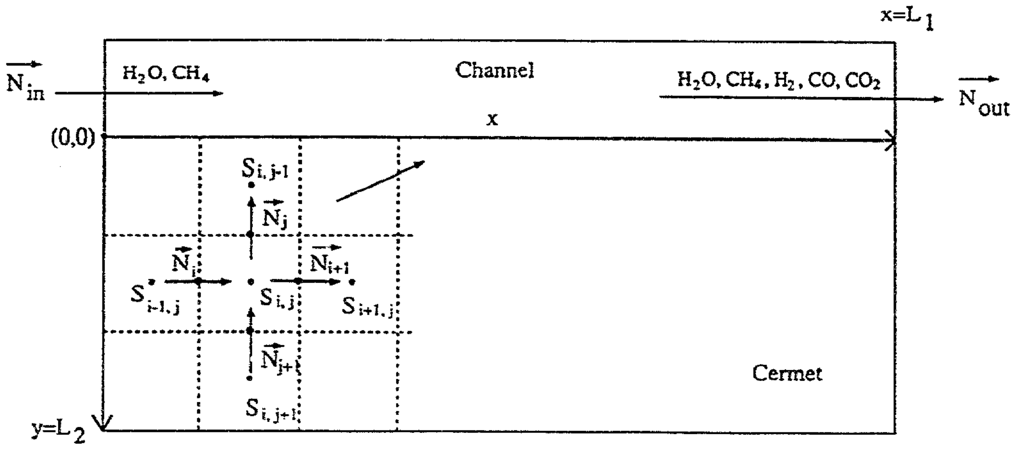

Fig. 5a: Concentration profile of the reformer gases in the cermet
t = 802°C, anode thickness 1900µm

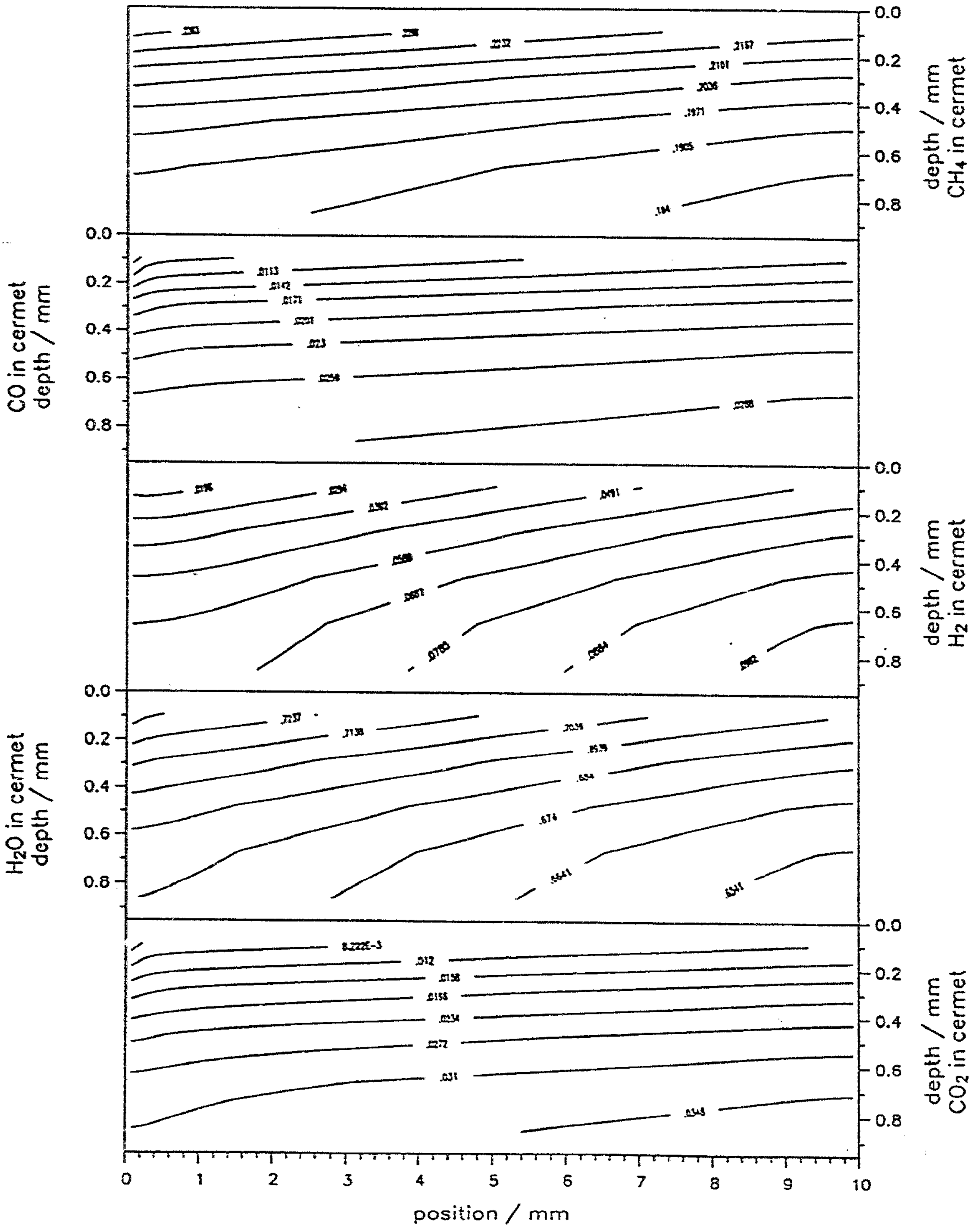

Fig. 5b: Concentration profile of the reformer gases in the gas channel

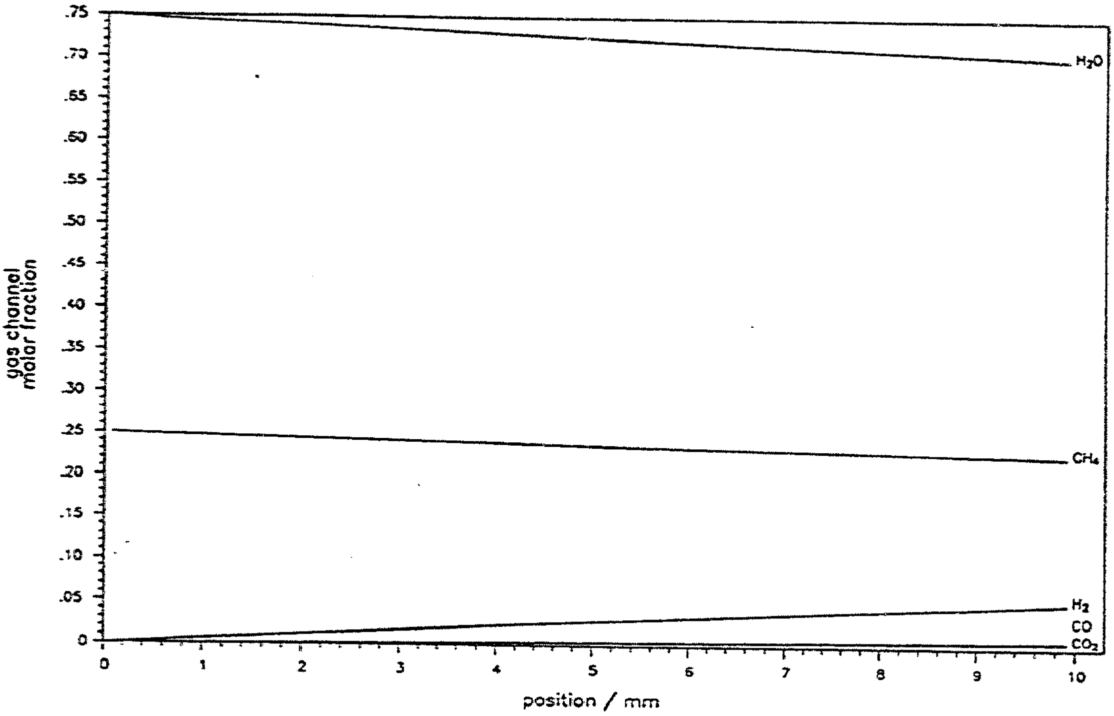

Long-Term Changes in Microstructure and Electrical Characteristics of Cermet Anodes

A. Naoumidis[#], A. Gupta[#], H. Hoven[#], Th. Kloidt[‡], D. Simwonis[#], and F. Tietz[#]
[#]*Institut für Werkstoffe der Energietechnik,* [‡]*Institut für Energieverfahrenstechnik*
Forschungszentrum Jülich GmbH, D - 52425 Jülich

Introduction

Degradation phenomena during long-term operation of solid oxide fuel cells (SOFCs) at temperatures of about 950 °C result in a steady decrease of power output. The cell voltage usually decreases with a rate of several percentages per 1000 h operating time [1]. The reasons for the increasing electrochemical losses with time are versatile and can be regarded as the sum of all degradation mechanisms occuring in an SOFC. For each SOFC component deteriorations with time have been observed: i) formation of pyrochlore compounds at the cathode-electrolyte interface [2], ii) decrease of ionic conductivity of the solid electrolyte (8 mol% yttria-stabilized zirconia, 8YSZ) due to ageing [3,4], iii) agglomeration or coarsening of Ni particles within the Ni/8YSZ anode cermet [5], iv) corrosion of metallic interconnector materials [6] and v) chromium evaporation from Cr containing interconnector materials and contact layers [7,8]. However, today it is not clear which of these processes significantly contribute to the electrical losses and to which extend.

In the case of anode cermets containing metallic nickel and 8YSZ it is known that Ni shows a rather bad wettability of the ceramic component [9] and tends to minimize its surface energy by agglomeration of Ni grains. For an investigation of the long-term stability of anode materials various specimens were exposed at 1000 °C for 1000 h and the microstructural as well as the electrical properties were used to evaluate the stability of these materials. This work reports the results of three anode materials in more detail: screen-printed thick anode layers made from 1) conventional powders and 2) from xerogel-powder as well as 3) an anode substrate synthesized by the coat-mix process.

Experimental

For the preparation of screen-printed anodes each mixture of starting powders has to be pre-conditioned (milling, calcination etc.) to obtain well sintered oxide layers without sintering fissures. Furthermore, preparation parameters like sintering temperature and dwell time can be used to optimize the surface structure of the anode layers. In the following the two kinds of screen-printed specimens made of conventional powders (NiO from J. T. Baker, USA and 8YSZ from Tosoh, Japan) and xerogel-powder are abbreviated as A66 and A90, respectively. The xerogel was synthesized by dissolving $Zr(OC_3H_7)_4$ in acetic acid, to which alcoholic solutions of $Y(NO_3)_3 \cdot 6\ H_2O$ and $Ni(Ac)_2 \cdot 4\ H_2O$ were added, followed by subsequent gelation and drying [10]. With increasing drying temperature NiO and *c*-ZrO_2 are formed. The NiO content in the oxide mixture was 55 wt%. For the screen-printing paste A90 the xerogel was calcined at 1400 °C and small quantites of the commercial powders were added to adjust the sinterability. The other paste, A66, contained 65 wt% NiO in the powder mixture,which was calcined at 1300 °C. Anode stripes (4 × 0.5 cm) were screen-printed onto tape-casted 8YSZ foils and sintered at 1500 °C for 4 h.

The fabrication of anode substrates by the coat-mix technique is described elsewhere [11]. Rectangular substrate samples were cut from large substrate plates sintered at 1400 °C.

All samples were reduced at 900 °C in Ar / 4% H_2 atmosphere for 2 h before long-term annealing. For each kind of sample at least 5 specimens were exposed in Ar / 4% H_2 / 4% H_2O atmosphere at 1000 °C for 1000 h. After each exposure time, i. e. after 0, 100, 300 and 1000 h, one specimen of each sample set was contacted with Pt paste and wires. The sintering of the Pt paste was carried out at 1000 h for 0.5 h in Ar / 4% H_2 atmosphere. The electrical conductivity of the freshly contacted samples was then measured at room temperature by a standard four-probe d.c. technique.

Screen-printed ring anodes of pastes A66 and A90 as well as a graded A66/A90 sample were tested electrochemically at various temperatures in Ar / 20% H_2 / 3% H_2O atmosphere up to 120 h. The configuration of the cell test is described in [12]. LSM cathodes were used as counter electrodes.

Results & Discussion

Electrical Conductivity

The electrical conductivity data obtained after different exposure times is shown in Fig. 1. The screen-printed anodes show a much lower conductivity of about one order of magnitude and a completely different behaviour with annealing time compared with the coat-mix samples. It is emphasized here that the measured conductivity data are effective in-plane conductivities, which are not corrected for Ni volume fraction or porosity. Therefore it is worth to note that the coat-mix substrates have a higher porosity (about 45%) and nevertheless better electrical properties. The anode layers all have a porosity between 20-30% and show an increasing electrical conductivity with annealing time. Instead, the coat-mix samples loose about 9% of the initial conductivity.

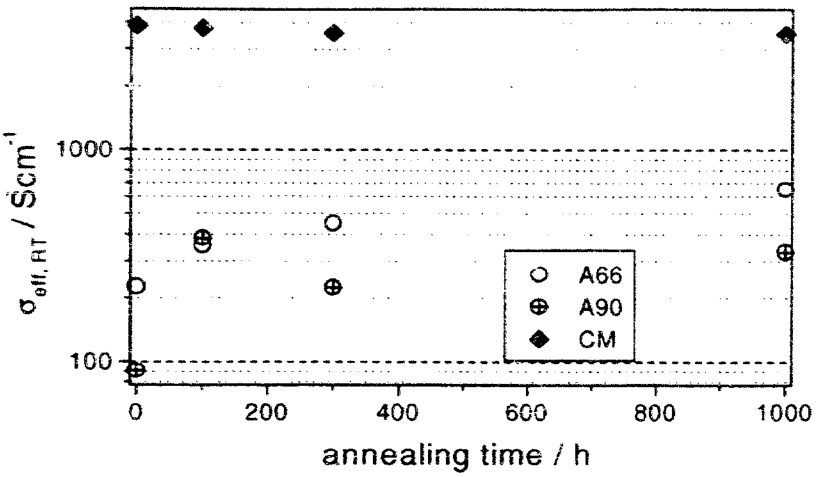

Fig. 1: Room temperature conductivity of exposed coat-mix substrate (CM) and screen-printed anodes (A66 and A90).

This different behaviour may be explained by percolation-based theories of composite materials [13,14], in which the conducting phase is separated into two parts, namely a contiguous fraction contributing to the electrical properties and a fraction isolated from the conductivity pathways. With increasing time of exposure and ongoing agglomeration it is assumed that in microstructures with low porosity the latter fraction gets contact with the continuous Ni fraction and is therefore improving the conductivity. On the other hand, in microstructures with high porosity, there is enough empty volume to be filled with creeping metal particles leading to an increase of the isolated Ni fraction and to lower conductivities. However, this is a first attempt to describe the phenomena shown in Fig. 1 and further experimental evidences are necessary to confirm this hypothesis (see also section *Microstructure*).

Electrochemical Testing

In the case of the substrate samples no electrochemical testing could be performed so far due to difficulties in the preparation of samples with adequate electrode geometry. However, with respect to the stack performance and the low decrease of power output under operating conditions [15], it can be assumed that the small decrease in electrical conductivity of the anodes merely effects the i-η-characteristics of anode-supported SOFCs.

The selected screen-printed anodes were tested at different temperatures. In Fig. 2 the cell voltages at 950 °C for the three samples A66, A90 and A66/90 are shown in dependence of the testing time. In this case a current density of 200 mA/cm^2 was applied and air was used as cathode gas. The fluctuations of the cell voltages are smaller than 1.5 % and reflect the temperature variations within the testing rig

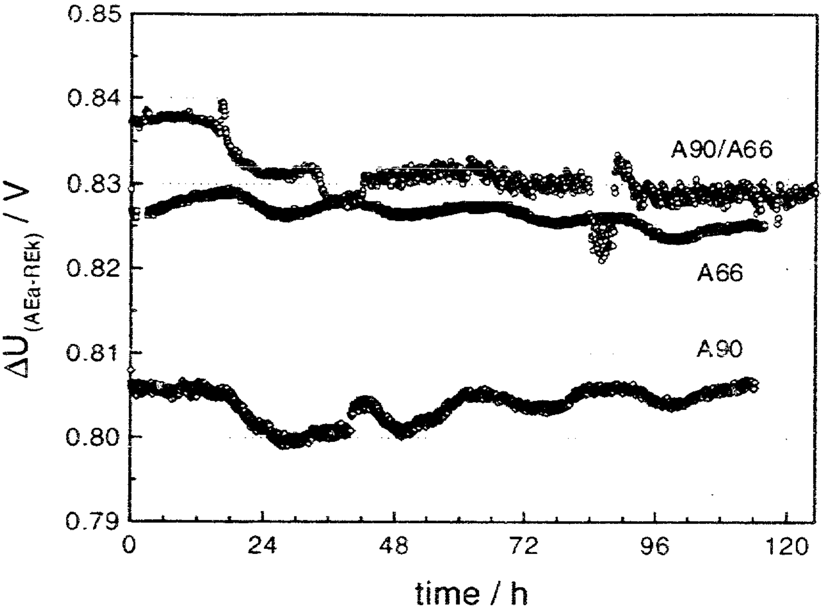

Fig. 2: Performance of single test cells. Experimental conditions: T = 950 °C, i = 200 mA/cm^2, anode gas: (80 % Ar, 20 % H_2) + 3 % H_2O, cathode gas: air

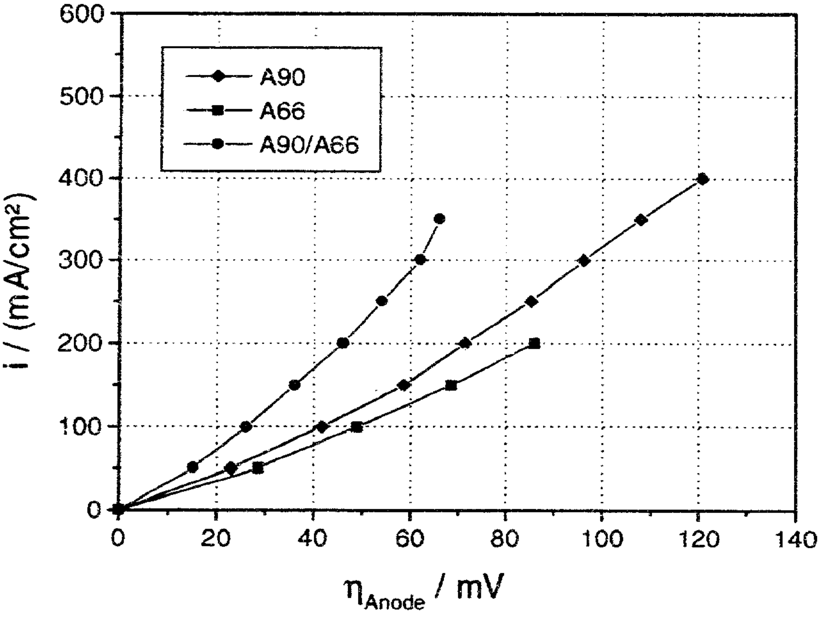

Fig. 3: i-η-characteristics of screen-printed anodes. Experimental conditions: T = 800 °C, all others see Fig. 2 and text.

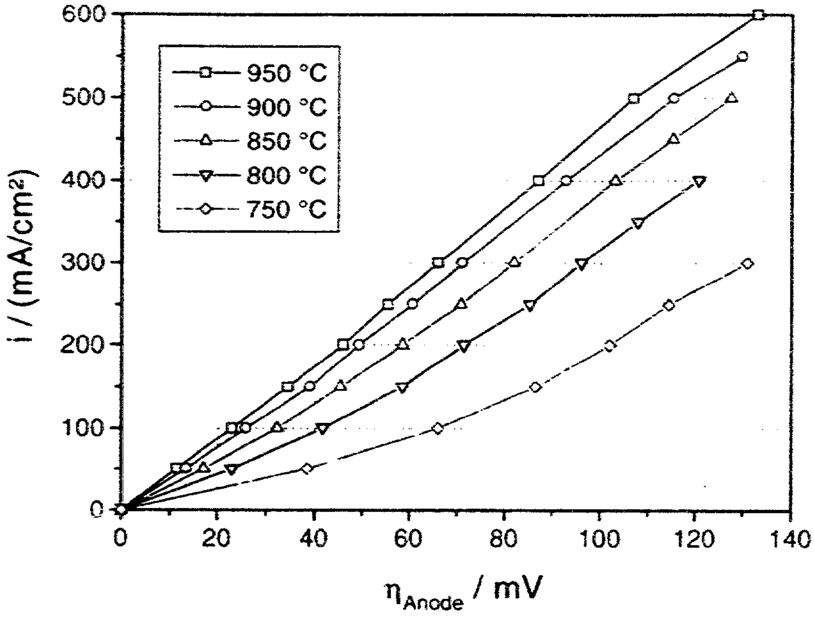

Fig. 4: Temperature dependence of i-η-curves for anode A90. Experimental conditions see text.

($\Delta T \approx 2.5$ K). Therefore, the performance of the screen-printed anodes can be regarded as stable over the whole period of testing and the i-η-characteristics before and after annealing for 120 h are nearly identical. In an i-η-diagram for T = 950 °C the three anodes have the same electrochemical quality with 60-65 mV and 110-130 mV at i = 300 and 600 mA/cm^2, respectively. At lower temperatures, e. g. at T = 800 °C (Fig. 3), there are significant deviations indicating different activation energies for the electrocatalytic reaction mechanism.

For A90 the temperature dependence of the i-η-curves is shown in Fig. 4. Looking at a constant overpotential, e. g. 100 mV (dashed line in Fig. 4), the obtained current densities reveal an excellent performance of the cell for temperatures ≥ 800 °C.

Microstructure

Samples were characterized by ceramography and quantitative image analysis at different stages of exposure (0, 100, 300 and 1000 h). The strongest changes in microstructure were observed after 1000 h of annealing. In all samples investigated Ni particle coarsening was detected by measuring the grain size distribution. Furthermore, the shape factor of the Ni particles tended to smaller values indicating elongated grains instead of spherical shapes. The coarsening can be observed easily from ceramographic images of the microstructures as given in Figs. 5 and 6 for coat-mix samples and screen-printed anode layers, respectively.

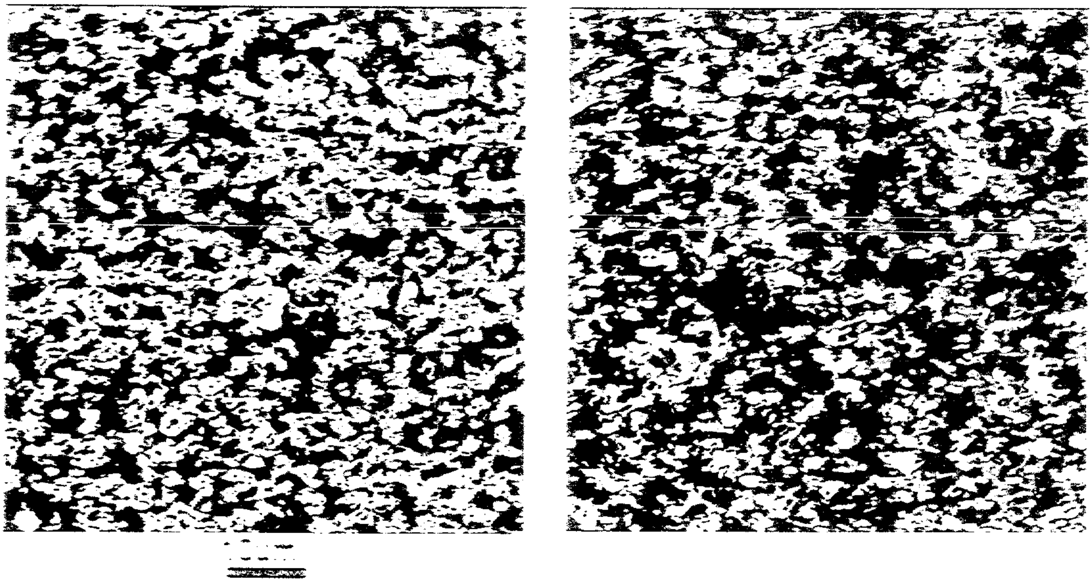

d_{50}(Ni) = 1.50µm
Circularity shape factor: 0.74

d_{50}(Ni) = 1.55µm
Circularity shape factor: 0.74

Fig. 5: Microstructure of the reduced coat-mix substrates before and after long-term exposure at 1000°C for 1000 h (grey: YSZ, white: Ni, black: pores).

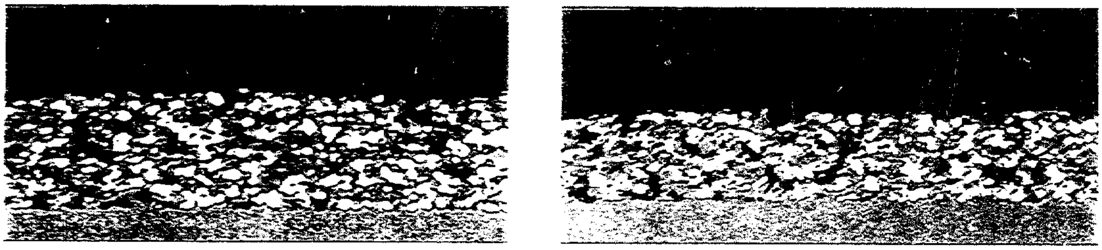

d_{50}(Ni): 1.48 µm
Circularity shape factor: 0.78

d_{50}(Ni): 1.40 µm
Circularity shape factor: 0.75

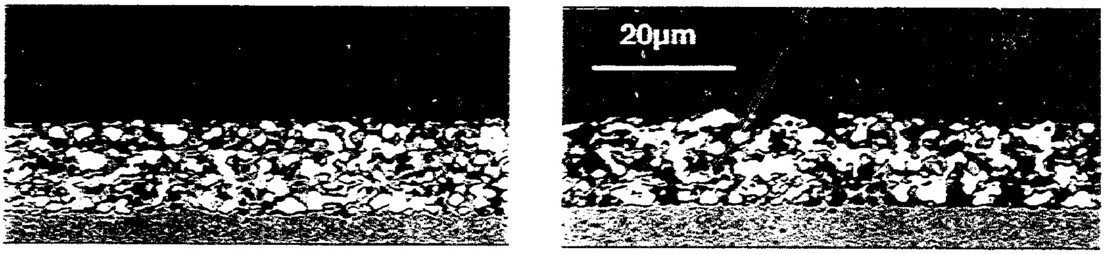

d_{50}(Ni): 1.82 µm
Circularity shape factor: 0.72

d_{50}(Ni): 1.96 µm
Circularity shape factor: 0.71

Fig. 6: Microstructure of the reduced screen-printed anodes before (top) and after (bottom) long-term exposure. left: A90, right: A66.

In the case of the coat-mix samples it is evident, that the very fine Ni particles nearly disappeared in some areas after 1000 h at 1000 °C, but the shape of the grains remained unaffected. The resulting microstructure is still interwoven by the two solid phases. The Ni particles have grown due to Oswald ripening and the mean particle size of Ni, d_{50}(Ni), increased slightly from 1.50 µm to 1.55 µm.
The d_{50}(Ni) values of the screen-printed anodes initially were nearly the same, 1.48 and 1.40 µm for A90 and A66, respectively. After the exposure the values were significantly higher (1.82 and 1.96 µm), also compared with the coat-mix sample. In both layer materials the agglomeration of Ni grains led to better interconnection of the Ni phase as can be seen in the two lower photographs of Fig. 6 and therefore to a higher electrical conductivity (Fig. 1). However, the agglomeration is more pronounced in A66 containing more Ni. This fact confirms the good long-term stability of sol-gel material observed previously on exposed pressed pellets [10]. With respect to the coarsening tendency, parameterized by the d_{50}(Ni) values, the materials investigated can be ordered in the following row: CM < A90 < A66. Although the coat-mix substrates are also made from commercial powders, their tendency to agglomerate is low. This has to be attributed to the unique formation of two-phase agglomerates during the powder-coating procedure of this process [16]. These agglomerates lead to a geometrical stabilization of the metallic Ni by the ceramic YSZ in combination with excellent electrical conductivity.

Conclusions

The screen printing of anodes was optimized for various powders. The resulting Ni/YSZ cermets show a good long-term stability of the electrical conductivity and electrochemical activity. The latter property has to be tested for longer exposure times. Especially the anodes made from xerogel powder showed smaller agglomeration rates indicating the ageing of the anodes. Proper materials selection as well as optimized microstructures are the ways leading to stable physical properties and therefore to long service times of an SOFC.

References

[1] F. H. van Heuveln, J. P. P. Huijsmans, Final Report of Activity B1 "Long-term stability under operating conditions", Advanced Fuel Cells Programme, Annex II, International Energy Agency, 1996

[2] G. Stochniol, Ph. D. thesis, RWTH Aachen (1996)

[3] F. T. Ciacchi, K. M. Crane, S. P. S. Badwal, Solid State Ionics 73 (1994) 49

[4] T. Norby, P. A. Osborg, H. Ræder, in: Proc. 1st Eur. SOFC Forum, ed.: U. Bossel (1994) p. 671

[5] N. Q. Minh, J. Am. Ceram. Soc. 76 (1993) 563

[6] W. J. Quadakkers, H. Greiner, W. Köck, H. P. Buchkremer, K. Hilpert, D. Stöver, in: Proc. 1st Eur. SOFC Forum, ed.: B. Thorstensen (1996) p. 297

[7] J. Urbanek, M. Miller, H. Schmidt, K. Hilpert, *ibid.* 6, p. 503

[8] W. J. Quadakkers, H. Greiner, M. Hänsel, A. Pattanaik, A. S. Khanna, W. Malléner, Solid State Ionics 91 (1996) 55

[9] A. Naoumidis, A. Tsoga, P. Nikolopoulos, H. Grübmeier, in: Proc. 4th Int. Symp. on SOFC (SOFC-IV), eds.: M. Dokiya, O. Yamamoto, H. Tagawa, S. Singhal, The Electrochem. Soc., NJ (1995) p. 667

[10] A. Kontogeorgakos, Ph.D. thesis, RWTH Aachen, 1997

[11] D. Simwonis, A. Naoumidis, F. J. Dias, J. Linke, A. Moropoulou, J. Mater. Sci., to be published

[12] J. Divisek, L. G. J. de Haart, P. Holtappels, T. Lennartz, W. Malléner, U. Stimming, K. Wippermann, J. Power Sources 49 (1994) 257

[13] D. S. McLachlan, M. Blaszkiewicz, R. E. Newnham, J. Am. Ceram. Soc. 73 (1990) 2187

[14] Z. Fan, A. P. Miodownik, P. Tsakiropoulos, Mater. Sci. Techn. 9 (1993) 1094; Z. Fan, Phil. Mag. A 73 (1996) 1663

[15] H. P. Buchkremer, U. Diekmann, L. G. J. de Haart, H. Kabs, U. Stimming, D. Stöver, in: Fuel Cell Seminar, Orlando, Florida (1996) p. 175

[16] D. Simwonis, F. Dias, A. Naoumidis, D. Stöver, in: Proc. 5th Eur. Conf. on Advanced Materials, Processes and Applications (EUROMAT '97), Maastricht, The Netherlands, 1997 (to be published)

Workshop session - Wednesday

Chairman - J.A. Kilner

Discussion highlights on cathode processes targeted first the appropriate diffusion coefficient for the steady state, it being self-diffusion for membranes. The surface exchange coefficient for oxygen transfer led to discussion of active sites: are they vacancies? how much is surface diffusion involved? Classical electrochemistry does not explain oxygen transfer across these surfaces.

On interfaces, H. Yokokawa brought up the question of mobilities of silicon and chromium oxides, the zirconate formation problem and manganese diffusion. The significance of in-situ experimental methods was emphasised, since otherwise it is mere extrapolation and deduction, with no direct observation.

On the appropriate diffusion coefficient, it was stated that the chemical diffusion coefficient is used in the presence of a concentration gradient in the transient, non-steady-state case. In a steady state situation it is self-diffusion. But in a cathode, with also a stoichiometry range, the diffusion coefficient may not be constant since there is a steady-state gradient situation. Nisancioglu agreed with this perspective, that if nonstoichiometry can be integrated into the model there will be no difference, but if the thermodynamic data is missing the chemical coefficient must be used even in steady-state conditions. Steele stated that this was addressed in 1972, and nothing has changed since then. Bossel raised the issue of interface transport, and it was admitted that effects in pores are important. The case can be regarded as heterogeneous catalysis.

Kilner questioned the extent of oxygen coverage on perovskites at that temperature. Van Heuveln noted that diffusion limitations are not seen, so there are not too many gaseous molecules in the surface. McEvoy asked about oxygen mobility at grain boundaries. Kilner presented transport in a LSMnCo, governed by LeClaire's equation for grain boundary diffusion, ref. Brit. J. Appl. Phys., 14 (1963) 351, when lattice diffusion distance is small compared to grain size, and there is a $^{6}/_{5}$ power of time dependence. When plotted on this scale a linear plot is evidence of grain boundary transport.

Yokokawa dealt with cation diffusion on grain boundaries, with a presentation of images on chromites.

	$Diff_{bulk}$	$Diff_{gb}$	
O^{--}	1.6×10^{-13}	7.1×10^{-14}	cm^2s^{-1} @ 1273K
Ca^{++}, Sr^{++}	5×10^{-16}	6.4×10^{-11}	cm^2s^{-1} @ 1273K

Steel pointed out the grain boundary is seen when bulk diffusion is slow.

Surface exchange coefficients. Kilner presented O^{18} anneal results at 1000°C with the consequent concentration profile. In mixed conducting perovskites the activation energy for surface exchange and for diffusion are related. Vacancy concentration is a controlling parameter for both!

Some ideas on oxygen transfer: low energy ion scattering (LEIS) shows the <100> AO surface is energetically favourable. This surface is essentially SrO since Sr segregates to the surface. This surface is not inactive; a surface O vacancy reveals a transition metal cation (Mn) below. But Goodenough says the BO chains are at the origin of conductivity. LEIS can reveal surface

vacancies. e^- is fed up from B cations to a neutral surface. Surface disorder can be higher than in the bulk. Consequences: high surface diffusivity, then exchange occurs with vacancy pairs. Hence isotope exchange where O_2^{18} goes in O_2^{16} comes out without mixing. Kilner also presented LSM images showing texture of grains by thermal etching.
A question from Divisek was on incorporation into the lattice as rate-determining step. Then is it not difficult to compare this to the electrochemical rate, since it is purely a "surface state" effect in the chemical case?
Steele recalled as rate controlling factor the surface exchange, explaining why LSM cannot give reasonable current densities at 700°C. Bossel countered that the cathode is not the problem as evidenced by the LBL published result of 2W cm^{-2} at 800°C. McEvoy noted that even for zero electrolyte ohmic resistance the interface polarisations normally observed do not permit that performance. While Ihringer recalled that in the LBL work all the losses are cathode side, van Heuveln repeated that the limitation is the interface.

On materials quality Steele mentioned silica contamination of electrolyte, up to 200 ppm in some powders. He also reported on work on LSCF, where etching a CGO surface reduced resistivity by a factor of 3. With a Rhone-Poulenc powder etching was not necessary, the performance of an etched SSC powder being achieved directly. McEvoy recalled similar observations of YSZ; Will of ETHZ pointed out that silica could come from the surfaces, and Bossel said it could be from seals. Kleitz stated that some results are taken in quartz tubes.

Yokokawa introduced the LSM/YSZ interaction topic. The best cathode of Osaka Gas by EVD never sees a temperature >1200°C. For a good cathode we must develop processing at these lower sintering temperatures. Following a remark by Kleitz, McEvoy recalled the observation of Ivers-Tiffee that redissolution of interphases may occur during electrochemical operation. Kilner stated that then Mn is getting mobile, with a liquid phase formed. Naoumidis questioned the source of the Mn, given that composite cathodes rapidly reach equilibrium. McEvoy pointed out that if the field pushes O^{--} in one direction, it pushes Mn^{++} in the other, as mentioned in the morning talk of Yokokawa.
On diagnostics Naoumidis queried the significance of EIS on cathodes in air, since in operation there is a different local P_{O_2} Effective than in air. Kilner stated that data are scarce, the isotope exchange work being done at 1 atm pressure.

Badwal wished to discuss thin electrolytes: 50m => 50 mV loss @ 0.5 Acm^{-2}. There is no appreciable gain for thickness <15m. Zirconate does form, maybe 4m once the temperature is >1100°C, but it may not be continuous. In a reducing environment zirconate will decompose. Mn^{II} dissolves easily in YSZ whereas Mn^{III} precipitates out. On silica, there is always a migration to the surface, the rate a function of oxygen partial pressure. So it may pose a cathode problem while the anode is immune. 20 - 50 ppm Si in powder cannot lead to surface coverage, so O^{--} transport is then maintained. This gives us a quality control parameter for the materials.

At that point a very lively discussion was suspended due to pressure of time.

A.J. McEvoy,
LPI-DC, EPFL

The relationship between the steam-methane ratio, anodic reaction and overpotential in SOFC

Manabu Ihara, Abulet Abudula, Ryuzaburo Kato, Keiji Sakaki,
Hiroshi Komiyama and Koichi Yamada
Department of Chemical System Engineering, University of Tokyo,
Hongo 7-3-1, Bunkyo-ku, Tokyo 113, Japan

Abstract

The power generation experiments of solid oxide fuel cell (SOFC) were carried out changing the water to methane ratio in fuel. The pre-mixed gases corresponding to the thermal equilibrium composition were used as fuel to separate electrochemical reactions on an anode from the steam reforming reactions. A kinetic behavior of the Langmuir-Hinshelwood type was observed for the anodic reactions. The reactions on the anode were quantitatively clarified at different steam to methane ratios by using the electron mass balance and the anode exit gas composition. The relationship between the steam to methane ratio and the overpotential could be explained by reaction mechanisms.

1. Introduction

Hydrocarbons(HCs) fuel have many advantages for SOFC including lower cost and lower storage pressure. However, the deterioration of the anode due to carbon deposition by thermal decomposition of HC has been pointed out. An internal steam reforming system has been suggested to prevent the carbon deposition on the anode. This reduces the power density of a cell and the fuel efficiency, and also requires a heat recovery system for heating the steam in the feed gas. If we can operate SOFC in dry methane fuel without carbon deposition, it increase the energy efficiency of SOFC.

In our previous reports [1,2], methane was found to be completely oxidized to carbon dioxide and water without carbon deposition on the three phase boundary under high current density and in low concentration fuel of dry methane (4~9%). The mechanism determining the threshold current density for the complete oxidation was also clarified.[3] But, in high concentration dry methane fuel, the threshold current density is estimated to be very high according to our suggested mechanism. Because the minimum addition of steam to fuel must be considered for the present SOFC, the anodic reaction mechanism is very important.

In this report, the relationship between the steam-methane ratio in the fuel, anodic reaction and anodic overpotential was investigated.

2. Experimental

The structure of the cell used for the experiments was shown in our previous reports [1,2,3]. The material of anode, cathode and electrolyte are Ni/ 8-YSZ cermet, $La_{0.85}Sr_{0.15}MnO_3$ and discs of 8-YSZ respectively. Operating temperature, feed rate of oxidant and total feed rate of fuel were 1000 °C, 50 mlNTP•min^{-1}(O_2 -100%),and 65.5 mlNTP•min^{-1} respectively. The pure H_2, pure CO, H_2O-CO and H_2O-CH_4 whose H_2O-CH_4 ratio (S/C) were 0, 0.5, 1, 1.5 and 2 were used as fuel. For H_2O-CH_4 fuel, the pre-mixed gases corresponding to the thermal equilibrium composition were used to separate electrochemical reactions on an anode from the steam reforming reactions. The equilibrium composition of H_2O-CH_4 fuel at 1000°C were shown in Table 1. The anodic overpotential was calculated from the potential difference between the anode and cathode, that between two reference electrodes, IR drop and cathodic overpotential measured by a current interruption method [3]. The product gas analyses were done by a gas chromatography to determine the product rates of carbon monoxide (CO), carbon dioxide (CO_2), hydrogen (H_2), methane (CH_4) and other hydrocarbons (HCs). Water(H_2O) formation rate in the cell were calculated using the mass balance (H,O) and the electron balance carried by the current.

Table 1 Equilibrium compositions of CH_4-H_2O fuel at 1000°C

S/C	CH_4 (%)	CO (%)	H_2 (%)	CO_2 (%)	H_2O (%)	Ar (%)	CO/H_2
0	29.2					70.8	
0.5	11.5	11.5	33.9			43.1	0.34
1		18.5	55.4			26.1	0.33
1.5		16.9	56.9	1.5	7.8	16.9	0.30
2		15.4	58.5	3	15.4	7.7	0.26

3. Results and Discussion

3-1. S/C and anodic reaction

At S/C=0, the product gas on anode were H2 and CO. The complete oxidation of methane with oxide ion [1,2,3] was not occurred because the concentration of CH_4 (29%) was much higher than that (4.6%) in our previous report. At S/C=0.5, H_2O was detected besides H_2 and CO. CO_2 was not produced. At S/C≧1, the products were CO_2 and H_2. Figure 1 shows the exit gas composition at S/C=2. The ratio of CO_2 production rate to H_2O production rate was shown in Fig. 2. The ratio at S/C=1 was much smaller than that at S/C=1.5,2.

The anodic reactions at each S/C were decided as follows by the analysis of anode exit gas composition.

S/C=0

$$CH_4 \rightarrow C + 2H_2 \quad (1)$$

$$C + O^{2-} \rightarrow CO + 2e^- \quad (2)$$

S/C=0.5

$$CH_4 \rightarrow C + 2H_2 \quad (1)$$

$$C + O^{2-} \rightarrow CO + 2e^- \quad (2)$$

$$H_2 + O^{2-} \rightarrow H_2O + 2e^- \quad (3)$$

S/C≧1 $2CO \rightarrow CO_2 + C$ (4)

$H_2 + O^{2-} \rightarrow H_2O + 2e^-$ (3)

$CO + O^{2-} \rightarrow CO_2 + 2e^-$ (5)

3-2. The dependence of anodic overpotential on the concentration of CO and H_2

The dependence of anodic overpotential on the concentration of H_2 was shown in Fig.3. The overpotential at a current density was constant at the H_2 concentration ranged from 100 to 20 % and it increased with decreasing H_2 concentration from 20 to 5. The dependence of CO concentration was almost same as that of H_2. This dependence indicate that the anodic reaction determining the overpotential is Langmuir-Hinshelwood type reaction.

3-3. Relationship between anodic reactions and anodic overpotential

3-3-1. Anodic overpotential and carbon deposition by CH_4 and CO

Figure 4 shows anodic overpotentials with CH_4-H_2O, pure H_2 and 20% CO. The highest, second and the lowest overpotential at a current density were with CH_4 , CO and H_2 respectively among the three kind of fuel (CH_4, CO and H_2). The dependences of anodic overpotential on current density with H_2O-CH_4 fuel were classified into two groups, which were the high overpotential group in S/C < 1 and the low one in S/C≧1. The fuel at S/C < 1 contain CH_4. On the other hand, the fuel at S/C≧1 don't contain CH_4. The difference of overpotential between two groups could be explained by much higher carbon deposition rate of CH_4 than CO because the carbon deposition increase the anodic overpotential. Furthermore, the dependence of overpotential with S/C≧1was likely to that in H_2.

3-3-2. Anodic overpotential and the ratio of reaction rate with CO to that with H_2

The anodic overpotential should be related to the oxidation rate of fuel by oxide ion. The relationship between the anodic overpotential and the ratio of reaction rate with CO to that with H_2 was investigated at S/C≧1. The ratio of CO_2 production rate to H_2O production rate at S/C=1 was much smaller than that at S/C=1.5,2 as shown in Fig. 2. The shift reaction after the electrochemical reactions has to be considered to estimate the ratio of reaction rate with CO to that with H_2 using the CO_2 and H_2O concentration in anode exit gas. But, at least the ratio of reaction rate with CO to that with H_2 at S/C>1 is higher than that at S/C=1. Although the ratio of reaction rate was change between at S/C=1 and at S/C>1, the change did not effect on the anodic overpotentials. It is expected to be involved with the removal of carbon on three phase boundary by steam in fuel.

References

[1] T.Aida, A.Abudula, M.Ihara, H.Komiyama,and K.Yamada, Proc.of the 4th Int.Sympo.on SOFC, 801 (1995)

[2] A.Abudula, M.Ihara, H.Komiyama, and K.Yamada, Solid StateIonics 86-88 (1996) 1203.

[3] M.Ihara, A.Abudula, H.Komiyama, and K.Yamada, Proc.of the 2nd European SOFC Forum, 637 (1996).

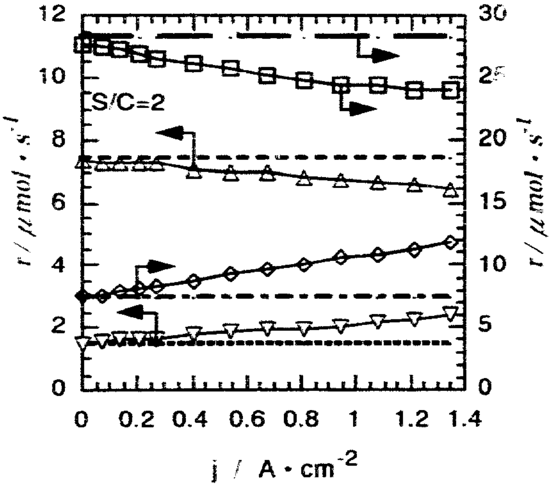

Fig.1 Reaction rate of fuel gas at S/C=2 under power generation.

(——)H_2 fed.(- - -)CO fed.(□)H_2 consumed.
(– - –)H_2O fed.(·····)CO_2 fed.(▽)CO_2 formed.
(△)CO consumed. (◇) H_2O formed.

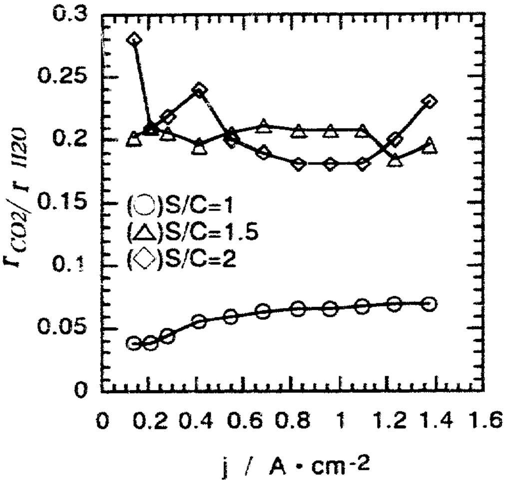

Fig.2 The ratio of CO_2 production rate to H_2O production rate versus current density

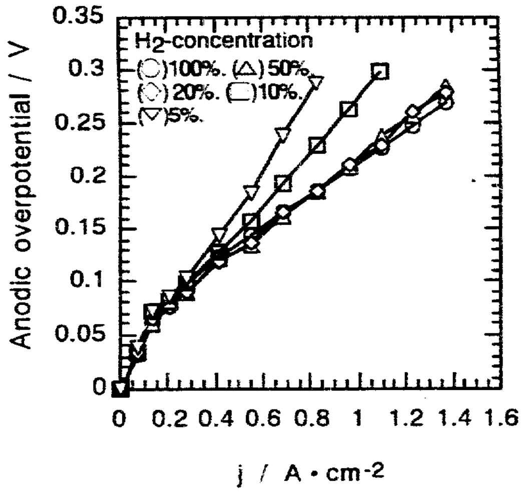

Fig.3 Dependence of anodic overpotential on hydrogen concentration in fuel.

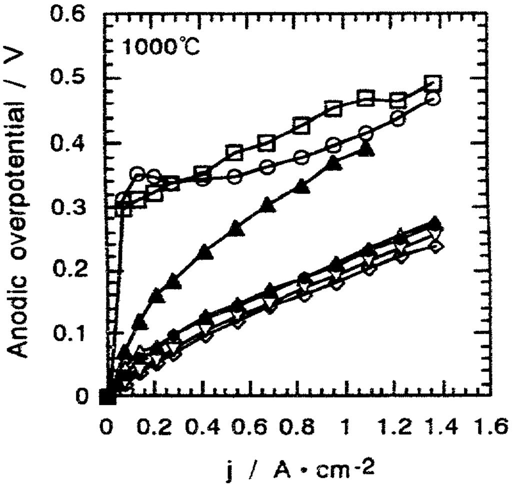

Fig.4 Anodic overpotentials with various fuels.

Fuel: (○) S/C=0. (□) S/C=0.5.
(△)S/C=1. (◇)S/C=1.5. (▽) S/C=2.
(●) H_2-100%. (▲) CO(20%)+Ar(80%).

Mixed Conducting SOFC Electrolytes

M. Gödickemeier and L.J. Gauckler

ETH-Zürich, Department of Materials, Nonmetallic Materials
CH 8092 Zürich, Switzerland

Abstract

Several mixed ionic electronic conductors exhibit a considerable ionic conductivity higher than the one of yttria stabilized zirconia, the most commonly used solid oxide fuel cell (SOFC) electrolyte material. The use of these materials would reduce the internal resistance of solid oxide fuel cells and allow for lower operating temperatures.

The tolerable amount of electronic conductivity within an electrolyte, and its influence on system design and performance are derived from a electrochemical and defect chemical model. The model is illustrated with the example of a fuel cell using ceria solid solutions as electrolytes. Model calculations for this electrolyte predict an open circuit voltage and a conversion efficiency in SOFCs which depends strongly on the thickness of the mixed conducting membrane and on the performance of the electrodes.

1. Introduction

Mixed ionic electronic conductors have not been considered as solid oxide fuel cells (SOFC) electrolytes due to their transference number. However, the commonly used electrolyte material yttria stabilized zirconia (YSZ) has a relatively low ionic conductivity.

Some mixed ionic electronic conductors (MIEC) like ceria solid solutions or δ-Bi_2O_3 exhibit an ionic conductivity which is 3 to 5 times higher than the one of YSZ [1, 2]. However, These materials are slightly reduced at low oxygen partial pressures and develop electronic conductivity besides their ionic one. The influence of this mixed conductivity in SOFCs on current-voltage characteristics was analyzed before [3] for an ideal system. Recently, also electrode contributions to the current-voltage characteristics were studied [4].

The aim of the present paper is to describe performance and efficiency of SOFC systems with mixed conducting electrolytes under real conditions, also taking into account electrode overpotential and varying electrolyte thickness. The electrolyte materials considered are mixed ionic electronic conductors which are ionic conductors at high oxygen partial pressures $p(O_2)$, but develop electronic conductivity when exposed to low $p(O_2)$ due to partial reduction. CeO_2 solid solutions with $SmO_{1.5}$ are a good example for such a material.

Experimentally, a decreasing open circuit voltage V_{OC} is found in fuel cells with mixed conducting electrolytes by reducing the thickness of the electrolyte. This finding is explained by a electrochemical and defect chemical model considering the electronic and ionic conductivity of the MIEC and the electrode overpotentials as a function of the actual operating conditions (cell voltage, applied $p(O_2)$).

2. Mixed ionic electronic conductors as SOFC electrolytes

If our mixed ionic electronic conductor is exposed to a oxygen partial pressure gradient, an ionic current will flow in direction of the $p(O_2)$ gradient and an electronic current will flow opposite (Fig. 1). Under open circuit conditions these currents are equal. The ionic current in this MIEC is driven by the oxygen chemical potential gradient. The electronic current is driven by the electric field built up between the surfaces of the MIEC facing the high and low $p(O_2)$ side according to the Nernst-equation. The total cell current, I_t, is always the sum of these ionic, I_i, and electronic, I_e, currents ($I_t=I_i+I_e$).

The driving forces for both the ionic and the electronic current obviously depend on the $p(O_2)$ on either side of the MIEC. These $p(O_2)$ are depending on the actual cell operating conditions, cell voltage (V_{Cell}) and electrode overpotential $\delta V_{th.C}$ at the cathode and $\delta V_{th.A}$ at the anode. In accorance with [4] the ionic current is expressed as:

$$I_i = \frac{V_{th.app} - V_{Cell} - \delta V_{th.C} - \delta V_{th.A}}{R_i} \tag{1}$$

The expression for the electronic current is more complex. It takes into account the dramatic changes in electronic conductivity upon a change in $p(O_2)$. It is expressed as [4]:

$$I_e = -\frac{S}{L}\left(V_{th.app} - V_{Cell} - \delta V_{th.C} - \delta V_{th.A}\right)\sigma_e^L \frac{e^{\beta q V_{Cell}} - 1}{1 - e^{-\beta q\left(V_{th.app} - V_{Cell} - \delta V_{th.C} - \delta V_{th.A}\right)}} \tag{2}$$

with

$$\sigma_e^L = \sigma_e(p(O_2)^{high})\exp\left(\frac{q\delta V_{th.C}}{kT}\right) \tag{3}$$

In Eqs. (1) and (2) $V_{th,app}$ denotes the Nernst voltage given by the applied $p(O_2)^{high}$ at the cathode and $p(O_2)^{low}$ at the anode, R_i is the ionic resistance of the MIEC, S is the effective electrode area $\beta=1/kT$ and L is the MIEC's thickness.

In electrochemical fuel cell measurements only V_{Cell} and I_t are immediately accessible to the measurement. I_i and I_e have to be calculated using Eqs. (1) - (3).

Based on Eqs. (1) - (3) the electrical conversion efficiency of a fuel cell with respect to the Gibb's free enthalpy of formation given by the difference of the oxygen chemical potentials on cathode and anode side can be expressed as:

$$\varepsilon = \frac{V_{Cell}}{V_{th,app}} \cdot \frac{I_t}{I_i} \qquad (4)$$

For the calculation of the efficiency as a function of operating conditions from Eqs. (1) to (4) we need to know:

- the electrode overpotentials as a function of the ionic current $\delta V_{\mathrm{th,C}}$ and $\delta V_{\mathrm{th,A}}$
- the electrical conductivity of the MIEC
- the geometry of the fuel cell (L, S)
- the cell operating parameters V_{Cell}, $V_{\mathrm{th,app}}$, T

3. Electrode overpotentials

The oxygen partial pressure at the edge of the mixed conductor on the cathode ($p(O_2)^L$) and anode side ($p(O_2)^0$), respectively, have a strong influence on the electrical conductivity of the MIEC. This oxygen partial pressure is defined by the electrode overpotentials which are a function of the ionic current in the MIEC (the influence of the electronic current on $\delta V_{\mathrm{th,C}}$ and $\delta V_{\mathrm{th,A}}$ is assumed to be negligible).

The electrode overpotentials can be measured either by impedance spectroscopy or by current-interruption method, by the use of a 4-electrode setup with working and reference electrodes on either side of the electrolyte. This measurement, however yields a measured overpotential η_C (cathode) and η_A (anode) versus the total current I_t. Obviously, a mixed conductor in an oxygen chemical potential gradient exhibits already a considerable ionic current even under open circuit conditions. This causes an additional overpotential which is not accessible by the above mentioned measurements. Therefore the measured data have to be transformed by converting the measured total current to I_i (Eqs. (1) - (3)) and by adding a constant to reflect the initial overpotential:

$$\delta V_{\mathrm{th,C}} = \eta_C + C \qquad \text{and} \qquad \delta V_{\mathrm{th,A}} = \eta_A + A \qquad (5)$$

The processing and measurement of electrode overpotentials is reported elsewhere [5].In Fig. (2) the overpotential of an $La_{0.84}Sr_{0.16}CoO_3$ (LSCo) cathode and an Ni-$Ce_{0.9}Ca_{0.1}O_{1.9-x}$ (NCC) anode are plotted against I_i. The solid lines are a fit indicating an electrochemical reaction mechanism including Butler-Volmer type charge transfer at the cathode and a superposition of charge transfer and diffusion of H-atoms at the anode side [6]. The electrochemical reaction mechanism is expressed by Eqs. (6) for the cathode and Eq. (7) for the anode [7].

$$\delta V_{th.C} = \frac{kT}{2q\alpha_C} \operatorname{arsinh}\left(\frac{I_i}{2I_{0.C}}\right) \tag{6}$$

$$\delta V_{th.A} = \frac{kT}{2q} \ln\left(\frac{p(H_2)}{\left((p(H_2))^{\frac{1}{2}} - A_2 I_i\right)^2}\right) + \frac{kT}{2q\alpha_A} \operatorname{arsinh}\left(\frac{I_i}{2I_{0.A}}\right) \tag{7}$$

where $I_{0,C}$ and $I_{0,A}$ are the exchange current densities at cathode and anode, respectively, α_C and α_A are the transfer coefficients $p(H_2)$ is the applied hydrogen partial pressure and A_2 is a constant.

4. Results and Discussion

4.1 Efficiency and power output

Fig. (3) shows the measured power output together with the calculated efficiency of a fuel cell with a 240 μm thick $Ce_{0.8}Sm_{0.2}O_{1.9}$ (CSO) electrolyte, a LSCo cathode and a NCC anode. The conductivity data for the electrolyte and the electrochemical parameters describing the electrodes are given in Table 1.

Electrolyte		**Cathode**	**Anode**
σ_i	3.47 S/m	Oxidant: air	Fuel: Ar-H_2-H_2O
σ_e ($p(O_2)$=0.21 atm)	$5.6 \cdot 10^{-5}$ S/m	$I_{0,C}$=0.18 A/cm^2	$I_{0,A}$=0.3 A/cm^2
σ_e ($p(O_2)=1.5 \cdot 10^{-20}$ atm)	3.47 S/m	α_C=0.45	α_A=1
			A_2=0.318 cm^{2}atm$^{1/2}$/A

Table 1 Electrical and electrochemical parameters for the electrolyte, the cathode and the anode at 700 °C.

The fuel cell exhibits a maximum power output of 0.24 W/cm^2 at a current density corresponding to about 1/2 of the short circuit current density. The maximum in efficiency (57%) is found at 1/3 of the short circuit current. The power output at maximum efficiency is 0.2 W/cm^2. Driving the cell in a current density range below the maximum in efficiency or above the maximum power output results in waste of fuel and low power output. The maximum efficiency of fuel cells with mixed conducting electrolytes is below that of fuel cells with SOFC using pure ionic conductors. They therefore might be considered for small combined heat/power co-generation systems rather than for large power plants.

4.2 Oxygen chemical potential across the MIEC

The variation of the oxygen chemical potential across the MIEC used as electrolyte can be expressed for the assumption of reversible electrodes as [6]

$$\frac{\mu(\mathrm{O}_2)(x)}{\mu(\mathrm{O}_2)(0)} = -4kT \ln\left(1 - \frac{\left(1-e^{-\frac{q}{kT}(V_{\mathrm{th,app}}-V_{\mathrm{Cell}})\frac{x}{L}}\right)}{\left(1-e^{-\frac{q}{kT}(V_{\mathrm{th,app}}-V_{\mathrm{Cell}})}\right)}\left(1-e^{-\frac{q}{kT}V_{\mathrm{th,app}}}\right)\right) \tag{8}$$

Where $\mu(O_2)(x)$ is the oxygen chemical potential at the location x across the MIEC, is the oxygen chemical potential at the anode ($x = 0$) and x/L is the dimensionless coordinate. The cathodes is at $x = L$.

For the case of non-reversible electrodes Eq. (8) has to be modified, since electrode overpotentials lead to a change in $\mu(O_2)$ at the interfaces just inside the MIEC. This jump in oxygen chemical potential is located within the electrochemical double layers at cathode and anode. The variation of $\mu(O_2)$ across the MIEC can be given for non-reversible electrodes, provided the overpotentials are known as:

$$\frac{\mu(\mathrm{O}_2)(x)}{\mu(\mathrm{O}_2)(0)} = -4kT\left\{1-\left(1-e^{-q\beta V_{\mathrm{th}}(\mathrm{MC})}\right)\frac{1-e^{-q\beta(V_{\mathrm{th}}(\mathrm{MC})-V(\mathrm{MC}))\frac{x}{L}}}{1-e^{-q\beta(V_{\mathrm{th}}(\mathrm{MC})-V(\mathrm{MC}))}}\right\}e^{-q\beta\delta V_{\mathrm{th,A}}} \tag{9}$$

where $\beta = 1/kT$. Eq. (9) describes the variation of the oxygen chemical potential where $\mu(O_2)(0)$ is the oxygen chemical potential in the fuel atmosphere.

In Fig. 4 the variation of the oxygen chemical potential versus dimensionless coordinate x/L is presented as $\log(p(O_2))$ (with $\mu(O_2) = kT \ln(p(O_2))$) using the electrode overpotential of a fuel cell with CSO electrolyte with a thickness of 239 μm, LSC cathode and NCC anode. The electrolyte parameters used for the calculations are from Table 1. Small numbers in the plot indicate the corresponding cell voltage V_{Cell} in [V]. The dotted line indicates the location of the electrolytic domain boundary (EDB) in the MIEC. At 700°C, the maximum efficiency is at a cell voltage $V_{Cell} = 0.656$ V, where ~75% of the MIEC's cross-section is predominantly ionically conducting.

4.3. Fuel cell design

By using the electrical and electrochemical data summarized in Table 1 together with Eqs. (1) to (7) we now can make predictions for the effect of the electrolyte thickness on power output and conversion efficiency of fuel cell with mixed conductors as electrolytes.

In Fig. (5) the maximum in efficiency and the corresponding power output are given in dependence of the electrolyte thickness for a fuel cell air/LSCo/ CSO /NCC/(H_2- H_2O) at 700 °C. These calculations predict a lower efficiency with decreasing electrolyte thickness. The power output also decreases at low electrolyte thickness, due to the rapid increase of the electrode overpotential at high ionic current densities. These findings are supported by experimental results which show a decreasing open circuit voltage for decreasing electrolyte thickness (i.e. increasing ionic current at V_{OC}) or for a decreasing electrode performance (i.e. higher overpotentials) [4]. From Fig. (5) the optimum electrolyte thickness can be determined for the given electrodes, if either the required maximum efficiency or the corresponding power output is specified.

6. Conclusions

Fuel cells with mixed ionic electronic conducting electrolytes exhibit high power output already at temperatures as low as 700 °C. Due to the mixed conductivity of the electrolyte they exhibit a maximum electrical conversion efficiency which is around 60%. The mixed conductivity leads to an operating range which is restricted to the current densities between maximum power output and maximum efficiency.

Model calculations predict a decrease in efficiency and power output with decreasing electrolyte thickness. To obtain an optimum fuel cell design the following procedure is suggested:

1. Determine the electrical conductivity of the MIEC as a function of $p(O_2)$.
2. Determine the electrochemical properties of the electrodes to be used (overpotentials).
3. Calculate the maximum efficiency and the corresponding power output.
4. Specify the desired power output or efficiency and determine the corresponding electrolyte thickness.

7. Acknowledgments

This work was supported by the Priority Program on Materials of the board of the Swiss Federal Institutes of Technology. Helpful discussions with I. Riess, Technion Haifa, and

Dr. A. McEvoy, Dr. J. Van Herle, EPF-Lausanne and Dr. K. Honegger, Sulzer Innotec are gratefully acknowledged.

8. References

1. T.H. Etsell and S.N. Flengas, Chem. Rev., **70**, 339 (1970).
2. N. Q. Minh, J. Am. Ceram. Soc., **76**, 563 (1993).
3. I. Riess, Solid State Ionics, **52**, 127 (1992).
4. I. Riess, M. Gödickemeier and L.J. Gauckler, Solid State Ionics, **90**, 91 (1996).
5. M. Gödickemeier, K. Sasaki, I. Riess and L.J. Gauckler, Solid State Ionics, **86-88**, 691 (1996).
6. I. Riess, J. Phys. Chem. Solids, **47**, 129 (1986).

9. Figures

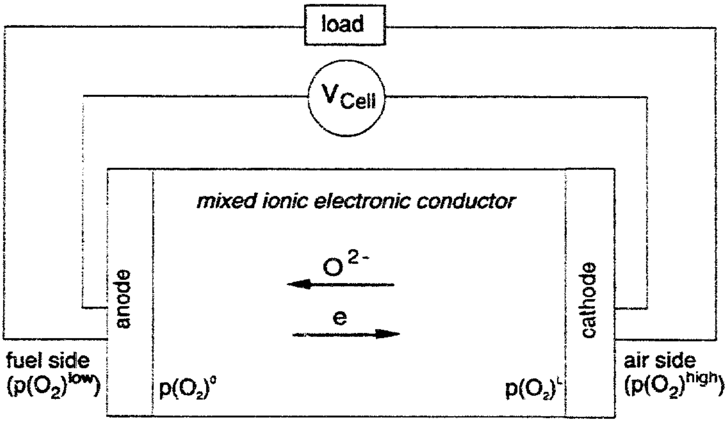

Fig. 1 Ionic (O^{2-}) and electronic (e) currents in a MIEC exposed to an oxygen partial pressure gradient. The oxygen partial pressures at the cathode and anode side are denoted as $p(O_2)^{high}$ and $p(O_2)^{low}$. $p(O_2)^L$ and $p(O_2)^0$ are the oxygen partial pressures just inside the MIEC on cathode and anode side, respectively.

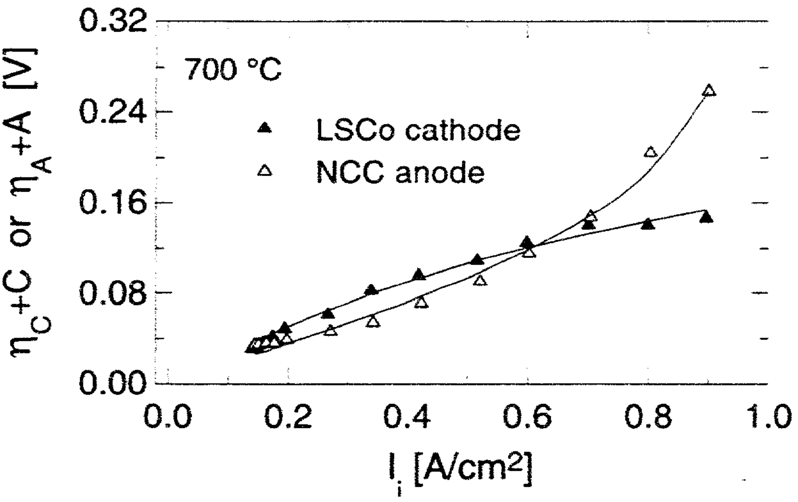

Fig. 2 Overpotential of a LSCo cathode (air) and a NCC anode (87.3% Ar + 9.7% H_2 + 3% H_2O) at 700 °C. The true overpotentials $\delta V_{th,C}$ and $\delta V_{th,A}$ versus ionic current are shown here.

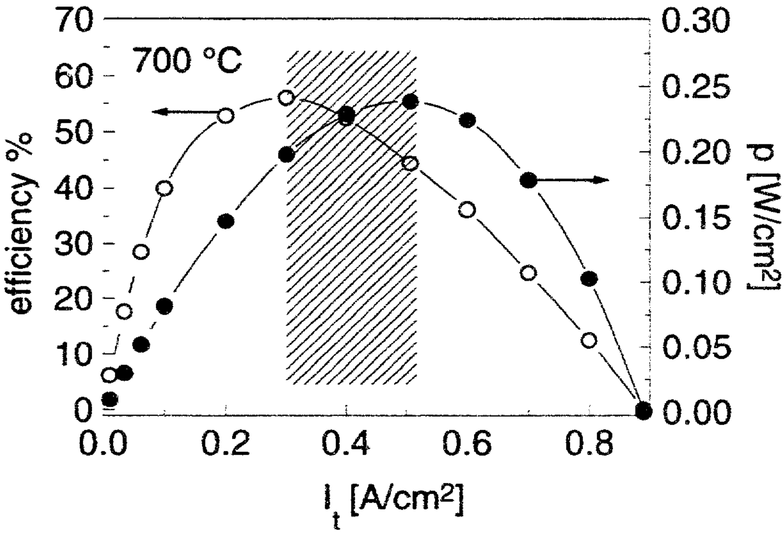

Fig. 3 Efficiency (left axis) and power output of a fuel cell (right axis) with a LSCo cathode and an NCC anode at 700 °C. The electrolyte is a $Ce_{0.8}Sm_{0.2}O_{1.9}$ membrane with a thickness of 240 μm. The shaded area indicates the useful operating range.

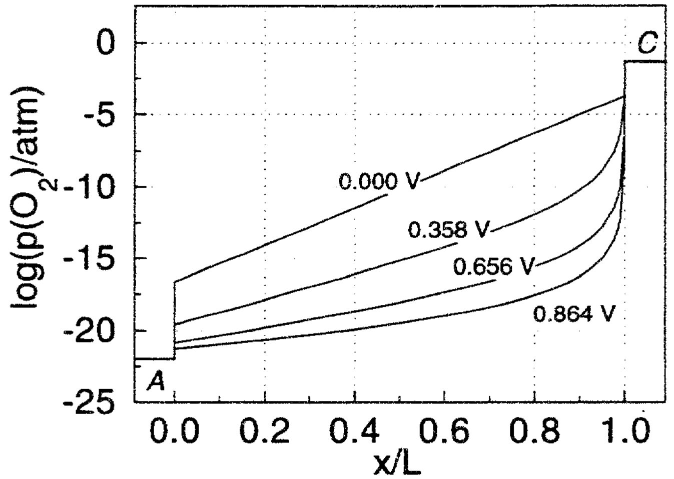

Fig. 4 Variation of oxygen chemical potential across a fuel cell with LSC cathode CSO electrolyte (239 µm) and Ni-CCO anode at 700°C. Anode side is on the left (*A*), cathode to the right (*C*). The numbers indicate the actual cell voltage in volts.

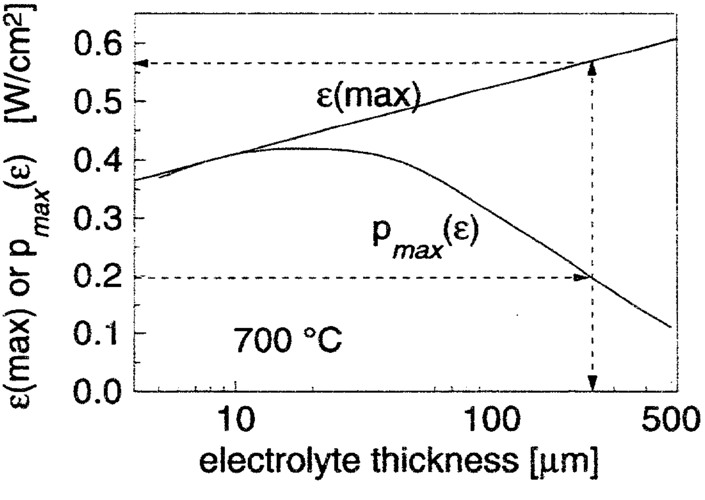

Fig. 5 Maximum efficiency and corresponding power output as a function of the thickness of the mixed conducting electrolyte. The electrochemical parameters for this calculation were taken from Table 1.

Morphology of the Pt-YSZ Interface

L. Bay and T. Jacobsen
Department of Chemistry,
Technical University of Denmark,
DK-2800, Lyngby, Denmark.

Introduction

In previous works [1,2] it has been shown that the SOFC cathode reaction on the platinum-zirconia interface exhibits a pronounced inductive hysteresis. The phenomenon is illustrated by the sequence of linear potential sweeps shown in fig. 1. Taking the fact that $RT/F=110$ mV at 1000°C into consideration the current voltage relation is very non-linear and a notable inductive hysteresis is seen. Decreasing the sweep rate the current increases, contrary to the normal behaviour of simple electrode reactions. Furthermore, it has been argued on the basis of the large time constants and charges involved, that this deactivation of the electrode at equilibrium and corresponding activation when the electrode is polarized can not be due to accumulation of catalytic active intermediates. Hence, it is not an inherent property of the reaction mechanism. And so far the effect has not been understood.

When the electrode reaction itself is excluded as responsible for the phenomenon another suggestion might be a modification of the three-phase boundary, induced by the transfer of oxygen ions across the Pt-YSZ interface. After all the main volume constituent of zirconia is the mobile oxygen ions. To investigate this possibility an Atomic Force Microscopy (AFM) study of electrode and electrolyte surfaces was carried out for platinum point electrodes.

Part of the investigation is described in more detail elsewhere [3]

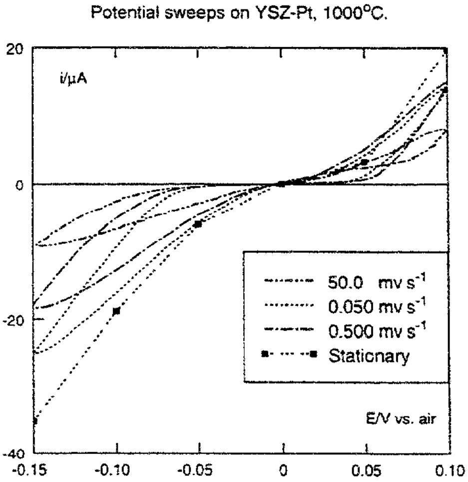

Figure 1: Linear sweep voltammetry for Pt-YSZ point electrode in air at 1000°C. Contact area ~ $3 \cdot 10^{-4}\,\mathrm{cm}^2$. Sweep rates and steady state potentials as given in inserts.

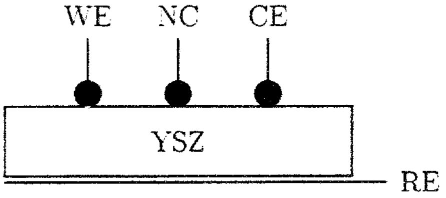

Figure 2: Eksperimental setup. WE cathode, CE anode, NC equilibrium electrode, i=0

Experimental

Three ball shaped Pt point electrodes were mounted on the surface of a 8 mol% Y_2O_3 stabilized zirconia disk (Viking Chemicals) furnished with a separate Pt-paint reference electrode as outlined in fig. 2. After heating to 1000°C in air one of the electrodes, WE, was polarized to -0.15 V vs. air under potentiostatic control. During polarization the counter electrode, CE, was driven to an anodic overvoltage not exceeding 0.12 V. The third electrode serving as a blind was not connected. 50 hours later the oven was cooled down, the electrodes were removed from the disk and the surface was inspected by Atomic Force Microscopy (AFM).

Results and discussions

Fig. 3 shows AFM images from the YSZ surface recorded on the edge of the Pt-YSZ contact zone for the three electrodes. For the unpolarized electrode in fig. 3a-b it is seen that both the YSZ and the Pt surface are fairly smooth. This is in contrast to the pictures of the interface at the cathode shown in fig. 3c-d. Here the Pt surface has apparently been bonded to the zirconia, and EDX-analyzes reveals grains torn from the other phase to adhere to the surface. However, along the three-phase boundary a border of YSZ peaks has grown from the bulk. The width is around 5μm and the height 0.5μm. The composition determined by EDX can not be destinguished from that of the surface further away from the contact point and does not show any presence of Pt. Below the Pt anode (fig. 3e-f) a big crater in the YSZ surface was found. Again a rim of YSZ surrounds the contact zone. But, unlike that of the cathode it is shallow with a width of 5-20μm and 0.1μm high.

Apparently the reaction at the electrodes implies a modification of the electrode-electrolyte interface. Impedance measurements show a large low frequency capacity at anodic potentials which can be explained by the presence of a gas volume in the interface. If this volume is evolving when current is passed across the interface and forms a channel structure it may extent the triple-phase boundary considerably. Since the transport of zirconia is slow this activation process will have large time constants in accordance with the experimental observations [2]. Reshaping of the structure interface at porous (La, Sr)MnO_3 electrodes on YSZ has recently been reported by Mitterdorfer et al. [5,6]. They identified a phase of $La_2Zr_2O_7$ growing from the zirconia at the interface, which may originate from interdiffusion of the phases rather than the electrode process itself.

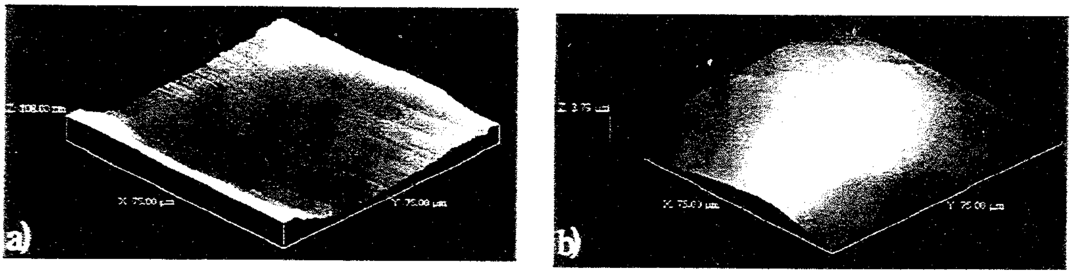

Unpolarized YSZ surface

Unpolarized Pt electrode

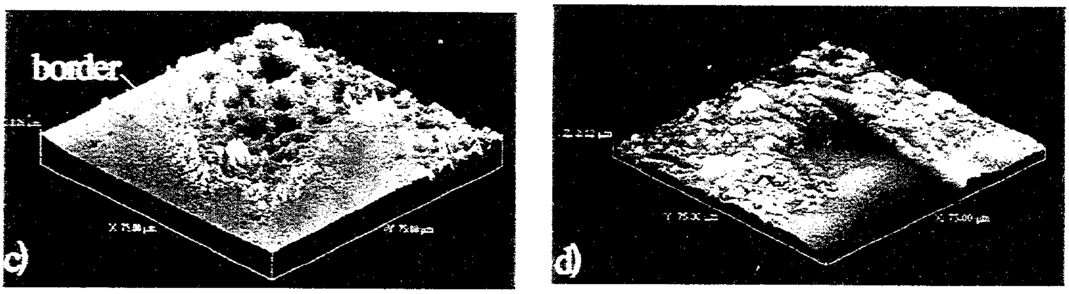

YSZ surface at the cathode

Pt cathode

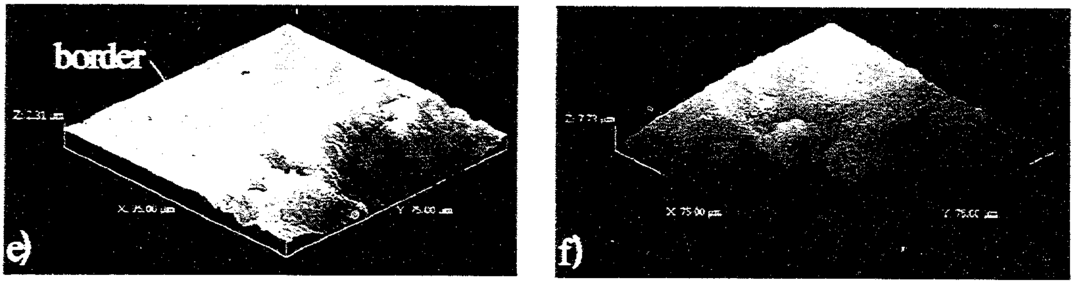

YSZ surface at the anode

Pt anode

Figure 3: AFM images from the electrode-electrolyte configuration shown in fig. 2 after polarisation for 50 hours at 1000°C.

The change in the surface structure could a reversible phenomenon - in the sence that surface forces would smoothen the "mountains" under no load conditions - depending on the mobility of the surface. To investigate this possibility, surface structures prepared at anodic as well as cathodic conditions were annealed at 1000°C for 35 hours. The following AFM investigation did not show any significant effect of the annealing process.

Conclusions

It has been shown that the electrode-electrolyte interface is a dynamic entity, the structure of which changes during the passage of charge, whereas it is stable without current. At present the driving force for these modifications of the surface close to the triple phase boundary has not been identified and it is still an open question whether the phenomenon is responsible for the activation-deactivation of the SOFC cathode.

References

1. T. Jacobsen, B. Zachau-Christiansen, K. West and S. Skaarup, *2nd Nordic Symp. on High Temp. Fuel Cells*, Geilo, Norway 1994, pp. 139-145.
2. T. Jacobsen and B. Zachau-Christiansen, *IEA, 7th SOFC Workshop* , Wadahl, Norway, January 1995, pp. 7-12.
3. L. Bay and T. Jacobsen, *Solid State Ionics*, In press.
4. P. Fabry and M. Kleitz, *J. Electroanal. Chem.* 57 (1974) 165-177.
5. A. Mitteldorfer, M. Cantoni and L.J. Gauckler, *Proc. 2nd European Solid Oxide Fuel Cell Forum*, Oslo, Norway 1994, pp. 373-382.
6. A. Mitteldorfer, M. Cantoni and L.J. Gauckler, *Proc. 17th Symp. on Materials Science: Electrochemistry Ceramics and Metals*, Riso National Laboratory, Roskilde, Denmark 1996, pp. 357-362.

New Experimental Approaches to Electrochemical Kinetics on Solid Oxide Electrolytes

Tatsuya KAWADA, Koichi MASUDA, Atsushi KAIMAI, Ken-ichi KAWAMURA,
Yutaka NIGARA, and Junichiro MIZUSAKI,
Research Institute for Scientific Measurements, Tohoku University
2-1-1 Katahira, Aoba-ku, Sendai 980-77 JAPAN
Hiroo Yugami and Haruo Arashi,
Faculty of Engineering, Tohoku University
Aramaki, Aoba-ku, Sendai 980-77 JAPAN
Teruhisa HORITA, Natsuko SAKAI, Harumi YOKOKAWA and Masayuki DOKIYA
National Institute of Materials and Chemical Research
Tsukuba Research Center, Tsukuba, Ibaraki 305, JAPAN

ABSTRACT

Some attempts were made to investigate the electrochemical reaction kinetics on solid oxide electrolytes. Electrodes of well defined structure were prepared to eliminate the effect of electrode morphology. Isotope exchange experiments combined with three dimensional SIMS analysis were carried out to visualize the distribution of preferable electrochemical reaction sites on the electrolyte. In-situ measurements of oxygen potential on an electrode surface was attempted by using a porous oxygen sensor. Several examples of the measurements are reviewed.

INTRODUCTION

Steady state polarization measurement and impedance spectroscopy are the most general techniques to study electrode reaction kinetics for various electrochemical systems. Recently, in-situ techniques have been developed to observe electrode surface using optical spectroscopy or probe microscopes. However, experimental techniques are limited for a solid oxide fuel cell electrode since it must be operated at high temperature. The authors have been making attempts to develop new experimental techniques which give further information than usual dc/ac polarization measurements.

A characteristic feature of a solid oxide electrolyte / electrode system is that the electrochemical reaction site is not uniformly distributed around the interface. Triple phase boundary (TPB) is the most active reaction site where gaseous species, ions, and electrons meet together. However, the reaction site can expand from TPB to a wider area on the electrolyte and/or on the electrode surfaces according to mass transport properties. As Kleitz et al.[1)] have suggested, misunderstanding of the reaction pathway may lead to a wrong result in a kinetic study. Thus, it is important to determine the mass flow path and the location of the reaction site by an experimental method. The following techniques have been attempted for that purpose; (1) use of an electrode of a well defined structure, (2) visualization of ionic current flow around the electrode, (3) in-situ measurement of oxygen potential on the working electrode. Some results obtained with those methods are reported.

USE OF A WELL DEFINED ELECTRODE

In a practical SOFC, porous electrodes are used in order to obtain large current density. However, a simpler electrode is preferred to perform the kinetic studies in a quantitative way.

mixed conductor oxide electrode

As for mixed conductor oxide electrodes, dense film electrodes were used in several reports[2,3)] to study kinetics. Recently, the authors have succeeded in making a dense $(La,Sr)CoO_3$ electrode by a laser ablation method. By comparing the electrodes of different thickness, the following three results were obtained.

[1] The electrode resistance did not depend on the electrode thickness.

[2] The electrode capacitance was proportional to the electrode thickness and was attributed to the nonstoichiometry change of the electrode material.

[3] The electrode resistance showed a large temperature dependence.

The result [1] means that the oxide ion diffusion in the electrode bulk is fast enough and is not the rate determining step. The result [2] suggests that the oxygen potential gap is located at the surface of the electrode or in the gas phase. From the result [3], gas phase diffusion is not the rate determining step since the temperature dependence of gas phase diffusion is small. Therefore, it is concluded in a distinct way that the surface reaction on the electrode is the rate determining step. The kinetic parameters for the surface reaction rate can be obtained quantitatively since the surface area can be measured easily.

metal electrode

Kinetic study for a metal electrode (electronic conductor electrode) is much more difficult than for the mixed conductor electrode. Attempts have been made to control the length of TPB by using a point contact electrodes 1-4). Most of those electrodes, in actual, are not real "point" electrodes. They have rather large contact area with the electrolytes. In the analysis with such electrodes, current distribution inside the electrolyte is important. When high frequency ac current is applied to the electrode, current will distribute under all the contact area of the electrode / electrolyte boundary. On the contrary, dc current will be concentrated into the triple phase boundary. If the electrolyte impedance is estimated from the high frequency intercept of the complex impedance plot, the remaining part which is usually treated as the electrode impedance will include the electrolyte impedance due to the current concentration. The additional electrolyte impedance is a function of the width of active reaction site around TPB. It was calculated by finite element method and plotted in Figs. 1(a) and 1(b) for the electrodes of different shapes. In case of the point contact electrode (0.4 mm in diameter), the additional impedance is as large as 100 Ω when the reaction site width is less than 1μm. This effect should be taken into consideration in the data analysis. Another approach is to make an electrode of finer dimension. Mizusaki et al.6) used a patterned Ni electrode made by ion cluster beam and photo risography. From the calculation, the electrode of the line patterns, 20μm width and 20μm blank, shows much smaller additional impedance. The effect of the current concentration is negligible if the electrode resistance is larger than $1\Omega cm^2$.

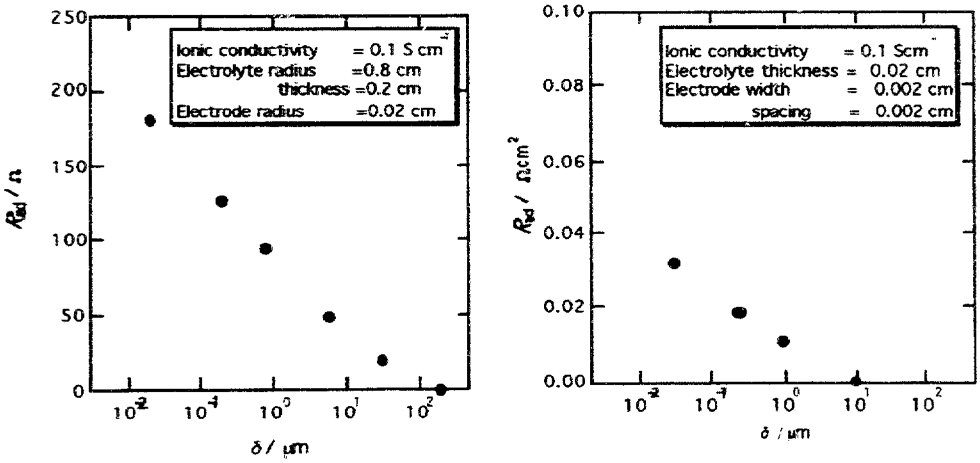

(a) (b)

Fig. 1 Calculated "additional" electrolyte resistance in an "electrode arc" in a complex impedance plot. It appears due to the different current distribution under ac and dc conditions. These are the result of FEM calculations for (a) point contact electrode (0.4mm in diameter) and (b) line pattern electrode (20μm width / 20μm interval). Uniform electrochemical potential of oxide ion was assumed in the length δ from TPB.

ISOTOPE EXCHANGE AND SIMS ANALYSIS

In oxide materials, oxygen isotope diffusion coefficients have been measured by using ^{18}O as a tracer. Secondary ion mass spectrometer (SIMS) is a powerful tool to analyze the isotope profile. From the profile, both the isotope diffusion coefficient and the surface isotope exchange rate can be obtained. The surface isotope exchange coefficient and the electrochemical impedance can be correlated if a reaction model is assumed.

Sirman and Kilner et al.[6] have been applying this method extensively to many oxide systems. Recently, they reported that the surface reaction rate of CeO_2 was enhanced by addition of porous $(La,Sr)(Co,Fe)O_3$ electrode. The present authors have obtained a preliminary results with dense $(La,Sr)CoO_3$ electrode on CeO_2-CaO electrolyte. As mentioned above, the electrochemical measurements suggested that the rate determining step for this electrode is surface reaction. This was confirmed by isotope exchange / SIMS analysis. Fig. 2 shows the depth profile obtained for oxygen isotope and other metal elements. The isotope concentration is almost constant in this depth range, but much smaller than in the gas phase (98%). Together with the deeper diffusion profile in the electrolyte, the surface reaction rate was obtained.

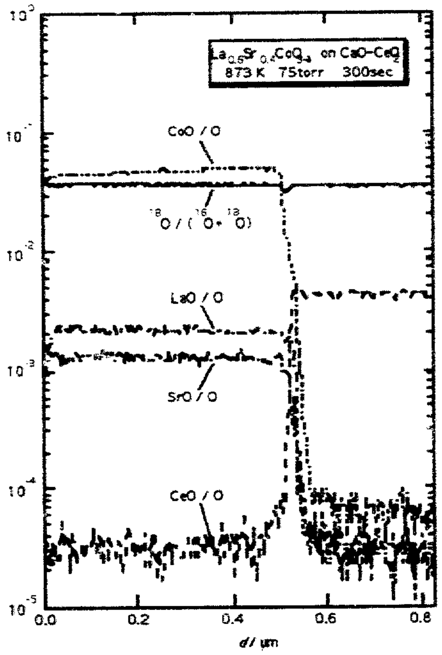

Fig.(2) Depth profile of oxygen isotope and metal elements obtained by SIMS. The sample, $La_{0.6}Sr_{0.4}CoO_3$ electrode (0.5mm) on CeO_2-10mol%CaO electrolyte, was treated at 873 K in 75 torr $^{18}O_2$ (98%) for 300 sec.

Isotope diffusion / SIMS analysis can be applied also to determine the location of the reaction site on the electrolyte surface. Kawada et al.[7] have attempted to visualize the active reaction site in porous Pt /YSZ system. Though bulk diffusion of oxygen is fast in YSZ, the surface reaction rate is slow without catalyst. This results in a small concentration of isotope at the surface during isotope exchange reaction. The surface isotope concentration varies with the existence of a catalyst or an electrode. If TPB is the preferable reaction site, the isotope concentration at TPB will be higher than that in the other parts. By applying cathodic current, the contrast of the isotope concentration will be enhanced. If the sample is quenched quickly, the isotope concentration profile will maintain the information about the active reaction site. Fig. 3 shows the secondary ion images for $^{16}O^-$ and $^{18}O^-$ at the surface of the sample which was treated under cathodic overvoltage (-0.5V) in $^{18}O_2$ (50torr) atmosphere. The dark part in the $^{16}O^-$ image is the place covered with Pt electrode particle. It is found that $^{18}O^-$ is distributed at the peripheries of the Pt particles, which means that the active reaction site is distributed around TPB. More quantitative analysis will be possible if the electrode morphology is controlled.

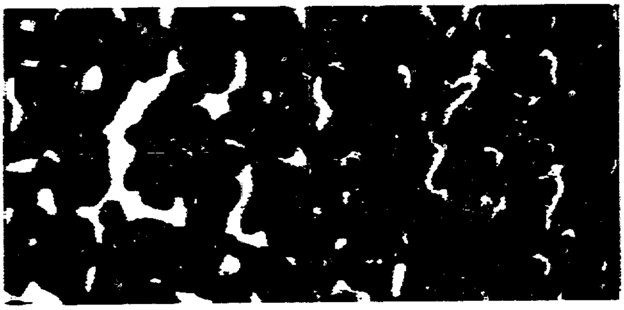

(a) $^{16}O^-$ (b) $^{18}O^-$

Fig. 3 Oxygen isotope distribution at the surface of the porous Pt / YSZ treated at 973 K in 50 torr $^{18}O_2$ (98%) for 300 sec under cathodic polarization (η=-0.5V). The scanning area is 50mm x 50mm. Cs+ primary ion beam (0.3μm in diameter) was used.

MEASUREMENT OF SURFACE OXYGEN POTENTIAL

In-situ observation of the electrode surface gives many information on the electrode kinetics. The authors have reported that the surface oxygen potential on an electrode can be detected by a potentiometric method using a porous oxygen sensor (POS). Fig.4 shows a schematic view of the in-situ measurement of surface oxygen potential. The highly porous pellet of YSZ or doped CeO2 was placed on the working electrode. A reference Pt electrode was formed on the upper side of the porous sensor. If the oxygen potential at the electrode surface was out of equilibrium during the polarization, it is detected as the emf over POS.

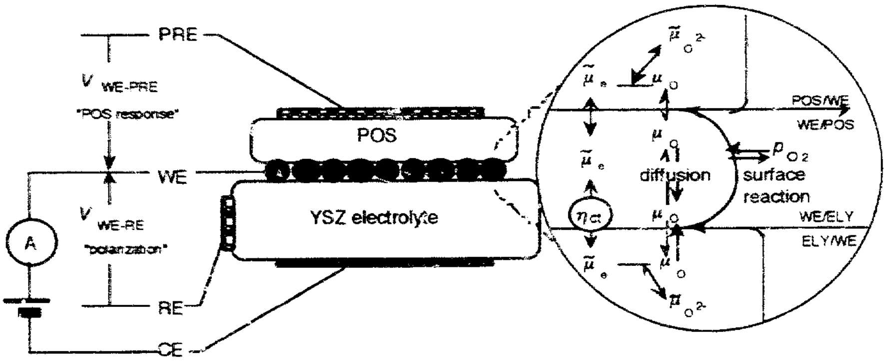

Fig. 4 Schematic diagram of surface oxygen potential measurement with a porous oxygen sensor (POS).

Kawada et al.[8] have applied this method to investigate porous Pt electrodes and Ni, Pt or other metal wire electrodes. The other example of the POS measurement is shown in Fig.5, which are obtained with the dense (La,Sr)CoO_3 electrode. In this case, doped CeO_2 was used as the sensor material to avoid the reaction with the electrode material. In Fig.5, the large response was observed on POS as expected from the impedance analysis and isotope exchange / SIMS analysis. At higher temperature, the POS response was close to the polarization potential which means that the electrode overvoltage comes from the deviation of the surface oxygen potential due to the slow surface reaction. At the lower temperature, however, the deviation of the POS and the electrode potential was large. There may be some potential barrier for the adsorbed oxygen to be incorporated into the electrode layer.

(ACKNOWLEDGMENT This work has been carried out as a research project of The Japan Petroleum Institute commissioned by the Petroleum Energy Center with the subsidy of the Ministry of International Trade and Industry.)

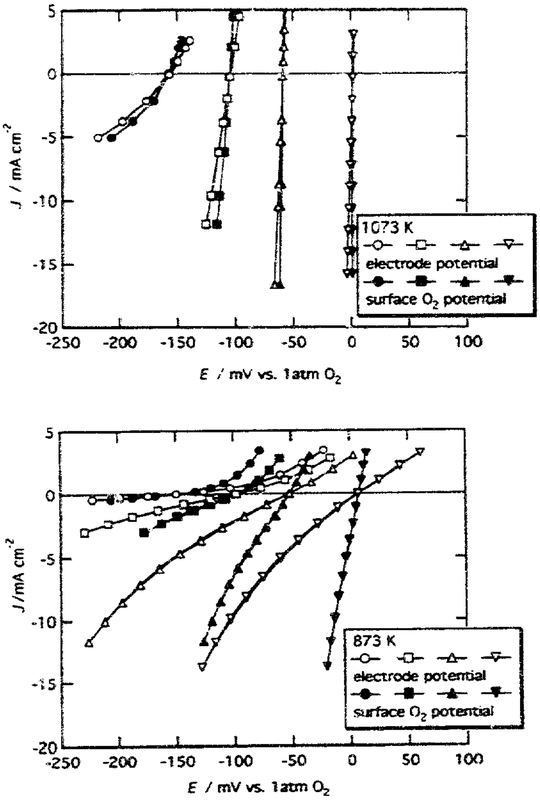

TFig. 5 Polarization curve (open symbols) and the surface oxygen potential measured by POS (closed symbols) for dense $La_{0.6}Sr_{0.4}CoO_3$ electrode on CeO_2-10mol%CaO at 1073 K and 873 K.

REFERENCES

1) M.Kleitz,et al., Proc.2nd European SOFC Forum, Oslo, edt. B.Thorstensen, pp.579 (1996)
2) J.Mizusaki et al., Proc. 14th Riso Intern. Symp. Mater. Sci., edt. F.W.Poulsen et al. pp. 343 (1993)
3) A.Momma, et al., Proc. Intern. Fuel Cell Conference, Tokyo, NEDO, pp381 (1992)
4) T.Horita, et al., Proc. 17th Riso Intern. Symp. Mater. Sci., Roskilde, Edt. F.W.Poulsen et al. pp.417 (1996)
5) J.Mizusaki et al., J. Electrochem. Soc., 141(8), 2129 (1994)
6) J.D.Sirman and J.A.Kilner, Proc. 17th Riso Intern. Symp. Mater. Sci., Roskilde, Edt. F.W.Poulsen et al. pp.417 (1996)
7) T.Kawada et al., to be published in Proc. PacRim2, Kairns, Australia 1996
8) T.Kawada et al., Solid State Ionics 70/71., 65(1994)

The IEA Advanced Fuel Cells Programme

Background

The International Energy Agency (IEA) Implementing Agreement for a programme of research, development and demonstration on advanced fuel cells was signed by seven countries in Paris on April 2nd, 1990. Since that time a further eight countries have signed the Implementing Agreement and the programme has grown from two to ten annexes. Each annex defines a different task and is managed by an Operating Agent.

The aim of the IEA Advanced Fuel Cells programme is to advance the state of understanding of all Contracting Parties in the field of advanced fuel cells. It achieves this through a co-ordinated programme of research, technology development and system analysis on Molten Carbonate (MCFC), Solid Oxide (SOFC) and Polymer Electrolyte Fuel Cell (PEFC) systems.

There is a strong emphasis on information exchange through Task meetings, workshops and reports. The work is undertaken on a task-sharing basis with each participating country providing an agreed level of effort over the period of the Task.

Participants

There are currently fifteen signatories to the Implementing Agreement: Australia, Canada, Denmark, France, Germany, Italy, Japan, Netherlands, New Zealand, Norway, Spain, Sweden, Switzerland, United Kingdom, United States, and the programme continues to actively encourage new participants.

Programme (1990-1995)

The first phase of the programme ran from April 1990 to December 1995 and comprised the following tasks.

Annex I	Molten Carbonate Fuel Cell Balance of Plant Analysis
Annex II	Solid Oxide Fuel Cells Modelling and Evaluation
Annex III	Molten Carbonate Fuel Cell Materials and Electrochemistry
Annex IV	Polymer Electrolyte Fuel Cells
Annex V	Systems Analysis

New Programme (1996-1998)

During 1996, the programme initiated five new tasks which form a co-ordinated programme for the period 1996-1998 covering fuel cell technology and its potential applications in stationary power generation and transport. The new tasks are as follows:

Annex VI	Molten Carbonate Fuel Cells under Real Operating Conditions
Annex VII	Solid Oxide Fuel Cells under Real Operating Conditions
Annex VIII	Polymer Electrolyte Fuel Cells
Annex IX	Fuel Cell Systems for Stationary Applications
Annex X	Fuel Cell Systems for Transport Applications

IEA Advanced Fuel Cells Programme 1996-1998

No.	Annex	Subtasks and Activities	Operating Agent	Participating Countries
VI	MCFC Under Real Operating Conditions	1 Stack Performance and Endurance 2 Test Procedures and Standardisation 3 Development of Balance of Plant Technology	Dr L Plomp ECN The Netherlands	Germany Italy Japan Netherlands
VII	SOFC Under Real Operating Conditions	1 Balance of Plant Technology 2 Stack and Cell Operating Conditions 3 Materials Under Operating Conditions 4 Materials Innovation	Dr H Nabielek KFA Jülich Germany	Australia Denmark France Germany Japan Netherlands New Zealand Norway Switzerland UK USA
VIII	PEFC	1 Improved Single Cells 2 Improved Stack Materials and Concepts 3 Operating Parameters: Effects on Performance and Lifetime 4 Balance of Plant Components and Systems 5 Direct Methanol Fuel Cell	Dr R Kumar Argonne National Laboratory USA	Canada Germany Italy Japan Netherlands Switzerland UK
IX	Fuel Cell Systems for Stationary Applications	1 Parameters Affecting the Economy and Competitiveness of Fuel Cells 2 Current Technology Level to Commercialisation 3 Environmental Analysis	Mr L Sjunnesson Sydkraft AB Sweden	Germany Italy Japan Netherlands Norway Sweden
X	Fuel Cell Systems for Transport Applications	1 Economics and System Analysis 2 Balances of Life Cycles 3 Fuel Supply Systems	Dr B Höhlein KFA Jülich Germany	Germany Netherlands USA

Volume II

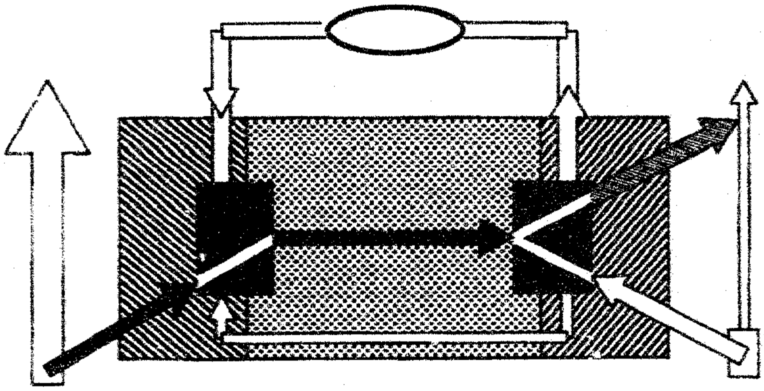

IEA Programme of R, D & D on Advanced Fuel Cells

Annex VII: Solid Oxide Fuel Cells
under Real Operating Conditions

Materials and Processes

10th SOFC WORKSHOP

A J McEvoy and K Nisancioglu

Date 28-31 January 1997 Les Diablerets, CH

INTERNATIONAL
ENERGY AGENCY

IEA Annex VII "SOFC under Real Operating Conditions" 1996-98

The main objective will be to assist - through international cooperation - the development of natural gas-fuelled Solid Oxide Fuel Cell (SOFC) technologies through:

(a) the exchange of information to tackle complex problems in stack and systems design and operation;
(b) the consideration of end-user requirements on stack operation with the goal to optimise lifetime of cells and stacks;
(c) a better understanding of interfacial and bulk charge and mass transport mechanisms to optimise cell components under actual SOFC operating conditions; and
(d) the study of alternative materials in case traditional concepts are too expensive or are too short-lived.

Participating countries are Australia, Denmark, France, Germany, Japan, Netherlands, New Zealand, Norway, Switzerland, United Kingdom, United States. The work in the Task is divided into the following four Subtasks:

Subtask 1: "Balance-of-Plant Technology"
Activity 1.1 "Balance-of-Plant Optimisation by Modelling"
Tackle complex problems in stack and systems modelling by exchange of information. Main Workshop September 1996.
Activity 1.2 "SOFC Activities World-Wide"
Establish an information directory to encourage information exchange on critical aspects of SOFC development (1996, update 1998).
Activity 1.3 "Regulatory Requirements"
Collection of legal, utility and user regulations for installing and operating SOFC plant with the goal to provide SOFC system design code and statutory regulation compliance.

Subtask 2: "Stack and Cell Operating Conditions"
Activity 2.1 "Stack Operating Experience and Evaluation"
Enable comparison of stack performances on a common basis.
Activity 2.2 "Lifetime of Cells": Evaluate effects of operating conditions typical for end-user applications with the goal to improve and demonstrate SOFC lifetime. Main Workshop October 1997.

Subtask 3: "Materials under Operating Conditions"
Develop a better understanding of interfacial/ bulk charge and mass transport mechanisms to optimise cells under actual SOFC operating conditions. The emphasis will be on novel designs and performance of components based on relatively well known materials. Main Workshop January 1997.

Subtask 4: "Materials Innovation"
Develop and qualify new SOFC materials for long-term stability and reduced manufacturing costs. Investigate materials for low-temperature operation < 800°C (Catalogue January 1997, main Workshop May 1998).

Dr. Heinz Nabielek from the Research Centre Jülich, Germany, acts as Operating Agent.

Volume II

IEA Programme of R, D & D on Advanced Fuel Cells

Annex VII: Solid Oxide Fuel Cells
under Real Operating Conditions

Materials and Processes

10th SOFC WORKSHOP

A J McEvoy and K Nisancioglu

Date 28-31 January 1997 Les Diablerets, CH

INDEX

IEA Workshop: "Materials and Processes"

Annex VII: SOFC under Real Operating Conditions

January 28 - 31 , 1997
Les Diablerets, Switzerland

in Volume I

Volume II

Corrosion of the Cathode/Electrolyte Interface by Chromium Forming Alloy Interconnects in a Solid Oxide Fuel Cell

SPS Badwal, R Deller, K Foger, Y Ramprakash and JP Zhang

Ceramic Fuel Cells Limited
710 Blackburn Road
CLAYTON VIC 3168
AUSTRALIA

Interconnect Materials and Requirements

Materials : Ceramics, alloys and cermets
Requirements :

- High density, no open porosity impervious to gases to avoid mixing of air and fuel.
- High electronic conductivity to avoid short circuiting.
- High thermal conductivity (above 20 W/mK).
- High creep resistance .
- Stability in both oxidising and reducing environments at 900-1000°C.
- Low thermal expansion mismatch with other fuel cell components
  (TEC for other fuel cell components : 10-12 x 10^{-6} K^{-1})

Ceramic Interconnect fulfils most of the requirements except for thermal conductivity whic [illegible] w [illegible] and imposes severe thermal gradients in the fuel cell stack, and it has different thermal ex [illegible] in oxidising and reducing environments imposing stresses on the material itself. Also cost of [illegible] fabrication for Ceramic interconnect is relatively high.

Metals are preferred due to their high thermal conductivity leading to uniform heat di [illegible] n.

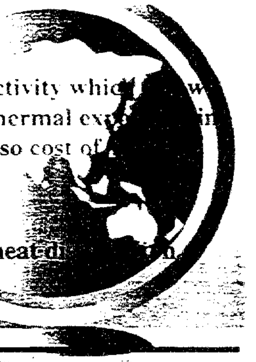

Materials and Conditions

Cathode :	**LSM**
Electrolyte :	**TZ3Y**
Anode :	**Ni-Zirconia**
Interconnect :	**$Cr5Fe1Y_2O_3$ (Plansee-Siemens)**
Oxidant :	**Air**
Fuel :	**H_2 - 3% H_2O**
Temperature Range :	**900 - 1000 ° C**
Evaluation Time :	**Several hundred to three thousand hou**

Problems with Metallic Interconnect

- High coefficient of thermal expansion, much higher that other fuel cell components.
- High creep rates.
- High corrosion rates.
- Need to use high temperature oxidation resistance alloys with built in protection mechanism and/or protective coatings are required.

High temperature oxidation resistant alloys

- Chromia forming alloys (reasonable electrical conductivity).
- Alumina forming alloys (insulator).
- Silica forming alloys (insulator).

Alumina and silica forming alloys cannot be used as these form insulating layer in the conduction path.

For this reason chromia forming alloys are preferred.

Also high chromium content alloys have coefficient of thermal expansion c other fuel cell components.

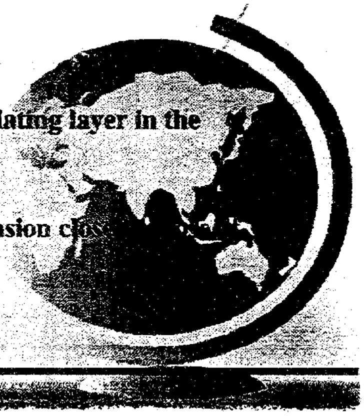

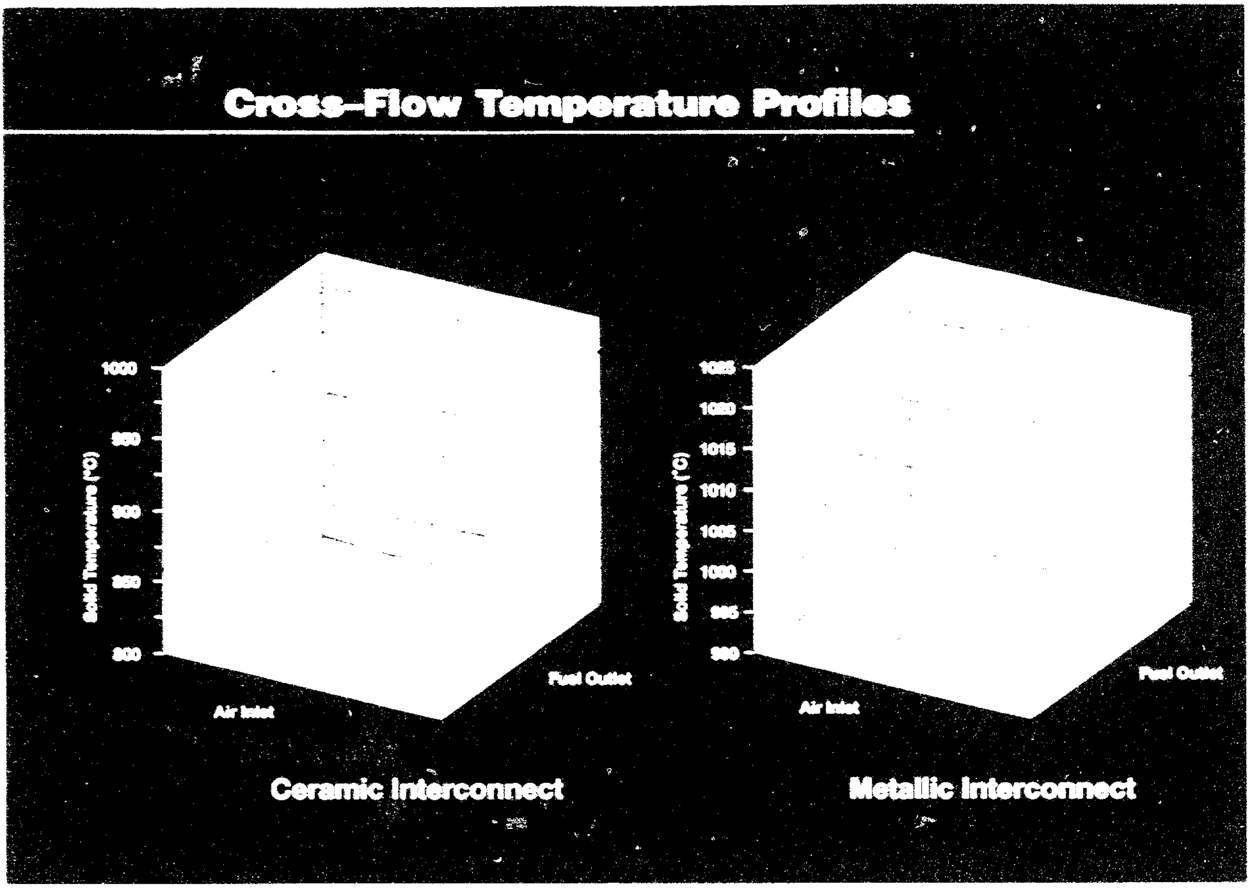

Cross-Flow Temperature Profiles

Ceramic Interconnect

Metallic Interconnect

Electrochemical Experiments

- Cell Evaluation
  - 50 mm x 50 mm single cells
  - with and without the interconnect in contact with electrodes
- Galvanostatic Current Interruption
  - Half cells (no fuel electrode) - 12 mm dia cells
  - Pt - counter and reference electrodes
  - With and without LSM in contact with the interconnect
- Impedance Studies
  - Half cells (no fuel electrode) - 12 mm dia cells
  - Pt - counter and reference electrodes
  - With and without LSM in contact with the interconnect

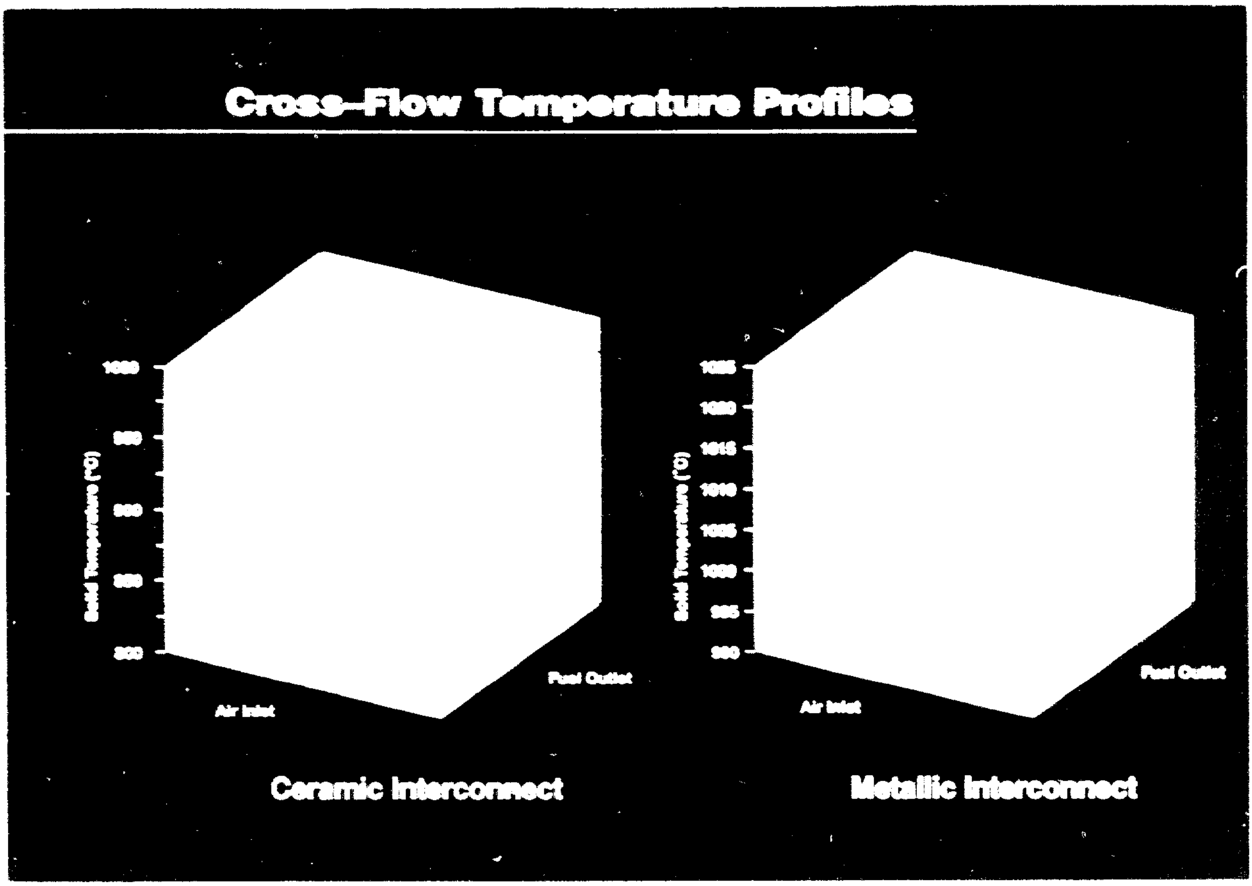

Cross-Flow Temperature Profiles

Ceramic Interconnect

Metallic Interconnect

Electrochemical Experiments

- Cell Evaluation
  - 50 mm x 50 mm single cells
  - with and without the interconnect in contact with electrodes
- Galvanostatic Current Interruption
  - Half cells (no fuel electrode) - 12 mm dia cells
  - Pt - counter and reference electrodes
  - With and without LSM in contact with the interconnect
- Impedance Studies
  - Half cells (no fuel electrode) - 12 mm dia cells
  - Pt - counter and reference electrodes
  - With and without LSM in contact with the interconnect

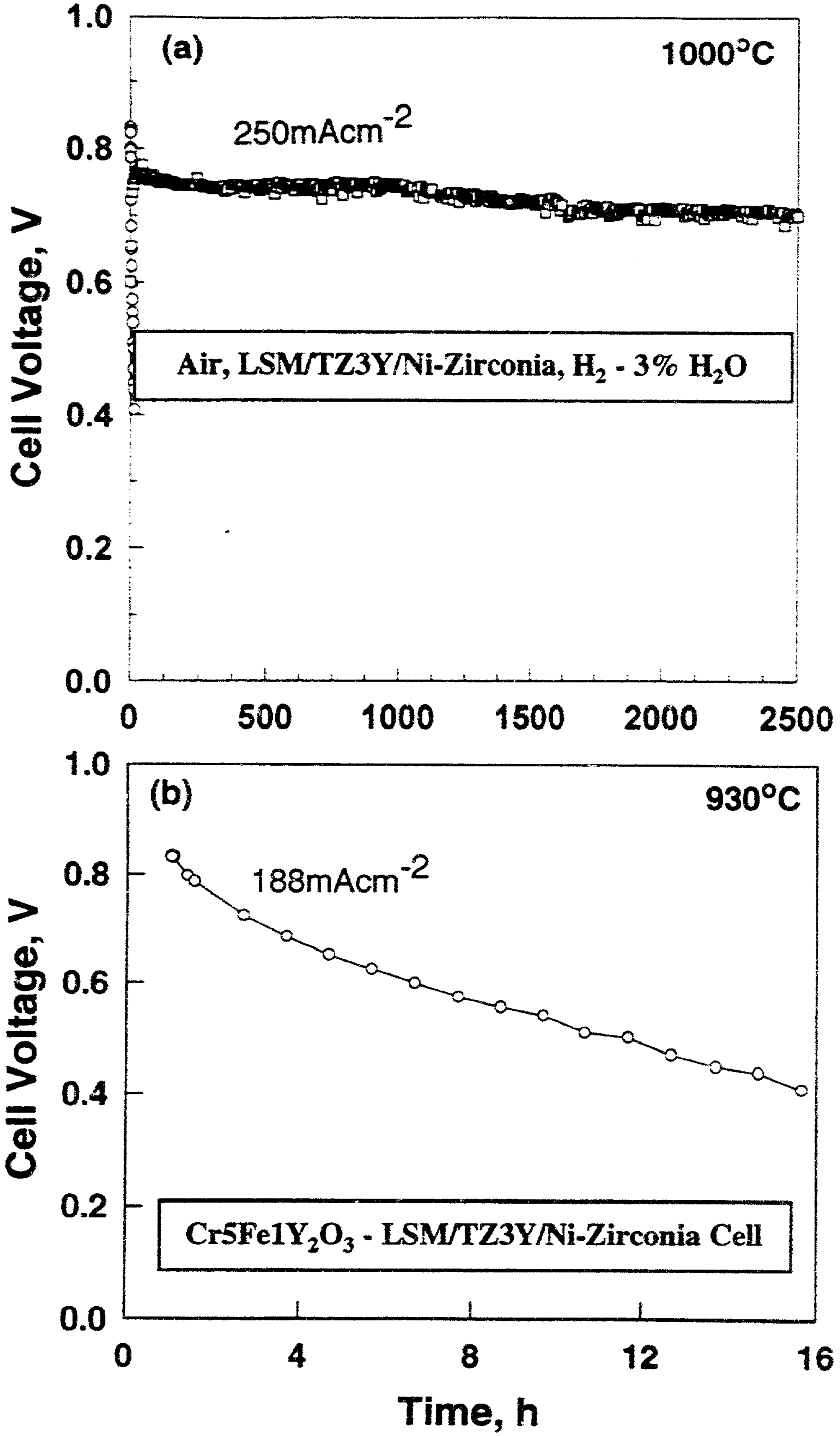
(a)
1000°C
250mAcm-2
Air, LSM/TZ3Y/Ni-Zirconia, H2 - 3% H2O
Cell Voltage, V
1.0
0.8
0.6
0.4
0.2
0.0
0
500
1000
1500
2000
2500
(b)
930°C
188mAcm-2
Cr5Fe1Y2O3 - LSM/TZ3Y/Ni-Zirconia Cell
Cell Voltage, V
1.0
0.8
0.6
0.4
0.2
0.0
0
4
8
12
16
Time, h

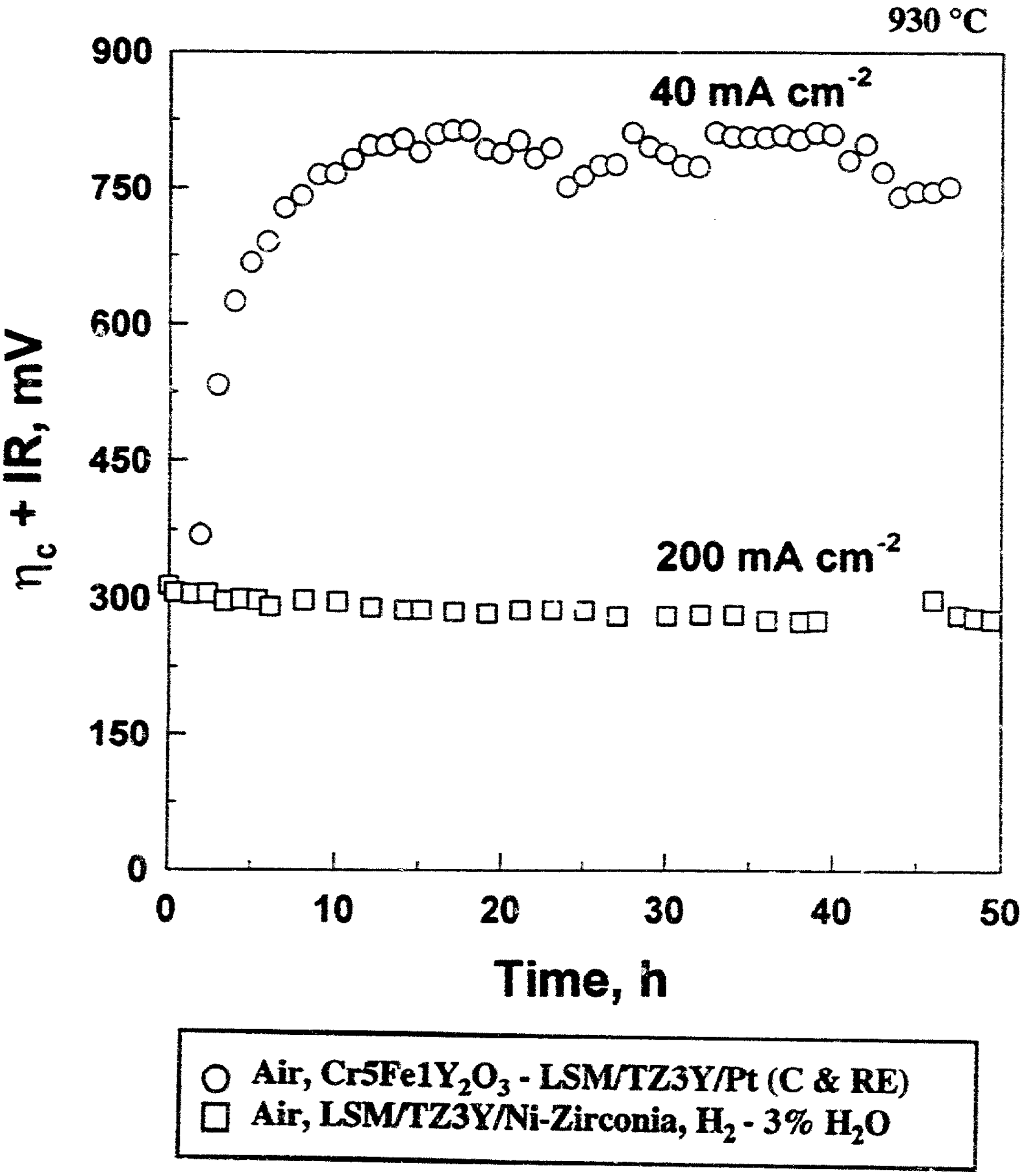
930 °C
40 mA cm^{-2}
200 mA cm^{-2}
η_c + IR, mV
900
750
600
450
300
150
0
0
10
20
30
40
50
Time, h
○ Air, Cr5Fe1Y_2O_3 - LSM/TZ3Y/Pt (C & RE)
□ Air, LSM/TZ3Y/Ni-Zirconia, H_2 - 3% H_2O

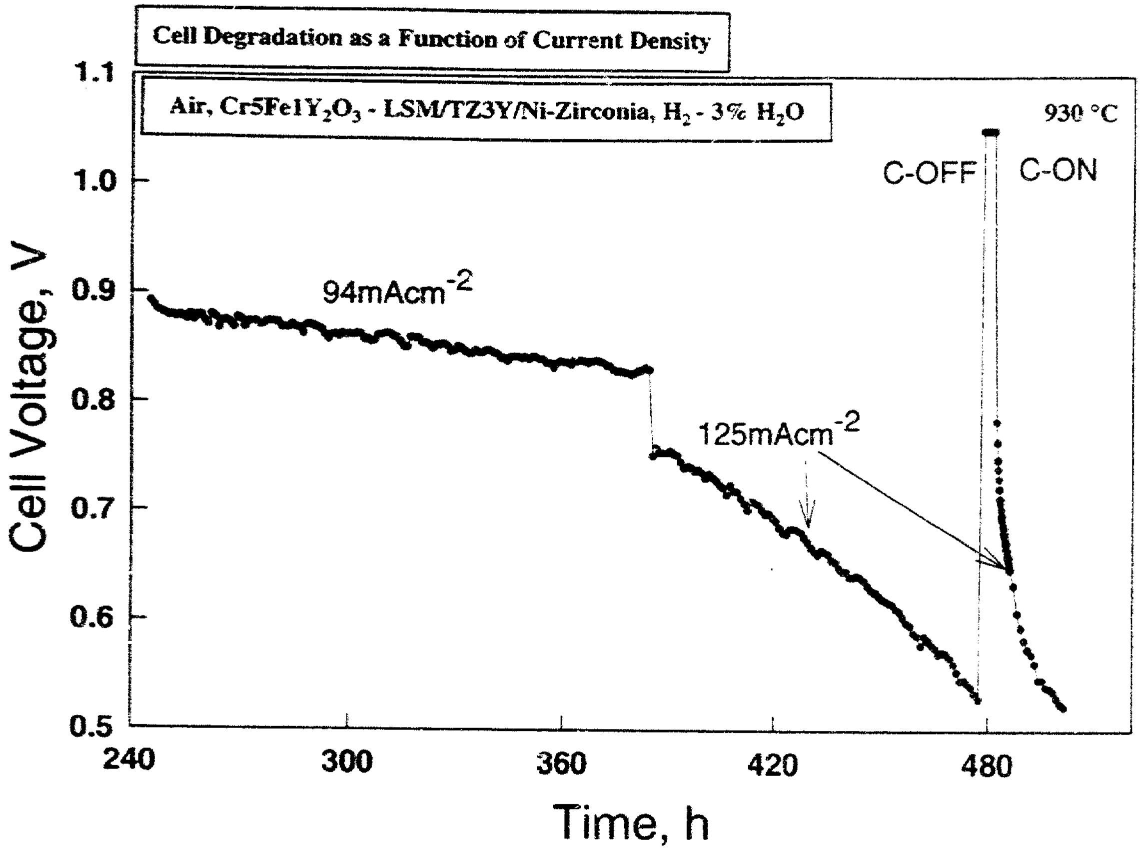
Cell Degradation as a Function of Current Density
Air, Cr5Fe1Y$_2$O$_3$ - LSM/TZ3Y/Ni-Zirconia, H$_2$ - 3% H$_2$O
930 °C
C-OFF
C-ON
94mAcm^{-2}
125mAcm^{-2}
Cell Voltage, V
Time, h
1.1
1.0
0.9
0.8
0.7
0.6
0.5
240
300
360
420
480

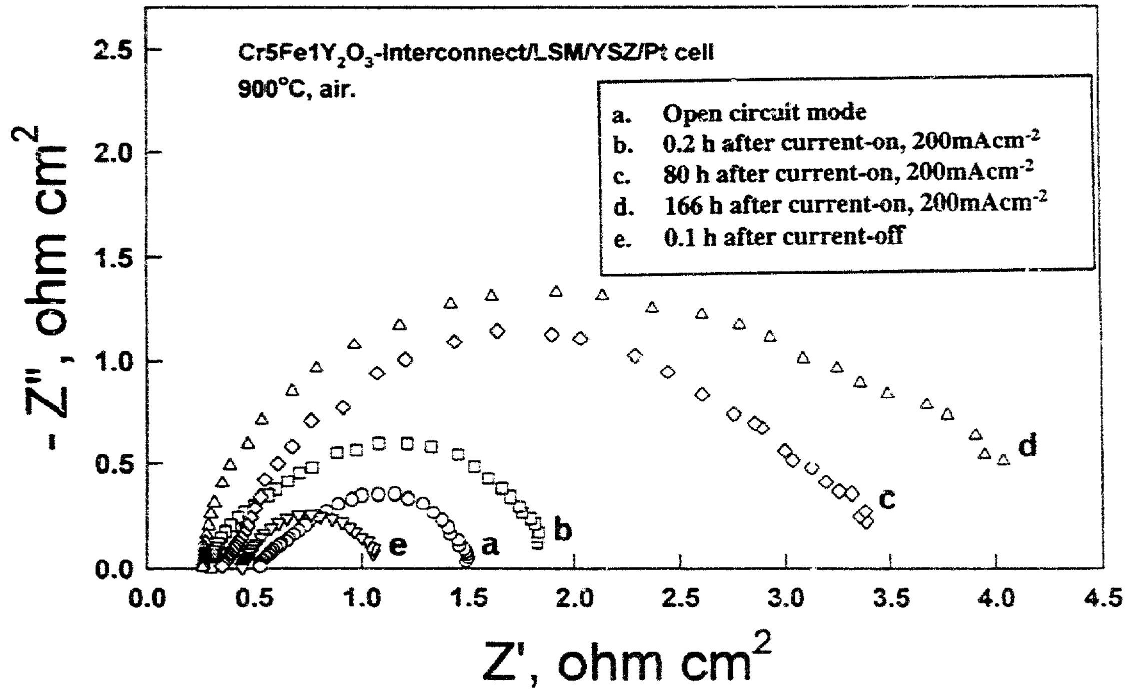
Cr5Fe1Y$_2$O$_3$-Interconnect/LSM/YSZ/Pt cell
900°C, air.
a. Open circuit mode
b. 0.2 h after current-on, 200mAcm^{-2}
c. 80 h after current-on, 200mAcm^{-2}
d. 166 h after current-on, 200mAcm^{-2}
e. 0.1 h after current-off
a
b
c
d
e
- Z'', ohm cm^2
Z', ohm cm^2
0.0
0.5
1.0
1.5
2.0
2.5
3.0
3.5
4.0
4.5

Cathode (LSM)/Cr alloy Interconnect Interface

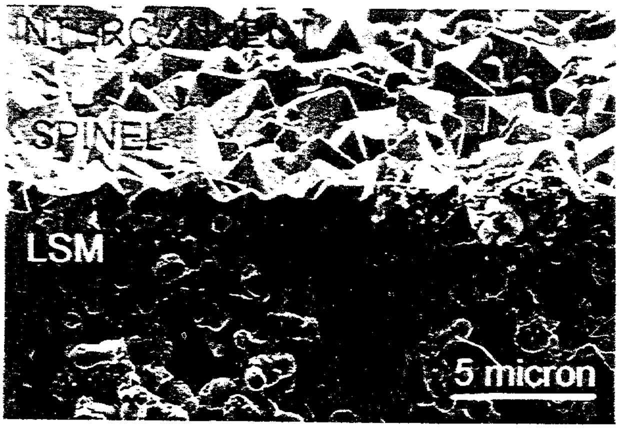

Fuel cell test specimen

930°C, air/H_2-H_2O

Summary of Observations

Electrochemical

- In the absence of a Cr-based interconnect plate in contact with electrodes, the cell voltage degradation with time was relatively small.
- In the presence of a Cr-based interconnect plate, the cell voltage degraded rapidly with time, during current passage.
  - The degradation rate more related to the period of current passage and less dependent on the time when no current is flowing through the cell.
  - The voltage degradation occurs due to an increase in the cathodic overpotential losses. Ohmic losses increase insignificantly by comparison.
  - Higher the current density, higher the cathode losses and faster the cell deterioration.
  - The behaviour during cell degradation was similar to concentration polarisation with a much larger time constant.
  - **Impedance Data : During current passage, the electrode arc increase switching the current-off, the original value before current passage however, the subsequent degradation rate on current switch on is much**

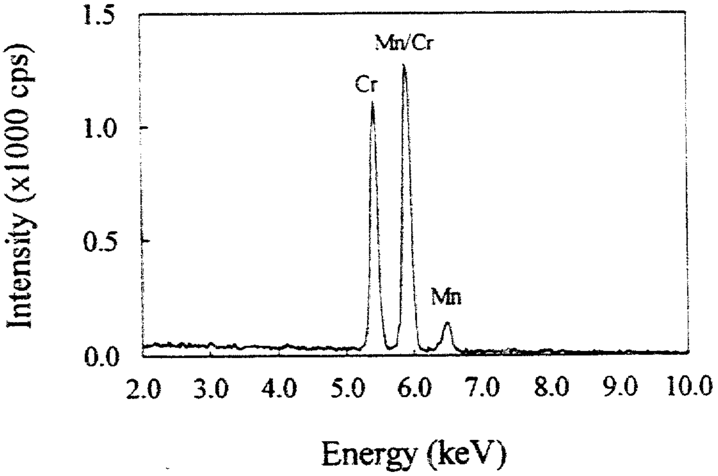
EDS Spectrum of Faceted Crystals at LSM/Cr5Fe1Y_2O_3 Interface

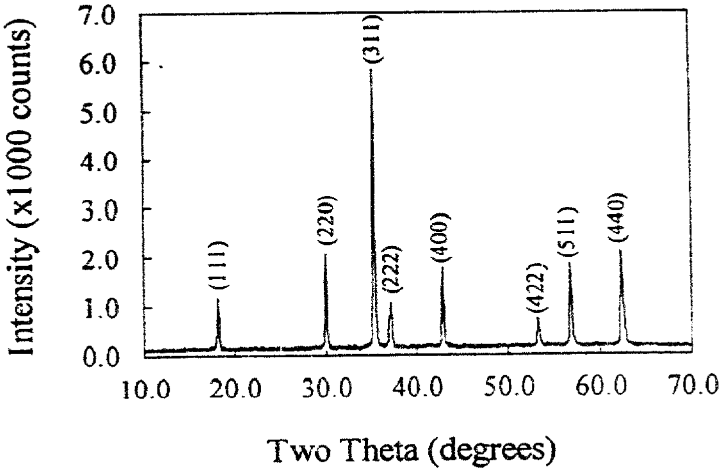
XRD Trace of Well Faceted Crystals - Identified as $(CrMn)_3O_4$ Spinel Phase

Spinel phase formation at LSM/Electrolyte Interface

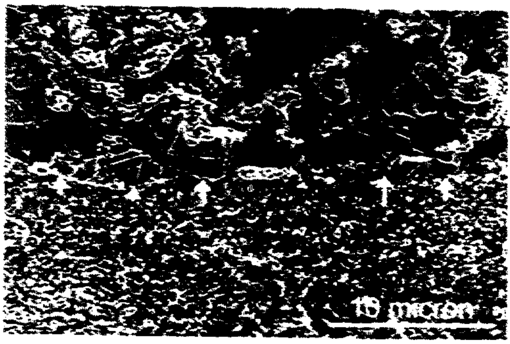

$(LaSr)MnO_3$

$(CrMn)_3O_4$ Spinel

Zirconia-Yttria

Spinel crystals on top surface of Zirconia-Yttria after removal of $(LaSr)MnO_3$ layer

---

Spinel Phase Formation Inside LSM Coating

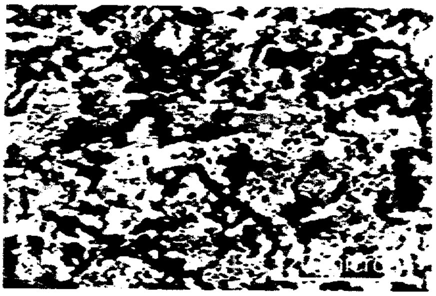

Polished cross section

Dark areas: Spinel
Light areas: LSM

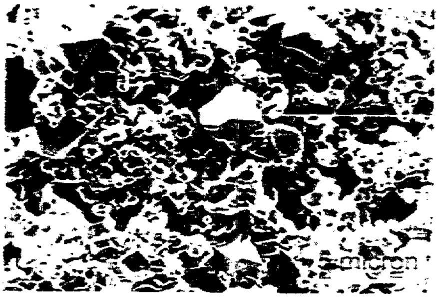

Fractured cross section

$(CrMn)_3O_4$ Spinel Phase

ITN-LSM-YSZ-Ni/ZrO_2-ITN
930°C Test

Cr_2O_3 deposition & Spinel formation at LSM/YSZ Interface

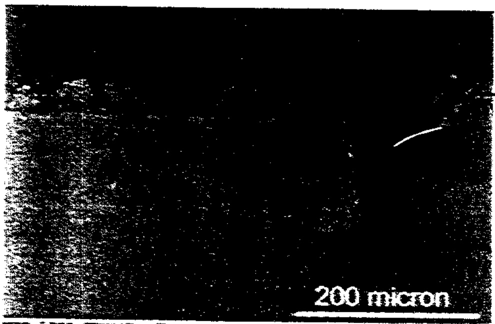

Polished Surface

Cr_2O_3 + Spinel

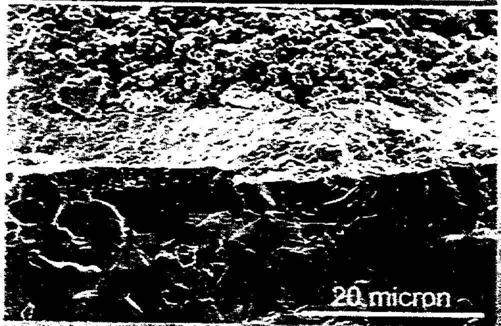

Fractured Surface

Cr_2O_3 + Spinel

ITN-LSM-YSZ-Ni/ZrO_2-ITN
930°C Test

Dense layer of spinel phase at LSM/YSZ Interface

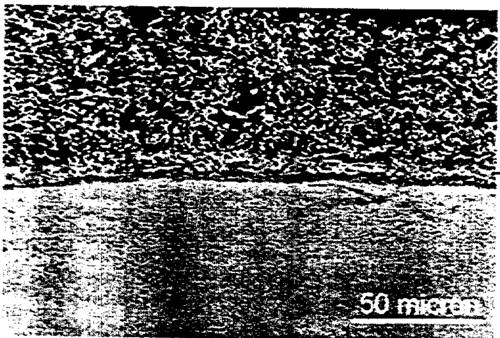

LSM

Dense layer of Spinel phase

Zirconia-Yttria

Enlarged View

LSM

Spinel phase

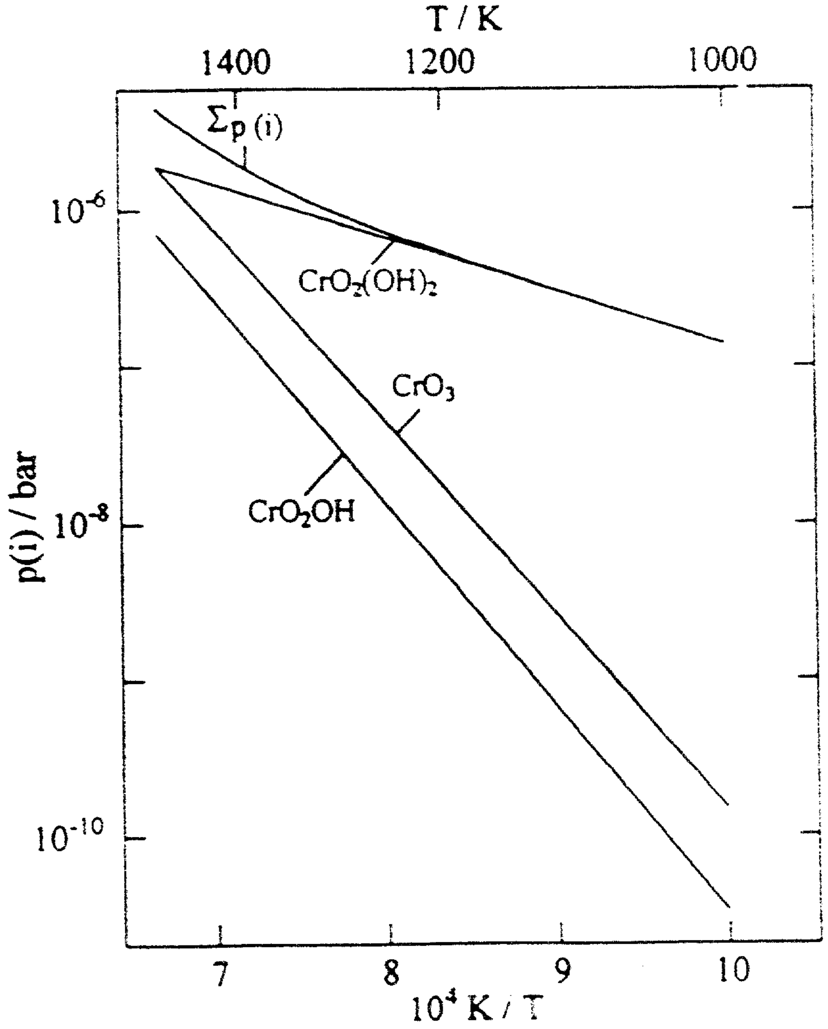

Partial pressure of most abundant Cr containing vapour species over Cr_2O_3 in humid air.
$pO_2 = 0.213$ bar, $p(H_2O) = 0.02$ bar (Hilpert - KFA)

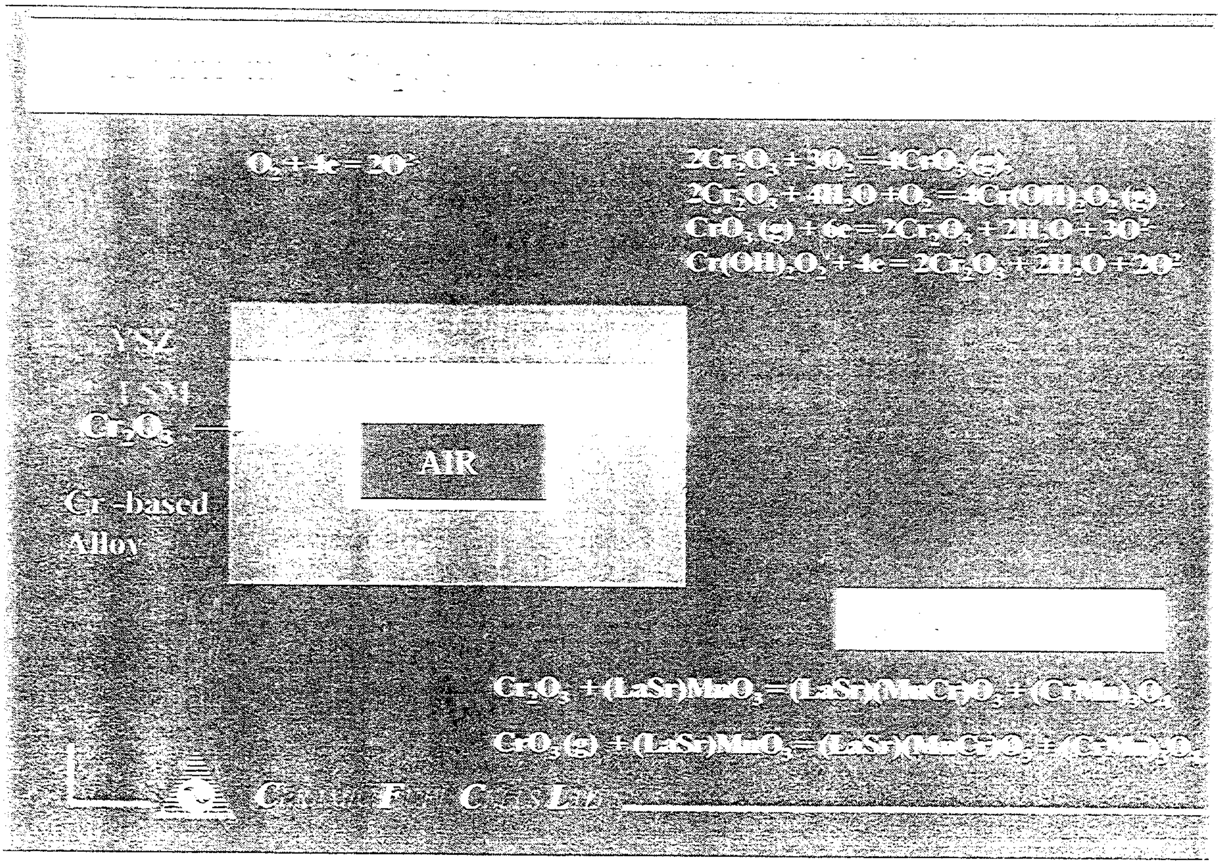

$O_2 + 4e = 2O^{2-}$

$2Cr_2O_3 + 3O_2 = 4CrO_3(g)$,
$2Cr_2O_3 + 4H_2O + O_2 = 4Cr(OH)_2O_2(g)$
$CrO_3(g) + 6e = 2Cr_2O_3 + 2H_2O + 3O^{2-}$
$Cr(OH)_2O_2 + 4e = 2Cr_2O_3 + 2H_2O + 2O^{2-}$

$Cr_2O_3 + (LaSr)MnO_3 = (LaSr)(MnCr)O_3 + (CrMn)_3O_4$

$CrO_3(g) + (LaSr)MnO_3 = (LaSr)(MnCr)O_3 + (CrMn)_3O_4$

Ceramic Fuel Cells Ltd

Spinel formation along a crack in Zirconia - Yttria

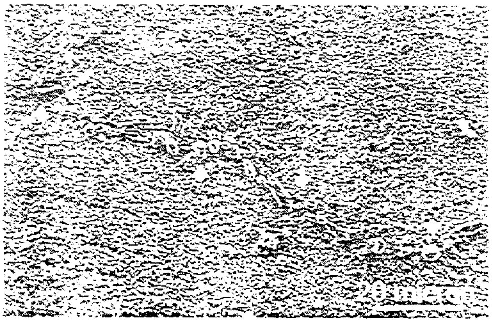

Fuel cell test specimen
LSM/YSZ/Ni-zirconia cell
Tested at 930°C

Enlarged view

$(CrMn)_3O_4$ Spinel phase on air side

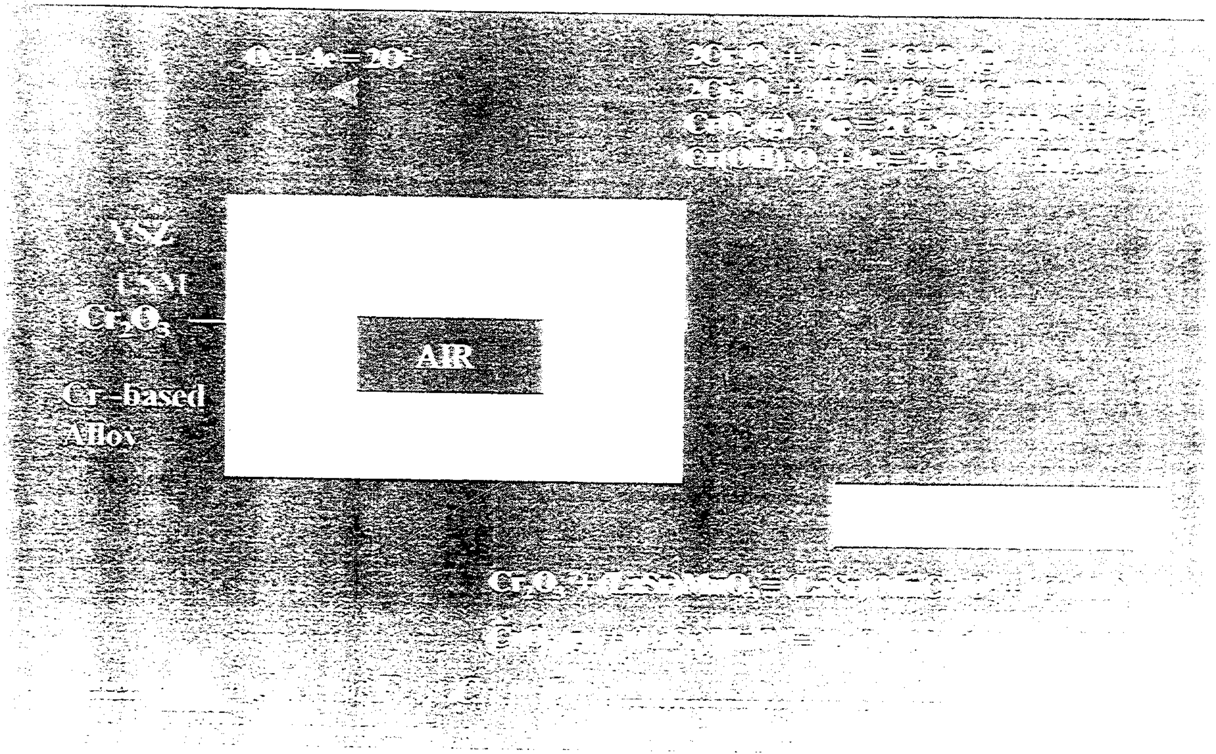

Spinel formation along a crack in Zirconia - Yttria

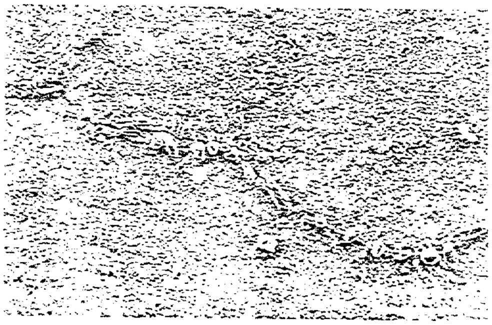

Fuel cell test specimen
LSM/YSZ/Ni-zirconia cell
Tested at 930°C

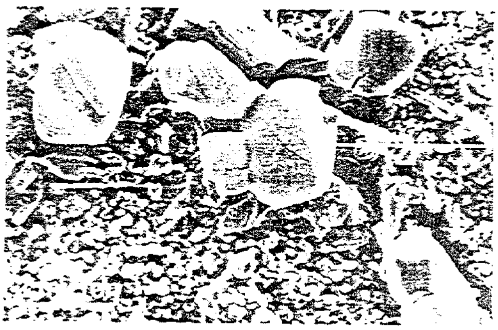

Enlarged view

$(CrMn)_3O_4$ Spinel phase on air side

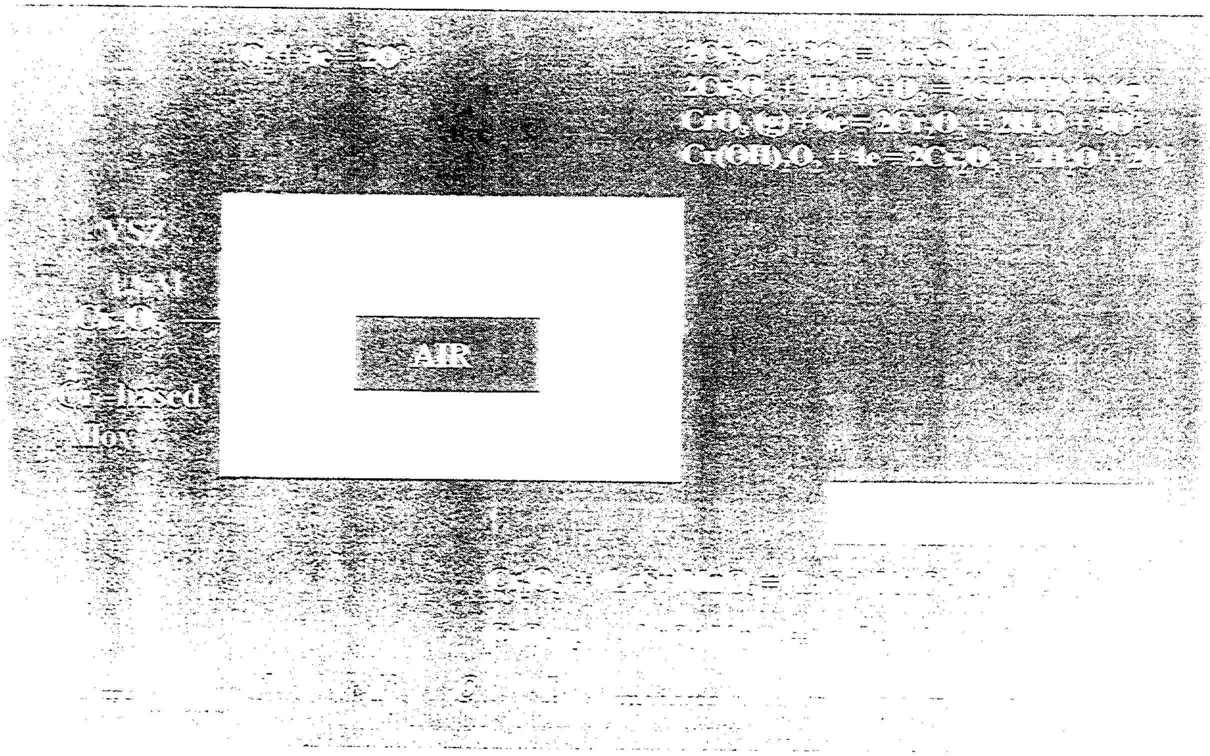

Spinel formation along a crack in Zirconia - Yttria

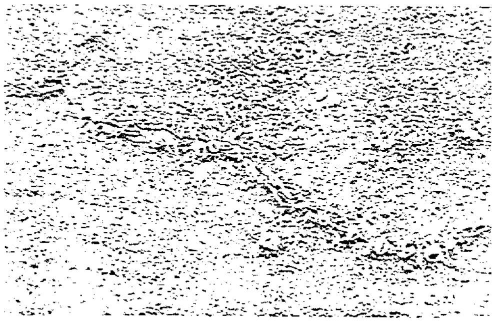

Fuel cell test specimen
LSM/YSZ/Ni-zirconia cell
Tested at 930°C

Enlarged view

$(CrMn)_3O_4$ Spinel phase
on air side

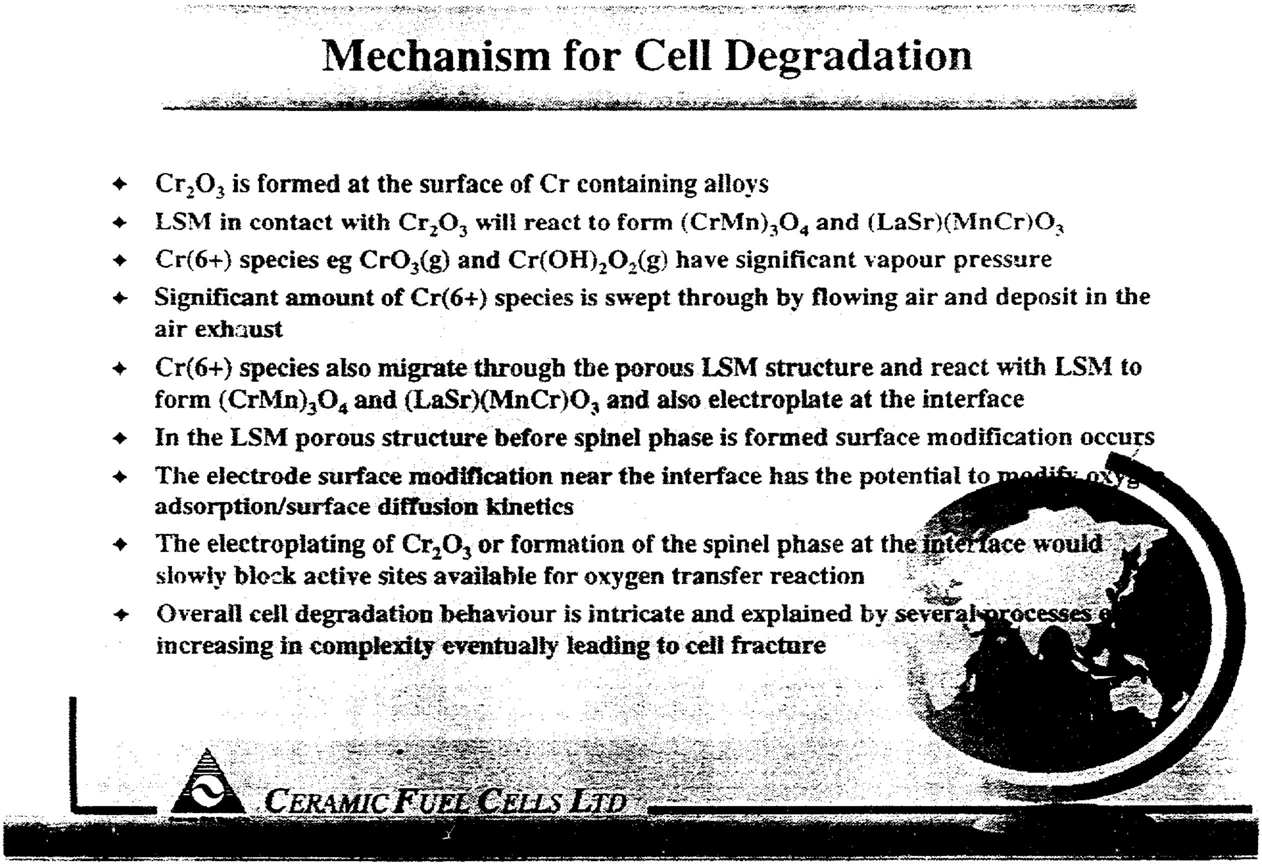

Mechanism for Cell Degradation

- Cr_2O_3 is formed at the surface of Cr containing alloys
- LSM in contact with Cr_2O_3 will react to form $(CrMn)_3O_4$ and $(LaSr)(MnCr)O_3$
- Cr(6+) species eg $CrO_3(g)$ and $Cr(OH)_2O_2(g)$ have significant vapour pressure
- Significant amount of Cr(6+) species is swept through by flowing air and deposit in the air exhaust
- Cr(6+) species also migrate through the porous LSM structure and react with LSM to form $(CrMn)_3O_4$ and $(LaSr)(MnCr)O_3$ and also electroplate at the interface
- In the LSM porous structure before spinel phase is formed surface modification occurs
- The electrode surface modification near the interface has the potential to modify oxyg[illegible] adsorption/surface diffusion kinetics
- The electroplating of Cr_2O_3 or formation of the spinel phase at the interface would slowly block active sites available for oxygen transfer reaction
- Overall cell degradation behaviour is intricate and explained by several processes e[illegible] increasing in complexity eventually leading to cell fracture

---

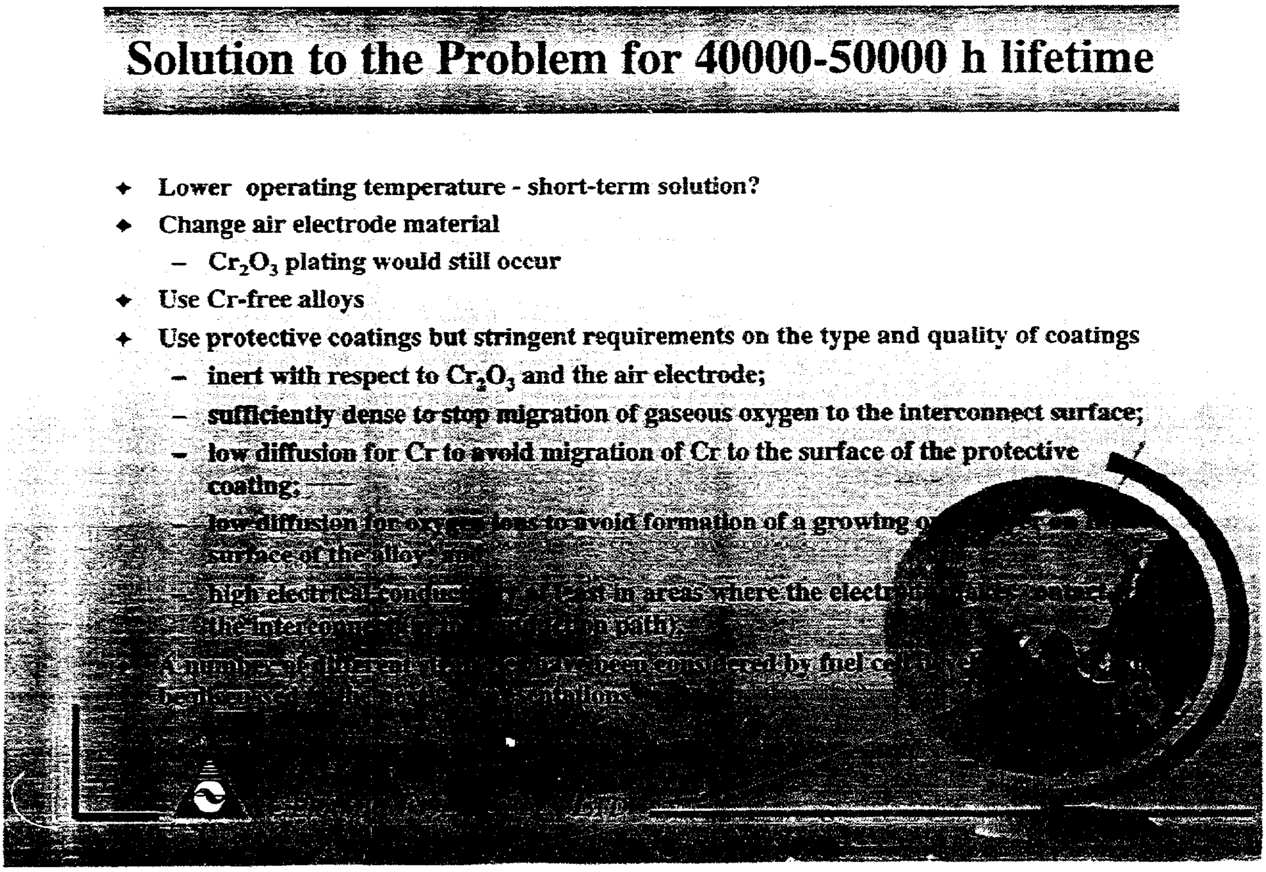

Solution to the Problem for 40000-50000 h lifetime

- Lower operating temperature - short-term solution?
- Change air electrode material
  - Cr_2O_3 plating would still occur
- Use Cr-free alloys
- Use protective coatings but stringent requirements on the type and quality of coatings
  - inert with respect to Cr_2O_3 and the air electrode;
  - sufficiently dense to stop migration of gaseous oxygen to the interconnect surface;
  - low diffusion for Cr to avoid migration of Cr to the surface of the protective coating;
  - low diffusion for oxygen ions to avoid formation of a growing o[illegible] surface of the alloy; and
  - high electrical conductivity [illegible] in areas where the electr[illegible] the interconnect [illegible] path);
- A number of different [illegible] have been considered by fuel cell [illegible] be discussed [illegible] presentations

Mechanism for Cell Degradation

- Cr_2O_3 is formed at the surface of Cr containing alloys
- LSM in contact with Cr_2O_3 will react to form $(CrMn)_3O_4$ and $(LaSr)(MnCr)O_3$
- Cr(6+) species eg $CrO_3(g)$ and $Cr(OH)_2O_2(g)$ have significant vapour pressure
- Significant amount of Cr(6+) species is swept through by flowing air and deposit in the air exhaust
- Cr(6+) species also migrate through the porous LSM structure and react with LSM to form $(CrMn)_3O_4$ and $(LaSr)(MnCr)O_3$ and also electroplate at the interface
- In the LSM porous structure before spinel phase is formed surface modification occurs
- The electrode surface modification near the interface has the potential to modify oxyg adsorption/surface diffusion kinetics
- The electroplating of Cr_2O_3 or formation of the spinel phase at the interface would slowly block active sites available for oxygen transfer reaction
- Overall cell degradation behaviour is intricate and explained by several processes increasing in complexity eventually leading to cell fracture

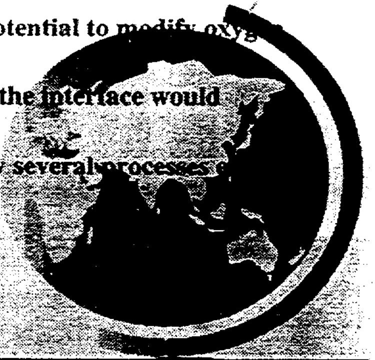

Solution to the Problem for 40000-50000 h lifetime

- Lower operating temperature - short-term solution?
- Change air electrode material
  - Cr_2O_3 plating would still occur
- Use Cr-free alloys
- Use protective coatings but stringent requirements on the type and quality of coatings
  - inert with respect to Cr_2O_3 and the air electrode;
  - sufficiently dense to stop migration of gaseous oxygen to the interconnect surface;
  - low diffusion for Cr to avoid migration of Cr to the surface of the protective coating;
  - low diffusion for [illegible] to avoid formation of a growing [illegible] surface of the alloy;
  - high electrical [illegible] in areas where the elect[illegible] the interconn[illegible]
- A number of [illegible] by fuel c[illegible] be discussed [illegible]

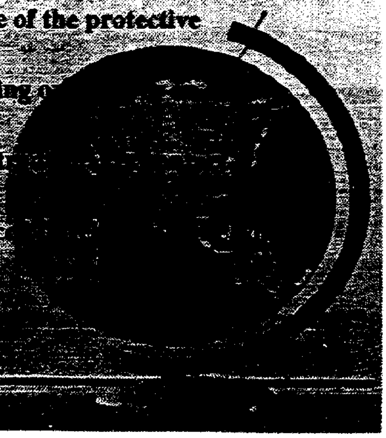

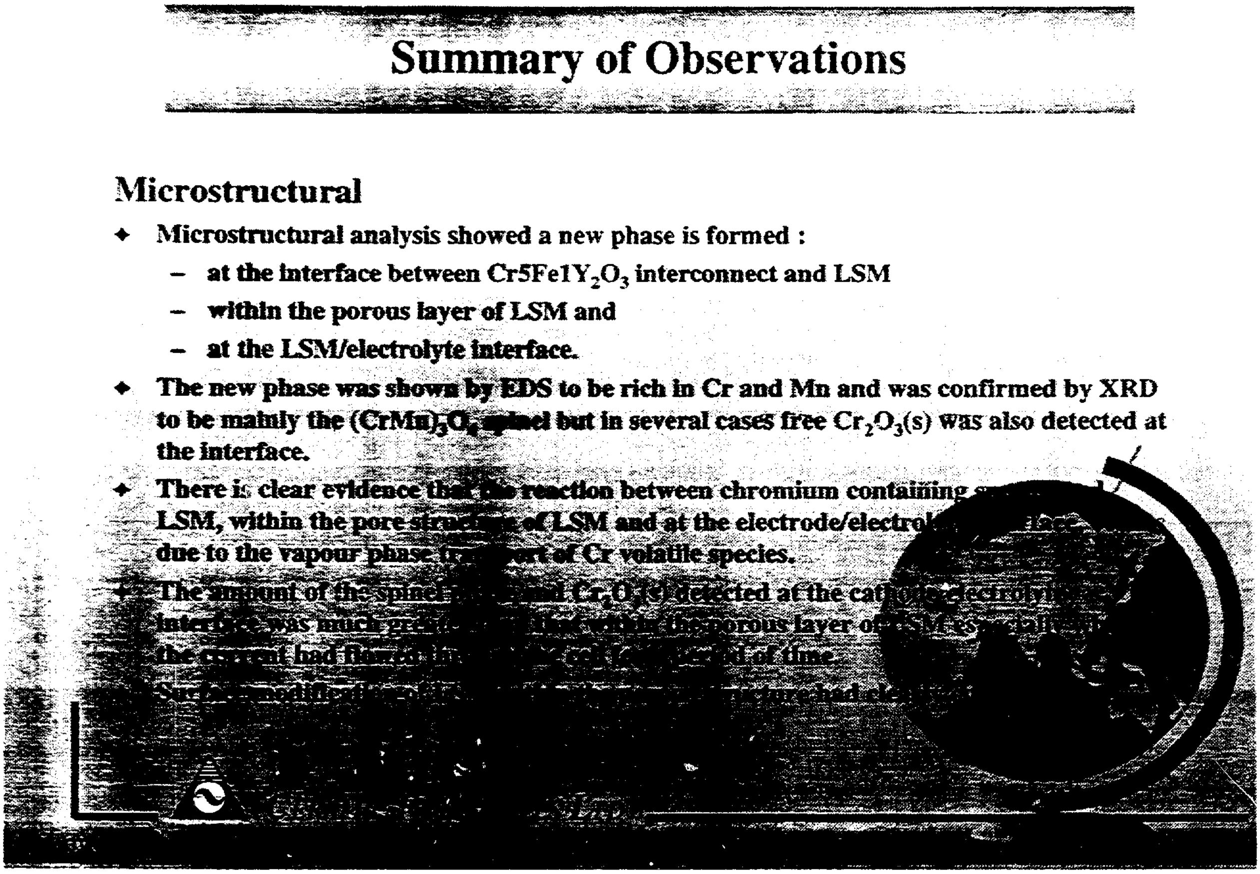

Summary of Observations

Microstructural

- Microstructural analysis showed a new phase is formed :
  - at the interface between Cr5Fe1Y_2O_3 interconnect and LSM
  - within the porous layer of LSM and
  - at the LSM/electrolyte interface.
- The new phase was shown by EDS to be rich in Cr and Mn and was confirmed by XRD to be mainly the $(CrMn)_3O_4$ spinel but in several cases free Cr_2O_3(s) was also detected at the interface.
- There is clear evidence that the reaction between chromium containing [illegible] LSM, within the pore structure of LSM and at the electrode/electrol[illegible] due to the vapour phase transport of Cr volatile species.
- The amount of the spinel [illegible] and Cr_2O_3(s) detected at the cat[illegible] interface was much gre[illegible] within the porous layer o[illegible] the current had flowed th[illegible] cell [illegible] period of time.
- Surface modification [illegible] structure had ele[illegible]

Dense Perovskite coatings by Vacuum Plasma Spraying as Chromium diffusion barriers

K. Barthel and B. Gut

Swiss Federal Laboratories for Materials Testing and Research, EMPA

Contents

- ☐ Introduction
- ☐ Materials screening
- ☐ Perovskite spray powders
- ☐ VPS-results
- ☐ Coatings: Structure & morphology
- ☐ Outlook & summary

Protective coatings on Chromia forming alloys

Requirements:

- ☐ gastight but thin coatings
- ☐ low partial Cr-diffusion coefficient
- ☐ low electrical contact resistance
- ☐ low Oxygen-ion conductivity
- ☐ thermodynamic stability
- ☐ thermal expansion match

Materials screening

Perovskite type	Conductivity range at 950°C (S/cm)	Chromium permeability	Protective layer
$La_{0.6}Sr_{0.4}CoO_3$	≈ 1250	high [1]	thick
$La_{0.8}Sr_{0.2}MnO_3$	≈ 150	low [2]	medium
$La_{0.7}Ca_{0.3}CrO_3$	≈ 10	low [2]	thin

1) Batawi et al.1996
2) Fendler et al.1996

Composition

☐ $La_{0.5}Sr_{0.5}MnO_3$ - improved conductor (320 S/cm)

(compared to $La_{0.8}Sr_{0.2}MnO_3$) - adapted thermal expansion coefficient (13.2 10^{-6}/K)

☐ $La_{0.7}Ca_{0.3}Cr_{0.85}Co_{0.15}O_3$ - improved conductor (50 S/cm)

(compared to $La_{0.7}Ca_{0.3}CrO_3$)

EMPA

VPS-Sprayability Results

Plasma power - refered to pure phase coatings:

☐ LSCo:	- electrical plasma power max. 25 kW - very porous structure
☐ LSM:	- electrical plasma power > 40 kW - dense but microcracks
☐ LCCr and LCCrCo:	- > 40 kW possible, dense, crack-free

EMPA

$La_{0.6}Sr_{0.4}CoO_3$

VPS processing: 25 kW electrical plasma power, pure Ar/He-plasma

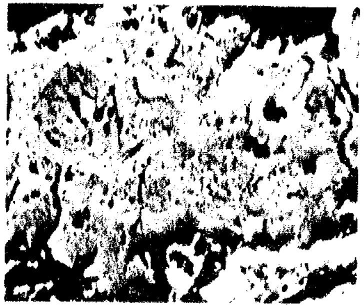

VPS processing: 30 kW electrical plasma power, Ar/H_2-plasma (back scattered electron contrast)

EMPA

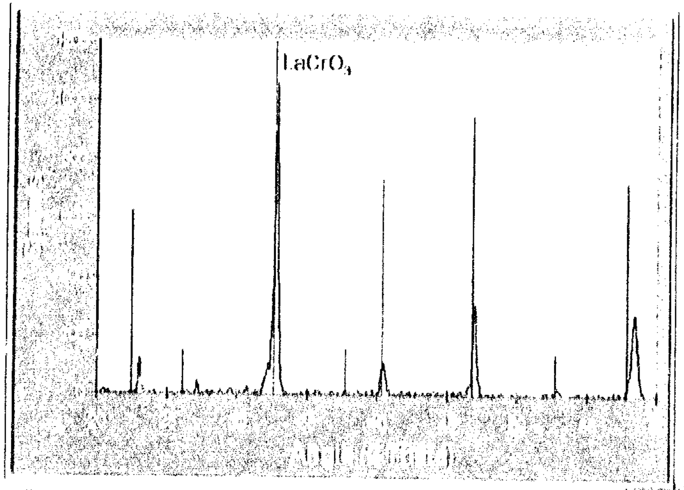

Structure and electrical resistance

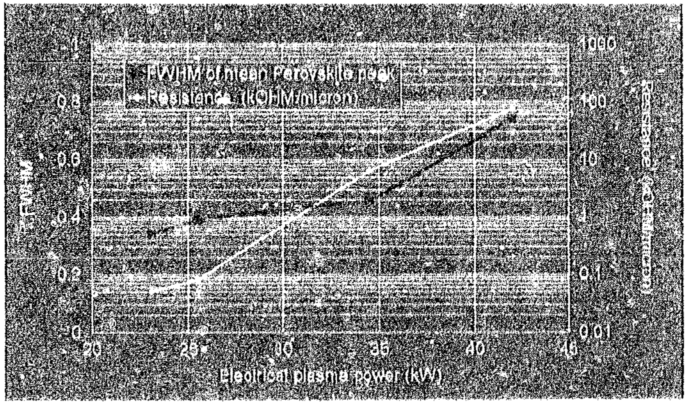

$La_{0.5}Sr_{0.5}MnO_3$

SEM-Morphology

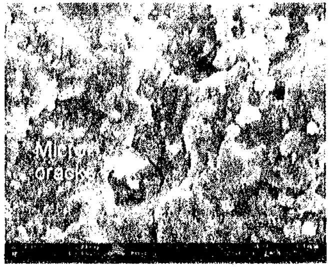

$La_{0.5}Sr_{0.5}MnO_3$ on HS 230,
thickness 50 µm,
VPS: 45 kW, Ar/H_2-plasma

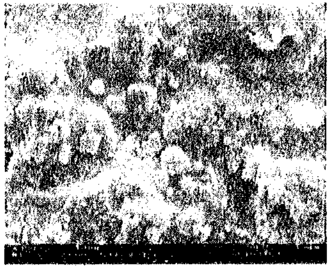

$La_{0.7}Ca_{0.3}CrO_3$ on HS 230,
thickness 30 µm,
VPS: 45 kW, Ar/H_2-plasma

Outlook

Evaporation test rig:

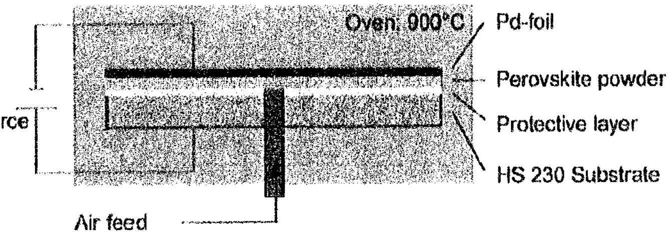

Test criterion: - Cr-concentration profile in the protective layer
(after some 100 h) - Cr-concentration in the Perovskite powder

Summary

- ☐ Cell operation temperatures > 800°C require protective coatings on the interconnect
- ☐ LSM & LCCr are candidates for protection by VPS
- ☐ Dense coatings require high electrical plasma power
- ☐ LSCo, LSM and LCCr are sensitive for decomposition if processed at high plasma power
- ☐ Further work necessary for integral characterization

Processing of Ni-alloy-Alumina-Cermets as Interconnect Materials

U. von der Crone, R. Vaßen, H.-P.-Buchkremer

Introduction

Interconnects of the solid oxide fuel cells (SOFCs) separate the gas atmospheres and provide the conduction of electrons. Established materials are doped $LaCrO_3$-perovskites [1] and Cr-based alloys [2]. Some groups presented cermets as interconnect materials [3,4,5]. All these materials were developed to match the thermal expansion of the 8YSZ electrolyte of about 10.8×10^{-6}/K to avoid thermal stresses between the components. At the Forschungszentrum Jülich GmbH an anode supported planar SOFC concept was designed [6]. The electrolyte has a thickness of only about 15-20 µm instead of 100-300 µm while the thickness of the anode is increased to 2 mm. Because of this concept the electrolyte does not determine the thermal expansion of the PEN, but the anode becomes dominating. The average thermal expansion coefficient (TEC) of the anode up to 1000°C is about 12.3×10^{-6}/K. Therefore the mentioned interconnect materials possess too low thermal expansion coefficients. At the reduced operative temperatures, which are made possible by the thin electrolyte, alternative materials are ferritic steels or cermets.

Cermets can cover a wide range of thermal expansion coefficients due to the variability in the choice of their composition. Hence they remain interesting even if the materials of the other SOFC components are modified. The metal provides the electrical conduction and the ceramic reduces the thermal expansion coefficient. To keep the processing easy it was tried to find a way for pressureless sintering of the cermets to high densities. In the Ni-alloy-alumina cermets, which were investigated in the present study, this was tried to achieve with Al_2O_3-powder of high sintering activity. This seemed necessary because due the poor wettability of alumina by nickel melt [7] no liquid phase sintering will occur. A further problem is described by the percolation theory [8] which shows that high amounts of a rigid second phase obstructs densification.

Different compositions of Al_2O_3 and Ni-alloy were investigated concerning their sintering behaviour, their gastightness, their electrical conductivity and their thermal expansion.

Experimental

Different Ni-alloys and alumina were used as starting materials. For the Ni-alloy Ni80Cr20 (5-22 µm, Valco), Ni-SA 625 (< 20 µm, H. C. Starck) and Hastelloy X (< 150 µm, Coldstream) were used. The used Al_2O_3 (TM-DAR, Taimei Chemicals, Tokyo, Japan) has a particle size of about 0.22 µm. The starting powders were mixed with additions of PVAC as binder and acetone. After drying the powders were sieved through a 1 mm sieve, uniaxial pressed and sintered in vacuum. Some samples were hot isostatically pressed (hiped) to complete density. The relative densities after sintering were determined geometrically.

The electrical conductivity was measured at room temperature using the 4-point method.

The thermal expansion was measured with a high-temperature push-rod dilatometer in flowing Ar/ 4% H_2 atmosphere between room temperature and 1100°C.

The gastightness was measured using a two-chamber apparatus where the sample divides the chambers. The chambers were evacuated, one chamber was afterwards filled with Helium. On the other side of the sample the increase of pressure after a certain time was measured. The applied difference in pressure was 200 mbar.

X-ray diffraction (XRD) was performed at a sintered sample of 60 vol% Ni80Cr20 and 40 vol% Al_2O_3 after heat treatment in air at 1200°C for 100 h.

Results

Figure 1 shows the comparison of Hastelloy X with a particle size of about 150 µm and the Ni80Cr20 with particle sizes between 5-22 µm. While the use of the large particles resulted in isolated metal grains the smaller grains had more contacts to each other.

The use of Ni-SA 625 resulted in melting of the alloy at temperatures of 1280°C and above. A sample with 50 vol% Al_2O_3 and 50 vol% alloy, that was sintered at 1250°C, attained only a relative density of about 85%.

The pure Ni80Cr20 sintered to about 90 % relative density at temperatures between 1250 and 1340°C (fig. 2). The porosity was closed. The main difference between samples sintered at 1250°C and 1340°C lied in the pore-structure. While the sample sintered at 1250°C had many small pores within the grains, sintering at 1340°C led to less but bigger pores at grain boundaries. On the contrary the density of the alumina samples was strongly influenced by the choice of the sintering temperature as shown in figure 2. After sintering at 1340°C a relative density of 97.7 % was measured.

Cermets of 50 vol% alloy and 50 vol% Al_2O_3 also showed a strong dependence upon the sintering temperature (fig. 2). With a sintering temperature of 1340°C relative densities up to 95.5 % were attained. However, none of the samples was completely gastight. The leakage decreased with increasing relative density. The lowest measured value was 7.8×10^{-9} mol /s cm^2 for the sample with 95.5 % relative density.

Figure 3 presents the dependence of the TECs on the amount of Ni80Cr20. The TECs are lower than predicted by the rule of mixtures. Samples with less than 50 vol% Ni80Cr20 showed only a slight increase in TEC with increasing Ni80Cr20 content. Between 50 and 70 vol% of Ni80Cr20 a strong increase in TEC occurs. At higher contents of Ni80Cr20 the results are similar to those calculated from the rule of mixtures. This behaviour seems to depend on the change of the matrix. At Al_2O_3 contents of more than 50 vol% the alumina determines the thermal expansion. The composition for matching thermal expansion coefficients of cermet and anode is in the range of 55-65 vol% Ni80Cr20. The exact composition seems to depend on the used powders and the distribution of the components in the specimen.

Figure 4 shows the electrical conductivity in dependence upon the Ni80Cr20 content. The pure Ni80Cr20 has a conductivity of more than 10000 S/cm while alumina has a conductivity of less than 10^{-12} S/cm at room temperature [9]. All samples with more than 50 vol% Ni-alloy had conductivities of more than 1000 S/cm.

XRD (fig. 5) revealed the presence of a spinell after heat treatment in air. The exact composition of the spinell could not be determined because of the low intensity. It did not seem to be pure $NiAl_2O_4$ or $NiCr_2O_4$ but a mixture of both.

Conclusions

Alumina seems a good choice for the ceramic of the cermet. It has to be evaluated if other ceramics, for example of ternary systems, have advantages concerning the sintering activity without causing problems with too many chemical reactions.

Because of the high discrepancy between the melting points of alumina and Ni-based alloys it is difficult to sinter the cermets to densities near theoretical density. Alumina powders with very high sintering activity seem to be necessary. Furthermore the Ni-alloy needs a high solidus temperature. The particle size of the nickel alloy should be small to increase the number of contacts between the particles. The use of binder was obligatory to avoid breakage of the samples directly after uniaxial pressing. With uniaxial pressing and sintering in vacuum relative densities of 95.5 % with gastightness of about 8×10^{-9} mol / s cm^2 were attained for mixtures of 50 vol% Al_2O_3 and 50 vol% Ni80Cr20. Because of the melting of the Ni80Cr20 it seems difficult to achieve higher densities. It might be necessary to use other ways for processing of fully gastight interconnects like the use of additional pressure during sintering.

At Ni-alloy contents between 50 and 80 vol% the TEC increases strongly. It seems to depend significantly on the distribution of the components in the cermet. This dependence demands that for every new powder and processing the right composition has to be determined.

The electrical conductivity of more than 1000 S/cm seems reasonable well for cermets with more than 50 vol% Ni-alloy compared with 0.15 S/cm at 1000°C for the electrolyte or 30 S/cm at 1000°C for ceramic interconnects [10].

The XRD data showed that some reactions between Al_2O_3 and the alloy will occur. Long-term experiments have to reveal if this will significantly deteriorate the function as an interconnect. Reactions with the atmospheres will depend mainly on the chosen Ni-alloy. Ni80Cr20 might not be the best Ni-alloy concerning the resistance against corrosion. On the other hand Ni-SA 625 has a too low melting temperature.

The chromium evaporation is not expected to decrease by replacement of chromium alloys by cermets. Also for cermets a layer for the reduction of the evaporation will be needed.

References

1. Q. Minh, J. Am. Cer. Soc. 76 (1993): 563
2. J. Quadakkers et al., Proc 1st Europ. SOFC Forum, Oct. 3-7, 1994, Lucern, CH, ed. U. Bossel: 525
3. Seto et. al., Proc 3rd Int. Symp. SOFC, Honolulu, Hawaii, USA, May 16-21, 1993, ed. S. C. Singhal, H. Iwahara: 421
4. Seto et. al., Ext. Abstracts 4th Symp. SOFC in Japan, Dec, 14-15, 1995, Tokyo, Japan: 41
5. R.-H. Song , D. R. Shin, M. Dokiya, Abstracts 1996 Fuel cell sem., Nov 17-20, 1996 Orlando, Fl., USA: 179
6. H.-P. Buchkremer et. al. , Proc. 2nd Europ. SOFC Forum, May 6-10, 1996, Oslo, N, ed. Bernt Thorstensen: 221
7. P. Nikolopoulos, S. Agathopoulos, J. Europ. Cer. Soc. 10 (1992): 415
8. O. Sudre, F. E. Lange, J. Am. Cer. Soc. 75 [3] (1992): 519
9. H. Salmang, H. Scholze: Keramik-Teil 2, Springer-Verlag, 1983
10. U. Bossel, „Facts and Figures. Report to the Swiss Federal Office of Energy", ed. L. Dubal, Berne, 1992

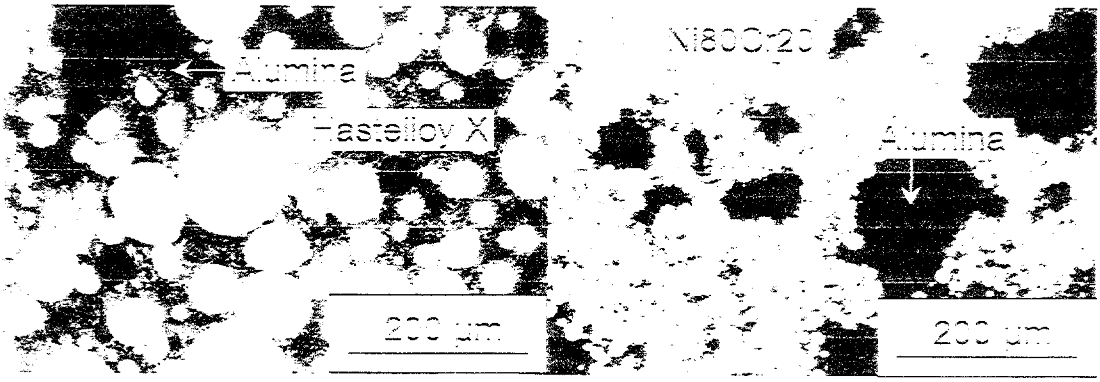

Figure 1:
Microstructure of hiped samples with different starting powders. The left micrograph shows a sample with 60 vol% Hastelloy X (<150 µm) 40 vol% Al_2O_3 and the right micrograph shows a sample with 60 vol% Ni80Cr20 (5-22 µm) and 40 vol% Al_2O_3.

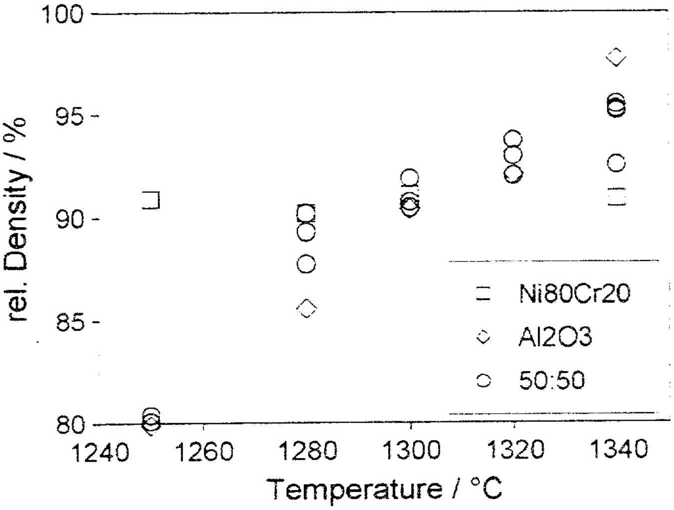

Figure 2:
Relative densities in dependance on the sintering temperature for Ni80Cr20, Al_2O_3 and cermets of 50 vol% alloy and 50 vol% Al_2O_3

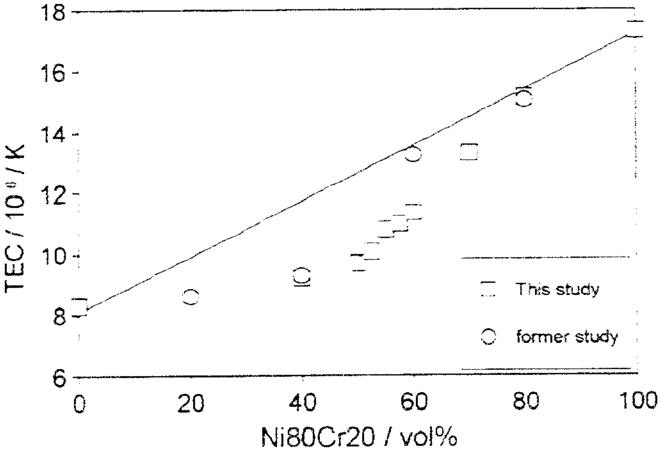

Figure 3:
TEC ($\alpha_{RT-1000°C}$) of cermets in dependance on the Ni80Cr20 content. For comparision the calculation using the rule of mixtures is given. In the former study a different alumina powder was used.

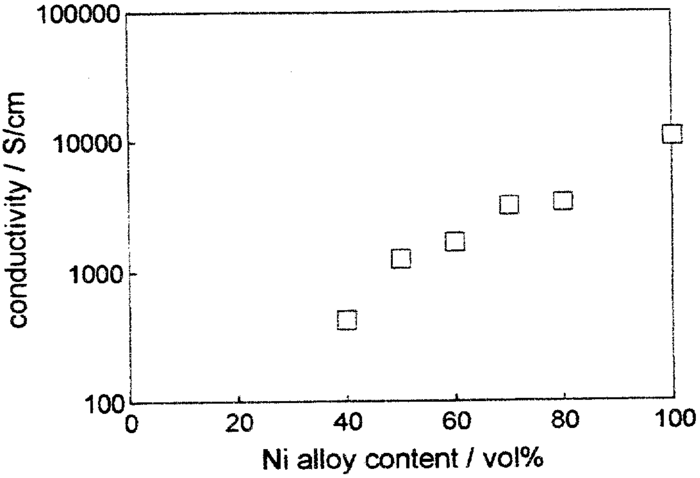

Figure 4:
Electrical conductivity of cermets at room temperature in dependance on the Ni80Cr20 content.

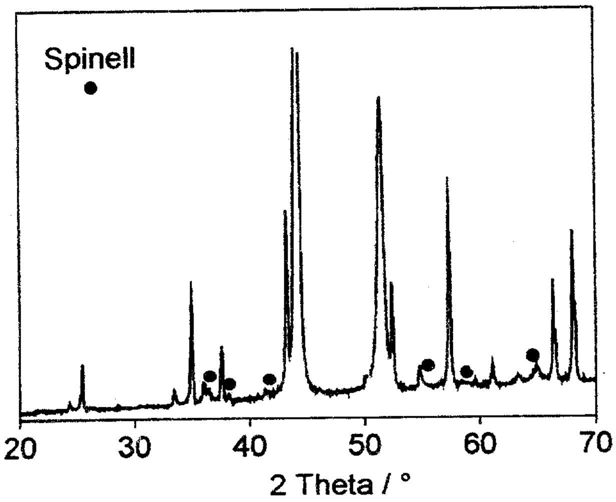

Figure 5:
X-ray dffraction diagramm of cermet with 60 vol% Ni80Cr20 and 40 vol% Al_2O_3 after heat treatment of 100 h at 1200°C in air.

Development of a ferritic alloy separator for a planar SOFC

Shunsuke TANIGUCHI, Masataka KADOWAKI, Takashi YASUO,
Yukinori AKIYAMA, Yasuo MIYAKE and Koji NISHIO

New Materials Research Center, SANYO Electric Company

Heat-resistant ferritic alloys were investigated for use as a SOFC separator material in order to reduce the difference in thermal expansion between the electrolyte and separator. Furthermore, the material cost for iron-based ferritic alloys is lower than that for nickel-based austenitic alloys. The heat resistance of ferritic alloys were improved by adding a small amount of lanthanum, making it possible to use them as a SOFC separator. The thermal cycle characteristics were improved in a 50 mm ×50 mm single cell using this ferritic alloy in comparison with a cell using a nickel-based alloy. The single cell was operated for about 7000 h. Degradation of the cell performance was apparently caused mainly by gas leakage.

Table 1 Specifications of the alloys.

Alloy	Composition	Thermal expansion coefficient/°C^{-1} (30°C-1000°C)
A	Ni-based, Cr16, Fe9 (wt%)	16.7×10^{-6}
B	Fe-based, Cr22 (wt%)	13.0×10^{-6}
C	Fe-based, Cr22 (wt%), La	12.7×10^{-6}
	(YSZ	10.5×10^{-6})

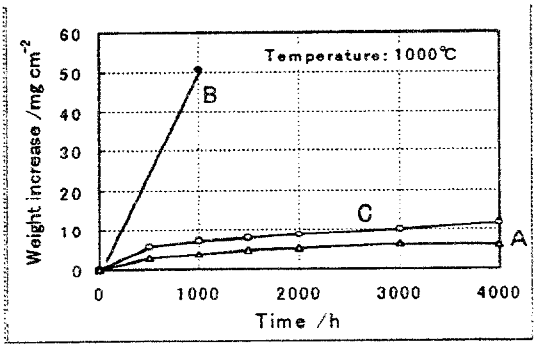

Fig. 1 Change in weight increase in alloys after heating at 1000 ℃ in air.

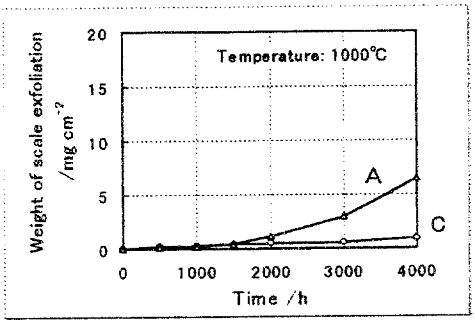

Fig. 2 Change in weight of scale exfoliation from alloys A and C after heating at 1000 ℃ in air.

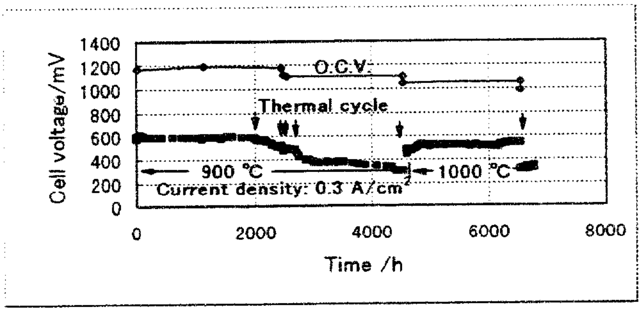

Fig. 3 Cell voltage change for a 50 mm × 50 mm single cell using the ferritic alloy separator (C).

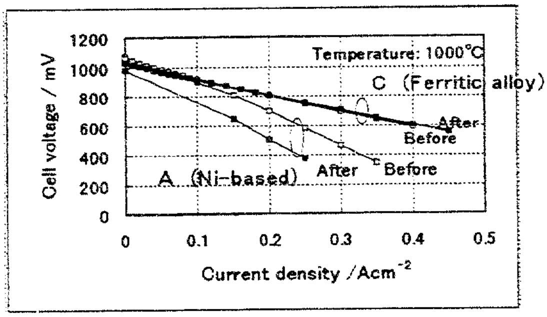

Fig. 4 Thermal cycle characteristics for cells using alloys A and C.

A part of this work was performed as an R&D program of the New Energy and Industrial Technology Development Organization (NEDO) under the New Sunshine Project of the Agency of Industrial Science and Technology, MITI.

Oxygen Permeation through (La,Ca)CrO_3 Interconnects

N. Sakai, T. Horita, K. Yamaji, H. Yokokawa, M. Dokiya and T. Kawada*
National Institute of Materials and Chemical Research
1-1 Higashi Tsukuba Ibaraki 305 JAPAN
*Research Institute of Scientific Measurements, Tohoku University,
2-1-1 Katahira, Aoba-ku, Sendai, 980-77 JAPAN

Abstract: The oxygen permeability through $La_{1-x}Ca_xCrO_{3-\delta}$ is determined using an electrochemical method as a function of oxygen potential gradient. The experimental data can be well explained by using oxygen tracer diffusion coefficients (D^*) determined by SIMS analysis under a wide range of oxygen partial pressure. The assumption of the simple point defect model and constant D_V is found to be insufficient to explain the oxygen permeability for heavily doped $La_{1-x}Ca_xCrO_{3-\delta}$ under a large $p(O_2)$ gradient.

Introduction

Lanthanum chromite-based materials have been focused as interconnects of Solid Oxide Fuel Cells (SOFC) in recent a couple of decades. The base material $LaCrO_3$ has good chemical stability in the wide range of oxygen potential at high temperature, which is one of the most important requisites for SOFC interconnects. Furthermore, its thermal and electrical properties can be regulated by selecting suitable dopants concentration, which is a reason why it has a good compatibility with other SOFC components such as YSZ electrolytes.

The most suitable dopant concentration must be determined by taking into account SOFC types and operation conditions. High electrical conductivity is raised by substituting lanthanum or chromium with alkaline earths such as calcium, strontium, or magnesium, which result in the formation of Cr(IV) as a hole carrier. However, Cr(IV) is no longer stable in reducing atmosphere at high temperature, so that it normally is reduced to Cr(III) and the charge neutrality is maintained by the formation of oxygen vacancy ($V_O^{\bullet\bullet}$). This reaction is represented by using Kröger-Vink notation as:

$$2Cr^{\bullet}_{Cr} + O^{\times}_{O} \rightleftarrows 2Cr^{\times}_{Cr} + V^{\bullet\bullet}_{O} + \frac{1}{2}O_2$$

The oxygen vacancy formation results in some undesirable effect on thermal and electrical properties of doped lanthanum chromites. The lattice expansion generated by oxygen vacancy may cause a large stress on an interconnect plate, which must be considered preferentially for utilization of a planar-type SOFC interconnect. On the

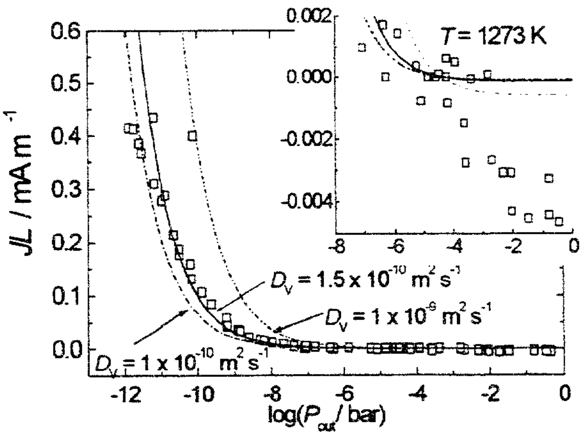

Oxygen Permeability through $La_{0.90}Ca_{0.10}CrO_{3-\delta}$ normalized by sample thickness (L = 1.371 mm): Solid and dashed lines are theoretical JL with different D_V. P_{in} = 4.5 x 10^{-5} bar, K_{ox} = 3.22 x 10^{-8} bar$^{0.5}$.

other hand, the effect of oxygen permeation generated by ambipolar diffusion of oxygen vacancy and hole is much more significant for tubular-type SOFC interconnect, which is attached as a thin layer on a porous substrate tube. There are several reports of oxygen permeability of $LaCoO_3$ based materials with technological interest as the dense ceramic membranes for oxygen separation [1], however very few for $LaCrO_3$ based compounds. This paper reports the research activities done for oxygen permeation and materials transport phenomena in calcium doped lanthanum chromite, $La_{1-x}Ca_xCrO_3$.

Oxygen permeability determined by an electrochemical method

Oxygen permeability normalized by sample thickness (*JL*) through $La_{0.90}Ca_{0.11}CrO_{3-\delta}$ and $La_{0.75}Ca_{0.25}CrO_{3-\delta}$ at 1273 K is determined under a oxygen potential gradient by using an electron blocking method, and the results are shown as symbols in figure 1 and 2 [2,3]. The solid lines in figures represents the "theoretical values", and they are derived from oxygen vacancy content (δ = $V_O^{\bullet\bullet}$ in $La_{1-x}Ca_xCrO_{3-\delta}$) determined by the point-defect model and vacancy diffusion coefficient (D_V) which is assumed to be independent from oxygen partial pressure, $p(O_2)$. The experimental and theoretical value have good coincidence at vacancy diffusion coefficient D_V = 1.5×10^{-10} m^2s^{-1}, which D_V value is very similar to the literature value reported by Yasuda *et al.*(3.01×10^{-10} m^2s^{-1} [4])

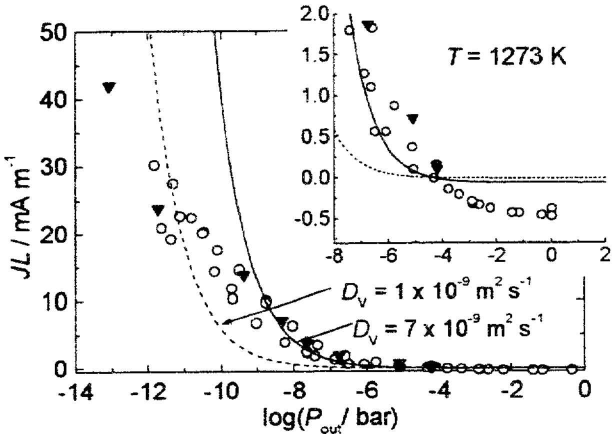

Figure 4 Oxygen Permeability through $La_{0.75}Ca_{0.25}CrO_{3-\delta}$ normalized by sample thickness (L = 0.521 mm), P_{out} atmosphere: ○ CO-CO_2, or O_2-Ar, ▼ H_2-CO_2.
Solid lines are theoretical *JL* with different D_V. P_{in} = 4.8×10^{-5} bar, K_{ox} = 3.22×10^{-8} $bar^{0.5}$.

However, both figure show that some deviation is observed: experimental value becomes larger than theoretical value at $p(O_2) > 10^{-5}$, which probably represents the effect of fast oxygen transport via grain boundary. In contrast, experimental *JL* is depressed when $p(O_2) < 10^{-10}$ bar. Such deviation becomes more significant for $La_{0.75}Ca_{0.25}CrO_{3-\delta}$ having large *JL*, which indicates that the simple treatment with point defect model and constant D_V is no longer sufficient to explain the experimental values. The oxygen permeability through an 1mm-thick interconnect is estimated by extrapolating the experimental value, and result in 10 mA/cm² for $La_{0.90}Ca_{0.11}CrO_{3-\delta}$ and 30 mA/cm² for $La_{0.75}Ca_{0.25}CrO_{3-\delta}$.

Oxygen transport investigated by tracer diffusion and SIMS analysis

In the previous chapter, we showed the assumption of simple defect model and a constant D_V is not sufficient to explain the $p(O_2)$ dependence of oxygen permeability of $La_{1-x}Ca_xCrO_{3-\delta}$. Since the uncertainty is included both in oxygen vacancy content (δ) and in oxygen vacancy diffusion coefficient (D_V), investigation must be carried out for determination of the diffusion coefficient of oxygen ($\tilde{D}$) itself. If the effect of surface reaction is assumed to be negligibly small, the oxygen permeability can be derived from the following equation:

$$JL = -\frac{4F}{RT}\int \sigma_{O^{2-}} d(\ln p(O_2))$$

$$\sigma_{O^{2-}} = \frac{(3-\delta)\tilde{D}4F^2}{V_m RT}$$

Although there are some reports for $\tilde{D}$ $La_{1-x}Ca_xCrO_{3-\delta}$ derived from the relaxation behavior of electronic conductivity [5], or for tracer diffusion coefficient (D^*) of $La_{1-x}Ca_xCrO_{3-\delta}$ [6], however, the obtained diffusion coefficients are quite large than expected values from JL. We have obtained the $p(O_2)$ dependence of oxygen tracer diffusion coefficient (D^*) for $La_{0.80}Ca_{0.22}CrO_{3-\delta}$ in the $p(O_2)$ range of 1 ~ 10^{-13} bar by using Ar-$^{18}O_2$ or H_2-$C^{18}O_2$ gas mixture and secondary ion mass spectrometry (SIMS, CAMECA ims5f), and the results are shown in figure 3. The data is also plotted as a function of calculated oxygen vacancy content (δ) in figure 4 in which the δ is estimated by using the following equation originated from the point defect model with the equilibrium constant $K_{ox} = 3.22 \times 10^{-8}$ bar$^{0.5}$.

$$p(O_2) = \left[\frac{K_{ox}(x-2\delta)^2(3-\delta)}{(1-x+2\delta)^2\delta}\right]^2$$

The slope of log D^* vs. log δ should be almost unity if the constant D_V is assumed on the relation $(3-\delta)D^* = \delta D_V$. However, the present data show the slope ca. 0.7 in the δ range of 10^{-9} ~ 10^{-1}. This deviation is probably due to the uncertainty of δ or some $p(O_2)$ dependence of D_V. Future investigation is required to solve this problem.

The oxygen permeability derived from the obtained D^* ($\cong \tilde{D}$) is shown in figure 5 as a dotted line, which exhibits much better coincidence with the experimental data than theoretical values. A little lower oxygen permeability is estimated, which is definitely because the D^* data are of $La_{0.80}C_{0.22}CrO_{3-\delta}$. $La_{0.75}Ca_{0.25}CrO_{3-\delta}$ is supposed to have larger D^* which may result in better coincidence with experimental data.

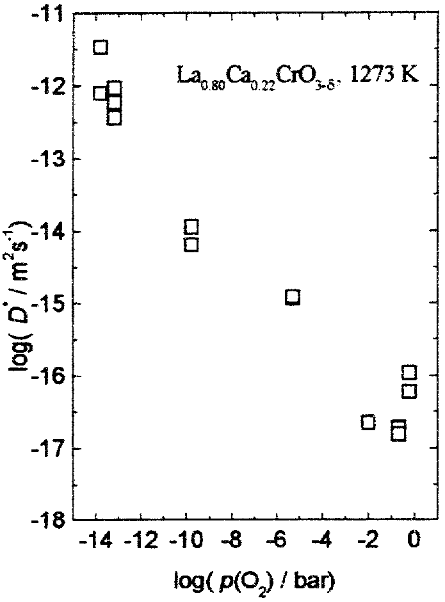

Figure 3 Oxygen tracer diffusion coefficient as a function of oxygen partial pressure.

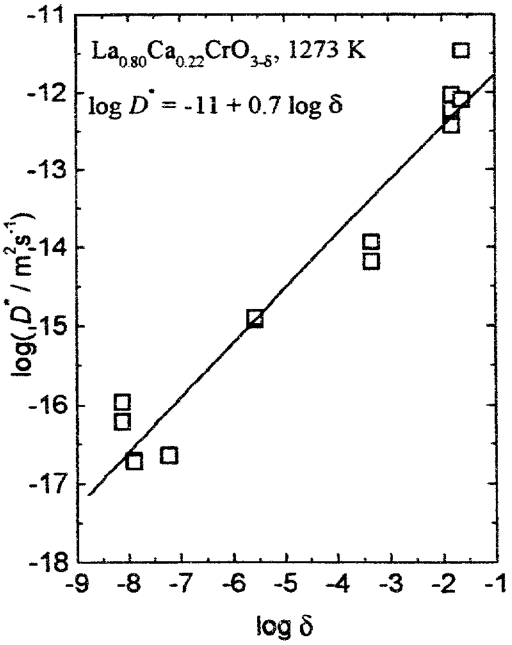

Figure 4 Oxygen tracer diffusion coefficient as a function of oxygen vacancy content.

Acknowledgments

Authors would like to thank Professor H. J. M. Bouwnmeester at University of Twente, and Prof. J. A. Kilner at Imperial College, UK for giving valuable comments. The cooperation of TOTO Ltd. Japan is greatly acknowledged for making $La_{0.75}Ca_{0.25}CrO_3$ samples.

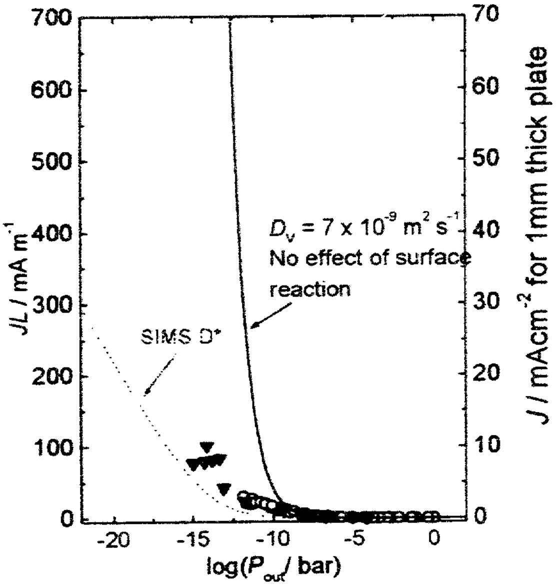

Experimental data and theoretical estimation of oxygen permeability through $La_{0.75}Ca_{0.25}CrO_{3-\delta}$: 1273 K,
$P_{in} = 4.8 \times 10^{-5}$ bar, $L = 0.541$ mm
○ , ▼ observed data

References

[1] H. J. M. Bouwnmeester, and A. J. Burggraaf, in Fundamentals of Inorganic Membrane Science and Technology, ed. by A. J. Burggraaf and L. Cot, Elesevier Science B. V., The Netherlands, p. 435 (1996).

[2] N. Sakai, T. Horita, H. Yokokawa, M. Dokiya and T. Kawada, *Solid State Ionics*, **86-88**, 1273 (1996).

[3] N. Sakai, T. Horita, H. Yokokawa, M. Dokiya, T. Kawada, A. Ueno, K. Hiwatashi and M. Aizawa, in the Proceedings of the 2nd European SOFC Forum, ed. by B. Thorstensen, ISBN 3-922148-19-O, p.531 (1996).

[4] I. Yasuda and T. Hikita, *J. Electrochem. Soc.*, **141**, 1268 (1996).

[5] I. Yasuda and M. Hishinuma, *J. Electrochem. Soc.*, **143**, 1571 (1996).

[6] I. Yasuda, K. Ogasawara and M. Hishinuma, in the Proceedings of the 2nd International Symposium on Ion and Mixed Conducting Ceramics, ed. by T. A. Ramanarayanan, W. L. Worrel, H. L. Tuller, The Electrochemical Sociery Proceedings Volume 94-12 p.164 (1994).

CORRELATED PERCOLATION MODEL OF SOFC ANODES. PATTERNS OF DEGRADATION

J.Abel*, A.Ioselevich[=], A.A.Kornyshev*, and W.Lehnert*

**Institut für Energieverfahrenstechnik, Forschungszentrum Jülich GmbH*

[=] *Institut für Theoretische Physik, RWTH Aachen*

A problem for solid oxide fuel cells (SOFC) is their performance variation in time[1]. "Degradation" of the porous metal-solid electrolyte anode due to changes in the composite structure may give a key contribution to such variation. Characterization of these changes in relation to performance is a subject of great current interest[2]. At SOFC typical operation temperatures (≈950°C), high enough to provide fast anion transport in the electrolyte but lower than the melting temperature of the metal in the cermet, the metal exhibits high plasticity. Poor "wetting" of solid electrolyte grains by the metal may result in a spontaneous sintering[3] of neighboring metal particles. This affects the three phase boundary where the anode reaction takes place; the amount of the boundary usually decreases which diminishes the generated current. The process is complex because an occurrence of each sintering act depends on the surrounding of the grains to coalesce, whereas the surrounding changes in the course of the agglomeration. A *dynamical correlated percolation model* of the process was developed and investigated in Ref.[4] using computer simulation.

The model of Ref.[4] considers sites on a densely packed fcc lattice, which are occupied randomly by either a metal or a solid electrolyte particle, or a pore. Sintering (fusion) of two given metal particles was assumed to depend on the neighbors of the bond between them. As in the fcc lattice every bond has four nearest neighbors, one may distinguish stronger or weaker constraints on sintering, depending on *how many solid electrolyte neighbors is sufficient to block the fusion event.* The cases of *hard* and *weak* constraints where distinguished in Ref.4. Under the hard one it is enough to have only one solid electrolyte neighbor to block the fusion, while the weak constraint requires four such neighbors. Two extreme modes of sintering were considered separately: a *weak sintering* act detaches one of the fusing particles from its metal neigbors, while a *strong sintering* act opens a pore behind the particle. An algorithm for the simulations of a sequence of sintering events in real time was developed, and their effect on the variation of the amount of the chemically active three phase boundary was simulated for the two extreme modes of and the two constraints on sintering.

The problem of anode performance (or anode resistivity) reduces to the problem of correlated *statistical geometry* (to the calculation of the *active* three phase boundary) if one assumes that there is no diffusion limitations for the O^{2-} ions, i.e. the overall process is reaction-limited. The active boundary is proportional to the number of *active bonds*, a key notion in Ref.[4]. A bond between two neighboring sites, one of which occupied by a metal and the other one by a solid electrolyte particle, will be called *active* if -

- the metal sites belongs to a cluster connected to the current collector,
- the solid electrolyte site belongs to a cluster connected to the membrane,
- the bond has an empty site as neighbor, a "pore", which belongs to the cluster of empty sites connected to the current collector with gas channels.

The subject of Ref.[4] was the calculation of the variation of the number of active bonds in the course of the spontaneous sintering process. The plots shown in Ref.[4] give the following lessons.

- The active three phase boundary in SOFC anodes does degrade with sintering of metal particles. The degradation always reaches saturation once the number of particles capable for sintering is exhausted.
- The degradation is *catastrophic* when the content of the metal component is close to the percolation threshold[5]. Then, after a few sintering events the electronic percolation path between the current collector and membrane breaks down, and the three phase boundary scales as a surface, while it starts from the volume-scaled value.
- The same is true when the system is initially close to the percolation threshold in porosity, unless the sintering open new pores, as in the "strong sintering" mode when one observes a rise in amount of the active three phase boundary, i.e. anode improvement rather than degradation. However, in the case of light constraints on sintering such an increase is always overwhelmed by degradation driven by further agglomeration of metal particles. Observations of non-monotonous changes would be indicative of this type of sintering.
- The degradation is sensitive to the constraints imposed by the solid electrolyte backbone on the elementary act of fusion of two neighboring metal particles. The vacancies in the solid electrolyte matrix in the neighborhood of the pair of metal particles make the fusion possible. The constraint, which requires only one such vacancy for the elementary act of sintering to take place leads to catastrophic degradation. "Harder" constraints make the probability of the elementary acts less probable, and - unless the starting composition is very close to the percolation threshold - the degraded values of the three phase boundary have the same order of magnitude as in the starting configuration.

- Providing stronger constraints on sintering is shown to be crucial for depressing this degradation mechanism. Therefore, special procedures to hamper the spontaneous sintering of metal particles in the composite would be of primary importance for manufacturing long-term-stable anodes. The temperature increase would likely to reduce the constraints on sintering, and thereby stimulate degradation.
- Even when the measures providing "hard constraints" on sintering are undertaken, the porosity and the relative portion of the metal component in a sample must not lie too close to the corresponding percolation thresholds. Otherwise, there will be a a moment when the active three phase boundary will drop down catastrophically. Ref.[4] shows the diagrams determining the range of proportions of metal, electrolyte and pore components which would retain the volume-scale magnitude of the active three phase boundary after degradation. Though the particular values depend on the lattice structure they may be, nevertheless, used for orientation.

Ref.[4] focused entirely on the statistical geometry aspects of the problem. An investigation of the degradation in the correlated resistor network (which attributes (i) *reaction resistors* to the *active* bonds between the metal and solid electrolyte particles, (ii) *ion transport resistors* to the bonds between solid electrolyte particles and (iii) *electron transport resistors* to the bonds between the metal particles) is in progress[6]. It illuminates the interplay between the ion transport and the geometry of the reaction-active space, provides an estimate of the actual thickness of the reaction zone measured from the edge of the membrane, and describes its changes in time. The results reported in the Ref.[4] have a direct significance only for sufficiently thin samples, for which the ion diffusion limitations could be assumed negligible. The investigation of the more general case[6] allows to establish the validity criteria of this assumption. In ref.6 we calculate the current through the active bonds and show, thereby, that the stronger the reaction limitations the deeper lying fragments of the three phase boundary inside the anode are involved into the current passage, while when the ion diffusion limitations dominate only the portions of the three phase boundary very close to the membrane are used.

The statistical geometry study performed in Ref.[4] and the correlated resistor network calculations of Ref.6 deal, of course, with a strongly idealized model: just let the metal and the solid electrolyte particles be of significantly different size, the whole "fcc-construction" would fail. However, it would not have been wise to start with a percolation model on a more complicated, disordered, random or even fractal lattice, before understanding the basic effects on the fcc lattice. Furthermore, the fcc lattice is certainly a better model for a random packing than the cubic lattice.

A comparison of the cross-section microphotos for anodes before and after degradation as a function of the current-voltage history could be instructive for understanding degradation. However, the structure monitoring, which would not use such brutal, destructive methods as imaging of the composite cross-sections or cracks, but could distinguish metal, ceramic and pore components *in situ* is, today, a pressing necessity and a challenge for material science. The study performed in Refs.[4,6] shows the relevant structural features of the particle agglomeration to focus on in that type of studies.

REFERENCES

1. *Fuel Cell Systems*, L.J.M.J.Blomen and M.N.Mugerva, Editors, Plenum, New York, 1993.

J.Appleby and F.R.Foulkes, Fuel Cell Handbook, Krieger, Malabar, Florida (1993).

2. N.Q.Minh, *J.Am.Ceram.Soc.* **76**, 563 (1993)
3. Ja.E.Geguzin, *Physik des Sinterns*, VEB Deutsche Verlag für Grundstoffindustry, Leipzig (1973), in German; original: *Physics of Sintering*, Nauka, Moscow (1967), in Russian.
4. A.Ioselevich, A.A.Kornyshev, and W.Lehnert, *J.Electrochem.Soc.* 1997 (in Press).
5. D.Stauffer and A.Aharony, *Introduction to Percolation Theory* (Taylor and Francis, London, 1992).
6. A.Abel, A.A.Kornyshev, and W.Lehnert (in Preparation).

Improved power density at 800°C with standard SOFC components, emphasizing the anode

J. Van herle, R. Ihringer, A.J. McEvoy

Laboratory of Photonics and Interfaces, Department of Chemistry,
Swiss federal Institute of Technology EPFL, 1015 - Lausanne

The ideal receipe for Ni-YSZ cermets is still controversial. Several solutions exist and may differ as widely as (i) mixing fine NiO with coarse YSZ particles or (ii) rather the inverse, mixing coarse NiO with fine YSZ powder. It is plausible that both fine and coarse YSZ particles are required, the latter to fix the frame of the cermet structure through which small NiO can percolate and assure electronic conductivity after reduction, the former to improve the adhesion to the YSZ electrolyte upon sintering of the anode and, during operation, to avoid nickel aggomeration to some extent.
Adding to this the facts that (i) lower nickel amount in the cermet will delay agglomeration (hence degradation) and (ii) that the use of smaller Ni particles will increase the TPBL (hence lower the interface resistance), we formulated our standard receipe as follows : 56 wt% of fine NiO (1-2 µm) mixed with 44 wt% of crushed 8YSZ of very broad particle size distribution (0.2-15 µm), to give 40 vol% Ni in the reduced cermet.

Screenprinted anodes of these mixtures were fired at 1300°C on 8YSZ electrolyte tiles (30 x 30 x 0.125 mm), fabricated in our lab by tape casting, and tested at 700-900°C in H_2/H_2O (3%) by current-overpotential and impedance measurements. As presented in the figures on the following pages, the anode voltage loss at around 800°C amounted to typically 150 mV for 1 A/cm^2 current density. This behaviour was reproduced from one screen-printing ink to the other. After initial activation, no degradation over test durations of up to 400 h was noted. Impedance spectroscopy evaluation with varying current featured a rapid and important decrease in high frequency interface resistance as well as the appearance of an inductive loop at low frequencies. The latter is related to the adsorbed intermediates, H^+_{ad} and H_2O_{ad}, whereas the former corresponded to charge transfer limitation across the TPB region, involving adsorbed hydrogen on the nickel and surface oxygen species on the YSZ ceramic. Current-overpotential curves could be fitted with the Butler-Volmer type equation as established in the literature. The most effective anode will consequently be one that shows the highest possible TPB length. This has to be weighted against the need for stabilisation against nickel agglomeration, which implies reducing the TPBL to some extent.

Cell tests were conducted against $La_{0.65}Sr_{0.3}MnO_3$ cathodes, screenprinted and fired at 1100°C. Acceptable power output of 0.35 W/cm^2 at 800°C was obtained. By impregnating both sintered cathode and anode with silver (1 mg/cm^2) and ruthenium (0.15 mg/cm^2) metal catalysts respectively, this value further improved to 0.48 W/cm^2 at the same temperature. As the OCV of our small cells lay rather low due to an "open flow" testing arrangement, higher values can still be expected. High power densities of 0.5 W/cm^2 with low fuel utilisation conditions, as was the case here, have to be demonstrated in order to achieve practical power output (0.2 W/cm^2) at realistic operating conditions (u_f 70%).

1	YSZ > NiO or YSZ < NiO ?	mixture of both (YSZ of broad PSD)
2	interface resistance inversely proportional to TPBL	small NiO
3	lowest Ni percolation level	40 vol% Ni
4	Activation, Performance and Stability	800°C / 150 mV η / 1 Acm^{-2} 400 h
5	Reproducibility	good
6	Reaction mechanism. Impedance	Charge transfer across TPBL H^+ intermediate adsorbate
7	Cell power output	0.35 resp. 0.48 Wcm^{-2} / 795°C 0.66 resp. 0.82 Wcm^{-2} / 890°C

REPRODUCIBILITY

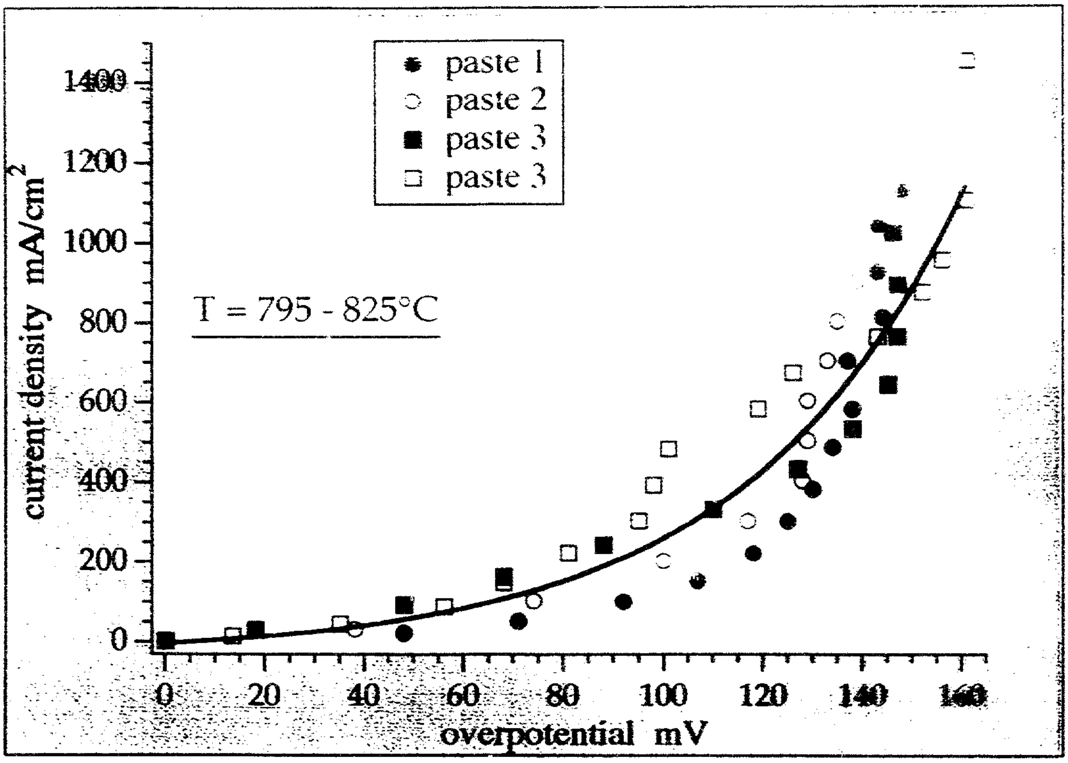

PERFORMANCE & STABILITY

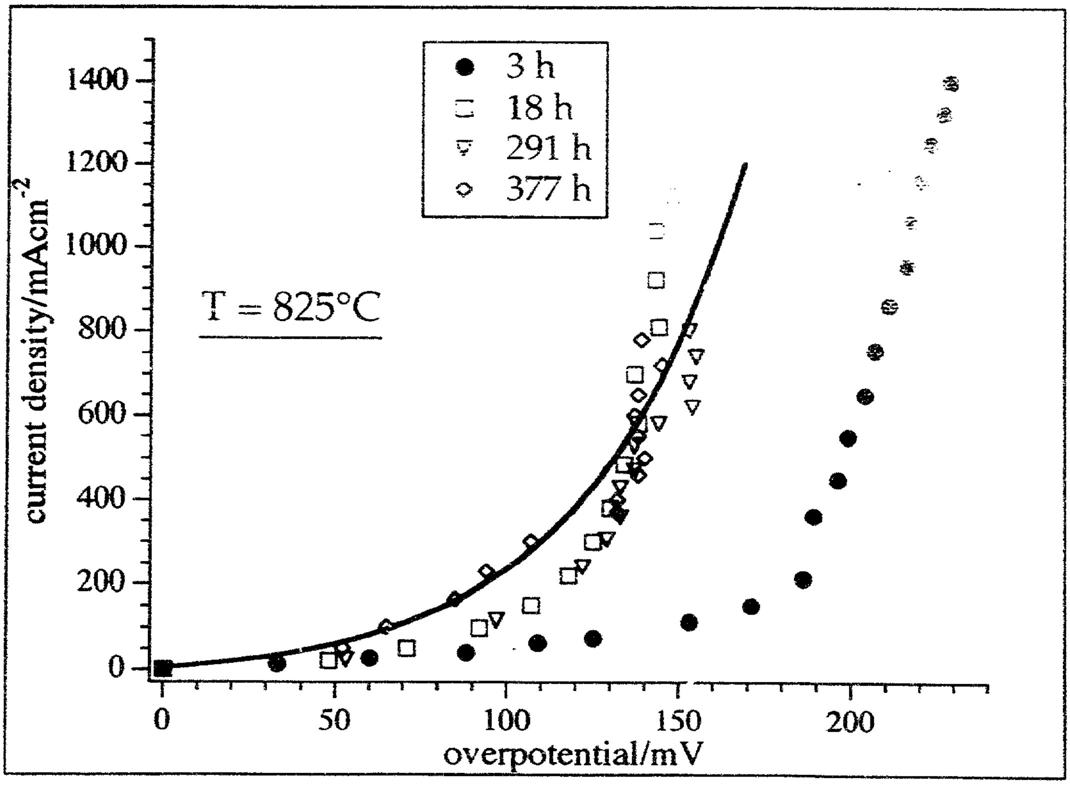

ANODE IMPEDANCE UNDER CURRENT LOAD

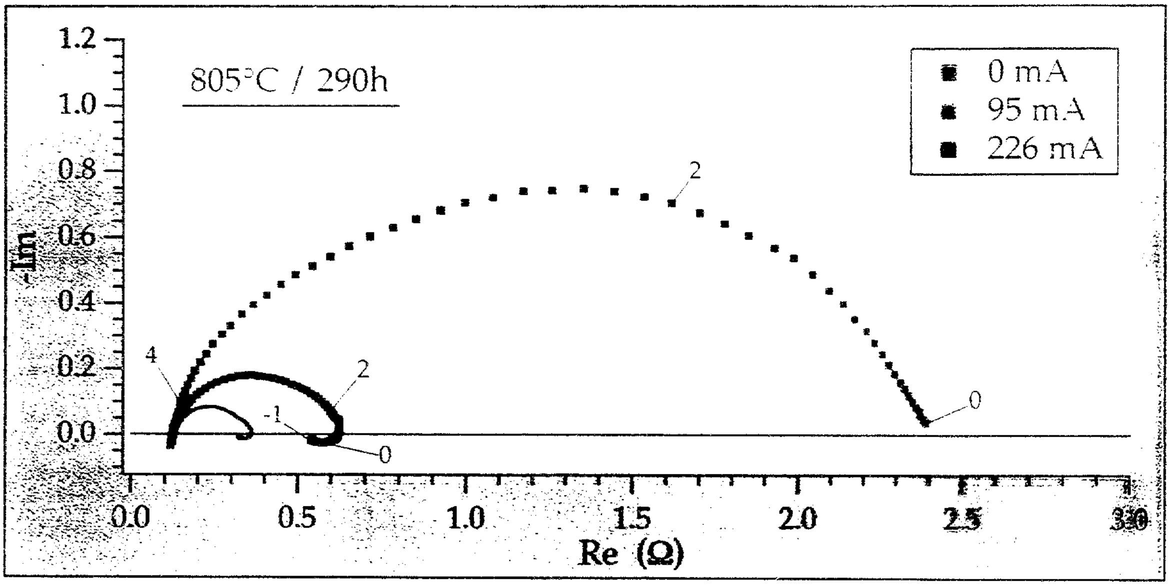

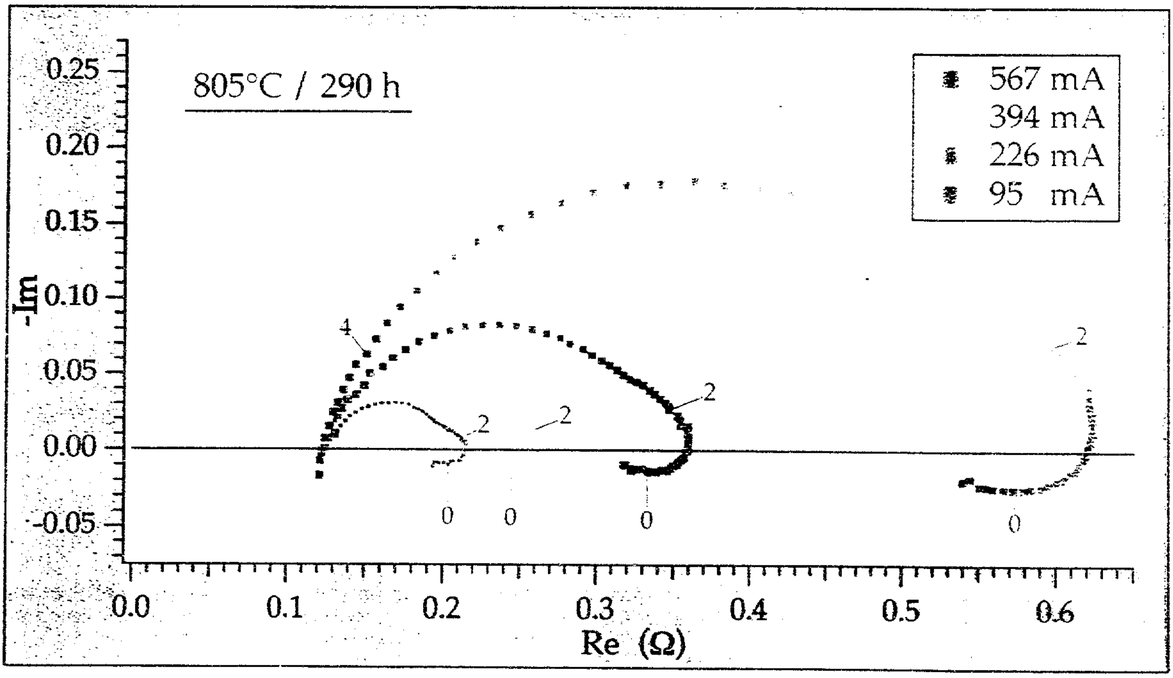

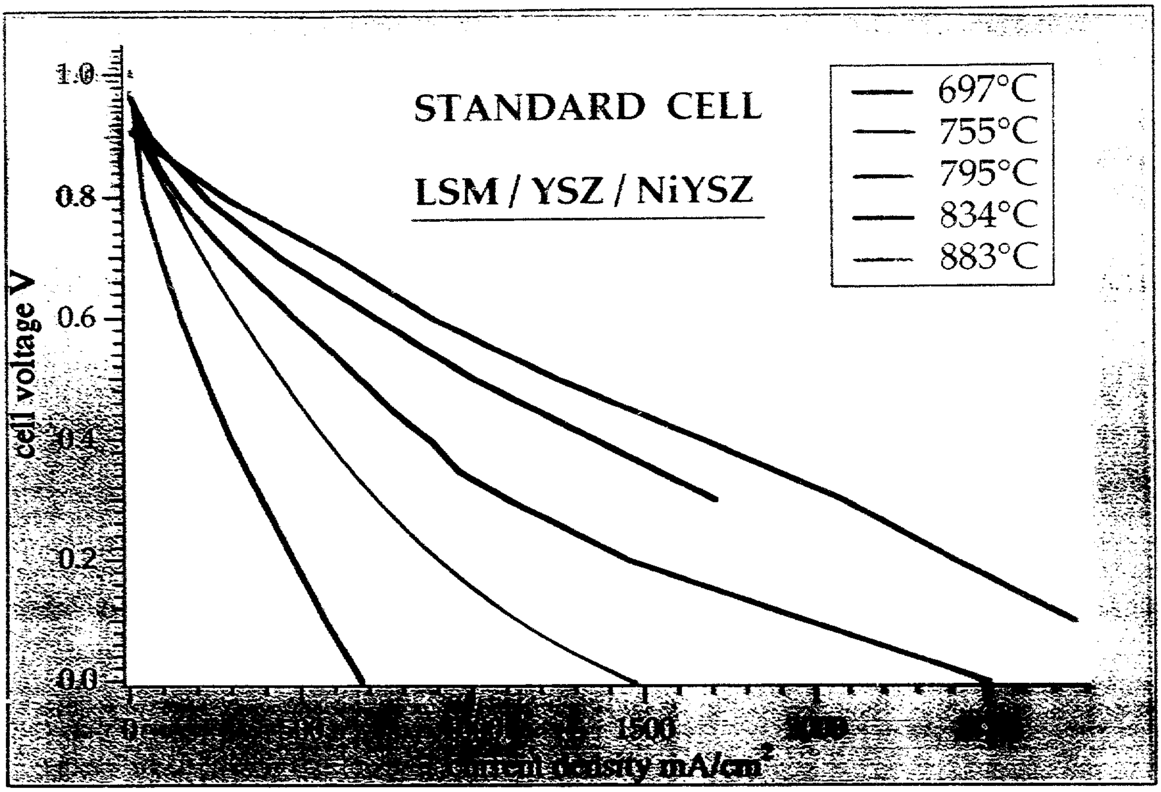
STANDARD CELL
LSM / YSZ / NiYSZ
697°C
755°C
795°C
834°C
883°C
cell voltage V
1.0
0.8
0.6
0.4
0.2
0.0
0
500
1000
1500
2000
2500
current density mA/cm²

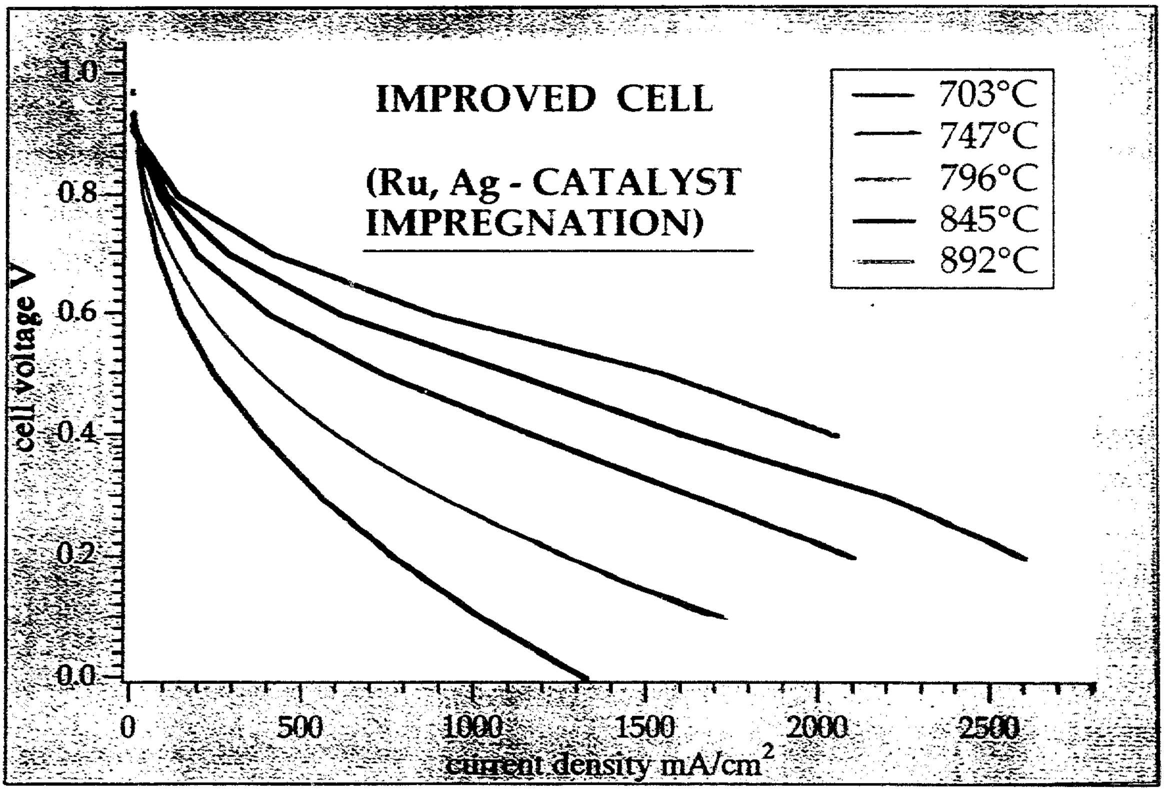
IMPROVED CELL
(Ru, Ag - CATALYST
IMPREGNATION)
703°C
747°C
796°C
845°C
892°C
cell voltage V
1.0
0.8
0.6
0.4
0.2
0.0
0
500
1000
1500
2000
2500
current density mA/cm²

Impedance Modelling of Composite Electrodes

Svein Sunde[†]
Materials Department, Risø National Laboratory, DK-4000 Roskilde, Denmark

Introduction

Composite electrodes consisting of particles of an electronic conductor and a solid electrolyte are used in solid oxide fuel cells (SOFCs) operating at high temperatures (typically 800 to 1000 °C) [1,2]. For the SOFC anode, cermets of Ni and yttria-stabilized zirconia (YSZ) are common. The principal arguments for the use of such electrodes in SOFCs, are associated with stability and compatibility [1,2], but many authors now agree that the electrolyte particles may play an active part also in reducing polarization losses in composite electrodes [2,3].

Impedance measurements are frequently used for characterizing composite anodes and cathodes for SOFCs, as well as in studies of single-phase porous cathodes or electrodes with simplified geometry on solid electrolytes (References in [3] through [6]). Often, the spectra are merely used as instruments for obtaining the polarization resistance of the electrode, by separating out the ohmic resistance. In other studies attempts are made to interpret impedance data in terms of reaction mechanism, despite the fact that composite electrodes possess a very complex structure, in some respects resembling porous electrodes in aqueous electrochemistry [3]. In this work, we intend to show by computer simulations that the shape of the impedance-plane plot for a composite may deviate significantly from that for the corresponding single electrolyte-electrode interface, and discuss the origin of these differences.

Impedance Model

For the calculation of the impedance of the composites it is assumed that the electrode and electrolyte particles occupy the nodes of a continuous lattice. The lattices are generated on computer by sequential deposition of such particles in random order to create a random packing of particles ([5] and references therein). The composites are made in the shape of sheets, which are furnished with current collectors at opposite ends (x=0 and x=L, L being the composite thickness) and connected to the outermost layers of particles [4]. In the present work, one of the current collectors was always taken to consist of the same metal as the electrode particles, whereas the other was taken to be a bulk electrolyte of the same material as the electrolyte particles. The dimensions for all lattices were equal in all directions. The x-direction was taken as the average direction of current flow. In y- and z-directions, cyclic boundary conditions were employed for all lattices.

Between each pair of particles i and j in both lattice types, current is conducted through a 'bond admittance' Y_{ij}, the value of which will depend on which particles reside in sites i and j. (We use a dimensionless formulation of the model here, and Y_{ij} is, as all other variables, dimensionless. For details, see Ref. [6].) All nearest neighbours are therefore identified after having produced the particle packings as described above [5]. From the list of neighbours an impedance network is constructed. Between particles i and j of the same kind Y_{ij} is ohmic, and the conductance of such a contact has been estimated as $\kappa l_{ij}/4$, where the particle

---

[†] Present address: Centre for Materials Science, Department of Chemistry, University of Oslo, Gaustadallèen 21, N-0371 Oslo, Norway

conductivity is κ and the neck circumference is l_{ij} [5]. Therefore, we use

$$Y_{ij} = K\Lambda_{ij}/4 \qquad (1)$$

for a dimensionless bond conductance in this case. In Eq. 1, K is a dimensionless conductivity and Λ a dimensionless neck circumference [6]. For the admittance Y_{edel} of a bond between an electrode and an electrolyte particle we will use (see References [3] through [6])

$$Y_{edel} = \left[2K_{ed}^{-1} + 2K_{el}^{-1} + Y_p^{-1}\right]^{-1} \qquad (2)$$

where K_{el} and K_{ed} are the conductivities of electrolyte-electrolyte bonds and electrode-electrode bonds, respectively. Y_p is the admittance associated with the adsorption, desorption and electrochemical steps occurring at the contact, plus a double-layer admittance. We assume that a potential varying harmonically with time and with the dc value kept at the open circuit potential with respect to some reference electrode is applied. Application of the Kirchhoff current-law to site i now gives [3-8]

$$\hat{I}_i = \Sigma_j \hat{I}_{ij} = \Sigma_j (\hat{H}_j - \hat{H}_i) Y_{ij} \qquad (3)$$

where $\hat{H}_i$ is the complex amplitude of the voltage at site i, $\hat{H}_j$ is the dimensionless complex amplitude of the voltage at site j, $\hat{I}_i$ the dimensionless complex amplitude of the external current going into site i, and $\hat{I}_{ij}$ the complex amplitude of the current flowing through the bond (all dimensionless). $\hat{I}_i$ is zero for all sites except at the current collectors, into which a finite current flows. As boundary conditions for the set of coupled difference equations, Eq. 3, zero voltage amplitude at one end of the lattice and a finite value at the other were used. This system of equations was solved numerically by writing complex versions of the routines for solving linear sets of equations by the preconditioned biconjugate-gradient method in Ref. [9]. The total current was then calculated by summing all (complex) currents entering the current collectors at either side, and the impedance calculated as the ratio between the complex amplitude of applied voltage and the resulting total current amplitude.

Results and Discussion

The majority of published impedance data for SOFC electrodes are presented in impedance-plane plots, i. e. plots of minus the imaginary part v. the real part of the impedance. We will therefore use a similar representation here, and concentrate on the features apparent in these plots.

In Figure 1 is shown the imaginary part v. the real part of the impedance $Z_p=1/Y_p$ for a single electrode-electrolyte contact, calculated from the generic three-step reaction model in Ref. [6]. The details of this model is not important here, but we note that one arc dominates the spectrum, and that the impedance was in this case excellently approximated by the impedance of a resistor in series with a parallel circuit with a capacitor in one branch and another resistor in the other. In Figure 2 is shown the corresponding plot for a composite with a ratio between the electrolyte-particle radius and the electrode-particle radius equal to 1/2. The volume fraction of electrode-particles is 0.5. The plot now contains two clearly distinguishable arcs. The low-frequency arc corresponds in shape and frequency range to the impedance shown in Fig. 1, whereas that at high frequencies has no equivalent in the single-contact spectrum, Fig. 1. The impedance spectra of composites were for the parameter set used in Fig. 1 completely insensitive to the value of the double-layer capacitance, and it made no difference whether the

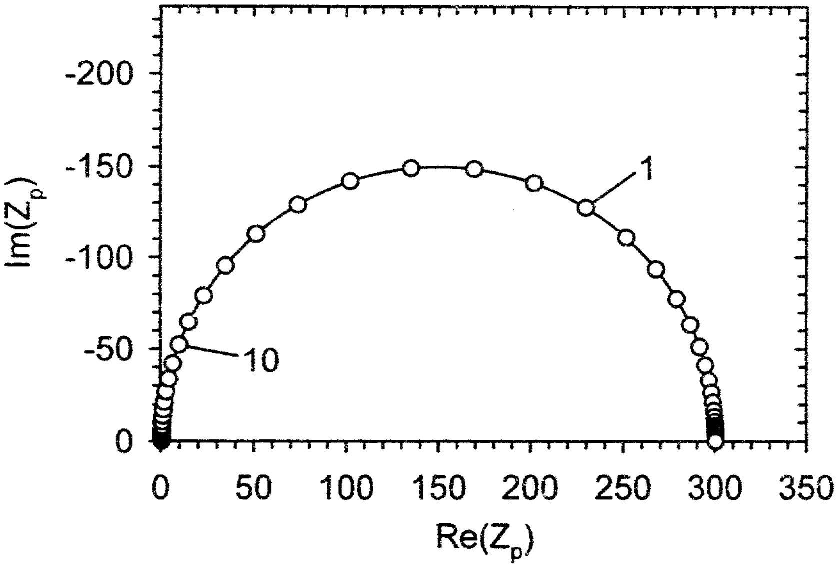

Fig. 1. Imaginary part v. real part of the impedance Z_p for a single electrode-electrolyte contact. Dimensionless angular frequencies 1 and 10 are indicated.

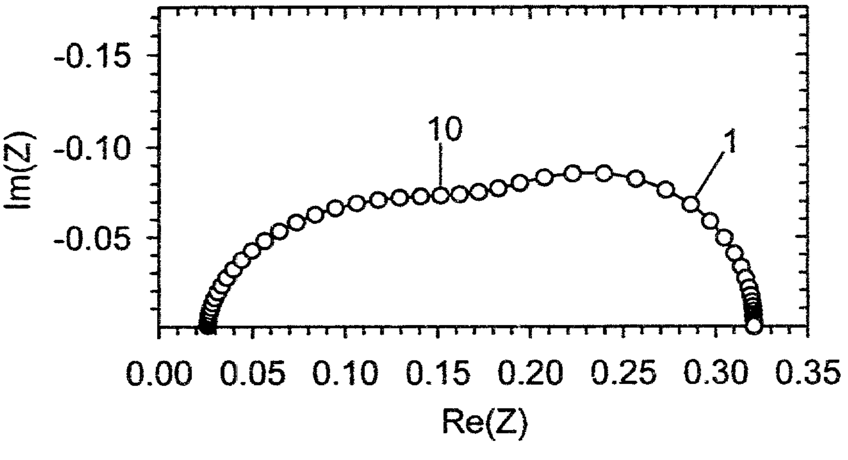

Fig. 2. Imaginary part v. real part of the impedance Z of a composite with volume fraction of electrode particles of 0.5. Thickness is 40 particle radii, and the ratio between electrolyte-particle radius and electrode-particle radius is 1/2. Dimensionless angular frequencies 1 and 10 are indicated.

calculations were performed with the simplified equivalent circuit or the full expression for Y_p [6]. (As a consequence of the large number of electrolyte-electrode contacts in the composite, the impedance of the composite is at any frequency much lower than that of Fig. 1, see Refs. [3,4].)

From Figures 1 and 2 it thus appears that features not solely associated with the interfacial impedance of a single electrode-electrolyte contact appear in the impedance of the corresponding composite. This result may be rationalized in terms of the different types of interfaces present in the composite, as introduced in Ref. [3]. The interfaces responsible for reducing the polarization resistance at intermediate volume fractions of electrode particles are those between electrode clusters connected to the current collector and electrolyte clusters connected to the bulk electrolyte [3]. The impedance of these corresponds roughly to a number of single-contact impedances in parallel, and results in a low-frequency arc in the spectrum of the composite which has its equivalent in the single-contact spectrum. In addition, the composite may contain electrode clusters entirely surrounded by electrolyte particles [3]. These clusters are also electrically connected to the surrounding electrolyte particles by a number of single-contact impedances in parallel, but are not in contact with the current collector. When current is passed through the composite, these electrode enclaves are at low frequencies simply bypassed by the surrounding electrolyte clusters due to the high interfacial impedance, insulating them from the surrounding electrolyte cluster. With increasing frequency, however, the interfacial impedance drops (Fig. 1), and the enclosed electrode clusters do to an increasing extent conduct current. (Usually the conductivity of electrode particles is by orders of magnitude larger than that of the electrolyte particles, see Refs. [3-5] and references therein.) In this case, new time constants may appear in the system, formed between the impedance of an enclave's interface with the surrounding electrolyte cluster, and the ohmic resistance of the latter. This explanation was found to agree well with a more extended set of calculations than those presented here [6].

Acknowledgements

This work was performed under the Danish SOFC project, and sponsored by the Danish Energy Agency and by the Danish utility group ELSAM. The author wishes to acknowledge useful discussions with coworkers at Risø National Laboratory.

REFERENCES

1. A. Hammou, in *Advances in Electrochemical Science and Engineering*, Vol. 2 (Edited by H. Gerischer and C.W. Tobias), p. 87 - 139, VCH, Weinheim (1992)
2. N. Q. Minh and T. Takahashi, *Science and Technology of Ceramic Fuel Cells*, Elsevier, Amsterdam (1995)
3. S. Sunde, *J. Electrochem. Soc.*, **143**, 1930 (1996)
4. S. Sunde, *J. Electrochem. Soc.*, **142**, L50 (1995)
5. S. Sunde, *J. Electrochem. Soc.*, **143**, 1123 (1996)
6. S. Sunde, *Electrochimica Acta*, To be published (1996)
7. D. Stauffer and A. Aharony, *Introduction to Percolation Theory*, Revised 2nd ed., Taylor & Francis, London (1994)
8. S. Kirkpatrick, *Rev. Mod. Phys.*, **45**, 574, (1973)
9. W. H. Press, S. A. Teukolsky, W. T. Vetterling, and B. P. Flannery, *Numerical Recipes in Fortran*, 2nd ed., p. 63 - 82, Cambridge University Press, (1994)

CERMET CATHODES COMPOSED OF SMALL PARTICLES: MODEL AND VALIDATION

P. Costan. gna[a], V. Antonucci[b], P. Costa[a], E. Arato[a]

[a] ISTIC, Istituto di Ingegneria Chimica e di Processo 'G. B. Bonino'
via Opera Pia 15, Genova, Italy

[b] CNR - TAE, Istituto Trasformazione e Accumulo Energia
via Salita Santa Lucia 39, Messina, Italy

INTRODUCTION

Cermets formed by a mixture of electronic and ionic conductor particles are at present under study as possible solid oxide fuel cell (SOFC) electrodes (Fig. 1). In order to correctly evaluate the electrode performance, simulation models have to take into account the electrode composition and granulometry, in particular with reference to the percolation thresholds of the electronic and ionic conductor phases.

The evaluation of the electrode performance for a low ratio electrode thickness/particle diameter (a/d) requires a Monte Carlo technique [1]. In the following the simulation of an electrode characterised by a/d>100 will be presented on the basis of an analytical model [1,2] and a comparison with literature experimental data will be discussed as well. Some considerations concerning the electrode optimisation will also be presented

THEORY

The model [2] is based on the following assumptions:

- steady state conditions,
- one-dimensional model as a function of the x co-ordinate (Fig. 1),
- each of the two conducting phases is considered as continuous and homogeneous, having a resistivity independent of the x co-ordinate,
- uniformity of temperature, pressure, reactant and product concentration over the x co-ordinate.

The following equations have been considered:

- Ohm's law for the charge transfer along the two conducting phases:

$$\nabla V=-\rho^{eff} i \qquad \text{Eq. 1}$$

- charge balance:

$$\mathrm{div}(i_{io})=-\mathrm{div}(i_{el})=Ai_n \qquad \text{Eq. 2}$$

- linearised form of the Butler-Volmer equation for the electrode kinetics.

$$i_n=i_0\eta F/(R_gT) \qquad \text{Eq. 3}$$

The above equations can be integrated analytically. The results can be expressed on the basis of the total electrode resistance R:

$$\frac{1}{R}=\frac{I_{tot}}{\eta_0}=\frac{\Gamma\sinh(\Gamma)}{a\left(\rho_{io}^{eff}+\rho_{el}^{eff}\right)\left\{\cosh(\Gamma)+\Omega\left[2+\Gamma\sinh(\Gamma)-2\cosh(\Gamma)\right]\right\}} \qquad \text{Eq. 4}$$

In cermet electrodes, ohmic and polarisation phenomena are not strictly 'in series' with each other, and consequently the total electrode loss is not given by a univocal sum of ohmic losses and polarisation losses. So, we used the above definition (Eq. 4) for the electrode resistance R, where η_0 is the overall electrode overpotential:

$$\eta_0=\left(V_{io}^{eq}-V_{el}^{eq}\right)-\left(V_{io}\big|_{x=a}-V_{el}\big|_{x=0}\right) \qquad \text{Eq. 5}$$

and where Γ can be named as 'Thiele modulus' [3], in analogy with chemical catalysis, and is the ratio between the electrode thickness and the characteristic thickness where the electrochemical reaction takes place:

$$\Gamma = \frac{a}{\sqrt{\dfrac{R_g T}{i_0 A F(\rho_{io}^{eff} + \rho_{el}^{eff})}}} \qquad \text{Eq. 6}$$

Finally, in Eq. 4 Ω is:

$$\Omega = \frac{\rho_{io}^{eff} \rho_{el}^{eff}}{\left(\rho_{io}^{eff} + \rho_{el}^{eff}\right)^2} \qquad \text{Eq. 7}$$

A few parameters appearing in the model, i.e. the effective resistivities ρ^{eff}_{io}, ρ^{eff}_{el} and the overall active area for the electrochemical reaction A, have been expressed [2] as a function of the electrode composition by means of the theory of particle co-ordination number in a random packing of spheres [4,5], together with percolation theory [6]. In particular A has been calculated considering the overall contact area between electronic and ionic conducting particles being electrochemically active; the fact that small particles have been considered in the following (d=0.1 μm) supports this hypothesis.

RESULTS

The model previously discussed has been applied to the simulation of a cermet cathode composed of a mixture of EDB, i.e. $(Bi_2O_3)_{0.7}(Er_2O_3)_{0.3}$, and Pt. We set the exchange current density at i_0=400 A/m^2; the electrical conductivity of pure Pt was set at 2,2 10^6 S/m [7]. Literature data [8] indicate a conductivity of 37 S/m at 700°C for EDB; below, the EDB conductivity has been assumed to be equal to 20 S/m at 900°C. The diameter of Pt and EDB particles has been taken to be 0.1 μm.

In Fig. 2, 1/R is plotted as a function of the electrode composition: the percolation thresholds are clearly visible at a volume fraction φ=0.294 for each of the phases present in the structure. Maximum performance is achieved when φ_{el}^{max} = 0.37, for an electrode thickness of 90 μm. The 1/R value is about 8.2 10^4 S/m^2, corresponding to an overvoltage of 0.037 V at a current density I_{tot}=3000 A/m^2.

Some optimisation considerations can be made on the basis of the theoretical model: it can be demonstrated that the maximum value of 1/R is reached near to the percolation threshold of the electronic conducting phase for a thick electrode (a≈90 μm), and for φ_{el}≈0.5 for a thin electrode (a≈10 μm).

In the region outside the thresholds the model gives the approximated result 1/R=0, while literature experimental data [9] show 1/R≈0.4 10^4 S/m^2 for a pure platinum electrode coupled with an EDB electrolyte. So, performance outside the thresholds is much lower than the values obtained within the thresholds; the model result 1/R=0 is affected by a degree of uncertainty and it only indicates an electrode with such characteristics as not to be very interesting from an applicative point of view.

In Fig. 3 and 4 the preceding theoretical results for 1/R have been compared with the literature experimental data [9]: the agreement is satisfactory. As the experimental data do not take the ohmic contribution into account, the ohmic loss has been roughly evaluated as the total electrode resistance in the case where zero polarisation losses arise, i.e. for $i_0 \rightarrow \infty$. Having ascertained that ohmic loss is negligible for each of the compositions under analysis, the comparison herein presented has real interest and validity. EDB/Pt values are weight ratios: EDB/Pt=0.2 corresponds to φ_{el}≈0.6, EDB/Pt=0.3 to φ_{el}≈0.5, EDB/Pt=0.4 to φ_{el}≈0.4, and EDB/Pt=0.6 corresponds to φ_{el}≈0.32.

Fig. 5 directly derives from Fig. 2; 1/R is plotted against the electrode thickness for various electrode compositions. In agreement with the results shown in Fig. 2 the curve for φ_{el}=0.37 has the highest values.

Two composition ranges can be differentiated: if $0.294<\varphi_{el}<0.31$ (that corresponds to $0.1<\Omega<0.25$) a visible maximum is present (for a thickness corresponding to $\Gamma\approx(10\Omega)^{-1/2}$) that represents a compromise between a sufficiently large active area for the electrochemical reaction and acceptable ohmic losses. If $0.31<\varphi_{el}<0.706$ (i.e. $\Omega<0.1$) each curve increases up to a maximum value (corresponding to $\Gamma\approx3$) and then remains almost constant (for an electrode thickness up to $\Gamma\approx2+(10\Omega)^{-1}$): in this range the charges can flow on the electron conducting phase with negligible ohmic losses; in such conditions the electrochemical reaction takes place in a thin area in the vicinity of the electrode/bulk electrolyte interface.

The theoretical model applied to the YSZ/Pt electrode (YSZ is $(ZrO_2)_{0.92}(Y_2O_3)_{0.08}$, all model parameters to be the same as for EDB/Pt electrodes, except for the ionic conductivity of pure YSZ, that has been assumed to be 6 S/m), for a composition $\varphi_{el}\approx0.6$ (weight ratio YSZ/Pt=0.2) would allow the calculation of a value $1/R\approx1.5\ 10^4$ S/m^2 almost constant for an electrode thickness a>10μm, that is in close agreement with the literature experimental data [9] as shown in Fig. 6.

CONCLUSIONS

An analytical model has been discussed for the simulation of SOFC electrodes, with particular reference to EDB/Pt and YSZ/Pt cathodes. Comparison with the available literature shows a close agreement between simulation data and experimental results. Some considerations concerning the optimisation of the electrodes have been made on the basis of the model: the composition and the thickness of the electrode have to be optimised at the same time in order to get the best performance.

NOTATION

a	electrode thickness	[m]
A	active area per unit volume	[m^2 m^{-3}]
d	particle diameter	[m]
F	Faraday's constant	[C mol^{-1}]
i	current density	[A m^{-2}]
i_o	exchange current density	[A m^{-2}]
i_n	transfer current density per unit of active area	[A m^{-2}]
I_{tot}	overall current density	[A m^{-2}]
R	total electrode resistance	[ohm m^{-2}]
R_g	gas constant	[J mol^{-1} K^{-1}]
T	temperature	[K]
V	potential	[V]
x	spatial co-ordinate along the electrode thickness	[m]
	Greeks	
η	overpotential	[V]
η_o	overall electrode overpotential	[V]
φ	volume fraction	[-]
ρ	resistivity	[ohm m]
σ	conductivity	[S m^{-1}]
Γ	dimensionless variable defined in Eq. 6	[-]
Ω	dimensionless parameter defined in Eq. 7	[-]

Index		**Apex**	
el	electronic conductor	eff	effective
io	ionic conductor	eq	equilibrium

REFERENCES

1. S. Sunde, J. Electrochem. Soc., **143**, 1930, (1996).
2. P. Costamagna, P. Costa, V. Antonucci, submitted to Electrochimica Acta.
3. N. Satterfield, *Mass Transfer in Heterogeneous Catalysis*, M.I.T. Press, Cambridge, (1970).
4. D. Bouvard, F.F. Lange, Acta Metall. Mater., **39**, 3083, (1991).
5. C.H. Kuo, P.K. Gupta, Acta Metall. Mater., **43**, 397, (1995).
6. D. Stauffer, *Introduction to Percolation Theory*, Taylor & Francis, London, (1985).
7. U.G. Bossel, *Facts and Figures*, an International Energy Agency Task Report, Berne (Switzerland), (1992).
8. S.P.S. Badwal, Proc. First European SOFC Forum, Lucerne (Switzerland), 399, (1994).
9. T. Kenjo, S. Osawa, K. Fujikawa, J. Electrochem. Soc., **138**, 349, (1991).

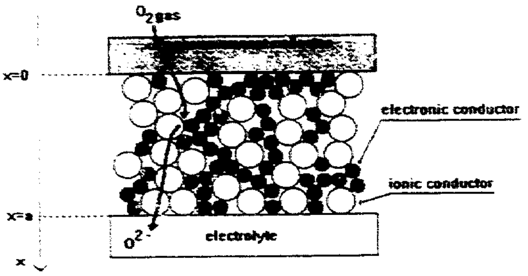

Fig. 1 - Scheme of an SOFC composite cathode.

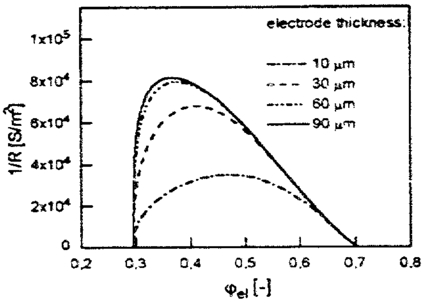

Fig. 2 - Reciprocal electrode resistance as a function of the electrode composition for EDB/Pt cathodes at 900°C.

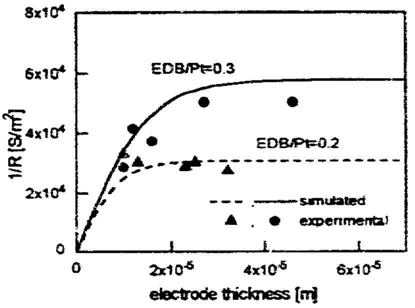

Fig. 3 - Simulation results compared to literature experimental data [9] for EDB/Pt cathodes at 900°C.

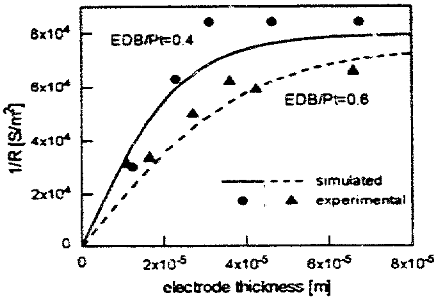

Fig. 4 - Simulation results compared to literature experimental data [9] for EDB/Pt cathodes at 900°C.

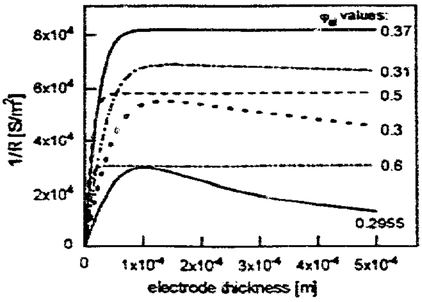

Fig. 5 - Reciprocal electrode resistance as a function of the electrode thickness for EDB/Pt cathodes at 900°C.

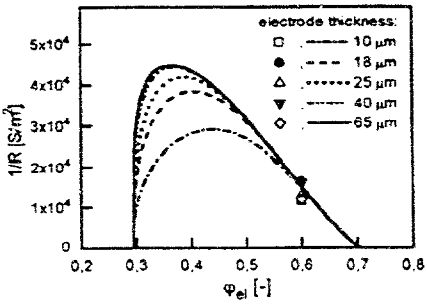

Fig. 6 - Simulation results and literature experimental data [9] for YSZ/Pt cathodes at 900°C.

Current distribution and partial blocking at cathode/electrolyte interfaces

Ann Mari Svensson and Kemal Nişancioğlu
Department of Electrochemistry
Norwegian University of Science and Technology
N-7034 Trondheim, Norway

Introduction

The causes of potential losses on the cathode side of SOFC's are not fully understood. Most of the existing information about SOFC cathode kinetics is based on work on noble metal electrodes [1-5]. Cathode polarization data for metal electrodes interfaced with an YSZ electrolyte have been attributed to various rate limiting steps, such as diffusion at the electrode/electrolyte interface [1-3], and on the porous Pt surface [4] or a combination of slow adsorption of oxygen and surface diffusion limitations [5].

Previously, we developed a model for the porous SOFC cathode incorporating these limiting steps [6] by use of the well known porous electrode theory [7]. However, this one-dimensional approach did not allow for a proper treatment of lateral diffusion of adsorbed oxygen along the electrode/electrolyte interface, although its importance was suggested in a nonrigorous manner. In the present work, we study this effect further by developing a two dimensional model of the metal electrode/electrolyte interface, including two dimensional treatment of the potential distribution in the electrolyte, the latter resulting from constriction at the cathode/electrolyte interface.

Theory

A cell which consists of a porous metal electrode placed on top of a slab of yttria stabilized zirconia (YSZ) electrolyte is considered. A counter electrode (CE), assumed to be reversible, covers the bottom surface of the electrolyte entirely. The overall oxygen exchange reaction can be written as

$$O_2(g) + 2(V_O^{\ddot{}})^{\Upsilon} + 4e^- \rightleftharpoons 2(O_o^{x})^{\Upsilon} \qquad (1)$$

where superscript Υ refers to the electrolyte phase. A segment of the three phase region of the porous electrode-electrolyte system is depicted in Fig. 1

It is assumed that oxygen adsorbs on the pore walls of the porous metal electrode according to the reaction

$$O_2(g) + 2ads \underset{k_{des}}{\overset{k_{ads}}{\rightleftharpoons}} 2O_{ads} \qquad (2)$$

The adsorbed species is thus assumed to be neutral, monoatomic oxygen. The equilibrium concentration of the adsorbates is assumed to be expressed by the Langmuir adsorption isotherm. The adsorbates diffuses along the pore surface towards the electrode/electrolyte interface, and they obey a steady state material balance of the form

$$D_{\theta 1}\Gamma_1 \frac{d^2\theta_1}{dy^2} + R_\theta(\theta_1, P_{O_2}) = 0 \tag{3}$$

where D_θ is the surface diffusion coefficient, Γ is the density of adsorbtion sites [mol cm^{-2}], θ is the degree of coverage, and subscript 1 refers to the gas/metal interface. R_θ is the net adsorption rate, given by

$$R_\theta = k_{ads} P_{O_2} \Gamma_1^2 (1-\theta_1)^2 - k_{des}\Gamma_1^2\theta_1^2 = 0 \tag{4}$$

Adsorbed oxygen atoms are also allowed to diffuse along the electrode/electrolyte interface as shown in Fig. 1. They exchange with vacancies from the electrolyte according to the reaction

$$O_{ads} + (V_O^{\cdot\cdot})^{\Upsilon} + 2e^- \underset{k_{oa}}{\overset{k_{ra}}{\rightleftharpoons}} ads + (O_o^{x})^{\Upsilon} \tag{5}$$

where the electrons are provided from the metal phase. The possibility of a similar elementary step at the gas/YSZ interface is neglected due to the low electronic conductivity of YSZ. The material balance for adsorbates at the electrode/electrolyte interface is given by

$$D_{\theta 2}\Gamma_2 \frac{d^2\theta_2}{dx^2} + \frac{i(x)}{2F} = 0 \tag{6}$$

where subscript 2 refers to the electrode/electrolyte interface. The current density through the electrolyte will be nonuniform, as is schematically illustrated in Fig. 1. The local current density at the interface obey the Butler-Volmer relationship

$$i(x) = i_o(x)[\exp(\frac{(1-\beta)2F}{RT}\eta_s(x)) - \exp(\frac{-\beta 2F}{RT}\eta_s(x))] \tag{7}$$

The exchange current density, as well as the concentration overpotential

$$\eta_c(x) = \frac{RT}{2F}\ln(\frac{\theta_2(1-\theta^{eq})}{\theta^{eq}(1-\theta_2)}) \tag{8}$$

are functions of position.

At the tpb, *i.e.* at $x = L^e$, $y = 0$, the following continuity conditions apply

$$\theta_2(L^e) = \theta_1(0) \tag{9}$$

and

$$\left(D_{\theta 2}\Gamma_2 \frac{d\theta_2}{dx}\right)_{x=L^e} = \left(D_{\theta 1}\Gamma_1 \frac{d\theta_1}{dy}\right)_{y=0} \tag{10}$$

Blocking conditions are assumed at the boundaries $x = 0$ and $y = L^m$.

In the absence of concentration gradients, Laplace's equation is applicable for the potential distribution in the electrolyte,

$$\nabla^2\Phi = 0 \tag{11}$$

The boundary conditions are

$$\frac{\partial\Phi}{\partial x} = 0 \qquad \text{at } x = 0, L \text{ (symmetry condition)} \tag{12}$$

$$-\kappa\frac{\partial\Phi}{\partial y} = \begin{cases} i(x) & \text{at } y = 0,\ 0 < x < L^e \\ 0 & \text{at } y = 0,\ L^e < x < L \end{cases} \tag{13}$$

$$\Phi = 0 \qquad \text{at } y = -\delta \text{ (reversible electrode)} \tag{14}$$

where L^e is the length of the electrode/electrolyte interface as depicted in Fig. 1, L is the width of the segment, and δ is the thickness of the electrolyte. The overpotentials as well as the ohmic potential drop of the electrolyte all vary locally, but at each location they have to sum up to the total cell voltage

$$V^{cell} = \eta_s(x) + \eta_c(x) + \Phi(x,0) \tag{15}$$

where $\Phi(x,0)$ is the potential distribution along the upper electrolyte surface. Equations (3), (4) and (6) through (15) are solved by a numerical iteration procedure.

Results and Discussion

In Fig. 2 the local current distribution is depicted at various cell voltages, V^{cell} for relatively slow interfacial diffusion, $D_\theta = 10^{-7}$ cm^{2}s^{-1}. The other paramaters used for the calculation are given in Table I. As expected, the current distribution becomes more nonuniform as the polarization of the cell is increased. The corresponding dimensionless interfacial concentration profile is shown in Fig. 3. As is clearly illustrated in the figure, the adsorbate concentration at the interface is depleted with increasing polarization, whereas the concentration of adsorbates is close to its equilibrium value at the tpb. We have not yet been able to obtain the current distribution at higher cell voltages, but Figs. 2 and 3 suggest the possibility of a partial blocking of the interface, which is further expected to cause an increase in the measured electrolyte resistance. Such behavior has been reported by [8] for Pt/YSZ cells.

In Fig. 4 a concentration profile is shown for the same cell parameters as in Fig. 3, but the interfacial diffusion process is assumed to be much faster. The profiles are nearly uniform, shifting to lower levels with increasing polarization.

For an experimental evaluation of possible reaction mechanisms, the polarization resistance is frequently plotted vs. oxygen partial pressure, P_{O_2}, and the relation $R_p \propto P_{O_2}^{-m}$ is assumed. The polarization resistance obtained from the current-voltage relationship at small currents is plotted with respect to the logarithm of the oxygen partial pressure in Fig. 5 for various interfacial diffusion coefficients, $D_{\theta 2}$. The value of m is found to increase as the interfacial diffusion coefficient decreases. However, the results obtained for $D_{\theta 2} = 10^{-6}$ and 10^{-4} cm^{2}s^{-1} are close, indicating that other processes than interfacial diffusion are rate limiting.

Acknowledgement

The Norwegian Research Council is acknowledged for the financial support.

References

[1] D.Y. Wang and A.S. Nowick, *J. Electrochem. Soc*, **126**, 1155,1166 (1979), **127**,113 (1980)

[2] B.A. van Hassel, B.A. Boukamp, A.J. Burggraaf, *Solid State Ionics*, **48**, 139,155 (1991)

[3] D. Braunshtein, D.S. Tannhauser, and I. Riess, *J. Electrochem. Soc.*, **128**, 82 (1981)

[4] J. Van Herle and A.J. McEvoy, *Ber. Bunsenges. Phys. Chem.*, **97**, 470 (1993)

[5] J. Mizusaki, K. Amano, S. Yamauchi and K. Fueki, *Solid State Ionics*, **22**, 313 (1987)

[6] A.M. Svensson, S.Sunde and K. Nişancioğlu, submitted to J. Electrochem Soc.

[7] J.S. Newman, *Electrochemical Systems*, 2nd Ed., Prentice Hall, New Jersey (1991).

[8] D.Y. Wang, *J. Electrochem. Soc.*, **137**, 3660 (1990)

Table I. Parameters.

Parameter	Value
k_{ads}	10^{14} atm^{-1}mol^{-1}cm^{2}s^{-1}
k_{des}	10^{16} mol^{-1}cm^2 s^{-1}
P_{O_2}	1 atm
$D_{\theta 1}$	10^{-6} cm^{2}s^{-1}
Γ	10^{-9} mol cm^{-2}
$k_{ra} \cdot k_{oa}$	10^8 mol^{-1} cm^3 s^{-2}
κ	0.1 Scm^{-1}
L	0.5 μm
L^e/L	0.1
δ/L	100

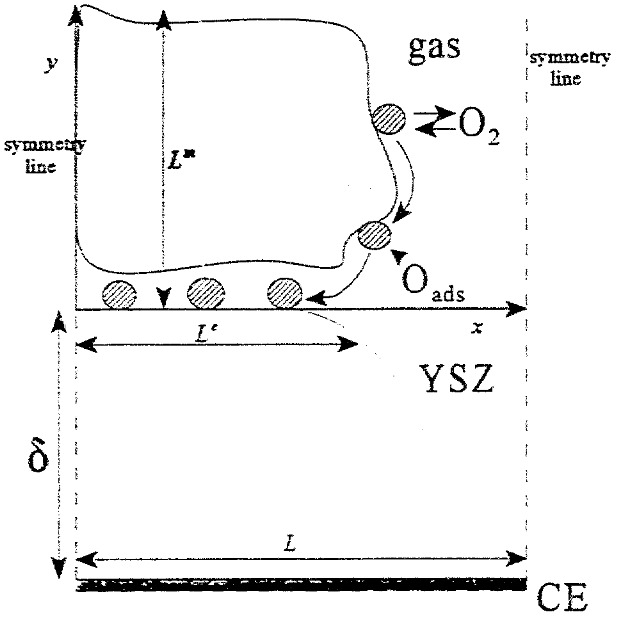

Figure 1: Segment of the tpb region of a porous metal electrode on top of a YSZ electrolyte.

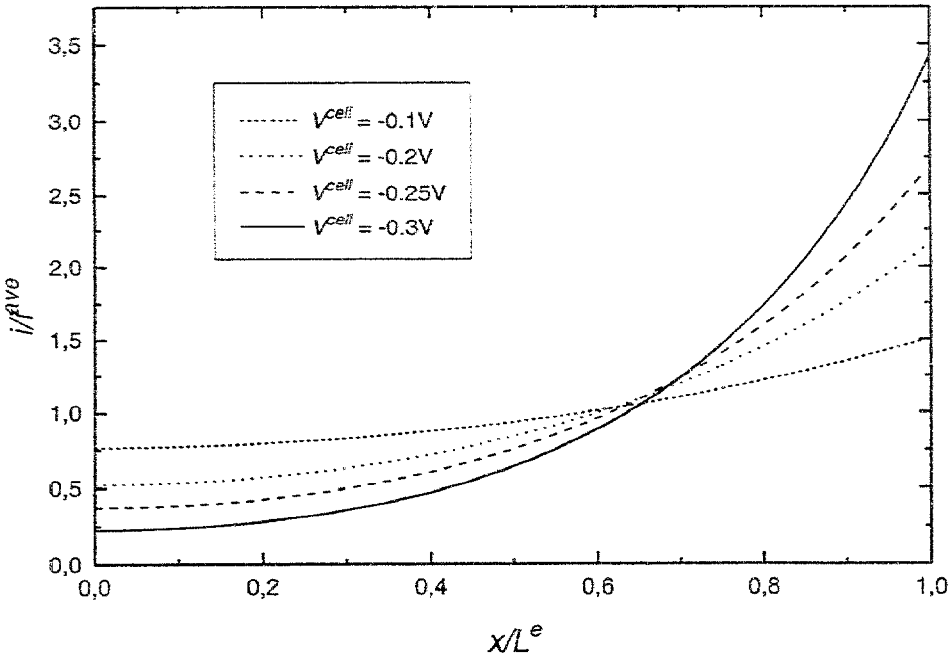

Figure 2: Current distribution at the electrode/electrolyte interface vs. dimensionless position for $D_{\vartheta 2} = 10^{-7}$ cm^{2}s^{-1} at various cell voltages, V^{cell}.

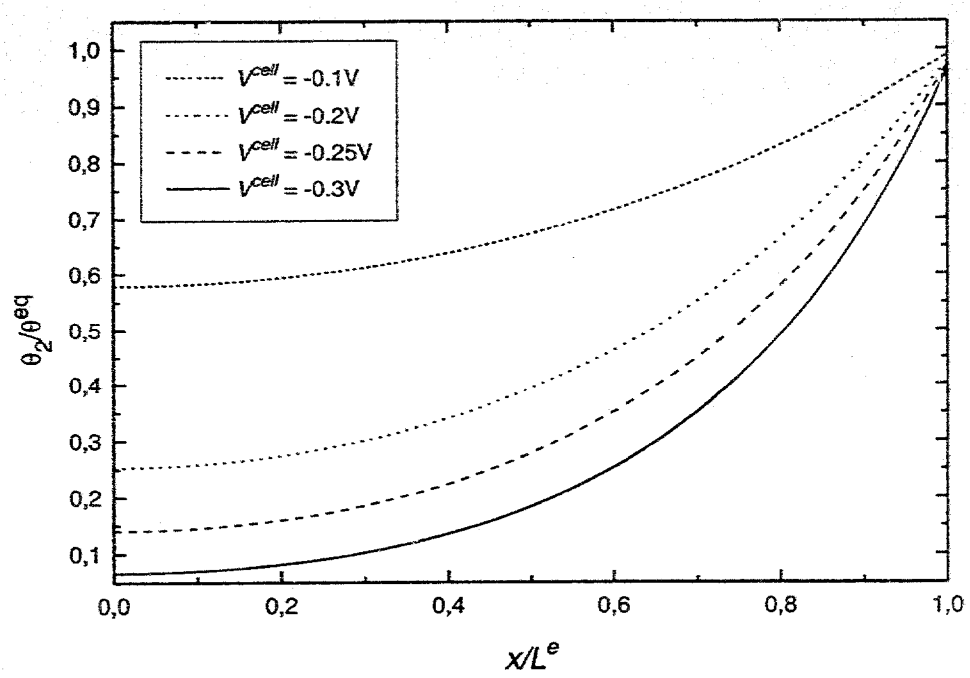

Figure 3: Distribution of interfacial adsorbates at the electrode/electrolyte interface, θ_2, corresponding to Fig. 2.

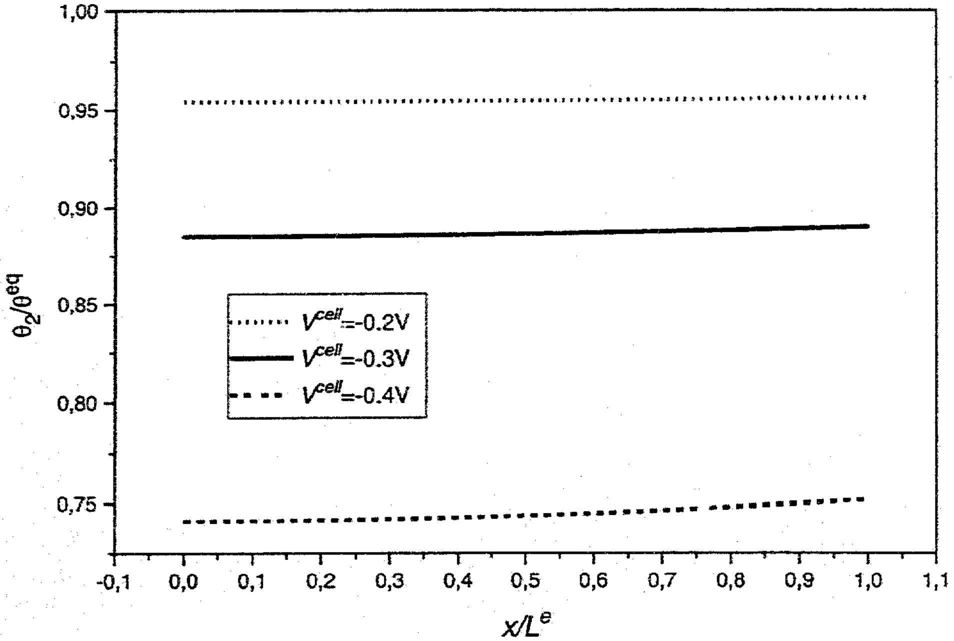

Figure 4: Distribution of interfacial adsorbates, θ_2, for $D_{\theta 2} = 10^{-4}$ cm^{2}s^{-1} at various cell voltages, V^{cell}.

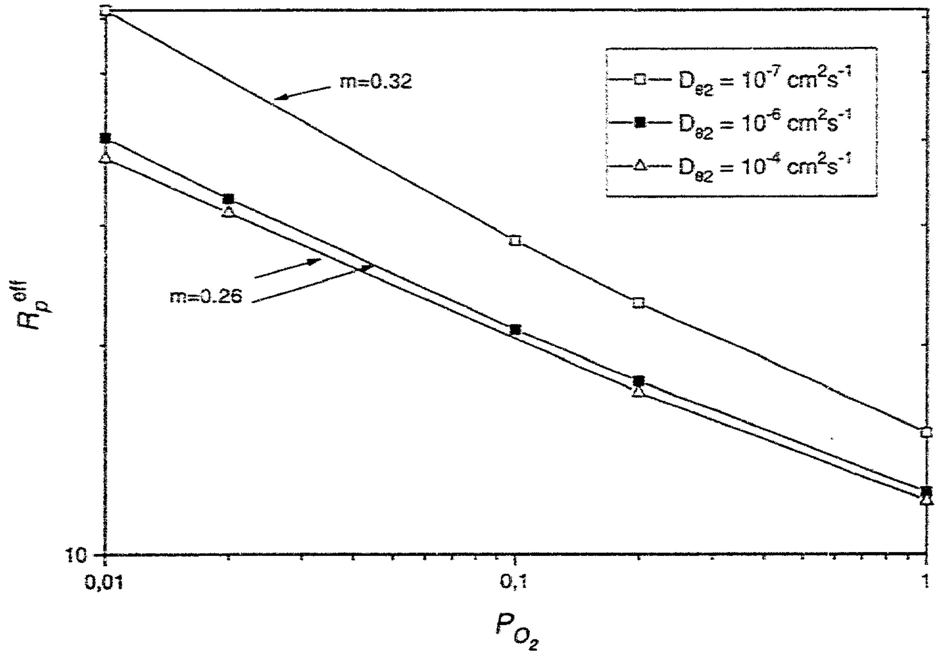

Figure 5: Polarization resistance, R_p vs. oxygen partial pressure, P_{O_2} for various values of $D_{\acute{e}2}$.

Evening Workshop, 30 Jan. 1997

Report by T.Kawada, Tohoku University. Japan
Chairman H. Yokokawa

The following three topics were the principal points of discussion:

1) Reaction site in composite (cermet) electrodes.
2) Electrode reaction kinetics and morphology change of the interface.
3) Use of mixed conductors as electrolyte.

1) Reaction site in composite (cermet) electrodes

In the "modeling" session, some reports dealt with the effective reaction site in a composite electrode or a Ni-YSZ cermet anode. They concluded from a percolation theory that the reaction site can penetrate into the electrode layer to some extent from the electrode / electrolyte boundary. The workshop discussion started from a comment to those reports: i.e."The penetration of the reaction site seems not realistic.....". The comment was based on such an experience that the electrode resistance is comparable to the electrolyte resistance in a usual SOFC with a thin YSZ electrolyte of about 30 micron. If so, the penetration depth must be less than 1 micron since the resistance of the ionic path in the electrode must be 30 to 100 times higher than that in a dense electrolyte. Though the percolation theory predicted a possibility of the penetration, it was hardly understood intuitively. A lively discussion was held on the effective resistance of the ionic path, the possible penetration depth, and the electrical field distribution inside the electrode. The discussion did not reach the thorough agreement but gave some common understandings: (1) The penetration depth is dependent on the ratio of the effective electrode resistance and the electrochemical reaction impedance. (2) Relatively large penetration is possible around the percolation threshold. There were some additional comments on the related topics as follows:

* The penetration depth may vary according to the current density since the electrochemical resistance has a nonlinear nature.

* If some isolated YSZ particles exist in the electrode layer, they can act as micro cells, which affect the mass transport inside the electrode.

* The important thing is not the total number of three phase boundaries but the number of "active" three phase boundaries which have connections both to the current collector and to the electrolyte.

* The analysis by percolation theory gives the reason of electrode degradation after operation. However, it is difficult to forecast the possibility of degradation without destroying the electrode.

2) Anode reaction mechanism and electrolyte

As for the anode reaction mechanism, the discussion focused on whether the electrolyte surface contribute to the electrode reaction kinetics or not. The first comment on this topic was on the paper presented in the "anode" session. In that paper, an anode reaction mechanism was studied by electrochemical measurements and a reaction model was proposed in which proton dissolved in the electrolyte plays an important role. The proposed rate determining step was the desorption of water molecule which was produced on the electrolyte surface by the reaction:

$$H_i + H_i + O_o \text{ (or } O_{ad}) \Rightarrow H_2O.$$

If this kinetic model is real, the electrolyte surface must have strong effect on the reaction rate. On the contrary, an opposite experimental result was reported in the discussion. Point contact Pt electrode was put on YSZ surfaces with and without CeO_2 coating films, and the ac and dc polarization behaviours were compared. Almost no difference in the electrochemical properties was observed between them suggesting that the modification of the electrolyte surface did not change the catalytic activity for hydrogen oxidation. The contradiction between those two reports were briefly discussed.

Then, the discussion shifted into another topic; i.e. morphology change of the electrolyte during polarization. In the "anode" session, there was a report on morphological change of YSZ under point contact platinum electrode. The similar phenomena were observed in the experiment with the CeO_2 film on YSZ. After experiments in a H_2-H_2O mixed gas, the CeO2 layer was found to be separated into cubic grains, and some of the grains peeled off from the surface. Though the morphology of the solid oxide electrolytes are usually expected to be stable, it may change during operation. Some comments were made on the morphological stability of the electrode / electrolyte boundary.

* Thermal expansion mismatch and the lattice expansion in a reducing atmosphere are possible reasons of the damage of the ceria coating film.

* Internal gas evolution might happen at YSZ/CeO_2 boundary since CeO_2 is an electronic conductor in a reducing atmosphere, which could be a reason for the breakdown of the CeO_2 layer.

* Mass transport of cation can be important in a long term operation.

(3) Use of a mixed conductor as the electrolyte

The use of ceria based electrolyte was discussed from two view points; i.e. the problem in evaluating the overvoltage in a basic study and the problem which may arise in a practical application.

To study the electrode polarization on CeO_2 based electrolyte, it is difficult to evaluate the overvoltage and ionic current because the electronic conductivity causes electronic leak current and oxygen permeation through the electrolyte, and the resulting polarization of the
electrodes are not negligible even at an open circuit condition. In the "electrolyte" session, a report was presented on a novel technique to evaluate anode and cathode polarization. They measured the external current density and the apparent overvoltage by current interruption method and converted them into the ionic current and the real polarization by using a parameter fitting. Some questions were asked on their method.
Q. The ionic current must go to zero when the Nernst voltage is applied between the electrodes. Was it confirmed experimentally ?
A. Yes.
Q. Is their any simpler technique to evaluate the overvoltage ?
A. No.

Several problems were pointed out in practical use of ceria based electrolytes.
* Mechanical strength may be a big problem in the fabrication and the operation.
* Reduction induced lattice expansion can be a problem.
* Electronic leak current (oxygen permeation) causes the efficiency loss.
Encouraging comments were also made.
* The expected large power density is the advantage of a ceria based electrolyte.
* There must be application fields where the power density is more important than the efficiency.

Though the topics on the interconnect materials were also to be discussed, time was not enough to proceed to the next topic, and the workshop was closed.

The Electrode Configuration of a Three-Electrode Cell

Fred van Heuveln and Gaby Janssen
Netherlands Energy Research Foundation ECN
P.O. Box 1, 1755 ZG Petten
The Netherlands
vanheuveln@ecn.nl, janssen@ecn.nl

Abstract

There are several electrode geometries that can be used to characterise the electrode losses. The potential distribution of the electrode geometry used at ECN is calculated and the results are compared with those from other electrode geometries. Several critical parameters influencing the quality of the measured polarisation loss of the working electrode are identified.

1 Introduction

Screening of the electrochemical properties of electrode materials is usually performed by measuring the electrode material in an out-off-cell arrangement, e.g., a three-electrode setup. The electrode material that has to be investigated (working electrode) is placed together with electrolyte and counter electrode in one and the same gas environment. Such a measurement setup is referred to as the *undivided setup* in contrast with the *divided setup* in which both the working and counter electrode have their own gas environment. The divided setup, for example, a solid oxide fuel cell, is much more complicated because different gases need to be kept separate. The fuel cell configuration is therefore less attractive for screening of electrode materials in a short time. The undivided three-electrode setup is more suitable for this purpose.

At ECN screening of electrode materials is performed by ac-impedance measurements and $I - V$ characteristics at different gas or temperature conditions [1–3]. Ac-impedance measurements are performed, e.g., to measure the effective cross sectional area A_{cs} of the electrolyte, which relates to the electrochemical performance. The higher the value of A_{cs} the lower the resistance when a dc-current is passed through the cell [2]. I-V characteristics are used to support electrode modelling. However, this is only useful if the electrode performance is measured in such a way that the measured potential difference reflects in some way the true overpotential at the electrode or that a valid correction can be carried out for the electrolyte loss when this is included in the measured potential difference. The reliability of the electrolyte correction depends on the electrode geometry used. In the literature, different electrode geometries are described.

The classical way to measure the electrochemical characteristics of the working electrode is to pass a current between working and counter electrode, measuring the potential difference between the working and the reference electrode. The reference electrode is preferably placed within the electrolyte near the working electrode, i.e., in a region where the potential distribution is homogeneous and well defined. Unfortunately, for a sample configuration like a solid oxide fuel cell, consisting of thin dense ceramic plates with thicknesses around 150 μm, and having electrodes on both sides with thicknesses of about 50 μm, it is not possible to place the reference electrode within the electrolyte. The question then arises: what is the preferred position of the reference electrode and what is the physical significance of the potential difference measured between working and reference electrodes?

In this study different electrode geometries that can be used in a half cell arrangement for characterising thin electrolyte/electrode structures are described and compared with respect to their ability to determine the correct electrode overpotential. The electrode configuration of a fuel cell with one or two reference electrodes is discussed elsewhere [4].

2 Electrode geometries

Different electrode geometries that are used for half cells are shown in Figs.1 and 2. The geometries given in Fig.1 are those for circular electrodes, which are used most often. Rectangular electrodes are not shown but for all electrode geometries a comparable rectangular configuration can also be considered. Literature references for the different geometries are given in Table 1.

For the electrode *WE* under investigation, we want to know the correct overpotential η_w or its resistance, R_w, also called polarisation resistance. What is measured in practice, is the potential difference $\phi_w - \phi_r$ between the working *WE* and reference electrode *RE*, defined as

$$U_w = \phi_w - \phi_r \qquad [1]$$

It is assumed that U_w contains a contribution from the electrode itself, the overpotential η_w, and a contribution from the electrolyte, U_{el}

$$U_w = \eta_w + U_{el} \qquad [2]$$

To measure correct values for η_w, the potential ϕ_r and thus U_{el} should be well defined. The overpotential η_w is usually obtained by measuring U_w and subtracting the electrolyte loss U_{el}. The electrolyte loss can be obtained from impedance measurements as the intercept at the real axis of the impedance diagram when the frequency ν goes to infinity. This intercept is usually referred to as the high frequency intercept, R_{hf}. If other ohmic contributions are negligible R_{hf} can be used to calculate the electrolyte loss $U_{el} = i \cdot R_{hf}$, where i is the current density. An alternative way to determine U_{el} is by measuring the ohmic drop from relaxation measurements as used in the current interruption method [5].

The differences between these geometries can be found using a model in which the electrolyte has a finite resistance, the electrodes being considered as ideal metallic non-porous media, with the current at the electrode/electrolyte interface perpendicular to the electrolyte surface. Lateral currents in the electrodes are not considered. Both electrodes are assumed to be equipotential in the immediate interface with the electrolyte. An effective resistance can be attributed to the working or counter electrode to model the overpotential at the electrodes. Using a numerical method to solve the Laplace equation, potential distributions and current distributions can be calculated for different electrode geometries. A recent example of such a modelling study was given by Winkler et al. [6].

Table 1: *Literature references for electrode geometries, shown in Fig. 1, which are used to measure porous electrodes.*

electrode geometry	literature reference	remarks
1	[2,7–9]	
2	[7,8,10,11]	
3	[12]	2mm thick electrolyte
4	[13–16]	
5	[17]	
6	[18,19]	
7	[18]	
8, 9	[6]	

A useful distinction is that between the primary and secondary distribution of the current and the potential [20]. The primary distribution is defined as the potential (or current) distribution when the working and counter electrodes have zero polarisation, i.e., $R_w = 0$ and $R_c = 0$ respectively. For ac-measurements, such as impedance spectroscopy, this corresponds to the situation where the frequency tends to infinity. At high frequencies the polarisation resistance is short-circuited through a parallel capacitance and only the ohmic electrolyte resistance remains. The secondary potential or current distribution is obtained when there is a polarisation resistance present at the electrodes, i.e., $R_w,\ R_c \neq 0$. For ac-measurements this corresponds to the situation where the frequency tends to zero. Thus, one can simulate frequencies of zero or infinity by excluding or including the polarisation respectively.

2.1 Electrode geometry 1

For electrode geometry 1 the dimensions and symbols are shown in Fig. 3 along with the sectioned area used in the calculations. This geometry is used at ECN for screening the

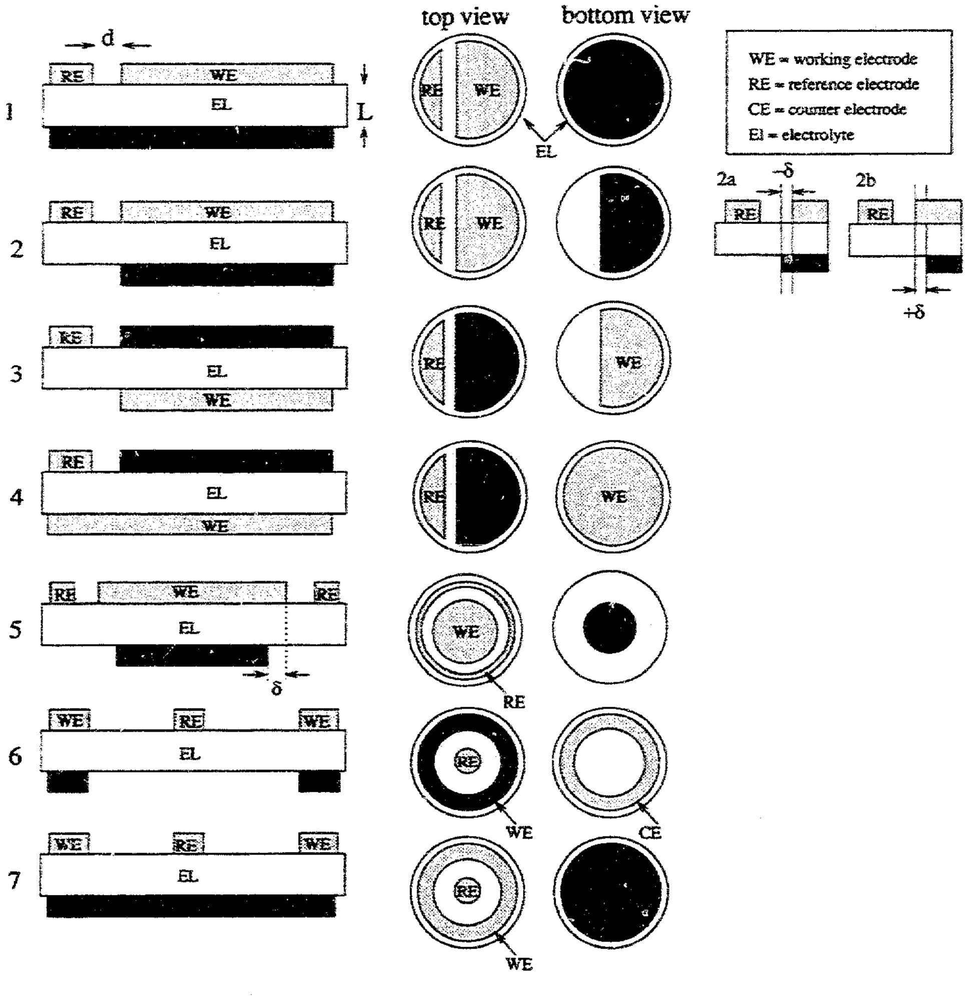

Figure 1: *Illustration of different electrode geometries. On the left hand side a cross section is shown and on the right hand side the corresponding top and bottom views are given for circular electrodes.*

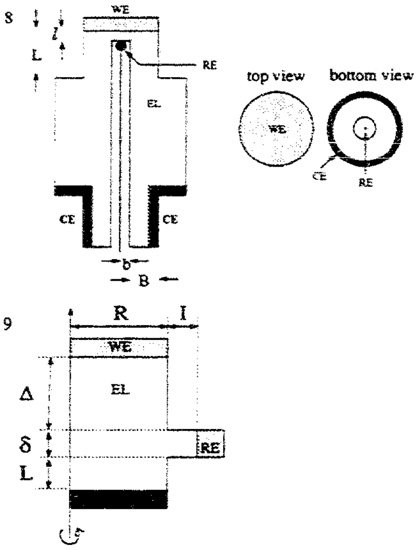

Figure 2: *Continuation of Fig. 1. Alternative electrode geometries, developed at RISØ, to measure the true polarisation resistance of the working electrode [6].*

electrochemical performance of cathode and anode.

Calculations were performed using an electrolyte thickness of 150 μm and a specific conductivity of 0.1 S/cm. The interfacial resistance of the working electrode was fixed at 0.15 Ohm cm^2. These are close to the values for solid oxide fuel cell components. To investigate the influence of the counter electrode resistance the value for R_c was varied. The potential ϕ_w at the working electrode was fixed at 0.4 V and that at the counter electrode ϕ_c at 0 V. Details of the method including a full presentation of the results is given elsewhere [4].

2.1.1 Primary distribution

The calculated primary potential distribution is shown in Fig. 4 for the situation where $d \gg L$ as defined in Fig. 1. As can be seen from Fig. 4, the potential distribution in the electrolyte is homogeneous in nearly the whole region between *CE* and *WE*. Only near the edge at *WE* there is an inhomogeneity that would give erroneous potentials if the reference potential would be probed in that region. This region is about 2-3 times the electrolyte thickness L. The reference potential, which is probed at the top of the electrolyte at position 0, is equal to the potential at the counter electrode that was fixed at 0 V. Hence, $R^{measured} = R_{el}$. There remains only a small error in the determination of R_{el} which is due to the inhomogeneity of the current near the *WE* edge, this error is estimated at about 1 %.

For $d \ll L$ the measured resistance at the working electrode contains only a part of the electrolyte resistance, the extent of which depends on the ratio d/L. Therefore under these conditions the electrode geometry is not suitable for measuring electrolyte resistances.

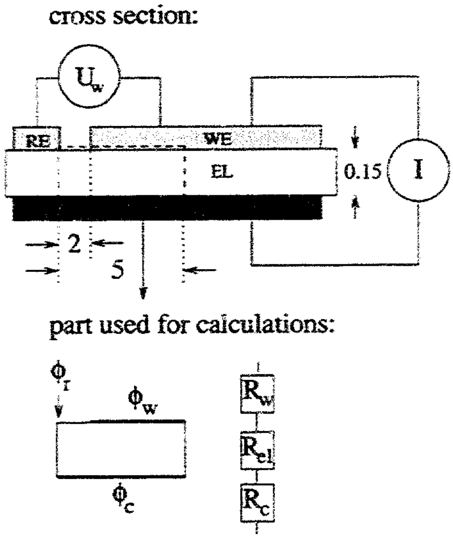

Figure 3: *Dimensions (mm) and symbols shown for electrode geometry* 1. *Also shown is the part of the cross section used for the calculations of the potential distribution.*

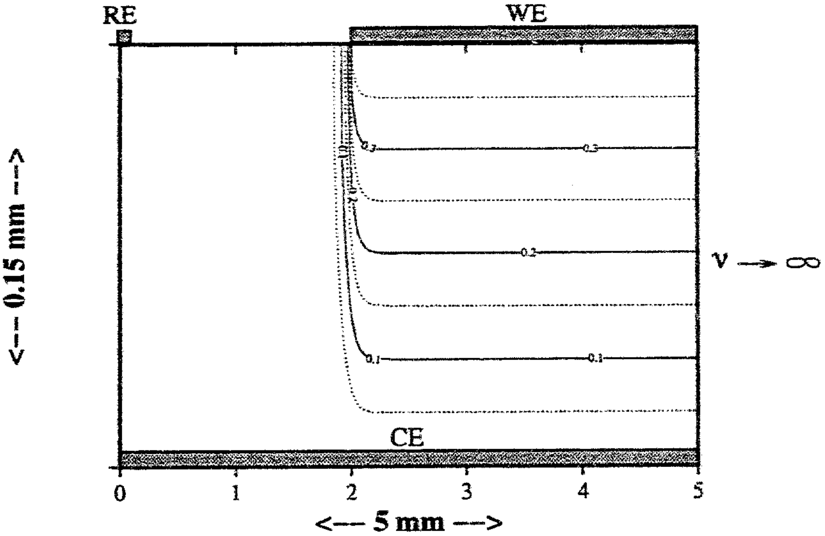

Figure 4: *Contour plot of the primary potential distribution in the electrolyte cross section of the three-electrode geometry* 1, *see Fig. 3. Potential values are indicated at the lines.*

2.1.2 Secondary distribution

In Fig. 5 the secondary potential distribution is given for the case that $R_w/R_c = 1$. This figure show that the potential distribution and hence the current distribution is homogeneous opposite the working electrode, but inhomogeneous opposite the edge *WE*/electrolyte and zero opposite the bare electrolyte. Since there are no current lines in the latter part of the electrolyte the potential will be constant and the potential probed at the reference electrode will be equal to the applied potential of the counter electrode. It follows that

$$\phi_w - \phi_c = U^{applied} = \phi_w - \phi_r \tag{3}$$

and for the resistance

$$U_w = \eta_w + \eta_c + i \cdot R_{el} \ or \ R^{measured} \approx R_w + R_c + R_{el} \tag{4}$$

Thus, after correction for the electrolyte loss U_w now includes the overpotential of the counter electrode. This means that the polarisation resistance of the working electrode, R_w^m, will be measured erroneously with respect to the true polarisation resistance, R_w. The error in R_w^m is defined as

$$Error = \frac{R_w^m - R_w}{R_w} \tag{5}$$

As shown in Fig. 6 the relative error increases rapidly with decreasing ratio R_w/R_c, e.g., when $R_w/R_c = 1$ the error is about 90 % and for $R_w/R_c = 2$ is about 50 %. It is therefore recommended that the counter electrode should perform better than the working electrode by at least a factor 10, i.e., $R_w/R_c \geq 10$.

Therefore, one should be careful in using absolute values of η_w or R_w. If possible a correction should be made for the contribution of the counter electrode. However, correcting the data will be difficult because η_c cannot be measured directly. Although a too high resistance will be measured at the *WE* electrode geometry 1 can still be used in a comparative way for screening electrode materials when all samples have comparable counter electrodes. Errors in the calculated resistance may yield about 10 % due to differences in inhomogeneities of the potential distribution because of different ratios R_w/R_c in a series of samples [4]. For impedance measurements the parasitic contribution of the counter electrode will also depend on the measuring frequency. At every frequency the value of R_c changes thereby causing a redistribution of potential lines in the electrolyte.

When $d \ll L$ the measured resistance at the working electrode only contain part of the electrolyte resistance, its magnitude depending on the ratio d/L. In this situation there is no contribution from the counter electrode resistance anymore because the potential probed at *RE* corresponds to a potential level somewhere in the electrolyte instead of that of the counter electrode. Since this position will depend on R_w/R_c it is not possible to determine U_{el} in a separate measurement, e.g., in impedance spectroscopy using high frequency measurements. Therefore at this condition the electrode geometry is not useful at all.

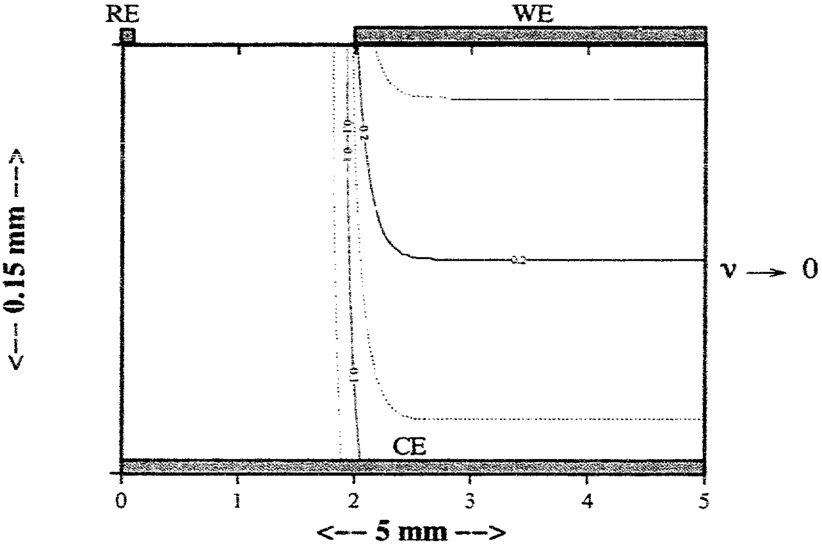

Figure 5: *Contour plot of the secondary potential distribution in the electrolyte cross section of the three-electrode geometry* 1, *see Fig. 3.* $R_w/R_c = 1$. *Potential values are indicated at the lines.*

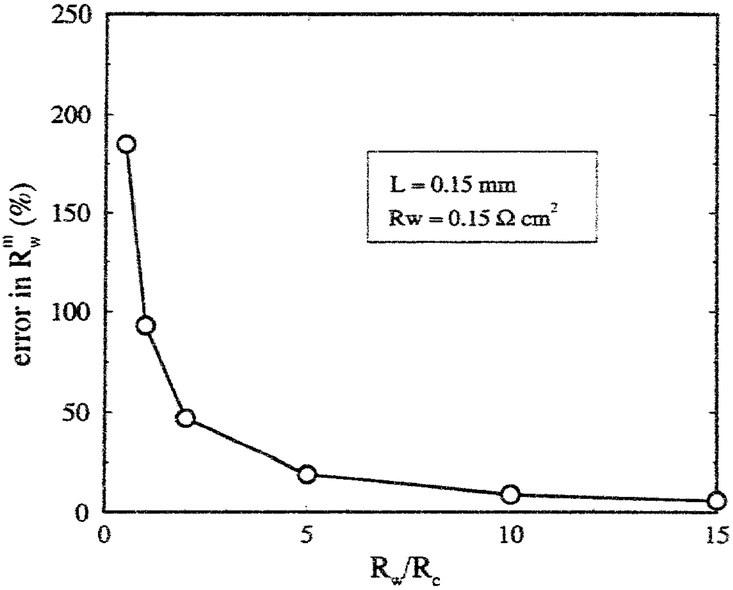

Figure 6: *Relative error in the measured polarisation resistance as a function of the ratio* R_w/R_c.

Summarising the above we can say that in order to measure true overpotentials at the working electrode for electrode geometry 1 the following requirements have to be fulfilled:

1. the distance between the working and reference electrode should be at least five times the thickness of the electrolyte, i.e, $d/L \geq 5$
2. the resistance of the counter electrode should be lower by a factor of at least 10 compared to the working electrode resistance, i.e., $R_w/R_c \geq 10$.

2.2 Other geometries

2.2.1 Electrode geometry 2 and 3

In geometries 2 and 3 the counter and working electrode are symmetrically placed opposite to each other. For both geometries the discussion with respect to the ratio d/L is similar as for geometry 1. Model calculations, with similar conditions as used in the previous section were performed to calculate potential and current distributions. These calculations showed that if the electrodes are at exactly symmetrical positions opposite to each other and if $R_c = R_w = 0$, then the lines of the primary potential distribution lie symmetrically with a mirror plane in the centre of the electrolyte. The consequence is that half of the true electrolyte resistance is measured; $R^{measured} = \frac{1}{2} R_{el}$.

However the situation changes when there is a displacement δ of both electrodes as indicated at 2*a* and 2*b* of Fig. 1. Depending on the direction of the displacement of the working electrode relative to the reference electrode the electrolyte resistance that will be measured, lies between 0 and R_{el} in case of the primary potential. For example, when the displacement δ is $0.2 \cdot L$ into the direction of *RE* (2b of Fig. 1) then 13 % of the electrolyte resistance is measured instead of 50 %. This means that for an SOFC electrolyte, having a thickness of 150 μm, a displacement of 0.03 mm already induces a significant error in the measured electrolyte resistance.

When polarisation of the electrodes is taken into account the effect is even more pronounced [4]. In this case the potential at the reference electrode does not necessarily correspond with a potential between the electrodes. At a given displacement δ the potential difference will depend upon the ratio R_w/R_c and the error in U_w can be several times the electrolyte loss U_{el}. What is measured too much at one electrode is missing at the other electrode. In Fig. 7 the relative error, defined by Eq. 5, is shown as a function of R_w/R_c for different values of the displacement δ. As can be seen from this figure for a similar resistance of working and counter electrode an error of $\approx$10% is made at already a displacement of only 20% of the electrolyte thickness. This means for example in case of thin electrolytes of 150μm that errors larger than 10% occur at displacements larger than 0.030 mm! During fabrication of porous electrodes it is practically impossible to avoid displacements of this order of magnitude. Even if this would be possible, such displacements often occur during testing because of microstructural changes such as sintering of the electrode. It is therefore not recommended to use this geometry for thin electrolytes.

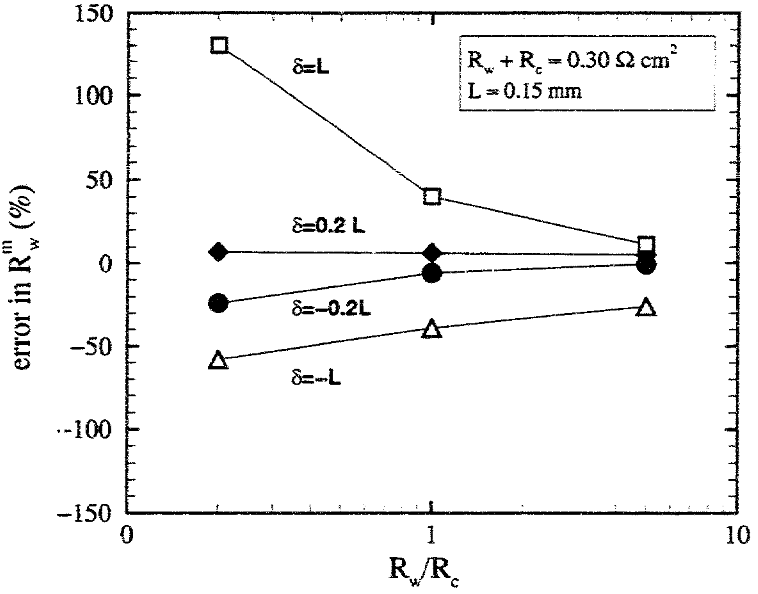

Figure 7: *Relative error in the measured polarisation resistance as a function of the ratio R_w/R_c for different values of the displacement distance δ between working and reference electrode, see right hand sight of Fig. 1.*

For thick electrolytes and satisfying the condition $d \gg L$ the displacement error can be avoided because the ratio δ/L can be kept small. In this case one always measures, independent of the ratio R_w/R_c, half of the electrolyte loss, i.e., $U_w = \eta_w + \frac{1}{2}U_{el}$. However, for thick electrolytes it is a practical problem to satisfy the condition $d/L \geq 5$.

For geometry 3 the discussion is similar to that of geometry 2 except that in case of the displacement the errors have an opposite direction compared to geometry 2.

2.2.2 Electrode geometry 4

This geometry is similar to 1 except that *WE* and *CE* are interchanged from position. For a thin electrolyte and no polarisation one measures a zero potential difference $U_w = 0$ because both *WE* and *RE* are at the same potential; $\phi_w = \phi_r$. For a thick electrolyte one measures an unknown part of the potential drop across the electrolyte U_{el}. This means that this geometry is not suitable for measuring the electrolyte resistance. When the electrodes are polarised and $d/L \geq 5$ it still holds that $\phi_w = \phi_r$ and consequently $U_w = 0$. For polarised electrodes and $d \ll L$ one measures an unknown fraction of $\eta_w + U_{el}$.

2.2.3 Electrode geometry 5

In this geometry the displacement is intentionally made to compensate partially for the ohmic drop in the electrolyte. According to the authors in Ref. [17] this geometry would reduce the electrolyte loss. The displacement between *WE* (diameter 10 mm) and *CE* was 1 mm at an electrolyte thickness of 130 μm. For thin electrolytes the discussion for this geometry is similar to that for geometry 2 but now including a large error due to the displacement between *WE* and *CE*. It should be noted further that for this geometry the electrolyte loss will be dependent on the ac frequency. Therefore for thin electrolytes this geometry is highly unsuitable. For thick electrolytes the displacement error disappears only when the electrolyte thickness is much larger than magnitude of the displacement, i.e., $L \gg \delta$.

2.2.4 Electrode geometry 6 and 7

Geometry 6 does not differ significantly from that of 2. Thus, the discussion is also similar except that for this geometry the displacement factor may be higher because of a total perimeter which is 2 times that of the electrodes in geometry 2. The error may differ little from that of geometry 2 because the current and potential distribution will be different for the ring-like electrodes compared to the electrode shape of geometry 2. The potential distribution was not calculated for this shape but from calculations on other different geometries it is expected that this will only have a minor effect [21]. The discussion for geometry 7 is similar to that for geometry 1. For thick electrolytes the discussion for geometries 6 and 7 is also similar to that for 2 and 1, respectively.

2.2.5 Electrode geometry 8 and 9

In a recent paper Winkler et al. [6] discussed the implications of improperly placed reference electrodes and presented two alternative configurations in order to measure the correct electrode overpotential. These configurations are shown in geometry 8 and 9 of Fig. 2. Both geometries consist of a thick electrolyte. Geometry 8, called the Risø 3-electrode pellet geometry, is based on the classical approach, i.e., the reference electrode is preferably placed within the electrolyte near the working electrode in a region where the potential distribution is homogeneous and well defined. Optimum values were calculated for the distances between *WE* and *RE*. It was shown that at distances smaller than $l = 2$ mm (and $b = 1.5$ mm) the current distribution becomes inhomogeneous and, hence, the error in η_w increases. Calculations show that geometry 8, with optimised dimensions, can be used to measure the correct polarisation loss at the working electrode within an error of 3 % with respect to the true polarisation loss. The disadvantage of this setup is the large serial resistance because of the thick electrolyte used in this geometry. A large serial resistance, especially the resistance of the electrolyte part between the working and reference electrode, causes relatively large errors when the polarisation loss at the electrode is small. To reduce the electrolyte loss geometry 9 was developed. The reference electrode is now positioned on a ridge at the outside of the electrolyte cylinder. Using this configuration the electrolyte series resistance was reduced by 33 % and the total resistance was reduced by 69 %. Errors in the polarisation resistance, which could be measured down $10^{-2}\Omega\,\mathrm{cm}^2$, were within 5 % of the true values when using optimised dimensions.

2.3 Summary and some practical implications

The use of electrode geometries 1 to 7 illustrated in Fig.1 have the advantage that they can be combined with the use of thin components and thus they can easily satisfy the requirement listed at the end of section 2.1. From the geometries 1 to 7 electrode geometry 1 is preferred when one wants to measure the electrolyte resistance. This geometry can be used to obtain correct values of the electrolyte resistance. This geometry has shown to be satisfactorily in practice at our institute and can be used to screen the electrochemical performance of different electrode materials [1–3].

The condition of having a distance of at least 5 times the electrolyte thickness can also be easily satisfied for these geometries using thin electrolytes. For polarised measurements, e.g., I-V characteristics, one should be aware that the counter electrode should perform better by a factor of at least 5 times that of the working electrode, otherwise erroneous results will be obtained. This condition is difficult to verify because the counter electrode cannot be measured separately. If the counter electrode condition cannot be satisfied one can still use geometry 1 in a comparative way as long as the counter electrode in a series of samples is the same.

Symmetrically placed electrodes should be avoided for measurements on thin electrolytes, because small displacements of the order of the electrolyte thickness already induce significant errors. Such small displacements, e.g., 0.03 mm cannot be avoided during fabrication or even during testing, e.g., shrinkage due to in situ sintering of the electrode material at a high operating temperature.

Alternative geometries, using thick electrolytes, were developed at RISØ to measure true polarisation resistances. These cell configurations are very useful for modelling I-V characteristics for example. Disadvantages of these geometries are: 1) because of their relatively complex configuration they are not suitable as a fast and simple method to screen a large set of electrode materials and 2) the electrode is supplied to an electrolyte pellet and thus it will very likely have a different interface than the same electrode supplied on a thin electrolyte plate.

From the literature it is known that the interface plays a key role in the electrochemical losses and this interface is determined mainly by the manufacturing method. Part of the properties are even determined in the *green* (unsintered) state of the samples. Therefore, screening of different electrode materials in a half cell configuration should be done on samples that are made with the same fabrication method adopted for real fuel cells. Preferably these samples should be prepared from the same stock as the single fuel cells. We consider this an absolute requirement for screening different electrode materials on their electrochemical performance. If this is not done it will always be questionable whether results from half cells can be translated to single fuel cells or not. This is a serious disadvantage of electrode geometries using thick electrolytes.

Summarising, calculation of the primary current and voltage distributions, as described in this appendix, has shown that under polarisation conditions serious errors are introduced in the measured overpotentials depending on the electrode geometry. For the evaluation of mechanistic pathways and reaction models of electrode materials these problems clearly need to be solved. A reliable electrode configuration for thin samples is urgently required. The theoretical calculations should be extended by including the 1) details of the electrolyte microstructure, 2) non-ohmic polarisation losses occurring at the electrodes and 3) influence of mass transport effects.

3 Conclusions

1. For all three-electrode geometries discussed the distance d between working and reference electrode should be at least 5 times the electrolyte thickness L; $d/L \geq 5$.
2. For impedance measurements in which only the electrolyte resistance has to be measured of thin electrolyte discs electrode geometry 1, as used by ECN, is preferred.
3. Erroneous values for the polarisation resistance R_w will be measured when the counter electrode resistance R_c is comparable with or higher than R_w. It is recommended that $R_w/R_c \geq 10$.
4. The electrode geometry 1 can be used in a comparative way to distinguish between the electrochemical performance of several electrodes in a series of samples when all samples have similar counter electrodes. Absolute values of R_w cannot be obtained.
5. Electrode geometries with symmetrically placed electrodes on both sides of the electrolyte should be avoided for thin electrolytes, because displacements of the order of the electrolyte thickness already cause significant errors.
6. Currently there is no suitable geometry to measure correct overpotentials of thin electrolyte/electrode structures.
7. Alternative geometries, as developed at RISØ, using thick electrolyte pellets can be used to measure the correct overpotential at the working electrode. These methods cannot be used in combination with thin electrolytes. It is doubtful of the results from these geometries can be translated to similar electrodes on thin electrolyte plates.

List of abbreviations and symbols

SLM	15 mole % strontium-doped lanthanum manganite
SOFC	Solid Oxide Fuel Cell
tpb	Three-phase boundary
WE	Working electrode
CE	Counter electrode
RE	Reference Electrode
El	Electrolyte

δ	Displacement of symmetrically placed electrodes
ρ	Specific resistance
ϕ_w	Local potential imposed at working electrode
ϕ_c	Local potential imposed at counter electrode
ϕ_r	Local potential sensed at reference electrode
η_w, η_c	Overpotential of working and counter electrode respectively
ν	Frequency of a.c. voltage

A_{cs}	Electrolyte effective cross sectional area used as a relative measure for the *tpb* area
d	Distance between working and reference electrode
i	Current density
L	Thickness of electrolyte
R_w,	True resistance at working electrode
R_m,	Resistance measured at working electrode (calculated from U_w and i)
R_c	True resistance at counter electrode
R_{hf}	High frequency intercept on the real axis in the impedance diagram
R_{el}	True electrolyte resistance
U_w	Potential difference measured between *WE* and *RE*
U_{el}	Potential difference across the electrolyte between *WE* and *CE*

References

[1] F.P.F. van Berkel, F.H. van Heuveln, and J.P.P. Huijsmans. Status of SOFC Component Development at ECN. In S.C. Singhal and H. Iwahara, editors, *Proceedings of the Third International Symposium on Solid Oxide Fuel Cells, 1993 Hawaii*, pages 744–751. The Electrochemical Society, Pennington, NJ, 1993.

[2] F.H. Van Heuveln, F.P.F. Van Berkel, and J.P.P. Huijsmans. Electrochemical Characterization of Porous Electrodes and Application in SOFC. In F.W. Poulsen, J.J. Bentzen, T. Jacobsen, E. Skou, and M.J.L. Østergård, editors, *High Temperature Electrochemical Behaviour of Fast Ion and Mixed Conductors. Proceedings of the 14th Risø International Symposium on Materials Science, 6-10 September*, pages 75–84. Risø National Laboratory, Roskilde, Denmark, 1993.

[3] F.H. van Heuveln, H.J.M. Bouwmeester, and F.P.F van Berkel. Electrode Properties of Sr-doped $LaMnO_3$ on Yttria Stabilised Zirconia. Part I.: Three-phase Boundary Area & Part II: Electrode kinetics. *J.Electrochem.Soc.*, **144**, 126-139 (1997).

[4] G.J.M Janssen and F.H. van Heuveln. The effect of the cell geometry on electrode overpotential measurements using thin electrolytes. *To be submitted to: Solid State Ionics.*

[5] F.H. van Heuveln. Analysis of Non-exponential Transient Response Due to a Constant Phase Element. *J. Electrochem. Soc.*, **141**, 3423-3428 (1994).

[6] J. Winkler, P.V. Hendriksen, N. Bonanos, and M. Mogensen. Geometric Requirements to Solid Electrolyte Cells with a Reference Electrode. *To be published in: J. Electrochem. Soc.*

[7] F.M. Figueiredo, J.R. Frade, and F.M.B. Marques. Geometrical Effects on Polarsiation Measurements of $La_{0.9}MnO_3$ Cathodes Deposited on YSZ Substrates. In J.L. Baptista, J.A. Labrincha, and P.M. Vilarinho, editors, *Electroceramics V. Proceedings of the Int. Conference on Electronic Ceramics & Applications. Sept.2-4.*, pages 179–182, University of Aveiro, Portugal, 1996. European Ceramic Society.

[8] M. Nagata, Y. Itoh, and H. Iwahara. Dependence of Observed Overvoltages on the Positioning of the Reference Electrode on the Electrolyte. *Solid State Ionics*, **67**, 215-224 (1994).

[9] N.L. Robertson and J. N. Michaels. Oyxgen Exchange on Platinum Electrodes in Zirconia Cells: Location of Electrochemical Reaction Sites. *J. Electrochem. Soc.*, **137**, 129-135 (1990).

[10] K. Sasaki, J.-P. Wurth, R. Gschwend, M. Gödickemeier, and L.J. Gauckler. Microstructure-Property Relations of Solid Oxide Fuel Cell Cathodes and Current Collectors. Cathodic Polarization and Ohmic Resistance. *J. Electrochem. Soc.*, **143**, 530-543 (1996).

[11] Da Yu Wang and A.S. Nowick. Cathodic and Anodic Polarization Phenomena at Platinum Electrodes with Doped CeO_2 as Electrolyte. *J. Electrochem. Soc.*, **126**, 1155-1165 (1979).

[12] Y. Takeda R. Kanno, M. Noda, Y. Tomida, and O. Yamamoto. Cathodic Polarization Phenomena of Perovskite Oxide Electrodes with Stabilized Zirconia. *J. Electrochem. Soc.*, **134**, 2656-2661 (1987).

[13] K. Tsuneyoshi, K. Mori, A. Sawata, J. Mizusaki, and H. Tagawa. Kinetic Studies on the Reaction at the $La_0.6Ca_{0.4}MnO_3$/YSZ Interface, as an SOFC Air Electrode. *Solid State Ionics*, **35**, 263-268 (1989).

[14] J. Mizusaki, K. Amano, S. Yamauchi, and K. Fueki. Electrode Reaction at Pt, O_2(g)/Stabilized Zirconia Interfaces. Part II: Electrochemical Measurements and Analysis. *Solid State Ionics*, **22**, 323-330 (1987).

[15] B. Gharbage, T. Pagnier, and A. Hammou. Oygen Reduction at $La_{0.5}Sr_{0.5}MnO_3$ Thin Film/Yttria-Stabilized Zirconia Interface Studied by Impedance Spectroscopy. *J. Electrochem. Soc.*, **141**, 2118-2121 (1994).

[16] A. Yamashita, H. Tsukuda, and T. Hashimoto. Anodic and Cathodic Electrode Reaction at $La_{1-x}Sr_xMnO_3$. In U. Bossel, editor, *Proceedings of the First European Solid Oxide Fuel Cell Forum, 3-7 October, Lucerne - Switzerland*, pages 661–669. European SOFC Forum, Baden - Switzerland, 1994.

[17] J. Divisek, L.G.J. de Haart, P. Holtappels, T. Lennartz, W. Mallener, U. Stimming, and K. Wippermann. The Kinetics of Electrochemical Reactions on High Temperature Fuel Cell Electrodes. *Journal of Power Sources*, **49**, 257-70 (1994).

[18] B.A. Boukamp, I.C. Vinke, K. Sesham, K.J. de Vries, and A.J. Burggraaf. Influence of Electrode Geometry and NLLS Fit Analysis of I-V Measurements in a Three-Electrode Cell. *Solid State Ionics*, **28-30**, 1187-1191 (1988).

[19] B.A. van Hassel, B.A.Boukamp, and A.J. Burggraaf. Electrode Polarization at the Au,O_2(g)/Yttria Stabilized Zirconia Interface. Part II: Electrochemical measurements and Analysis. *Solid State Ionics*, **48**, 155-171 (1982).

[20] N.Ibl. Current Distribution. In E.Yeager, J.O'M.Bockris, B.E. Conway, and S.Sarangapani, editors, ELECTRODICS: TRANSPORT, Volume 6. Comprehensive Treatise of Electrochemistry, chapter 4, pages 239–315. Plenum Press, New York and London, 1983.

[21] F.H. van Heuveln. *Constriction of Current Lines in the Electrolyte and its Effect on the Electrolyte Resistance. In: Characterisation of Porous Cathodes for Application in Solid Oxide Fuel Cells.* PhD dissertation, Twente University, The Netherlands, Department of Chemical Technology, Jan. 1997.

Error Resulting from Ohmic Resistance Compensation in a Single Cell

Ann Mari Svensson and Kemal Nişancioğlu
Department of Electrochemistry
Norwegian University of Science and Technology
N-7034 Trondheim, Norway

Introduction

Nonuniform current and potential distribution at an electrode may cause difficulties in the interpretation of electrochemical data [1-3]. The nonuniform reaction rate may result from the particular cell geometry, reaction kinetics, mass transfer limitations, or a combination. Measured quantities such as polarization resistance, and other kinetic parameters might deviate considerably from their true values based on material properties. A mathematical model can thus be a useful tool to relate measured quantities to the material and kinetic properties of the cell components.

An evaluation of the error in the measurement of electrode kinetics caused by nonuniform ohmic-potential drop to a disk electrode was presented by Tiedemann *et al.* [1]. A similar approach was applied by Nişancioğlu [2] to investigate the discrepancy between true and measured corrosion rates. West and Newman [3] considered a channel geometry and investigated possible errors in the measured exchange current density and charge transfer coefficient with respect to the placement of the reference electrode, assuming linear or Tafel kinetics.

Here, we consider rectangular shaped geometry of arbitrary size, thought to represent typical solid state electrochemical cells, like those used for the evaluation of electrode materials for application in a SOFC. Possible errors in the measured polarization resistance are investigated for various cell geometries, kinetic parameters and positions of the reference electrode. Emphasis is given to problems related to the use of thin electrolytes.

Theory

Basic Equations. When formulating the problem mathematically, ohmic losses in the electrode and concentration gradients are neglected. It is furthermore assumed that the exchange current density is a constant.

A single cell as depicted in Fig. 1 is considered, with a dense working electrode well adhering to the electrolyte at the top (WE), and a dense, well adhering material, acting as a counter electrode, CE, at the bottom. Two possible placements of the reference electrode, RE, are indicated in Fig. 1. The reference electrode probes the potential of the working electrode.

In the absence of concentration gradients, the potential in the electrolyte obeys Laplace's equation

$$\nabla^2\Phi = 0 \tag{1}$$

The relevant boundary conditions are

$$\begin{aligned}
\frac{\partial\Phi}{\partial x} &= 0 \qquad \text{at } x = 0 \text{ (symmetry condition)} && (2)\\
\frac{\partial\Phi}{\partial x} &= 0 \qquad \text{at } x = L \text{ (symmetry condition)} && (3)\\
-\kappa\frac{\partial\Phi}{\partial y} &= \begin{cases} i^w(x) & \text{at } y = \frac{1}{2}\delta,\ 0 < x < L^w \\ 0 & \text{at } y = \frac{1}{2}\delta,\ L^w < x < L \end{cases} && (4)\\
-\kappa\frac{\partial\Phi}{\partial y} &= \begin{cases} i^c(x) & \text{at } y = -\frac{1}{2}\delta,\ 0 < x < L^c \\ 0 & \text{at } y = -\frac{1}{2}\delta,\ L^c < x < L \end{cases} && (5)
\end{aligned}$$

where L is half the width of the model cell, δ is the electrolyte thickness, κ is the conductivity of the electrolyte, i is the current density, and superscripts w and c refer to the working and counter electrodes, respectively. Due to the symmetry of the problem, see Fig. 1, the Laplace equation is solved only for one half of the cell. The current distributions along the electrodes, i^w or i^c, are assumed to obey the linear relationship:

$$i(x) = i_o\frac{nF(\alpha_a + \alpha_c)}{RT}\eta_s(x) \tag{6}$$

where i_o is the exchange current density, and $\eta_s(x)$ is the surface overpotential, defined by

$$\eta_s^w(x) = V - \Phi(x, \frac{1}{2}\delta) \qquad \text{and} \qquad \eta_s^c(x) = \Phi(x, -\frac{1}{2}\delta) \tag{7}$$

Here, V is the cell potential, and the potential of the CE is arbitrarily set equal to zero.

Measured and True Polarization Resistance. The potential measured by the reference electrode can be expressed as

$$V^{RE} = \eta_s^w + \Phi_o^w - \Phi^{RE} \tag{8}$$

where Φ_o^w is the potential at the surface of the WE, and Φ^{RE} is the potential at the location of the reference electrode. To obtain the surface overpotential, V^{RE} has to be corrected for the ohmic drop. The measured surface overpotential is then given by [1]

$$\eta_s^{eff} = V^{RE} - \Delta\Phi_\Omega^{RE} \tag{9}$$

where

$$\Delta\Phi_\Omega^{RE} = \Phi_\Omega^w - \Phi_\Omega^{RE} \tag{10}$$

is the measured ohmic potential drop, and the subscript Ω refers to the primary potential distribution.

The effective polarization resistance is given by

$$R_p^{eff} = \frac{\eta_s^{eff}}{I} = \frac{V^{RE} - (\Phi_\Omega^w - \Phi_\Omega^{RE})}{I} = \frac{V - \Phi^{RE} - (\Phi_\Omega^w - \Phi_\Omega^{RE})}{I} \tag{11}$$

where I is the total cell current. The latter equality is valid since the CE is assumed to be grounded. The true polarization resistance, on the other hand, is given by

$$R_p = \frac{RT}{i_o^w(\alpha_a + \alpha_c)nFWL^w} \tag{12}$$

where W is the width of the cell perpendicular to the paper plane.

Results and Discussion

As is shown in the foregoing section, the measured and true values of the polarization resistance can be different. The measured value differs from the true value depending on the reaction kinetics and geometrical factors, such as the position of the reference electrode, and the nature of potential distribution in the electrolyte. Mathematical analysis of the potential distribution problem indicates that the effect of kinetics can be expressed by a dimensionless reaction rate constant for each electrode, expressed by [4]

$$J = \frac{i_o(\alpha_a + \alpha_c)nFL}{\kappa RT} \tag{13}$$

As shown in earlier work for other cell and electrode geometries [3], the error in the measured polarization resistance increases with increasing J^w. Depending on the cell geometry, the error can be significantly affected by the kinetics of the counter electrode, J^c, as demonstrated in Fig. 2, which compares the results of two cells with identical geometry, but different reaction kinetics at the counter electrode ($J^c = 10$ and $J^c = 100$).

The deviation from the true value is not significant unless the electrode reactions are fast, or the electrolyte conductivity is extremely low. For an YSZ electrolyte the conductivity at T = 1000°C is approximately $\kappa \approx 0.1$ Scm^{-1}. Typical exchange current densities are of the order 0.001-0.1 Acm^{-2}. Thus J^w/L lies in the range $0.2 - 20$ cm^{-1} which implies that J^w is not likely to be very large for ordinary cell geometries. The error does not seem to depend much on the placement of the reference electrode.

Figure 3 illustrates how the kinetics of the counter electrode affects the current distribution along the working electrode for the same cell as in Fig. 2. The results in Figs. 2 and 3 correspond to a relatively thin electrolyte (δ/L=0.1). For such cases, the kinetics of the counter electrode distorts the potential distribution at the working electrode and thereby affects R_p^{eff}. An investigation of the same cell geometry, but with a thick electrolyte (δ/L=1), revealed a negligible dependence of R_p^{eff} on the kinetics of the CE.

In Fig. 4 the primary and secondary potential distributions along the upper surface of the electrolyte, and the total cell voltage are plotted for a cell with a reversible counter electrode. The cell geometry is similar to the one considered in Figs. 2 and 3. The true value of the surface overpotential is indicated with an arrow. A more realistic situation is plotted in Fig. 5 for the same cell geometry, but where the finite kinetics of the counter electrode has been taken into account ($J^c = 10$). The additional overpotential at the CE leads to an increase in the total cell potential compared to Fig. 4. The values of V^{RE}, $\Delta\Phi^{RE}$, and η_s^{eff} are indicated with arrows for a reference electrode placed at $x^{RE} = 0.7L$. The discrepancy in η_s^{eff} with respect to the true value of η_s^w is considerable. This is related to the fact that the secondary, and primary potential distributions rapidly decrease to zero outside the domain of the WE, and the overpotential measured by the reference electrode becomes the sum of the overpotentials at the working and counter electrodes.

The problem is related to the specific cell geometry considered. The influence of the counter electrode on the measured polarization resistance can be minimized, e.g., by use of small working electrodes or symmetrical cells. The types of errors discussed in this paper are expected to occur in cells with thin electrolytes and where the reaction rate limitations at the two electrodes are of the same order of magnitude.

Acknowledgement

This work was supported by the Norwegian Research Council.

References

[1] W.H. Tiedemann, J. Newman and D.N. Bennion, *J. Electrochem. Soc.*, **120**, 256 (1973).

[2] K. Nişancioğlu in *The Measurement and Correction of Electrolyte Resistance in Electrochemical Tests, ASTM STP 1056*, L.L. Scribner and S.R. Taylor, Eds., American Society for Testing and Materials, Philadelphia, 1990, p. 61.

[3] A.C. West and J. Newman, *J. Electrochem. Soc.*, **136**, 3755 (1989).

[4] J.S. Newman, *Electrochemical Systems*, 2nd Ed., Prentice Hall, New Jersey (1991).

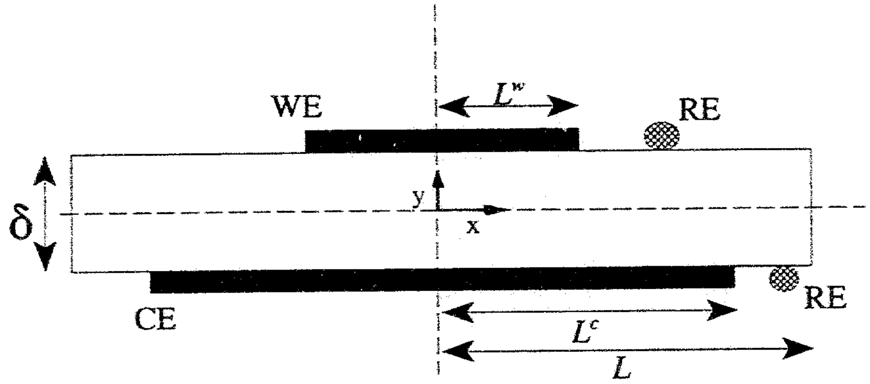

Figure 1: Single cell with partly covering working and counter electrodes (WE and CE). Two possible placements of the reference electrode, RE, are indicated.

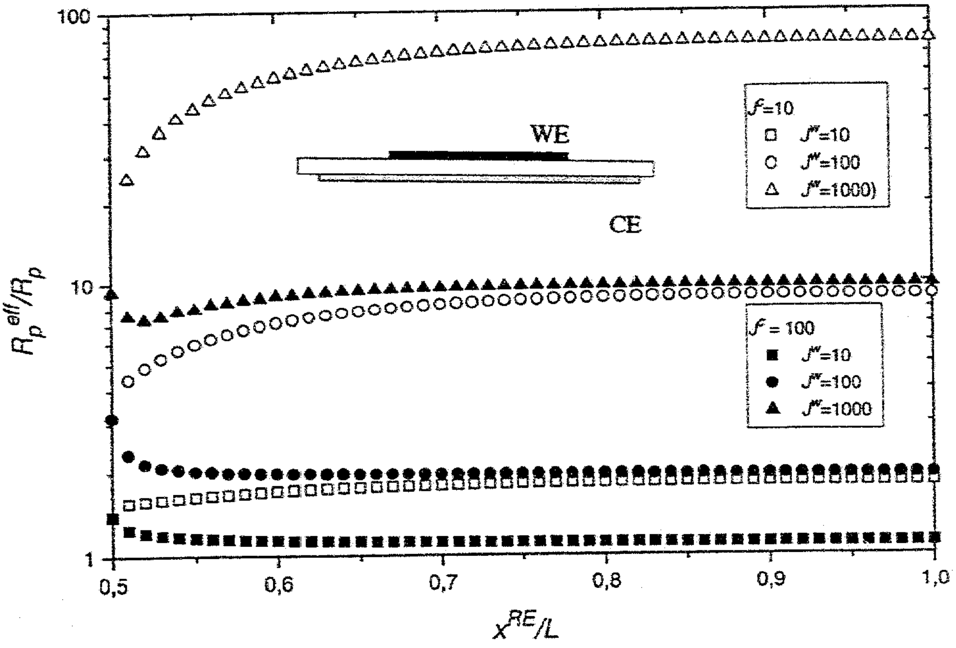

Figure 2: Calculated values of R_p^{eff}/R_p vs. dimensionless position of the RE for various values of J^w. Cell parameters: L^w/L=0.5, L^c/L=0.9, J^c=10, and δ/L=0.1.

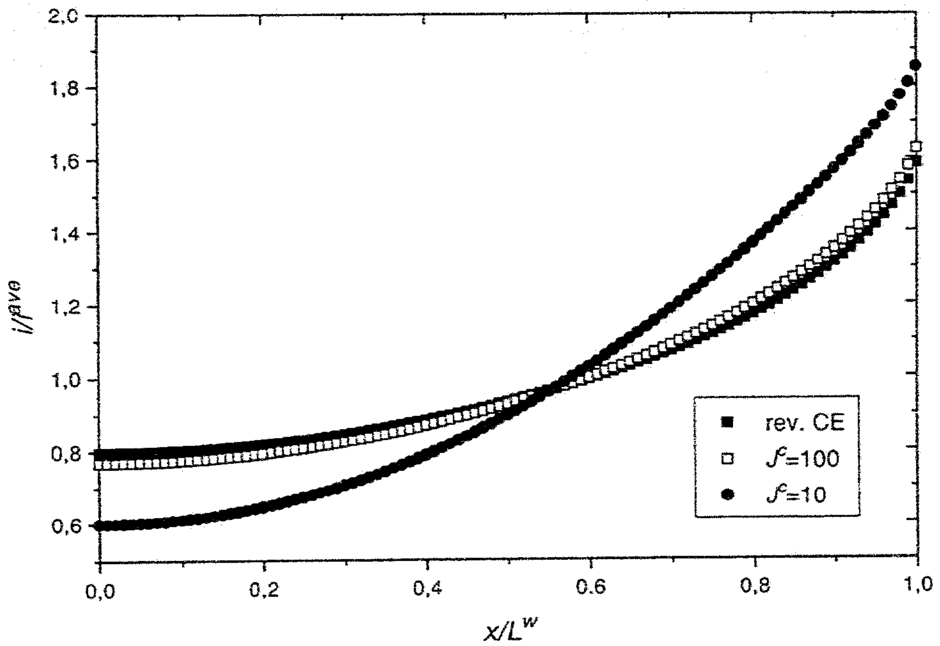

Figure 3: Current distribution on the WE of the cell geometry used in Fig. 2 for various values of J^c.

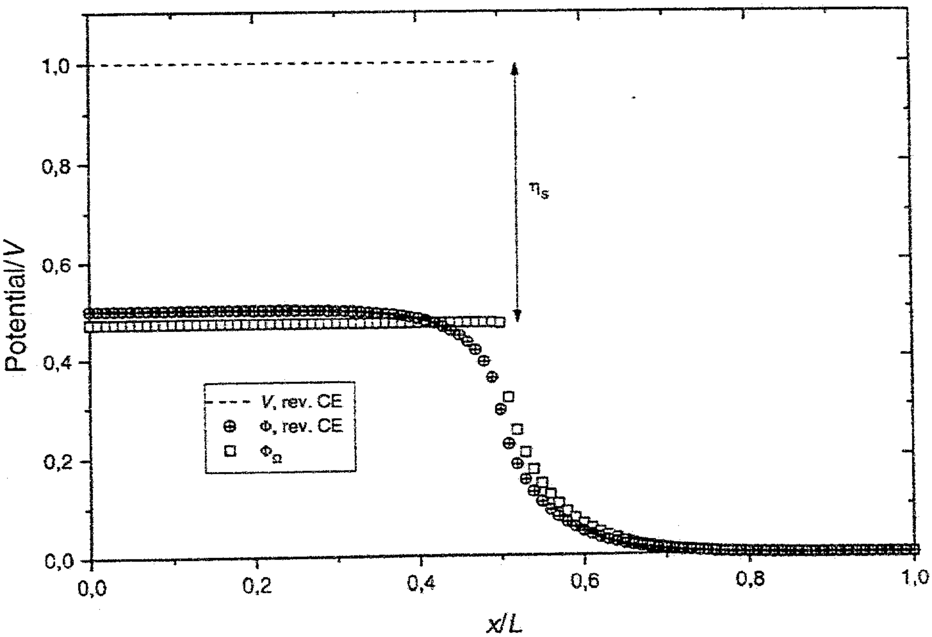

Figure 4: Comparison of primary and secondary potential distributions, and total cell voltage, V, for the cell in Fig. 2 with reversible CE, and $J^w = 10$.

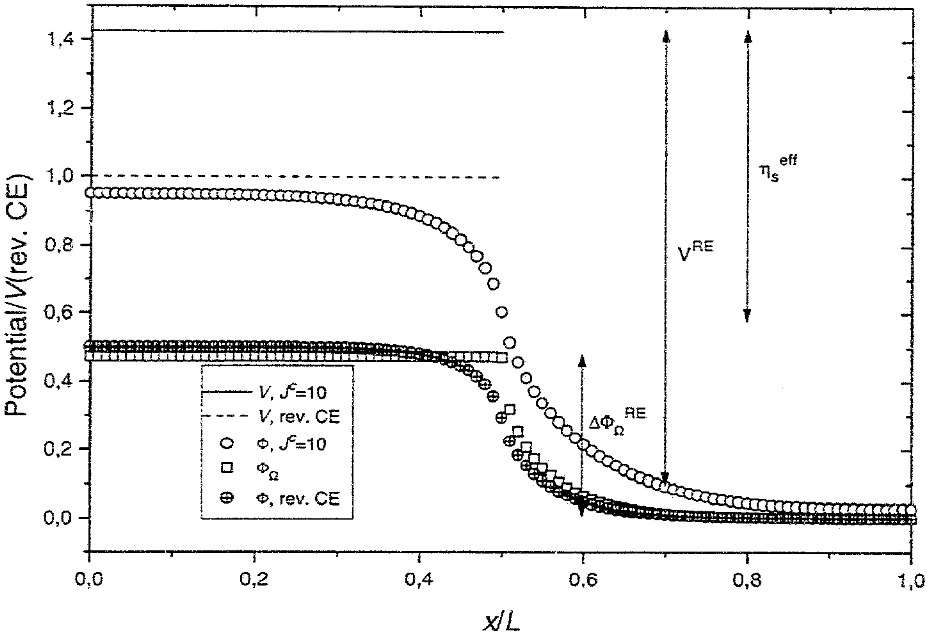

Figure 5: Comparison of primary and secondary potential distributions, and total cell voltage, V, for the cell in Fig. 2 for reversible and nonreversible ($J^c = 10$) CE.

Fabrication and properties of new materials for low temperature operation

K.L.Choy, W.Bai, and B.C.H.Steele
Department of Materials
Imperial College of Science, Technology, and Medicine
London SW7 2BP UK

The high oxygen-ionic conductivity and thermochemical stability of solid electrolytes are necessary to provide good electrochemical performance in solid oxide fuel cells. In the search for a new oxygen ion conductor, ABO_3 perovskite offers an interesting alternative because its structure is very tolerant to changes in the radii of the A and B ions and it can also accommodate large concentrations of cation vacancies particularly on the A sites[1,2] .

Recently, Ishihara et al [3-7] have reported that the $LaGaO_3$ perovskite with the A site substituted by Sr and B site by Mg exhibits good oxygen ionic conducting properties at elevated temperatures. This electrolyte is commonly known as LSGM. This new material is reported to be stable in both reducing and oxidising atmospheres up to 1223K, and the highest conductivity is observed in $La_{0.9}Sr_{0.1}Ga_{0.8}Mg_{0.2}O_{3-x}$. The chemical reactivity between electrolyte and electrodes is eliminated if both components are perovskites[8] .

At present, all investigations on LSGM have been focused on the bulk materials. There has been no reported literature on the study of LSGM films. This may be because it is difficult to deposit multicomponent oxide films using the conventional CVD and PVD techniques or the wet chemical routes as a high sintering temperature is required (~1500 ^{0}C). This paper reports the feasibility of producing LSGM film using a novel and cost-effective deposition method called Aerosol-assisted Chemical Vapour Deposition in an electric field (ACVDe)[9,10]. The ACVDe process involves spraying atomised precursor droplets across a heated environment where the droplets undergo combustion and chemical reaction in the vapour phase near the vicinity of the substrate. This leads to the formation of a stable solid film with excellent adhesion onto a heated substrate in an open atmosphere. The technical and economical viability of the ACVDe technique to produce SOFC components such as the dense $Zr(Y)O_{2-x}$ electrolytes, porous Ni-YSZ anode, porous $La(Sr)MnO_3$ cathode structure, and multilayer $La(Sr)MnO_3$ /$Zr(Y)O_{2-x}$ /Ni-YSZ PEN structure have been reported in this workshop[11]

This paper reports the preliminary study on the ACVDe of LSGM films. A dense and free-crack LSGM film without pinhole has been successfully deposited onto a porous electrode LSM at 350 ^{0}C, followed by sintering at 1000 ^{0}C. The sintering temperature is lower than the sintering temperature in bulk LSGM materials (1500 ^{0}C). The microstructure of the LSGM film depends on the deposition process and the sintering temperature. XRD result indicates that the deposited $La_{0.9}Sr_{0.1}Ga_{0.8}Mg_{0.2}O_{3-x}$ film has the $LaGaO_3$-perovskite phase.

Both Sr and Mg dopants have been dissolved substitutionally into the lattice of A and B sites in $LaGaO_3$ to form a solid solution. The ionic conductivity of LSGM film is higher than that of the 9mol%YSZ, but the ionic conductivity values of the bulk CGO ($Ce_{0.8}Gd_{0.2}O_{1.9}$) are comparable with the LSGM film in medium and high temperature ranges as shown in figure 1.

This preliminary study has demonstrated the feasibility of the cost-effective ACVDe method to produce dense LSGM films with good ionic conductivity. Further work is in progress to optimise the precursors and the processing parameters, in order to deposit LSGM in a single step, without further hear treatment.

Acknowledgement

We thank Mr. Rudkin for his technical assistance. The financial supports of the Royal Society, and Engineering, Physical and Science Research Council, UK(GR/K/86954) are gratefully acknowledged.

References

[1] B.C.H.Steele, in High Conductivity Solid Ionic Conductors, Recent Trends and Applications, T.Takahashi, Editor, p. 402, World Scientific, Singapore, 1989.
[2] S.P.S.Badwal, ibid., 52, 23(1992)
[3] T.Ishhihara, H.Matsuda and Y.Takita, J.Am.Chem.Soc., 116, 3801(1994)
[4] T.Ishihara, H.Matsuda and T.Takita, Solid State Ionics, 79, 147(1995)
[5] M.Feng and J.B.Goodenough, Eur.J.Solid State Inorg.Chem., 31, 663(1994)
[6] A.Petric, P.Huang and A.Skowron, Proc. 2nd Eur. SOFC Forum, ed B.Thorstensen, Druckerei J Kinzel, Gottingen, Germany, 1996, p751-760
[7] J.B.Goodenough, A.Manthiram and J.F.Kuo, Mater.Chem.Phys., 35, 221(1993)
[8] T.Ishihara, H.Minami, H.Matsuda, and Y.Takita, in Solid Oxide Fuel Cells IV, M.Kokiya, O.Yamamoto, H.Tagawa, and S.C.Singhal, Editor, PV95-1, p.344, The Electrochemical Society Proceedings Series, Penningto, NJ, 1995)
[9] K.L.Choy and W. Bai, British Patent, No.9525505.5, 1995
[10] K.L.Choy and W.Bai, Novel deposition process for ceramic film and coating, submitted the Journal of European Ceramic Society
[11] K.L.Choy and W.Bai, Novel fabrication of $La(Sr)MnO_3$/YSZ/NiO-YSZ PEN cells, IEA Workshop, Switzerland, January 28-31, 1997

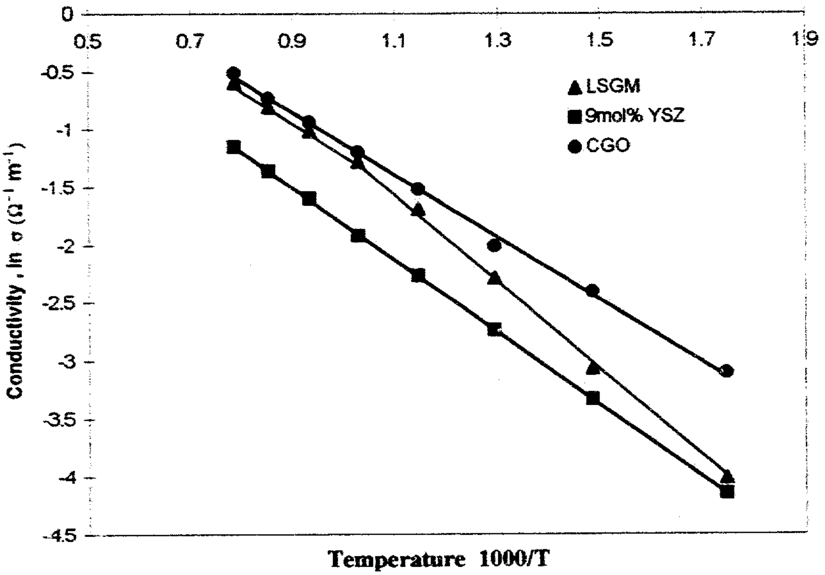

Figure 1 The Arrhenius plots of bulk conductivity of LSGM film with a symmetrical cell structure of LSM/LSGM/LSM

Electrostatic Spray Deposition of Doped YSZ Electrode Materials for a Monolithic Solid Oxide Fuel Cell Design

by

N.H.J. Stelzer, C.H. Chen, L.N. van Rij, and J. Schoonman

Laboratory for Applied Inorganic Chemistry, Delft University of Technology,
Julianalaan 136, 2628 BL Delft, The Netherlands

ABSTRACT

The recently in our laboratory developed Electrostatic Spray Deposition (ESD) technique is a cheap and powerful tool for synthesis of doped yttria-stabilized zirconia thin films. The influence of different deposition parameters on the morphology of Tb -YSZ, Ti-YSZ solid solutions, and a NiO-YSZ cermet is discussed. Dense and porous thin films of doped YSZ and NiO-YSZ electrode materials deposited on YSZ can be obtained by controlling the deposition parameters. A monolithic fuel cell design based on YSZ as electrolyte with Tb-YSZ as cathode and Ti-YSZ or NiO-YSZ cermet as anode prepared by ESD is proposed for its use in a mixed gas atmosphere.

INTRODUCTION

Electrostatic Spray Deposition (ESD) recently developed in our laboratory [1], and more recently referred to as Aerosol-Assisted Chemical Vapour Deposition [2], is a non-vacuum thin film method based on electrostatic atomization of liquid precursors. It has been applied for preparing thin film metal oxides for application in Solid Oxide Fuel Cells (SOFCs) and lithium-ion batteries, such as yttria stabilized zirconia (YSZ), Tb-YSZ and $BaCeO_3$, as well as $LiMn_2O_4$ and $LiCoO_2$, respectively [3-7]. This technique has the advantage of requiring only a simple and cheap set-up compared to conventional gas phase deposition techniques like Chemical and Electrochemical

Vapour Deposition (CVD) and (EVD) [8]. Due to a well defined trajectory of spray droplets towards a grounded substrate by the electric field, a high deposition efficiency and reliability for controlled layer compositions and morphologies can be obtained. In this respect, it is similar to the so-called corona spray pyrolysis technique [9]. ESD is a promising route to the synthesis of dense as well as porous thin films at relatively low deposition temperatures and, therefore, lower materials processing and fabrication costs. There are various chemical and physical processes involved which influence the morphology of the deposited layers.

Yttria-stabilized zirconia, doped either with terbia or titania, has been reported to exhibit mixed conductivity at elevated temperatures. Terbia-doped yttria-stabilized zirconia (Tb-YSZ) exhibits oxygen ion and p-type conductivity at high oxygen partial pressures and elevated temperatures (e.g. $P_{O_2} > 0.21$ atm at 800 °C) [10]. The oxygen ion conductivity in Tb-YSZ is due to the high concentration of oxygen ion vacancies in the lattice, which have significant mobilities at temperatures higher than 600 °C. The p-type conductivity in terbia-doped zirconia-based cubic fluorite structured solid solutions, such as $(ZrO_2)_{1-x-y}(Tb_2O_{3.5})_x(Y_2O_3)_y$, is believed to be due to hopping of mobile electronic charge carriers [8]. Titania-doped yttria stabilized zirconia (Ti-YSZ) exhibits oxygen ion and n-type conductivity at low oxygen partial pressures and elevated temperatures (e.g. $P_{O_2} < 10^{-15}$ atm at 800 °C) [11]. With respect to their mixed conducting behaviour, these doped YSZ materials may have potential electrode and catalytic applications in high-performance solid oxide fuel cells (SOFCs) [12]. Therefore, the fabrication of a monolithic fuel cell based on YSZ as electrolyte, using Tb-YSZ as cathode and Ti-YSZ as anode material becomes straightforward.

In this paper, we report the use of the electrostatic spray deposition (ESD) technique to deposit porous and dense Tb-YSZ, Ti-YSZ, and NiO-YSZ cermet on YSZ. Butyl carbitol / ethanol mixed solutions containing terbium-, titanium-, nickel-, yttrium- and zirconium metal organic precursors are used. The influence of the different deposition parameters for ESD is discussed. The control of the morphology formed under certain deposition parameters is investigated. A monolithic fuel cell design based on YSZ as electrolyte with Tb-YSZ as cathode and Ti-YSZ or NiO-YSZ as anode prepared by ESD is proposed for its use in a mixed gas atmosphere.

EXPERIMENTAL

An ESD set-up with a vertical configuration, as shown in Fig. 1, was used for the deposition of thin Tb-YSZ, Ti-YSZ, and NiO-YSZ layers. A resistively heated substrate holder was used to control the substrate temperature. Stainless steel and YSZ ($Zr_{0.84}Y_{0.16}O_{1.92}$, ECN, Netherlands) disks (12 or 20 mm in diameter) are used as substrates. The metal disks had a thickness of 1 mm, while the YSZ substrates had a thickness of 0.13 mm. A thin stainless steel disk was used to obtain a good contact between the thin YSZ substrates and the heated substrate holder. A positive high voltage of +10 kV was applied to the nozzle. The nozzle-to-substrate distance was 30 mm. The feed rate of the precursor solution was set to 0.5 ml/hour using a syringe pump.

Zirconium-(IV)-acetyl acetonate ($Zr(O_2C_5H_7)_4$, Alfa), yttrium-(III)-acetyl acetonate ($Y(O_2C_5H_7)_3$, 99.9%, Alfa), terbium-(III)-acetate hydrate ($Tb(CH_3COO)_3 \cdot H_2O$, 99.9%, Aldrich), titanium-(IV)-ethoxide ($Ti(C_2H_5O)_4$, Aldrich), and nickel-(II)-acetate ($Ni(C_2H_5OO)_2$, Aldrich) were used as precursors. Butyl carbitol (99.9%)-ethanol (99%) mixtures with ratios of 50:50 vol% and 80:20 vol% were used as solvents for precursor solutions. The cation ratios were set to $Zr_{0.55}Y_{0.18}Tb_{0.27}$, $Zr_{0.71}Y_{0.13}Ti_{0.16}$ in the solutions with total metal concentrations of 0.09 M and 0.05 M. For the NiO-YSZ a Ni:YSZ ratio of 60:40 vol% in a 0.05M solution was prepared. The morphology and composition of the layers were analyzed using a scanning electron microscope (SEM) (JEOL JSM-35 model) equipped with an energy dispersive X-ray microanalyzer (EDX) (Link ISIS, Oxford Instruments Ltd.).

Elemental analysis by EDX for Tb-YSZ, Ti-YSZ, and NiO-YSZ layers confirms that the overall composition of the layer is the same as that of the precursor solution within experimental error. This is in agreement with earlier investigations on various oxide compounds [13] and shows another advantage of the ESD technique compared to other deposition techniques.

ESD PARAMETERS

During our investigations of the ESD of Tb-YSZ thin layers, five types of layer morphologies are observed. Type I is a relatively dense but cracked layer, type II is a dense layer, type III consists of a dense bottom layer with some particles incorporated or some lamellar particles on top of the dense layer, type IV is a porous layer, and type V is a very porous layer of fractal-like agglomerates.

These five types of morphologies can be formed under certain deposition conditions. In the following we will give a comprehensive overview about the deposition parameters and their influence on the morphology of electrostatic spray deposited thin films.

A) With increasing deposition time, and accordingly increasing layer thickness, more agglomeration at the surface will occur resulting in a more porous layer. Therefore, the shorter the deposition time, the more dense the deposited layer.

B) The size of the droplets and their mass determine the deposition process that occurs above the required decomposition temperature. The larger the droplets, the more heat will be necessary to evaporate the solvent and to enable precipitation at the substrate. Therefore, with increasing precursor concentration the deposition temperature has to be increased to obtain a layer with same morphology.

C) The deposition temperature is one of the most important deposition parameters. By increasing the deposition temperature, the morphology of a layer deposited on a certain substrate usually shifts from a dense to a highly porous structure.

D) The applied voltage between needle and substrate is important to obtain a stable Taylor cone and thereby, to increase the reliability of the deposition. Within a voltage window, a higher voltage results in a more dense layer due to an increase in still wet incoming droplets at the substrate surface.

E) The boiling point of the solvent determines the spreading behaviour of the solvent droplets on the substrate. By using a solvent with a high boiling point the morphology of a layer becomes more dense due to the slower evaporation and precipitation rate of the droplet. At the same time a higher deposition temperature is required in order to obtain a certain evaporation rate. Otherwise, a cracked layer will be obtained.

F) The flow rate of the precursor solution can have the following influence on the layer morphology . To obtain a dense layer morphology a low flow rate is recommended, while for high flow rates porous and reticular structures can be obtained.

G-H) The substrate can influence the morphology of a deposited layer due to its porosity, surface roughness and surface tension. These properties may change during deposition due to the different properties of the deposited layer. The porosity of a substrate can affect the morphology of a deposited layer due to the lower thermal conductivity which lowers the heat necessary for the evaporation of the solvent near or at the surface of the substrate. A higher surface roughness will enhance preferential landing of the droplets leading to more agglomerates. A lower surface tension may result in the formation of discrete particles which also increases the surface roughness and thereby lead to preferential landing of the droplets.

Therefore, with increasing substrate density a more dense layer can be obtained. By changing the substrate from a conductive metal to a non conductive metal oxide, the temperature has to be increased to obtain the same morphology.

The above mentioned deposition parameters for ESD (shown schematical in Fig. 2) have to be controlled to obtain the desired layer morphology.

RESULTS

Effect of Deposition Temperature

Typical surface morphologies of Tb-YSZ and Ti-YSZ thin films deposited at different temperatures on YSZ substrates are shown in Fig. 3. It can be seen that for solutions with a total metal concentration of 0.09 M in 80 vol% butyl carbitol + 20 vol% ethanol mixed alcohol the layer deposited at 360 °C for 1 h [Fig. 3(A)] is cracked and tends to spill-off from the YSZ substrate. This morphology (type I) is always found to be present if the deposition temperature is too low. By increasing the deposition temperature up to 400 °C [Fig. 3(B)] a dense Tb-YSZ layer can be obtained, belonging to the type II morphology. Further increase in deposition temperature to 420 °C leads to minor agglomeration on top of a dense bottom layer and the deposited film [Fig. 3(C)] shifts to a type III morphology. At a deposition temperature of 450 °C [Fig. 3(D)], the deposited layer shows a porous type IV morphology. With increasing deposition temperature the morphology of the deposited layer changes from type I to type V (see Fig. 5).

As shown in Fig. 4, the dense Tb-YSZ layer deposited at 360 °C for 2 h on a stainless steel substrate, using an 80 vol% butyl carbitol + 20 vol% ethanol mixture as solvent for a 0.09 M precursor solution exhibits good adherence. Dense Tb-YSZ and Ti-YSZ deposited on YSZ showed no change in their layer morphology after thermal cycling between room temperature and 1100 °C with heating and cooling rates of 300 °C/h.

Effect of Solvent

By changing the solvent composition, the physical properties such as boiling point of the solvent, solubility of the precursor solutes, spreading behaviour on the substrate of incoming droplets, and the electrical conductivity of the solution will change. Therefore, the morphology of a deposited layer may also be modified. As shown in Fig. 5 the morphology changes quite radically from a fractal-like type V to a dense type II layer by using a mixture of 80 vol% butyl carbitol + 20 vol% ethanol instead of a mixture of 50 vol% butyl carbitol + 50 vol% ethanol as the solvent.

This extreme change in the layer morphology can be explained by the higher boiling point of the 80:20 alcohol mixture. Using high-boiling point solvents causes the evaporation rate to decrease and the spreading of the still wet droplets on the substrate will be slower than using butyl carbitol-ethanol mixtures with higher ethanol content and accordingly lower boiling point. Therefore, a relatively dense layer can be obtained.

Preliminary results showed that with the 50 vol% butyl carbitol + 50 vol% ethanol mixture no dense layers could be obtained on stainless steel and YSZ substrates. A very narrow temperature range, i.e. around 10 K, was found, in which the morphology of a deposited layer changes from type I to type IV on stainless steel, respectively, type I to type V on YSZ substrates.

NiO-YSZ by ESD

A NiO-YSZ cermet has been deposited at 380 °C for 2 h on YSZ, using an 80 vol% butyl carbitol + 20 vol% ethanol mixture as solvent for a 0.05 M precursor solution. As shown in Fig. 6, a porous type IV morphology has been obtained. With respect to the morphology-temperature diagram in Fig. 5, the morphology of the NiO-YSZ layer fits very well into the curve for the 80:20 alcohol mixture of 0.05 M doped YSZ layers deposited on YSZ. This result implies that the determined morphology-temperature diagram might be also used to control other YSZ based materials.

MONOLITHIC SOFC

Recently a monolithic SOFC design was proposed by Worrel et al. [11]. Based on our results on the synthesis of doped YSZ thin films by ESD, the general design of a Tb-YSZ/YSZ/Ti-YSZ cell with Tb-YSZ as cathode, YSZ as electrolyte, and Ti-YSZ as anode becomes easy to prepare. As shown in Fig. 7, we propose the use of this cell in a mixed gas atmosphere to investigate the performance of the cell and the catalytic activities of the doped YSZ electrode materials [14].

CONCLUSIONS

Our investigation on doped YSZ and NiO-YSZ thin films prepared by ESD shows that the electrostatic spray deposition (ESD) technique is a very promising synthesis method to lower materials processing and production costs for SOFC fabrication.

The desired morphology of doped YSZ and NiO-YSZ thin films can be obtained by controlling the deposition parameters. Dense and porous Tb-YSZ, Ti-YSZ, and NiO-YSZ can be deposited on YSZ by ESD.

Electrostatic spray deposition shows an easy and cheap way to prepare a monolithic solid oxide fuel cell.

ACKNOWLEDGMENT

N.H.J. Stelzer is grateful to the Delft University of Technology for a research fellowship. The authors are indebted to Dr. F.P.F. van Berkel of the Netherlands Energy Research Foundation (ECN) for providing the YSZ substrates.

REFERENCES

1. A.A. van Zomeren, E.M. Kelder, J.C.M. Marijnissen, and J. Schoonman, J. Aerosol Sci., **25**, 1229 (1994).
2. K.L. Choy, W. Bai, and B.C.H. Steele, this conference.
3. E.M. Kelder, O.C.J. Nijs, and J. Schoonman, Solid State Ionics, **68**, 5 (1994).
4. C.H. Chen, A.A.J. Buysman, E.M. Kelder, and J. Schoonman, Solid State Ionics, **80**, 1 (1995).

5. C.H. Chen, E.M. Kelder, and J. Schoonman, J. Mater. Sci., **31**, 5437 (1996).

6. C.H. Chen, K. Nord-Varhaug, and J. Schoonman, J. Mater. Synthesis and Processing, **4**, 189 (1996).

7. N.H.J. Stelzer, and J. Schoonman, J. Mater. Synthesis and Processing, in press.

8. G.-Z. Cao, J.Meijerink, H. W. Brinkman, K.J. de Vries, and A.J. Burggraaf, J. Mater. Chem., **3**, 773 (1993).

9. W. Siefert, Thin Solid Films, **120**, 267 (1984).

10. P. Han and W.L. Worrell, J. Electrochem. Soc., **142**, 4235 (1995).

11. S.S. Liou and W.L. Worrell, Appl. Phys., A **49**, 25 (1989).

12. W.L. Worrell and P.K. Davies, U.S. Patent 5,298,235, March 29, 1994.

13. C.H. Chen, E.M. Kelder, P.J.J. van der Put, and J. Schoonman, *J. Mater. Chem.*, **6**, 765 (1996).

14. N.H.J. Stelzer, L.N. van Rij, and J. Schoonman, to be published.

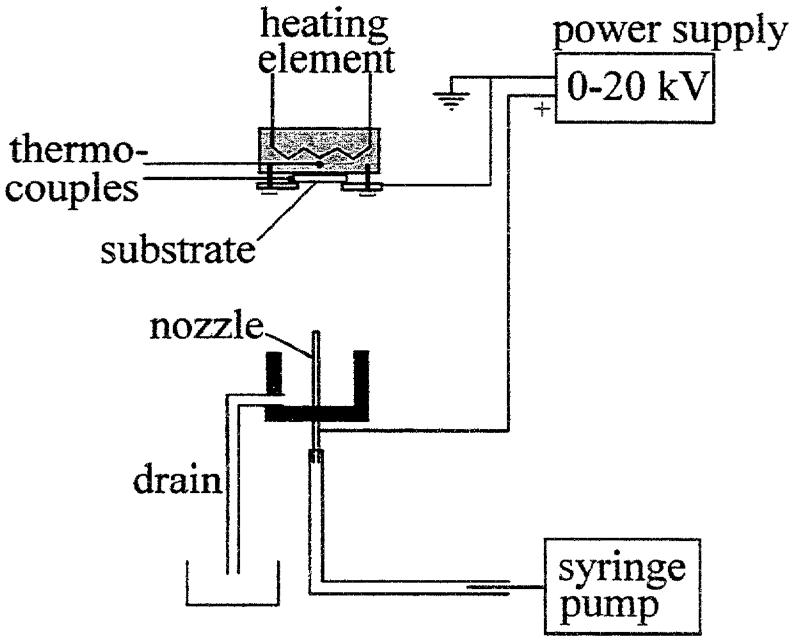

Fig. 1 ESD Set-Up

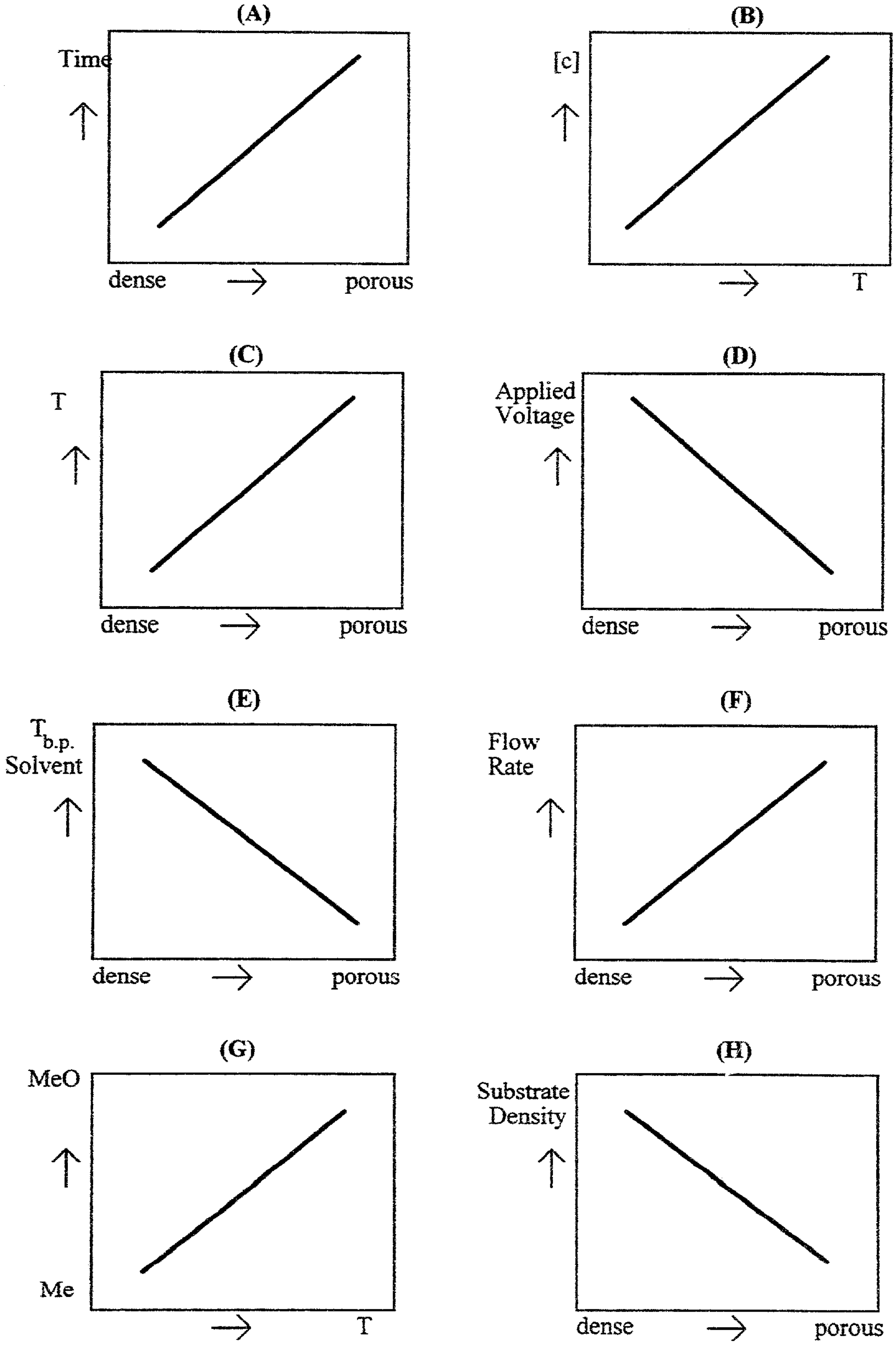

Fig. 2 Schematical graphs for morphology control of ESD thin films.

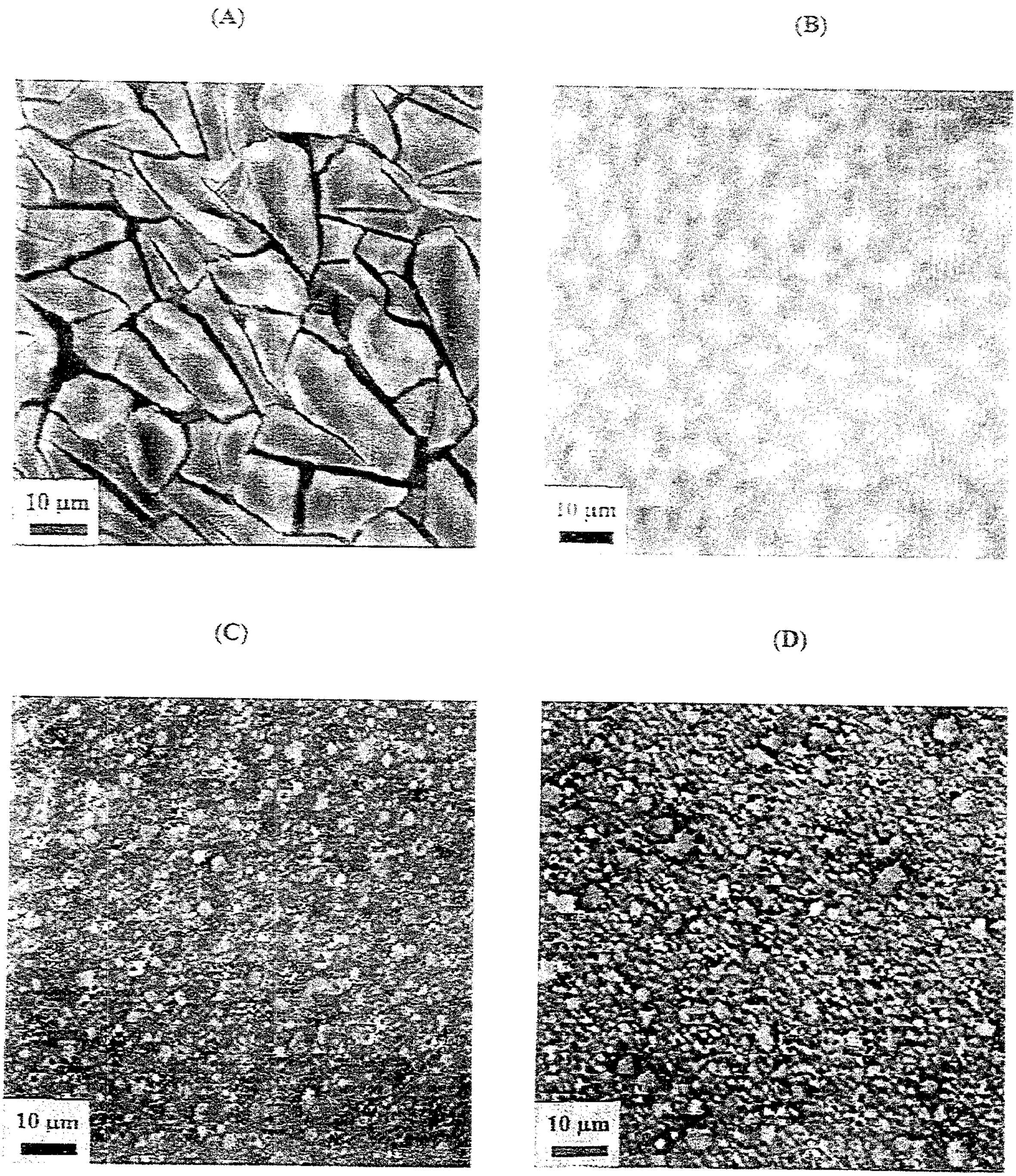

Fig. 3 Typical surface morphologies of Tb-YSZ and Ti-YSZ thin films deposited on YSZ at different temperatures for 1 h: (a) 633 K; (b) 673 K; (c) 693 K; (d) 723 K. An 80 vol% butyl carbitol + 20 vol% ethanol mixture as solvent for a 0.09 M precursor solution was used.

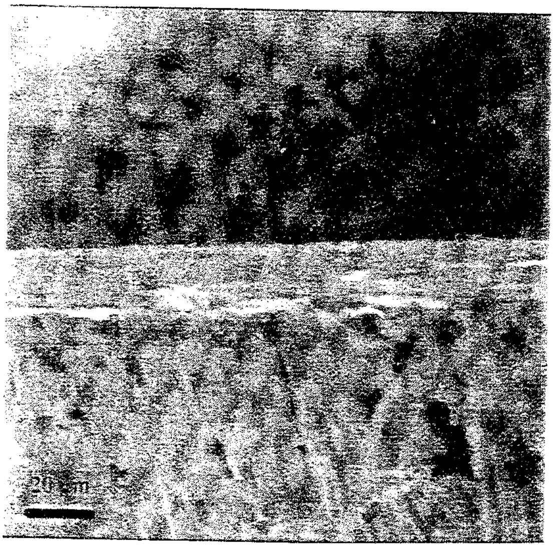

Fig. 4 Cross section of a non-annealed dense Tb-YSZ layer deposited at 360 °C for 2 h on stainless steel using an 80 vol% butyl carbitol + 20 vol% ethanol mixture as solvent for a 0.09 M precursor solution.

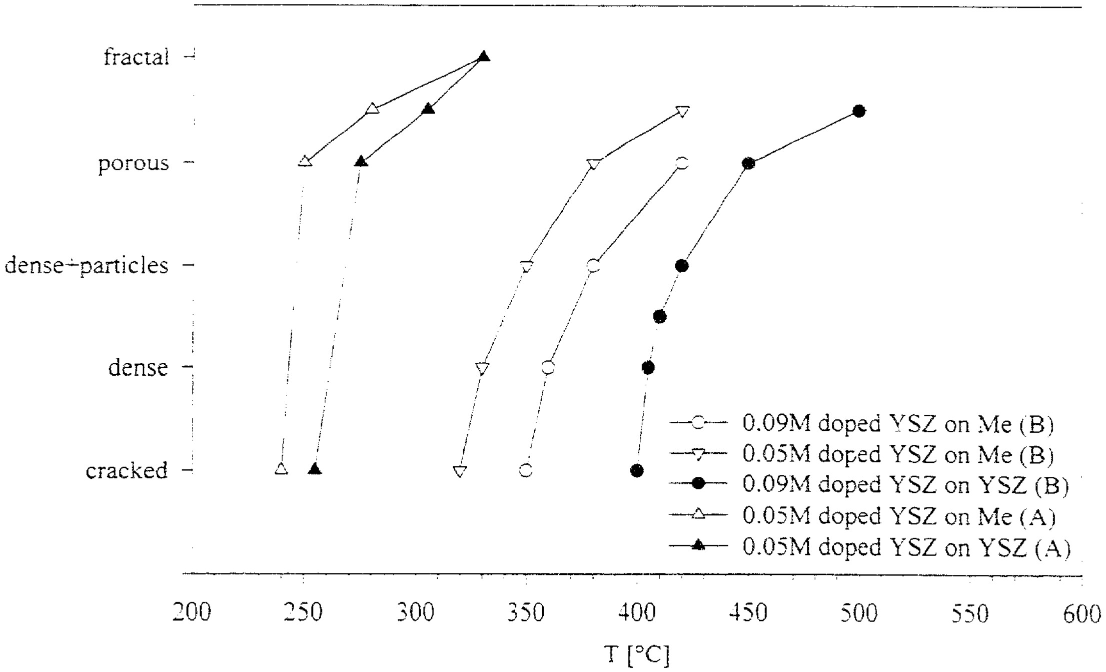

Fig. 5 Surface morphologies of doped YSZ layers deposited on stainless steel and YSZ using precursor solutions with different solvent compositions: (A) 50 vol% butyl carbitol + 50 vol% ethanol solution; (B) 80 vol% butyl carbitol + 20 vol% ethanol solution.

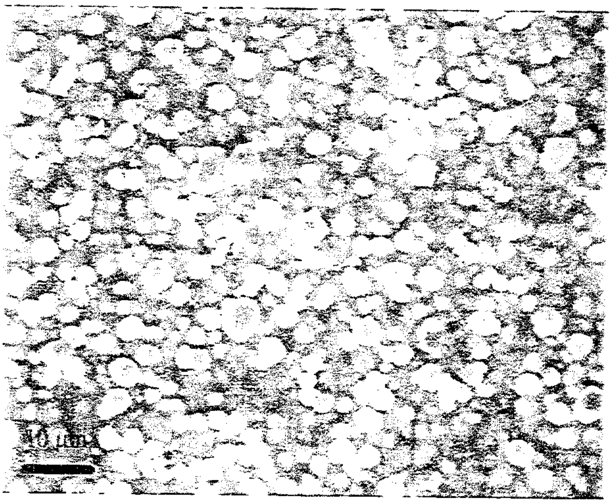

Fig. 6 Porous NiO-YSZ deposited at 380 °C for 2 h on YSZ using an 80 vol% butyl carbitol – 20 vol% ethanol mixture as solvent for a 0.05 M precursor solution.

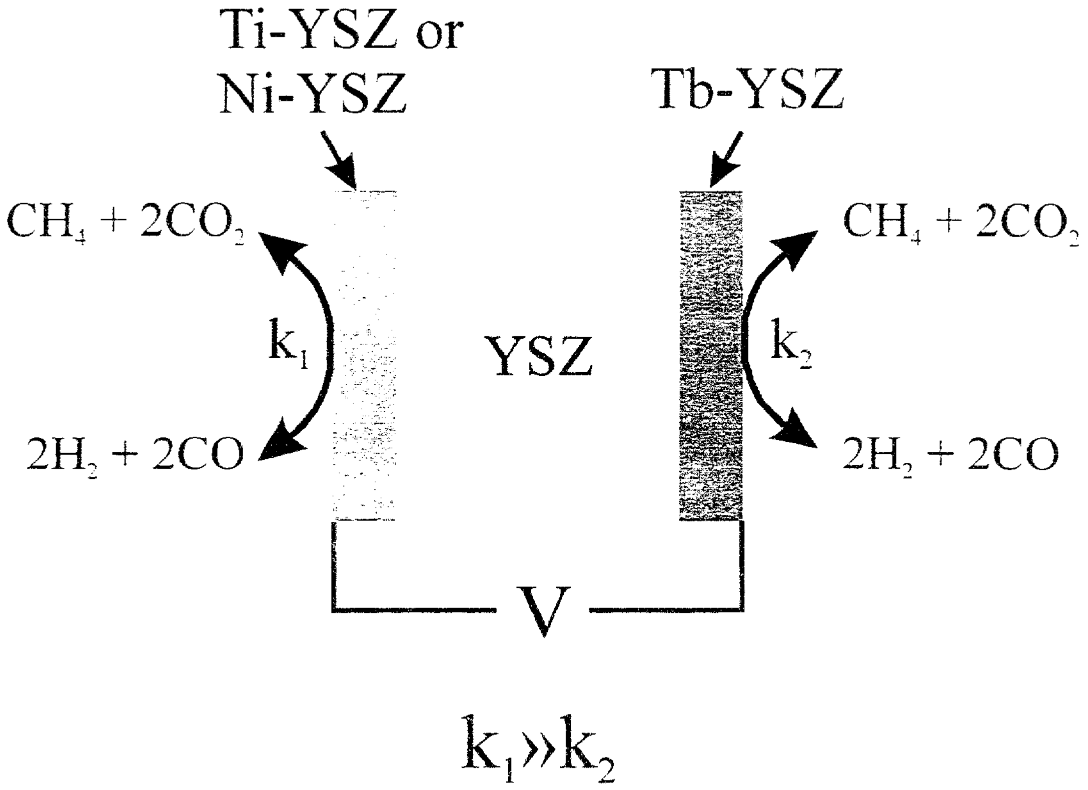

Fig. 7 Proposed monolithic SOFC design for its use in a mixed gas atmosphere.

MICROSTRUCTURED THIN FILM ELECTROLYTES

Raphaël Ihringer, JanVan herle and Augustin J. McEvoy

Laboratory of Photonics and Interfaces, Dpt. of Chemistry
Federal Institute of Technology (EPFL), 1015 - Lausanne, Switzerland

Apart from lowering the operating temperature, the thin film concept brings other benefits. One of those is the very low potential drop observed on the anode. Therefore the manufacture of thin film electrolytes co-fired on anode substrates, for example by calendering, screen printing or dipping processes (1,2,3), begins to be widely developed.

A technique was developed in our lab to co-cast and co-fired thin electrolyte on anode substrates.

To increase the effective surface of a thin electrolyte by a factor of two compared to the projected area, we added a step in the manufacturing process. This technique, used to make for instance microstructured ceramics (4,5), consists of embossing the green ceramic tape to obtain a three-dimensional shaped surface.

Our ceramics are manufactured through water based slurries. Polyelectrolyte is used as dispersant and PVA/glycerol as binder. Wetting, defoamer and viscosity modifier agents are also added to the pastes. Water based slurries have the advantage to be practically nontoxic, which implies, ease of handling and disposal, without hazardous vapor emissions.

YSZ films of 0.7 to 10 µm (figure 3 a) and b)) are cast with a blade we shaped especially for this application. On them, NiO-8YSZ green anode substrates are deposited, with a conventional doctor-blade technique. After the sintering step (1350 °C/4h), pieces of diameter 31 mm, thickness of 0.15-0.20 mm and relative density of 96-98 % are finally obtained.

Structured samples are obtained by embossing the green tapes with a mold of selected geometry. The negative form will then be reproduced (proportionally to the shrinkage factor) on the sintered ceramic as it is shown in figure 4 a) and b). Here a thin and dense shaped electrolyte about 5 µm thick covers the anode.
The use of water soluble and hygroscopic polymers such as PVA has the advantage, that the plasticity of the tapes can be adjusted simply by changing the relative humidity of the environment.

Table 1 shows the electrochemical results we obtained with a 7 µm thin electrolyte layer. The cathode is a mixture of 50/50 wt. commercial 8YSZ and $La_{0.85}Sr_{0.15}Mn_{1.1}O_3$ powders, which were sintered at 1200 °C for 2 hours. Its thickness is about 40 µm (6).

The cell power is clearly limited by the cathode potential drop. Contrarily, the anode presents a very low potential drop even at reduced temperature (see table 1) compared to conventional anodes sintered on thick electrolytes, which exhibit an overpotential above 150 mV at 1 A/cm^2 at 750 °C (7). This could be explained by the fact that the surface reaction is increased thanks to the percolation of the YSZ phase in the co-fired anode.

A degradation of the current density is always observed after a 48-100 hours testing period, which is caused by an additional ohmic resistance of 40 to 300 mΩcm^2 on the anodic side. This loss was identified to come from the anode current collectors. We noticed that each time a cell was reinstalled in our set-up, the degradation had disappeared initially, to reappear later during the test. We found then firstly that the pressure on the cell decreased drastically because of creep in our testing set-up, and secondly the nickel particulates of the collecting paste sintered during the test and did not collect the current as efficiently.

Only a preliminary electrochemical test has been made on a structured sample. The cathode was the same as for the cell presented above. The measured OCV of 1.0 (V) implies that the electrolyte tape is sufficiently plastic to deform as shown without tearing or punch-through.

ACKNOWLEDGMENTS

This work was supported by the Swiss Priority Programme for Materials. Thanks are also due to collaborators involved in our parallel programme supported by the Swiss Federal Energy Office.

One of the authors (R.I.) would also like to thank the Laboratory of Mechanical Metallurgy of EPFL for experimental support.

REFERENCES

1. N.Q. Minh, P. Kelly and K. Montgomery, Proceedings 2nd European SOFC Forum, B.Thorstensen ed., Oslo (N), May 1996, p.660.
2. M. Cassidy, K. Kendall and G. Lindsay, Proceedings 2nd European SOFC Forum, B.Thorstensen ed., Oslo (N), May 1996, p.669.
3. S. de Souza, S.J. Visco and L.C. de Jonghe, Proceedings 2nd European SOFC Forum, B.Thorstensen ed., Oslo (N), May 1996, p.679.
4. R. Knitter, E. Günther, C. Odemer, 3rd EURO-CERAMICS V.1 (1993), pp.555-560.
5. H.-J. Ritzhaupt-Kleissl, W. Bauer, E. Günther, J. Laubersheimer, J.Hausselt, Microsystem Technologies 2 (1996) 130-134.
6. M. Mogensen, S. Primdahl, J.T. Rheinländer, Proc. 7th SOFC Workshop, Wadahl, Norway (1995), p. 53
7. J. Van herle, R. Ihringer, A.J. McEvoy, to be published, SOFC V, Jülich Germany, June 1997.

T (°C)	ΔUr-a (mV) at 1 A/cm^2	ΔUr-c (mV) at 1 A/cm^2	Power Density (W/cm^2)
700	40	740	0.3 (at 0.45 V)
760	20	430	0.58 (at 0.42 V)
800	30	360	0.7 (at 0.5 V)

Table 1: Potential drop of the electrodes and Power densities achieved at different temperatures for a (H_2/ H_2O), Ni-YSZ/YSZ/LSM-YSZ, air cell

Figure 3 a) and b): SEM micrograph of dense 0.7 µm and 1.5 µm films co-fired at 1350 °C/4 h. on NiO-8YSZ substrate. The sample has been reduced in N2H2.

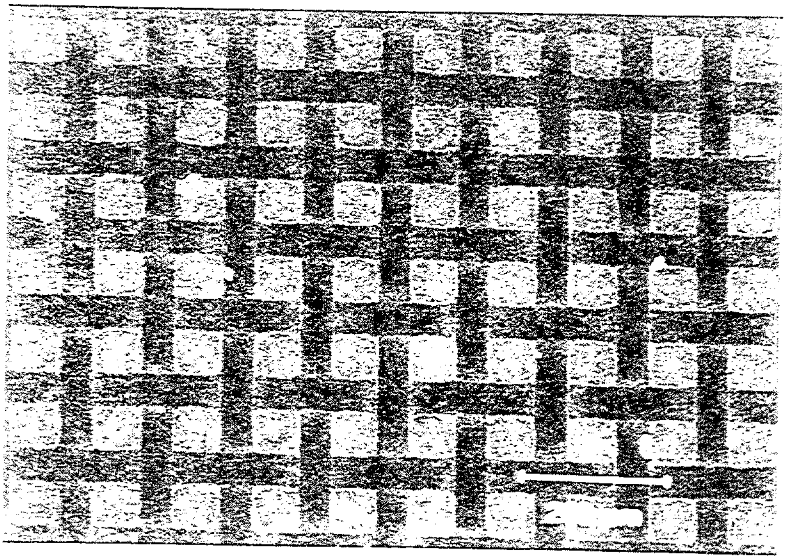

Figure 4 a): Optical micrograph (100 X) of a shaped sample. Top view.

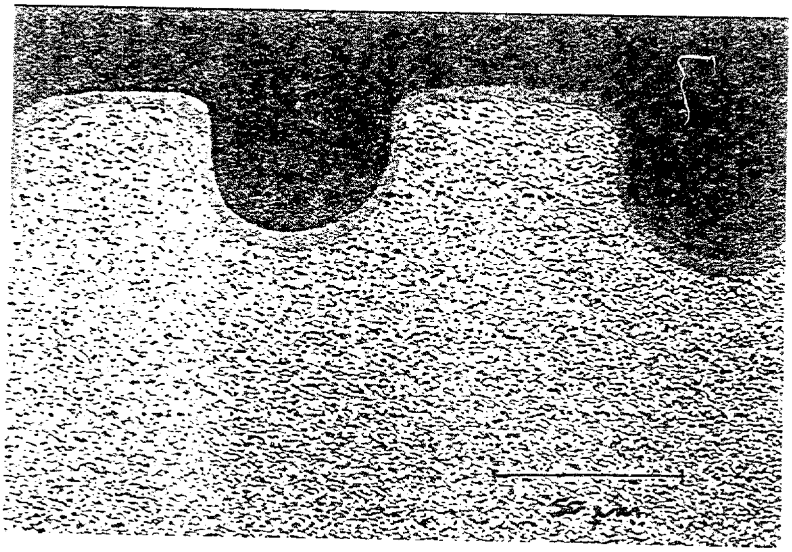

Figure 4 b): Optical micrograph (500 X) of a shaped sample.
Reduced and polished cross section. The Nickel particulates appear in white.

Novel fabrication of La(Sr)MnO_3/YSZ/NiO-YSZ PEN cells

Kwang-Leong Choy and Wei Bai
Department of Materials, Imperial College
London SW7 2BP, UK

Exploitation of high temperature solid oxide fuel cell (SOFC) systems for efficient power generation has still failed to reach commercial viability due to two crucial technical problems. These are (i) the relatively high fabrication costs of conventional tubular and planar SOFCs, and (ii) the long term degradation of SrO and CaO doped $LaCrO_3$ ceramic interconnects operated at temperatures greater than 900°C.

Recently, Imperial College has developed a novel processing method called *aerosol assisted chemical vapour deposition in an electric field* (ACVDe) [1] . This method offers a simple and cost effective method to manufacture planar supported thick film electrolyte(STFE) and multilayer PEN (P=positive electrode or cathode, E=electrolyte, N=negative electrode or anode) cells, in order to overcome the above technical problems. The ACVDe process involves spraying atomised precursor droplets across a heated environment where the droplets undergo combustion and chemical reaction in the vapour phase near the vicinity of the substrate. This leads to the formation of a stable solid film with excellent adhesion onto a substrate in a single production process. Dense electrolytes and porous electrode films have been deposited by varying the ACVDe processing parameters in order to control microstructure, porosity, grain size and composition. Individual thick films were characterised using a combination of XRD, SEM, and AC techniques for structural examination and electrical measurements.

The results from this study has clearly demonstrated for the first time both technical and economical viability of the ACVDe technique to produce SOFC components as well as PEN cell structure. Dense $Zr(Y)O_{2-x}$ electrolytes (Figure.1), porous Ni-YSZ anode, porous $La(Sr)MnO_3$ cathode structure (Figure.2) and multilayer $La(Sr)MnO_3$ /$Zr(Y)O_{2-x}$ /Ni-YSZ PEN structure (Figure.3) with well controlled microstructure and composition have been successfully deposited cost-effectively on ferrite steel bi-polar plate material and porous ceramic substrates in a single production process. Such fabrication can not be achieved by the existing vapour deposition techniques, including conventional CVD and PVD, except the very expensive technique like EVD. AC results showed that the ACVDe of YSZ films were dense and exhibit good electrical properties (bulk conductivity $0.8\text{x}10^{-3}Scm^{-1}$ at 500°C)[2] which are comparable to those fabricated using more costly methods, such as EVD, CVD and PVD.

In addition, the ACVDe method has a lower processing temperatures (e.g. 300-550°C) than conventional fabrication methods (e.g. CVD, PVD, EVD and tape casting). It can also deposit SOFC components onto metallic substrates. Thus, it enables a greater use of metallic components within the SOFC stacks which greatly reduces the operating temperature from 1000°C to 750-800°C. Other key advantages of the novel process over existing coating techniques include low consumption of precursor (e.g. as low as 5 ml to produce 3 μm thick film/cm^2) and minimal loss of the precursor to the surrounding. Multicomponent oxides, and doped oxides can be manufactured with well controlled crystal structure and stoichiometry. In addition, the deposition equipment used in this process is simple, flexible and economical. This novel deposition method has the potential to be scaled up for large-area and large-scale production. The study has demonstrated the promise of the cost-effective ACVDe technology in revolutionising the processing technology

Acknowledgment

We would like to thank Prof. B.C.H.Steele for his helpful advice, and Mr. R.Rudkin for his technical assistance. The financial supports provided by the Engineering, Physical and Science Research Council, UK (GR/K/86954) and Royal Society are gratefully acknowledged.

References:

[1] Choy, K. L. and Bai, Wei, " A method of depositing ceramic films and coatings", British Patent application filed No. 9525505.5., 1995

[2] K.L.Choy, W.Bai, and B.C.H.Steele, New deposition process for dense YSZ films onto porous electrodes, submitted to 5th Inter. Symp. SOFC, June 2-5, Germany, 1997

[3] K.L.Choy and W.Bai, Novel deposition process for ceramic film and coating, submitted to the Journal of European Ceramic Society, 1997

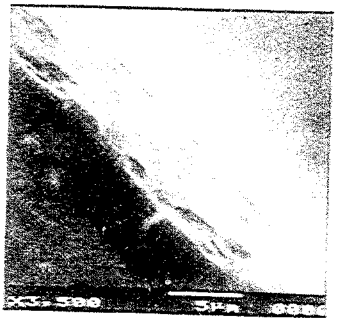

Figure 1

SEM of dense Y_2O_3-ZrO_2 film on stainless steel substrate

Figure 2

SEM of porous La(Sr)MnO_3 on Y_2O_3-ZrO_2 substrate

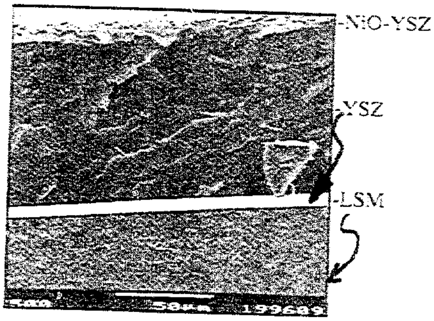

Figure 3

SEM of multilayer La(Sr)MnO_3/YSZ/NiO-YSZ PEN cell

RECENT IMPROVEMENT OF SOFC TECHNOLOGY IN MURATA

Hiroshi Takagi
R&D Division, Murata Manufacturing Co., Ltd.
2288 Ohshinohara, Yasu,
Shiga 520-23, Japan

ABSTRACT

We have developed a fabrication process for planar SOFC. We are conducting two R&D activities on planar SOFC, NEDO project and a joint program with Osaka Gas Co., Ltd. In this paper, the recent status of these activities is presented, especially, the long-term reliability and thermal cyclic characteristics are discussed.

INTRODUCTION

In order to commercialize the SOFC in market, a thermal cyclic characteristics and a long-term reliability are important. We must choose a proper stack design to realize the good thermal cyclic characteristics. To estimate the long-term reliability, we have to evaluate it under the practical condition of current density and fuel utilization. In order to decide the value of current density, we should consider the balance of the efficiency and the production cost of SOFC stack. For the fuel utilization, we must settle the proper value considering a system design such as an anodic cycling, a turbine used and so on. From these aspects, we use 300mA/cm^2 and 70% for the practical values of current density and fuel utilization.

We have developed a fabrication process for planar SOFC through two R&D activities. Through the project supported by NEDO, we intend to apply a cofiring technique to a fabrication process of SOFC[1-7]. There, we have been developing the electrolyte/electrode cofired multilayer and improving its long-term reliability. By a joint program with Osaka Gas, we have been developing a Osaka Gas (OG) type planar SOFC which has a new structure good for thermal cyclic characteristics[8-14]. In this paper, I would like to present our current status of two R&D activities on SOFC.

NEDO PROJECT

Large-scale electrolyte/electrode cofired multilayer

The planar SOFC, fabricated by a cofiring process can be expected to achieve high power densities and low production costs. On the other hand, the cofiring technique requires that the sintering temperature, the shrinkage profiles and the thermal expansion characteristics of component materials should be compatible with each other.

These technical hurdles have been tackled by manipulating the material composition, powder characteristics and firing condition such as firing profile or atmosphere.

Fabrication of electrolyte/electrode multilayer involves forming, cutting, laminating and cofiring of the thin green films. YSZ is used for the electrolyte, Ni-YSZ cermet for the anode and $(La,Sr)MnO_3$ for the cathode. The tape casting technique was used for forming the thin green films. These green ceramic films were cut into desired size and laminated as green bodies to form 3-layered membranes. The green membranes were then cofired below 1400°C and sintered into the rigid multilayers of 144, 225 and 400 cm^2. Figure 1 shows the cofired multilayers with various surface areas. The single cell testings were performed using the cofired multilayer and Ni-Cr alloy interconnects at 1000°C. Small sized cells (30mmϕ, active area:3cm^2) were cut from 144 and 400 cm^2 multilayers and tested also at 1000°C.

I-V characteristics of 400cm^2 (active area:353cm^2) single cell is shown in Fig. 2. Maximum power of about 80 W was achieved. Characteristics of the 400 cm^2 single cell are compared with the cells with smaller surface area in Table 1. The power density slightly decreased with increasing the surface area. On the other hand, the performance of small sized cell cut from the largist multilayer (400cm^2), shown in Fig. 3, was not lower than that from the smallist multilayer (144cm^2). Typical performance of small sized cells cut from the edge and center portion of 400 cm^2 multilayer are compared in Fig. 4. These two curves are almost same, therefore deviation of characteristics in the same cell plane is scarcely. From these results, we can conclude that tere is not any essential difference of microstructure among the single cells with various surface areas, and the inferiority of single cell performance of larger multilayers was due to the inferiority of gas sealing or current collection which was emphasized with increase in the surface area. Problems of gas sealing and current collection still remain in fabrication of SOFC stacks.

The fuel utilization dependence of terminal voltage at 300mA/cm^2 is shown in Fig. 5. The cofired multilayer of 144cm^2 was used for the measurement. The fuel utilization (U_f) was varied from 20% to 70%. And the calculated values were those which were subtracted the nernst loss at correspondent utilization from the terminal voltage of U_f=20%. From this figure, we can see a slight increase of the concentration overvoltage at higher utilization, however, the effect is not serious even at U_f=70%.

Long-term reliability of cofired multilayer

Conductivity of 3, 8 and 10mol% Y_2O_3 stabilized ZrO_2 (3, 8 and 10YSZ) was measured by DC and AC 4-probe methods in air and fuel atmosphere. Current density of 300 mA/cm^2 was applied during the measurement. The size of sample was 3x1.5x30mm. Conductivity of 3YSZ was also measured under the generation condition by current interruption method. Small sized cell was used in the measurement.

The time dependence of ionic conductivity of 10, 8 and 3YSZ in air is shown in Fig. 6. While ionic conductivity of 10YSZ did not change even after 1000h, those of 8 and 3YSZ decreased with time. However, the rate of decrease gradually reduced with increasing time, and the conductivity have a tendency to be saturated to the constant value after 2000-3000h. The conductivity of 3YSZ was smaller than that of 8YSZ, but the rate of decrease was also smaller than that of 8YSZ. Ionic conductivity of 8 and 3YSZ measured in fuel atmosphere are shown in Fig. 7 and 8. For comparison, the values measured in air are shown in these figures. The decreasing rate of conductivity in fuel atmosphere was smaller than that in air. This means the decrease of ionic conductivity depends on the atmosphere. Ionic conductivity of 3YSZ under the generation condition is also shown in Fig. 8. It was measured with a small sized cell prepared by a cofiring technique, and the conductivity was calculated from IR-drop (ohmic part) of current interruption. The time dependence of the conductivity, shown in Fig. 8, was similar to that in fuel atmosphere. It suggests that the oxygen potential in YSZ under the operation condition deviates to the reducing (fuel) state. Conductivity of YSZ was separated to those in grain and at grain boundary portions by AC impedance measurement. The time dependence of resistivities, shown in Fig. 9, reveals the decrease of ionic conductivity is due to the increase of resistivity in the grain, not at the grain boundary. From these results, we can conclude that the ionic conductivity change of YSZ is thought to correspond to the lattice change of YSZ, and it is the relaxation phenomenon such as phase transition.

The anodic and the cathodic overvoltages of cofired multilayer was evaluated using the small sized cell with the current interruption methode. In general, it is important to supress an increase of anodic overvoltage with time. For this purpose, we use highly dispersed Ni-YSZ cermet for anode where the aggregation of Ni particles and the separation of them from YSZ are inhibited under the operation condition. The anode was also improved to maintain the path of oxygen ion in itself for a long-term duration in fuel. The time dependence of overvoltages is shown in Fig. 10. Both of overvoltages decrease with increasing in time, and will be saturated to the constant values. The overvoltage after 40,000h operation was calculated by extrapolation of the time dependence of electrode overvoltages and electrolyte conductivity. Here, we assumed 3YSZ was used for clectrolyte. The estimated value is shown in Table 2. As a result, a decrease of terminal voltage of cofired single cell is supposed less than 10% after 40,000h operation.

JOINT PROGRAM WITH OSAKA GAS

Stack design

Osaka Gas has been conducting to develop a new design of planar SOFC which has a structure suitable for stacking and good thermal cyclic characteristics. The schematic design is shown in Fig. 11. Each single cell is made by bonding two cell components, an anode/electrolyte/cathode multilayer and a separator ditched air channels on one side. It is made separately from other cells so that it can be easily to control the quality of each cell. These single cells are sandwiched between nickel felts, which form fuel channels, and piled up. The nickel felts can release the thermal stress between cells. Each single cell is suspended by ceramic cell holder which form gas manifolds, so that each cell is saved from loading of the upper cells. As described above, the Osaka Gas (OG) type planar SOFC is characterized by easily stacking, good quality control capability and good thermal cyclic characteristics. This new structure was designed by Osaka Gas Co., and the technology of fabrication and staking has been developing through the joint probram with Murata.

Fabrication and quality control

We concentrated our efforts on developing the fabricating method of the cell and the stack without any crack and gas leakage. The crack-free cells could be obtained by minimizing the mismatch of thermal expansion coefficient between electrolyte/electrode multilayer and separetor. The size of multilayer and separetor was 12x12cm (active area : 120cm^2). The existence of cracks on multilayers and delamination between multilayer and separetor were examined before stacking of cells using acoustic micrography technique and thermography technique. After checking the cracks and the delamination of single cells, 5-cell stack (a unit) was fabricated. The sealing property of units was checked by a gas leakage test. The stacks having various scales were composed by combining the units examined their gas tightness. The OG type structure can examine the quality of individual cells and units like tubular type cells, so that this structure is suitable for quality control.

Performance

The power density of single cell, a unit (5-cell stack) and 2-unit stack (10-cell stack) are shown in Table 3. The current density was 300mA/cm^2 and the fuel utilization was 40%. The power density of these are almost equal, so that the stacking can be carried out without any performance loss. This result indicate that OG type structure is suitable for stacking.

Figure 12 shows I-V characteristics after performing 5 thermal cycles between operation and room temperature. Degradation of the stack performance can be scarcely observed. From this result, the good thermal cyclic characteristics of OG type structure is confirmed. 4-unit stack (20-cell stack) is shown in Fig. 13. Figure 14 shows the I-V/P characteristics of this stack. The fuel utilization was 70%. The power density was After 300h operation, 10 thermal cycles were performed. After 10 thermal cycles, the average reduction of OCV was about 0.1%/cycle.

SUMMARY

1. The anode/electrolyte/cathode multilayers with surface area of 144, 225 and 400cm^2 were fabricated using cofiring technique. There were not any essential inferiority of performance with increasing surface area of cofired multilayer. The

effect of concentration overvoltage in cofired anode at higher fuel utilization such as 70% was scarcely observed. The long-term reliability of cofired multilayer was estimated by extrapolation of overvoltages measured after 1000-3000h operation. The calculated degradation rate of terminal voltage was less than 10% after 40,000h operation.

2. The OG type planar SOFC stacks, which has a new design suitable for thermal cyclic characteristics, stacking and quality control, were evaluated. The stacking could be carried out without any performance loss comparing with the performance of single cell. The degradation of a unit (5-cell stack) after 5 thermal cycles and 4-unit stack (20-cell stack) after 10 thermal cycles was scarcely observed.

ACKNOWLEDGEMENT

A part of this work was performed as a R&D program of New Energy and Industrial Technology Development Organization (NEDO) under the New Sunshine Project of Agency of Industrial Science and Technology, MITI. I would like to express our thanks to NEDO and MITI for their assistance.

Another part of this work was performed as the joint program for SOFC development with Osaka Gas Co., Ltd. Some data were shown in this paper by courtesy of Osaka Gas Co.

I also gratefully acknowledge the help of our many colleagues, especially, K. Akagi of Osaka Gas.

REFERENCES

(1) H. Takagi, S. Kobayashi, A. Shiratori, K. Nishida and Y. Sakabe, Proceedings of The 2nd International Symposium on SOFC, Athens, pp.99-103 (1991).

(2) A. Shiratori, S. Kobayashi, H. Taira, Y. Sugimoto, S. Sakamoto, H. Takagi, and Y. Sakabe, Proceedings of The International Fuel Cell Conference, Makuhari, pp.297- 300 (1992).

(3) H. Takagi, H. Taira, A. Shiratori, S. Kobayashi, Y. Sugimoto, S. Sakamoto and K. Tomono, Proceedings of The 3rd International Symposium on SOFC, Honolulu, pp.738-743 (1993).

(4) H. Takagi, H. Taira, S. Kobayashi, S. Sakamoto and K. Tomono, Proceedings of The 1994 Fuel Cell Seminar, San Diego, pp.392-395 (1994).

(5) H. Takagi, H. Taira, S. Kobayashi, S. Sakamoto and K. Tomono, Proceedings of The 4th International Symposium on SOFC, Yokohama, pp.120-128 (1995).

(6) H. Taira, S. Sakamoto, H. B. Zhou, H. Nakai and H. Takagi, Proceedings of The 2nd International Fuel Cell Conference, Kobe, pp.235-238 (1996).

(7) H. Taira, S. Sakamoto, H. B. Zhou, H. Nakai, S. Towata, H. Takagi and Y. Sakabe, Proceedings of The 1996 Fuel Cell Seminar, Orlando, pp.167-170 (1996).

(8) K.Akagi, Proceedings of the 34th Battery Symposium in Japan, Hiroshima,pp.167-168(1993).

(9) K.Akagi, Extended Abstracts of the 2nd Symposium on SOFC in Japan, Tokyo, pp.33-36(1993).

(10)K.Akagi, A. Shiratori, M. Iha, and O. Chikagawa, Proceedings of The 1st FCDIC Fuel Cell Symposium, Tokyo, pp.300-303(1994).

(11)A.Shiratori, M. Iha, O. Chikagawa, and K. Akagi, Proceedings of The 1994 Fuel Cell Seminar in SanDiego CA, pp.37-40(1994).

(12)K.Akagi A. Shiratori, M. Iha, O. Chikagawa, and H. Takagi, Proceedings of the 4th International Symposium on SOFC, pp.255-263(1995).

(13)K.Akagi A. Shiratori, M. Iha, O. Chikagawa, and H. Takagi, Proceedings of the 2nd International Fuel Cell Conference, Kobe, pp.239-242(1996).

(14)M. Iha, A. Shiratori, O. Chikagawa, H. Takagi, Y. Sakabe and K. Akagi, Proceedings of The 1996 Fuel Cell Seminar, Orlando, pp. 163-166 (1996).

Table 1 Single cell performance of cofired multilayer

Cell size/cm	12x12	15x15	20x20
Cell area/ cm^2	144	225	400
Active area /cm^2	121	195	353
O.C.V. / V	1.035	1.019	1.021
Maximum power / W	30.2	44.0	77.7
Power density /Wcm^{-2}	0.25	0.23	0.22

Table 2 The evaluation of decrease of terminal voltage at $300mA/cm^2$ after 40,000h operation

Fuel	$H_2/H_2O(30°C)$, U_f=70%		H_2/CO_2=4:1, U_f=70%	
O.C.V./ mV ¹⁾	1049		948	
State	Initial	after 40000h	Initial	after 40000h
Electrolyte overvoltage/mV	108	150	108	150
Anodic overvoltage / mV	205	188-198	132	120-130
Cathodic overvoltage / mV	45	25-35	45	25-35
Other overvoltages / mV ²⁾	50	50	50	50
Terminal voltage / mV	646	636-616	613	603-583
Degradation rate / %	-	1.5-4.6	-	1.6-4.9

Operating temperature : 1000°C, Oxidant : Air, U_O=15%, Current density : $300mA/cm^2$, Electrolyte : 3YSZ

1) calculated value by Nernst equation

2) current collection resistivity ei al., empirical value

Table 3 The power density at $300mA/cm^2$ of single cell, a unit and 2-unit stack

	Single cell	Single unit	2-unit stack
Number of cells	1 cell	5 cells	10 cells
Power density / Wcm^{-2}	0.21	0.22	0.21

Fuel : $H_2/H_2O(30°C)$, U_f=40%

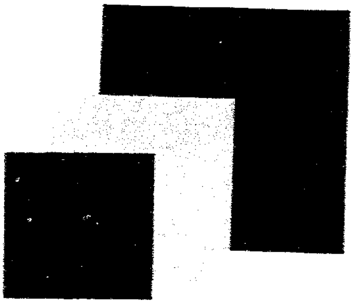

Figure 1 Cofired anode/electrolyte/cathode multilayer

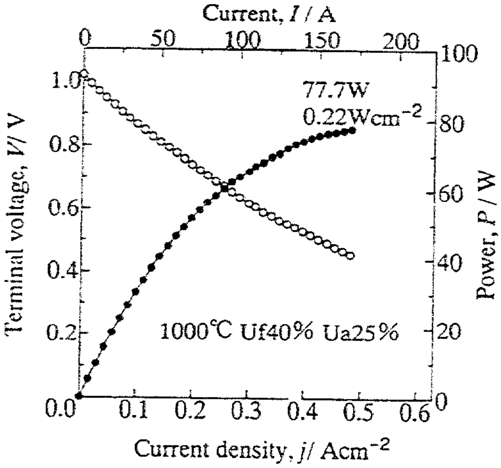

Figure 2 I-V characteristics of single cell with surface area of 400cm^2 (active area : 353cm^2)

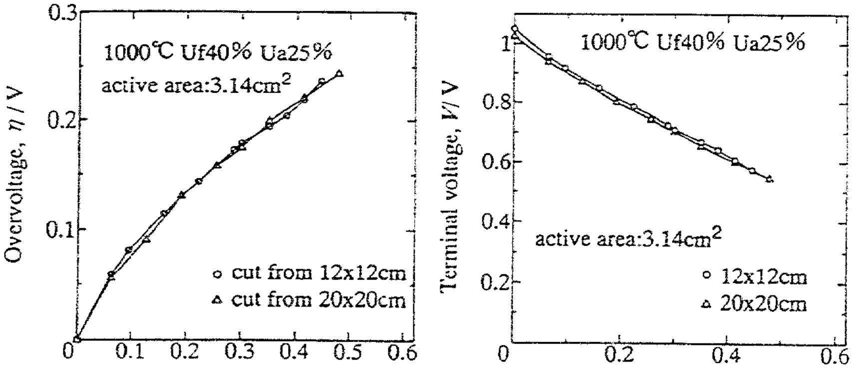

Figure 3 Typycal performance of small sized cell (30mmφ, active area:3cm^2) cut from cofired multilayers with surface area of 144 and 400 cm^2

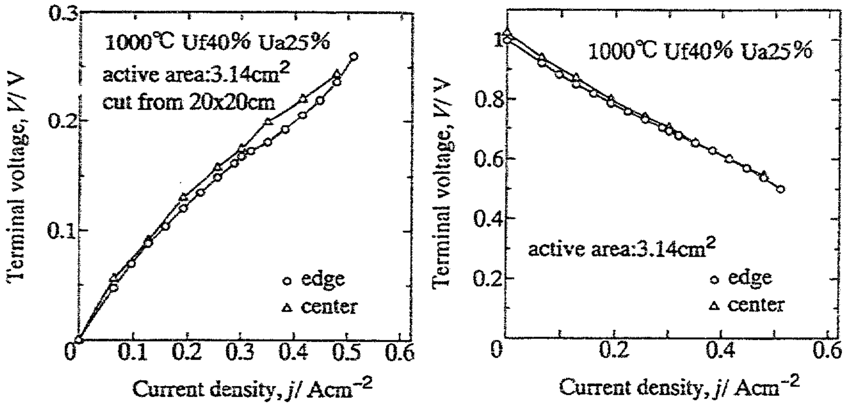

Figure 4 Typycal performance of small sized cell (30mmϕ, active area:3cm^2) cut from the edge and center portion of cofired multilayer with surface area of 400 cm^2

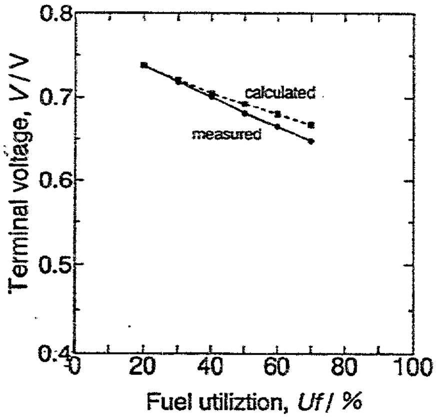

Figure 5 Fuel utilization dependence of terminal voltage at 300mA/cm^2 of cofired multilayer with surface area of 144cm^2

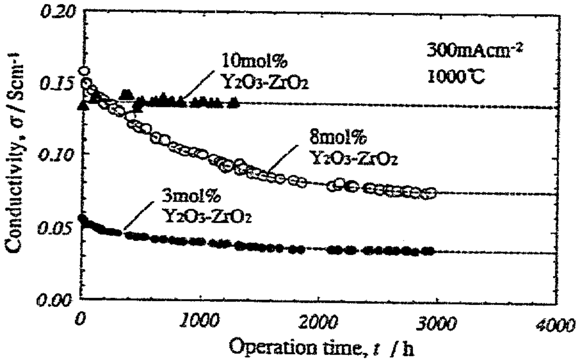

Figure 6 Time dependence of ionic conductivity measured in air of 10, 8 and 3YSZ

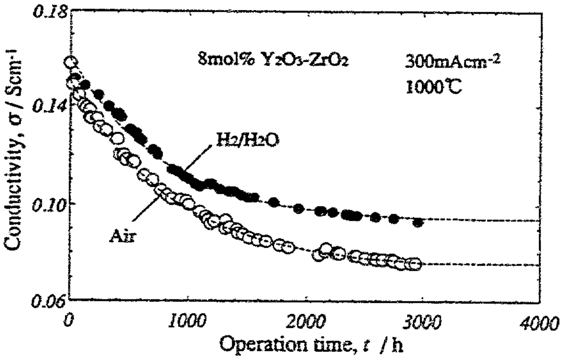

Figure 7 Time dependence of ionic conductivity measured in air and fuel atmosphere (H_2/H_2O(30°C)) of 8YSZ

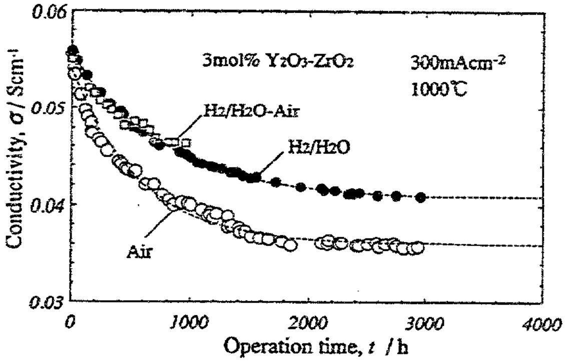

Figure 8 Time dependence of ionic conductivity measured in air, fuel atmosphere (H_2/H_2O(30°C)) and under the operation condition (air-H_2/H_2O(30°C), U_f=70%) of 3YSZ

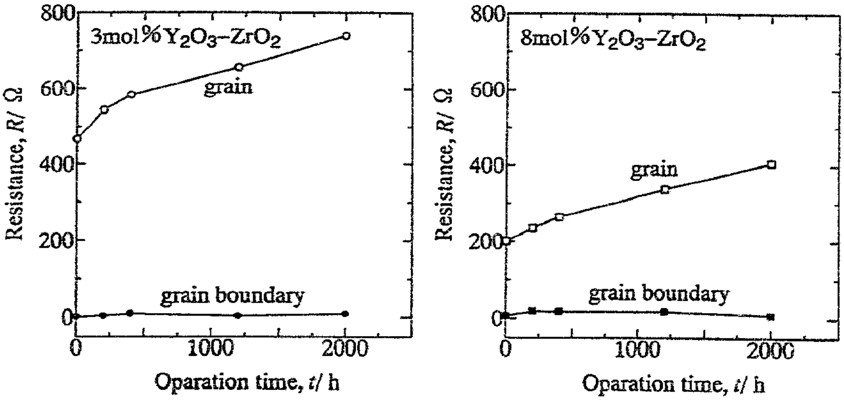

Figure 9 Time dependence of ionic conductivity in grain and at grain boundary of 3 and 8YSZ measured in air at 1000°C

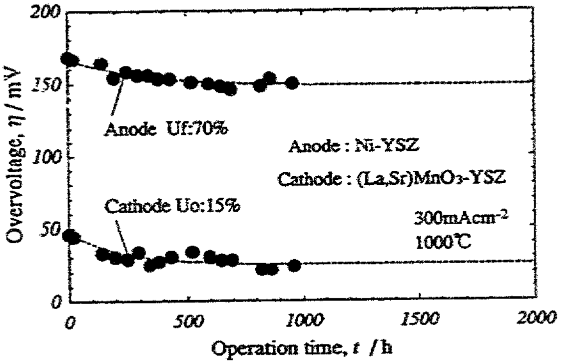

Figure 10 Time dependence of anodic and cathodic overvoltages at 1000°C with current density of 300mA/cm^2

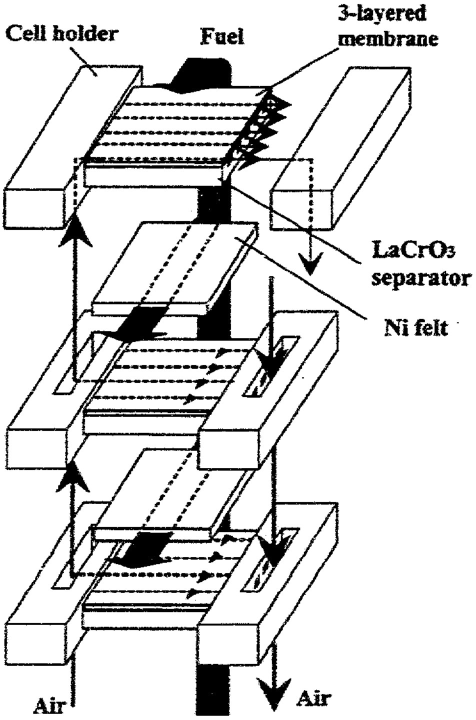

Figure 11 The schematic design of OG type planar SOFC

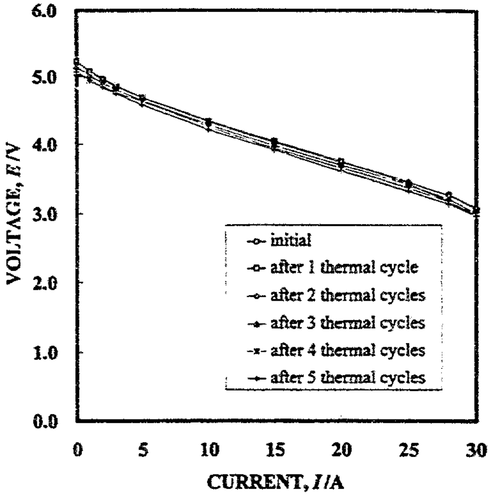

Figure 12 I-V characteristics of a unit (5-cell stack) after 5 thermal cycles from 1000°C to room temperature

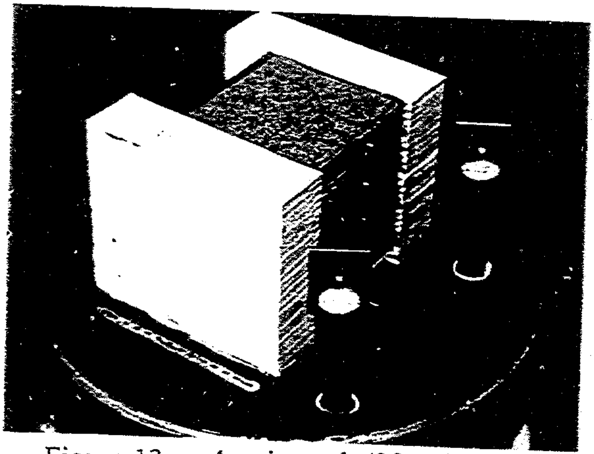

Figure 13 4-unit stack (20-cell stack)

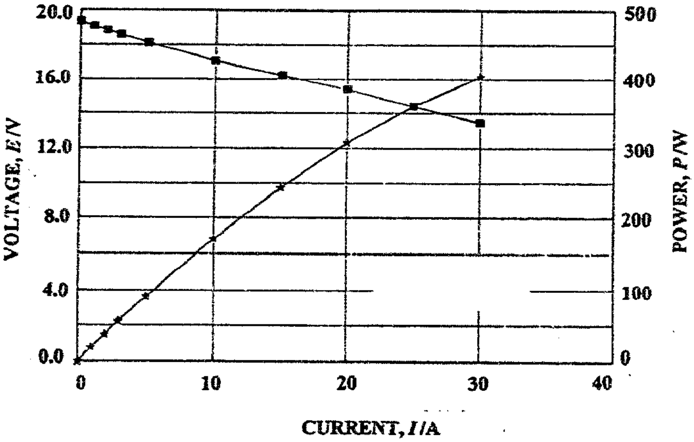

Figure 14 I-V/P characteristics of 4-unit stack (U_f=70%)

Final Workshop - Jan. 31st.

Chairman Hugh Middleton.

Topics treated were reference electrodes, novel fabrication methods, and SOFC modules. McEvoy asserted that the reference electrode responds to local oxygen activity, the local equilibrium between gaseous oxygen and the YSZ lattice. While Nisancioglu stated that there is also an electrostatic component, Jacobsen said the reference electrode is at equilibrium with its environment. Van Heuveln questioned the methods to measure overpotentials at a single electrode. With a fuel cell it is impossible to characterise anode and cathode separately. There are possibly alternative geometries, or the use of reversible counter-electrodes. There is a problem with Pt counterelectrodes, which sinter with loss of three-phase boundary. Also if the temperature is low there are problems because Pt requires high activation. Skou mentioned symmetrical cells as in battery research. A proposed test was a 4-point contact on a YSZ bar. Conventionally the test current is applied between the outer electrodes and the potential measured between the inner ones. If this arrangement is reversed and the potential measured between the outer electrodes, the polarisation drop, being confined in the intimate junction region, would not be measured across the bulk of the bar. McEvoy engaged to have this test carried out. According to Yokokawa any space-charge region has a thickness less than one grain size of the electrolyte. Middleton confirmed that rearrangement of the zirconia morphology shows that the activity of the interface is very close to the geometrical contact plane, and that local field strengths are very high. At that point came a query on the definition of terms - electrical or electrochemical potential. Bossel drew a distinction between fuel cell and oxygen pump modes, but Jacobsen stated that the potential lines are the same in each case. In the vigorous discussion that followed, the chairman suggested that the reference electrode problem should perhaps occupy a special session of a future Workshop!

On fabrication methods Stelzer pointed out the cost advantage of the electrostatic spray pyrolysis method - a capital cost of DM 10,000 to commence development. The most expensive part is the high voltage power supply. It should be able to coat complex shapes, as a true CVD, whereas PVD methods tend to be line-of-sight from source to deposit. Bossel queried the coverage of pores, to which Choy replied that a modified process was required. McEvoy asked about the field polarity, to be told by Choy that apparently it was not important but the details were being investigated. Stelzer asserted that for ceria a negative spray source with the substrate positive did not work, but that for YSZ both polarities are effective: Delft used a positive source, GH Duisburg negative for YSZ. Bossel compared the situation with electroplating where, due to electrostatic screening effects, the plating is most effective on peaks. Choy stated that on the contrary with the technique in question a very uniform conformal coating was obtained. Tagawa reported on Japanese experience with charged particle deposition, where the conductivity of the substrate is important. Choy stated that both conductive and nonconductive substrates had been used.

Steele pointed out, in regard to stability of electrostatic spray films, that Westinghouse had demonstrated 70,000 hours with 35m EVD films. A concern for submicron structures might be justified. Films >5m should be acceptable, at least for lower temperature operation. To the question of the most important component for degradation, Badwal suggested the interconnector, and after that the anode. Bossel pointed out that from a systems point of view 50,000 hours' service life may not be a favourable goal - it is chosen simply to compete with turbines. Combined cycle units have efficiencies approaching 60%, so fuel cells should not be offered in competition with such plants. Look for niche markets in order to launch the technology effectively: for emergency power supplies, only 20 hours' service may be demanded, for small single-cylinder motors ("lawn mowers") 500 hours, and for automotive 3000 - 5000 hours. So markets can be found if the costs are right - with cheap cells a 5000 hour lifetime can find applications. The same consideration applies for efficiency - for some applications 30% is more than enough! Steele said this was particularly true for <20 kW units, where IC engines are hopelessly inefficient. Here, however, heatup time and thermal cycling are important. The systems may be small and of lower efficiency, but operational flexibility is a must! Dubal accepted that there are niches, but these may be occupied by other types of fuel cell - for example PAFC, demonstrated to 30,000 hours in Geneva. For the IEA action commercial - natural gas - fuels were indicated. Natural gas is associated with stationary applications, for which lifetime is important. Badwal noted the two different markets mentioned, but stated that with time we cannot be content with niches, otherwise development funding will dry up. Bossel reaffirmed that these issues should not prevent marketing products in the reasonably short term.

The Meeting then ended with a reminder by the Operating Agent of future events: an Annex Meeting in association with the International Symposium in Aachen in June; a September Workshop in ECN specifically on these issues of lifetime and degradation which had just been discussed; and in May 1998, at a location still to be determined, a materials innovation joint workshop. There was also the possibility to organise a topical meeting on the issue which had stimulated so much discussion - the reference electrodes and theoretical definitions - should there be sufficient interest and motivation for that within the IEA SOFC group.

A.J. McEvoy,
LPI-DC, EPFL, Lausanne

Reference electrode configuration

A comment to the discussion on potential measurements, friday jan. 31.

First a few concepts dating back to the works of Brønsted and Guggenheim, but unfortunately deteriorating in modern textbooks on Physical Chemistry.

Electrochemical potential. Any charged species is subject to electrical as well as chemical interactions. The *escaping tendency* of a component, k, is described by the electrochemical potential

$$\bar{\mu}_k = \left(\frac{\partial G}{\partial n_k}\right)_{T,p} = \mu_k + z_k \mathrm{F}\phi \tag{1}$$

where ϕ is the electrical potential of the phase, ie. the work needed for transferring a unity charge without any chemical properties from infinity into the phase.

Voltmeter. A voltmeter is an instrument measuring the affinity, per unit charge, for electrons to pass through the instrument, from the *black* to the *red* terminal. Hence the reading is

$$\epsilon = \pi_{red} - \pi_{black} = -\frac{\bar{\mu}_{\mathrm{e}^-,red} - \bar{\mu}_{\mathrm{e}^- black}}{\mathrm{F}} \tag{2}$$

where $\pi = -\bar{\mu}_{\mathrm{e}^-}/\mathrm{F}$, the electromotive tension - or Fermi potential, is the measurable property, excluding contact potentials.

Electrochemical equilibrium. According to (1) the equilibrium condition for the general electrochemical reaction

$$\mathrm{Ox} + n\mathrm{e}^- \rightleftharpoons \mathrm{Red} \tag{3}$$

is

$$\bar{\mu}_{\mathrm{Ox}} + n\bar{\mu}_{e^-} = \bar{\mu}_{\mathrm{Red}} \tag{4}$$

yielding the single electrode potential equation

$$(\pi - \phi)^{eq} = (\pi - \phi)^{\circ} + \frac{\mathrm{R}T}{n\mathrm{F}} \ln \frac{a_{\mathrm{Ox}}}{a_{\mathrm{Red}}} \tag{5}$$

Non-equilibrium, overvoltage. Overvoltage, η, is defined as the deviation from equilibrium of the electrode reaction

$$\eta = (\pi - \phi) - (\pi - \phi)^{eq} \tag{6}$$

Potential gradients. In a homogeneous phase potential gradients are connected to non-equilibrium, i.e. to transport processes, and determined by

$$i = \sum z_j \mathrm{F} J_j = -\sum \frac{z_j \mathrm{F} u_j c_j}{\mathrm{N_A}} \frac{\mathrm{d}\bar{\mu}_j}{\mathrm{d}x} = -\sum \frac{z_j \mathrm{F} u_j c_j}{\mathrm{N_A}} \left(\frac{\mathrm{d}\mu_j}{\mathrm{d}x} + z_j \mathrm{F}\frac{\mathrm{d}\phi}{\mathrm{d}x}\right) \tag{7}$$

where u_j is the thermodynamic mobility (the reciprocal of the friction factor).

The statement here is:
If there is no gradient in the majority charge carrier concentration, (O^{2-} in YSZ), *any electric potential gradient in the electrolyte is entirely due to ohmic losses.*

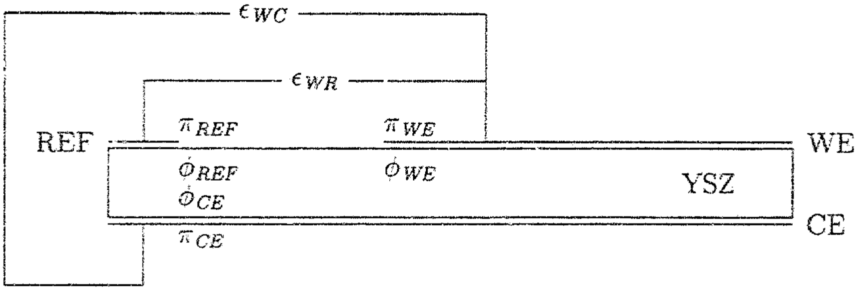

Figure 1: Fred van Heuveln reference electrode setup.

The Fred van Heuveln electrode configuration

In this electrode configuration the working electrode potential may be measured against the reference electrode or the counter electrode

$$\begin{aligned}\epsilon_{WR} &= \pi_{WE} - \pi_{REF} = (\pi - \phi)_{WE} + (\phi_{WE} - \phi_{REF}) - (\pi - \phi)_{REF} \quad (8)\\ \epsilon_{WC} &= \pi_{WE} - \pi_{CE} = (\pi - \phi)_{WE} + (\phi_{WE} - \phi_{CE}) - (\pi - \phi)_{CE} \quad (9)\end{aligned}$$

The difference between these two measurements are

$$\epsilon_{WR} - \epsilon_{WC} = (\pi - \phi)_{CE} + (\phi_{CE} - \phi_{REF}) - (\pi - \phi)_{REF} \quad (10)$$

Considering that the current density in the left part of the cell is extremely low, due to the electrolyte dimensions, there is no potential gradient in the electrolyte where the reference electrode is positioned, i.e.

$$(\phi_{CE} - \phi_{REF}) = 0 \quad (11)$$

For the same reason the reference electrode, as well as the reaction on the left part of the counter elctrode will be in equilibrium, and the difference between the two electrode potentials in eq.(10) is a thermodynamic quantity given by (5) - not depending on the overvoltage of the working electrode or the operating conditions of the counter electrode.

This brings us to the conclusion

Irrespective of the nature of the electrodes, the electrode configuration with asymmetrical working-counter electrodes is essentially a two-electrode configuration.

February 13, 1997
Torben Jacobsen, Dept. of Chemistry, Technical University of Denmark.
Eivind Skou, Dept. of Chemistry, University of Odense.

Registration list: 27 Jan. 1997

Badwal, S.P.S.,
Ceramic Fuel Cells Ltd.,
Monash Science & Technology Park,
710 Blackburn Road,
Clayton VIC 3168, Australia.
Phone: ()61 3 9558 6033
Fax: ()61 3 9558 6030
email: badwal@mst.csiro.au

Barthel, Knut Dr.
EMPA,
Feuerwerkerstr. 39,
Thun, Switzerland
Phone: ()41 33 228 2970
Fax: ()41 33 228 4490
email: knut.barthel@empa.ch

Bossel, Ulf Dr.,
Morgenacherstr. 2F,
CH 5452 Oberrohrdorf,
Switzerland
Phone: ()41 56 496 7292
Fax: ()41 56 4964412
email: ubossel@dial.eunet.ch

Choy, K.L. Dr.,
Dept. of Materials,
Imperial College,
Prince Consort Road,
London SW7 2BP, England.
Phone: ()44 171 594 6750
Fax: ()44 171 594 6750
email: k.choy@ic.ac.uk

Costamagna, Paola Dr.
ISTIC - Universita di Genova,
Via Opera Pia 15,
I-16145 Genova, Italy.
Phone: ()39 10 353 2589
Fax: ()39 10 353 2586
email: costama@istic.unige it

Divisek, Jiri Dr.
IEV- Forschungscentrum Jülich,
KFA - Jülich,
D-52425 Jülich, Germany
Phone: ()49 2461 613018
Fax: ()49 2461 616695,
email: rbe056@aix-sp.kfa-juelich.de

Dubal, Leo, Dr
Federal Office of Energy
CH.3003 Berne,
Switzerland
Phone: ()41 31 3225644
Fax: () 41 31 3842203
email: leo.dubal@bew.admin.ch

Goedickemeier, Martin, Dr.
Nonmetallic Materials Institute,
ETH - Zentrum, Sonneggstr. 5,
CH-8072 Zürich, Switzerland
Phone: ()41 1 632 3738
Fax: ()41 1 632 1132
email. mgoedi@nonmet.mat.ethz.ch

Gut, Beat, Dr.
EMPA, Abt. 123,
Ueberlandstr.129,
CH 8600 Dübendorf, Switzerland
Phone: ()41 1 823 4129
Fax: ()41 1 821 6244
email: beat.gut@empa.ch

Harvengt, Caroline Ms.,
Prototech AS,
Fantoftvegen 38,
N-5036 Fantoft, Bergen, Norway
Phone: ()47 5557 4110
Fax: ()47 5557 4114
email: caro@proto2.cmr.no

Ihara, Manabu Prof.
Dept. of Chemical System Engineering,
University of Tokyo,
Hongo 7-3-1, Bunkyo-ku, Tokyo 113, Japan.
Phone: ()81 3 5800 6940
Fax: ()81 3 5800 6940
email: ihara@chemsys.t.utokyo.ac.jp

Ihringer, Raphaele, Mr.
Labo. de Photonique et des Interfaces, LPI,
Ecole Polytechnique Fédérale de Lausanne,
CH-1015 Lausanne, Switzerland
Phone: ()41 21 693 4849
Fax: ()41 21 693 4111
email:

Jacobsen, Torben Dr.
Dept. of Chemistry,
Technical University of Denmark,
DK2800 Lyngby, Denmark
Phone: ()45 4525 2437
Fax: ()45 4593 4808
email: tj@kemi.dtu.dk

Kawada, Tatsuya Dr.,
Research Inst. for Scientific Measurements
Tohoku University,
2-1-1 Katahira, Aoba-ku,
Sendai 980-77, Japan.
Phone: ()81 22 217 5341
Fax: ()81 22 217 5343.
email: kawada@rism.tohoku.ac.jp

Kilner J.A. Prof.,
Dept. of Materials,
Imperial College,
Prince Consort Road,
London SW7 2BP, England.
Phone: ()44 171 594 6720
Fax: ()44 171 594 6720
email: j.kilner@ic.ac.uk

Kleinlogel, Christoph
Nonmetallic Materials Institute,
ETH - Zentrum, Sonneggstr. 5,
CH-8072 Zürich, Switzerland
Phone: ()41 1 632 3738
Fax: ()41 1 632 1132
email. cklein@nonmet.mat.ethz.ch

3

Kleitz, Michel Dr.,
LEPMI-ENSEEG BP75,
F-38402 St.-Martin d'Héres,
France
Phone: ()39 47682 6566
Fax: ()39 47682 6670
email: kleitz@ccomm.grenet.fr

Kornyshev, Alexei Prof.,
IEV, Forschungscentrum Jülich,
D-52425 Jülich,
Germany
Phone: ()49 2461 615171
Fax: ()49 2461 616695
email: a.kornyshev@kfa-juelich.de

Krugel, Albert Dr.-Ing.,
Institut für Werkstoffe der Elektrotechnik,
Universität Karlsruhe,
Hertzstrasse 16, Bau 40,
D-76187 Karlsruhe, Germany.
Phone: ()49 721 608 4532
Fax: ()49 721 608 4501
email:albert.krugel@etec.uni-karlsruhe.de

Lewin, Robert Dr.,
British Nuclear Fuels Ltd.,
Springfields, Preston, Lancs. PR4 0XJ,
England.
Phone: ()44 1772 763801
Fax: ()44 1772 762323
email: svb2@bnfl.co.uk

McEvoy, Augustin Dr. (Organiser).
Labo. de Photonique et des Interfaces, LPI,
Ecole Polytechnique Fédérale de Lausanne,
CH-1015 Lausanne, Switzerland
Phone: ()41 21 693 3689
Fax: ()41 21 693 4111
email: augustin.mcevoy@dcqm.epfl.ch

Middleton, Hugh, Dr.
Dept. of Chemical Engineering,
Imperial College,
London, England.
Phone: () 44 181 473 2553
Fax: () 44 171 584 3194
email: h.middleton@ic.ac.uk

Moens, Jan Dr.
Medicoat AG,
CH-5506 Mägenwil, Switzerland
Phone: () 41 62 889 7686
Fax: () 41 62 889 7688

Nabielek, Heinz Dr.,
IEV, Forschungscentrum Jülich,
D-52425 Jülich, Germany.
Germany
Phone: ()49 2461 613271
Fax: ()49 2461 618162
email: h.nabielek@kfa-juelich.de

Naoumidis, Aristides Dr.,
Forschungscentrum Jülich,
D-52425 Jülich, Germany
Phone: ()49 2461 613059
Fax: ()49 2461 625700
email: a.naoumidis@kfa-juelich.de

Nisancioglu, Kemal, Prof. (Organiser) 4
Labo. de Photonique et des Interfaces, LPI,
Ecole Polytechnique Fédérale de Lausanne,
CH-1015 Lausanne, Switzerland
Phone: ()41 21 693 6127
Fax: ()41 21 693 4111
email: kemal@igsun3.epfl.ch

Poulsen, Finn-Willy Dr.,
Materials Dept.,
Risoe National Lab.,
DK-4000 Roskilde, Denmark
Phone: ()45 4677 5721.
Fax: ()45 4635 1173
email: fwp@risoe.dk

Rambert, Serge Dr.,
Photonique et des Interfaces, LPI,
Ecole Polytechnique Fédérale de Lausanne,
CH-1015 Lausanne, Switzerland
Phone: ()41 21 693 3136Labo. de
Fax: ()41 21 693 4111
email: rambert@igcsun3.epfl.ch

Roux, Claude
LEPMI-ENSEEG, BP 75,
F-38402 St.-Martin d'Héres,
France
Phone: ()33 47682 6684
Fax: ()33 47682 6670
email:

Sasaki, Hirokazu Dr.
New Energy Development Orgainsation.
Sunshine 60, 29F, 3-1-1 Higashi-Ikebukuro,
Toshima-ku, Tokyo 170, Japan.
Phone: ()81 3 3987 9432
Fax: ()81 3 5992 5233
email: sasakihrk@nedo.go.jp

Schoonman, Joep Prof.
Faculty of Chemical Technology
and Materials Science,
Julianalaan 136,
2628 BL Delft, Netherlands
Phone: ()31 15 2782647
Fax: ()31 15 2788047
email: j.schoonman@stm.tudelft.nl

Sfeir, Joseph, Mr
Labo. de Photonique et des Interfaces, LPI,
Ecole Polytechnique Fédérale de Lausanne,
CH-1015 Lausanne, Switzerland
Phone:
Fax: ()41 21 693 4111
email:

Skou, Eivind Prof.,
Dept. of Chemistry,
Odense University,
DK-5230 Odense M,
Denmark
Phone:()45 66 5729 41
Fax: ()45 66 158780
email: ems@elkemi.chem.ou.dk

Steele, B.C.H. Prof.,
Dept. of Materials,
Imperial College,
Prince Consort Road,
London SW7 2BP, England
Phone: ()44 171 594 6744
Fax: ()44 171 584 3194
email: b.steele@ic.ac.uk

Stelzer N.H.L. Dr.,
Dept. of Chemical Technology and
and Materials Science,
Julianalaan 136,
2628 BL Delft, Netherlands.
Phone: ()31 15 2785536
Fax: ()31 15 2788047
email: n.stelzer@stm.tudelft.nl

Stochniol, Guido Dr.,
IWE - Forschungscentrum Jülich
D.52425 Jülich, Germany
Phone: ()49 2461 545994
Fax: ()49 2461 615700
email: g.stochniol@kfa-juelich.de

Sunde, Svein Dr.
Centre for Materials Science,
University of Oslo, N-0371 Oslo, Norway
Phone: ()
Fax: ()47 2295 8749
email:

Svensson, Ann-Mari Dr.,
Dept. of Electrochemistry,
National Technical University of Norway,
N-7034 Trondheim, Norway.
Phone: ()47 73 593969
Fax: ()47 73 594083
email: svensson@kjemi.unit.no

Takagi, Hiroshi Dr.,
R&D Division II, Murata Mfg. Co. Ltd.,
2288 Ohshinohara, Yasu,
Shiga 529-23, Japan.
Phone: ()81 775 868274
Fax: ()81 775 871923
email: takagihr@murata.co.jp

Taniguchi Shunsuke Dr.,
Sanyo Electric Co. Ltd.,
1-1 Dainichi-higashimachi,
Moriguchi City, Osaka 570. Japan
Phone: ()81 6 900 3553
Fax: ()81 6 900 3556
email: n55taniguchi@yd000.a1.sanyo.co.jp

Tunold, Reidar Prof.
Dept. of Electrochemistry,
Norwegian Technical University,
N-7034 Trondheim, Norway.
Phone: (947 7359 4043
Fax: ()47 7359 4083
email: tunold@kjemi.unit.no

Van herle, Jan
Labo. de Photonique et des Interfaces, LPI,
Ecole Polytechnique Fédérale de Lausanne,
CH-1015 Lausanne, Switzerland
Phone: ()41 21 693 3669
Fax: ()41 21 693 4111
email: vanherle@igcsun3.epfl.ch

6

van Heuveln, Fred, Dr.,
ECN, PO Box 1,
1755 ZG Petten,
Netherlands

Phone: ()31 224 564408
Fax: ()31 224 563491
email: vanheuveln@ecn.nl

von der Crone, Ulrich, Dr.,
IWE-2, Forschungscentrum Jülich,
D-52425 Jülich, Germany
Germany

Phone: ()49 2461 616056
Fax: ()49 2461 612455
email: u.v.d.crone@kfa-juelich.de

Weiss, Reinhard Dr.,
IWE - Forschungscentrum Jülich,
D-52425 Jülich,
Germany

Phone: ()49 2461 612898
Fax: ()49 2461 613699
email: r.weiss@kfa-juelich.de

Widmer, Sylvie Ms.,
Labo. de Photonique et des Interfaces, LPI,
Ecole Polytechnique Fédérale de Lausanne,
CH-1015 Lausanne, Switzerland

Phone: ()41 21 693 3136
Fax: ()41 21 693 4111
email: widmer@igcsun3.epfl.ch

Will, Julia Ms.,
Nonmetallic Materials Institute,
ETH - Zentrum, Sonneggstr. 5,
CH-8072 Zürich, Switzerland

Phone: ()41 1 632 3738
Fax: ()41 1 632 1132
email. jwill@nonmet.mat.ethz.ch

Yokokawa, Harumi, Dr.,
National Institute for Materials and
Chemical Research,
Tsukuba, Ibaraki 305, Japan

Phone: ()81 298 544542
Fax: ()81 298 544540
email: yokokawa@ccmail.nimc.go.jp

Deadline: 20 April 1997

SOFC-V

Forschungszentrum Jülich GmbH
Conference Service

D-52425 Jülich
Germany

Registration

SOFC-V Symposium

Deadline: 20 April 1997

Please use block letters

Name

First Name

Accompanying Person (non participant): Name

First Name

University / Institution / Company + Department

P. O. Box or Street Address

Postal Code Number + City

Country

Phone: .... Fax: .... E-Mail: ....

Registration Fee

Participants		DM 700	DM	______
Students		DM 250	DM	______
Accompanying	No. of adults	x DM 50	DM	______
Persons	No. of children......	x DM 25	DM	______
Scenic tour	No. of adults	x DM 120	DM	______
	No. of children......	x DM 60	DM	______
Technical Tour	....	x no charge		
	Total		DM	==========

Please pay the total in Deutsche Mark by one of the following alternatives:

- **Cheque** directly to Forschungszentrum Jülich GmbH, (preferred) Conference Service, 52425 Jülich, Germany
  Code: SOFC Symposium
- **Bank transfer to** Kreissparkasse Düren, D-52428 Jülich, Germany
  national: banking code 39550110
  international: swift code SDUEDE 33
  account No. 6569;
  in favour of Forschungszentrum Jülich GmbH;
  Code: SOFC Symposium

Hotel Reservation

Deadline: 20 April 1997

For a binding reservation please complete Category A B C D ☐ Single room ☐ Double room

☐ Shared double room

Date of arrival Date of departure No. of nights

Sex: ☐ male ☐ female

If the requested price category is not available, I will accept a room in category A B C D

Roommate:........................ ....

Special requests:

Date: .... Signature: ....

Return your registration before 20 April 1997 to Forschungszentrum Jülich, Conference Service, 52425 Jülich, Germany. Telefax: +49 2461 61-3830.

First Announcement

11th IEA SOFC Workshop: "SOFC Lifetime and Degradation"
Annex VII: SOFC under Real Operating Conditions
September 15-17, 1997
ECN, Petten, The Netherlands

This first announcement is to inform you about the planning of the 11th IEA SOFC Workshop in The Netherlands on 15-17 September 1997 and to invite for contributions to the Workshop. The Workshop is dealing with lifetime and degradation of SOFC and topics will include:

- Current status and demonstration of lifetime (systems, stacks, cells)
- Effects of operating conditions on lifetime
- Degradation strategy
- Materials aspects of degradation
- Improvement of lifetime

for which contributed papers are invited. Information about the format and submission of papers will be given in a next circular.

Please, use the attached form for pre-registration and for submitting titles.

For more information contact:
Joep Huijsmans
ECN
P.O. Box 1
1755 ZG PETTEN
The Netherlands
Phone : +31 224 564682
Fax : +31 224 563489
E-mail : huijsmans@ecn.nl

IEA
AIE

ECN

11th IEA SOFC Workshop: "SOFC Lifetime and Degradation"
Annex VII: SOFC under Real Operating Conditions
September 15-17, 1997
ECN, Petten, The Netherlands

PRE-REGISTRATION AND INVITATION FOR CONTRIBUTIONS

Name : ....
....

Address : ....
....
....

Telephone : ....
Fax : ....
E-mail : ....

☐ I am interested to participate in the Workshop and would like to obtain the next circular.

☐ I would like to present a paper.

Title : ....
....
....
....
....
....
....

Please, return to:

Dr. Joep P.P. Huijsmans
ECN
P.O. Box 1
1755 ZG PETTEN
The Netherlands

Phone : +31 224 564682
Fax : +31 224 563489
E-mail : huijsmans@ecn.nl

Distribution of copies of this form among interested colleagues is greatly appreciated.

The IEA Advanced Fuel Cells Programme

Background

The International Energy Agency (IEA) Implementing Agreement for a programme of research, development and demonstration on advanced fuel cells was signed by seven countries in Paris on April 2nd, 1990. Since that time a further eight countries have signed the Implementing Agreement and the programme has grown from two to ten annexes. Each annex defines a different task and is managed by an Operating Agent.

The aim of the IEA Advanced Fuel Cells programme is to advance the state of understanding of all Contracting Parties in the field of advanced fuel cells. It achieves this through a co-ordinated programme of research, technology development and system analysis on Molten Carbonate (MCFC), Solid Oxide (SOFC) and Polymer Electrolyte Fuel Cell (PEFC) systems.

There is a strong emphasis on information exchange through Task meetings, workshops and reports. The work is undertaken on a task-sharing basis with each participating country providing an agreed level of effort over the period of the Task.

Participants

There are currently fifteen signatories to the Implementing Agreement: Australia, Canada, Denmark, France, Germany, Italy, Japan, Netherlands, New Zealand, Norway, Spain, Sweden, Switzerland, United Kingdom, United States, and the programme continues to actively encourage new participants.

Programme (1990-1995)

The first phase of the programme ran from April 1990 to December 1995 and comprised the following tasks.

Annex I	Molten Carbonate Fuel Cell Balance of Plant Analysis
Annex II	Solid Oxide Fuel Cells Modelling and Evaluation
Annex III	Molten Carbonate Fuel Cell Materials and Electrochemistry
Annex IV	Polymer Electrolyte Fuel Cells
Annex V	Systems Analysis

New Programme (1996-1998)

During 1996, the programme initiated five new tasks which form a co-ordinated programme for the period 1996-1998 covering fuel cell technology and its potential applications in stationary power generation and transport. The new tasks are as follows:

Annex VI	Molten Carbonate Fuel Cells under Real Operating Conditions
Annex VII	Solid Oxide Fuel Cells under Real Operating Conditions
Annex VIII	Polymer Electrolyte Fuel Cells
Annex IX	Fuel Cell Systems for Stationary Applications
Annex X	Fuel Cell Systems for Transport Applications

IEA Advanced Fuel Cells Programme 1996-1998

No.	Annex	Subtasks and Activities	Operating Agent	Participating Countries
VI	MCFC Under Real Operating Conditions	1 Stack Performance and Endurance 2 Test Procedures and Standardisation 3 Development of Balance of Plant Technology	Dr L Plomp ECN The Netherlands	Germany Italy Japan Netherlands
VII	SOFC Under Real Operating Conditions	1 Balance of Plant Technology 2 Stack and Cell Operating Conditions 3 Materials Under Operating Conditions 4 Materials Innovation	Dr H Nabielek KFA Jülich Germany	Australia Denmark France Germany Japan Netherlands New Zealand Norway Switzerland UK USA
VIII	PEFC	1 Improved Single Cells 2 Improved Stack Materials and Concepts 3 Operating Parameters: Effects on Performance and Lifetime 4 Balance of Plant Components and Systems 5 Direct Methanol Fuel Cell	Dr R Kumar Argonne National Laboratory USA	Canada Germany Italy Japan Netherlands Switzerland UK
IX	Fuel Cell Systems for Stationary Applications	1 Parameters Affecting the Economy and Competitiveness of Fuel Cells 2 Current Technology Level to Commercialisation 3 Environmental Analysis	Mr L Sjunnesson Sydkraft AB Sweden	Germany Italy Japan Netherlands Norway Sweden
X	Fuel Cell Systems for Transport Applications	1 Economics and System Analysis 2 Balances of Life Cycles 3 Fuel Supply Systems	Dr B Höhlein KFA Jülich Germany	Germany Netherlands USA